THE UNIVERSITY OF
SYDNEY

Atomic Scale Microscopy of Zr-based Bulk Metallic Glasses Processed by Various Routes

A thesis submitted in fulfillment of the requirements for the degree of
Doctor of Philosophy

Huma Bilal
MS (Engineering)

School of Aerospace, Mechanical and Mechatronics Engineering
Australian Centre for Microscopy & Microanalysis

The University of Sydney

2022

THE UNIVERSITY OF
SYDNEY

COPYRIGHT AND USE OF THIS THESIS

THE UNIVERSITY OF
SYDNEY

Authorship Attribution Statement

Chapter 6 of this thesis contains materials from the published work.

Bilal, H., Nomoto, K., Gludovatz, B., Kruzic, J.J., Ceguerra, A.V. and Ringer, S.P., 2021. Atom Probe Analysis of a Zr-based Bulk Metallic Glass. *Microscopy and Microanalysis*, pp.1-11.

Kühbach, M., London, A.J., Wang, J., Schreiber, D.K., Martin, F.M., Ghamarian, I., Bilal, H. and Ceguerra, A.V., 2021. Community-driven methods for open and reproducible software tools for analyzing datasets from atom probe microscopy. *Microscopy and Microanalysis*, pp.1-16.

I am the first author in first publication, and I participated in the conceptualisation, methodology, investigation, visualization, writing - original draft, writing - review and editing. I contributed to the second publication for the APT mass spectra ranging method's conceptualisation, methodology, investigation and its writing.

Part of Chapter 10 of this thesis is published.

Nomoto, K., Ceguerra, A.V., Gammer, C., Li, B., Bilal, H., Hohenwarter, A., Gludovatz, B., Eckert, J., Ringer, S.P. and Kruzic, J.J., 2021. Medium-range order dictates local hardness in bulk metallic glasses. *Materials Today*, *44*, pp.48-57.

I participated in the methodology, investigation, writing - review and editing of this work.

Student name, signature, date
Huma Bilal, June 21st, 2022

Supervisor name, signature, date
Simon P. Ringer, June 26th, 2022

THE UNIVERSITY OF
SYDNEY

Atomic Scale Microscopy of Zr-based Bulk Metallic Glasses Processed by Various Routes

A thesis submitted in fulfillment of the requirements for the degree of
Doctor of Philosophy

Huma Bilal
MS (Engineering)

School of Aerospace, Mechanical and Mechatronics Engineering
Australian Centre for Microscopy & Microanalysis

The University of Sydney

2022

This thesis is dedicated to my family, especially my husband, as it would not be possible for me to complete my research without his constant backing. Their courage and unconditional support gave me strength to accomplish this goal. I am what I am because of all of them.

Certificate of Originality

This is to certify that the content of this thesis is my own work, to the best of my knowledge. This thesis has not been submitted for any degree or other purposes.

I certify that the intellectual content of this thesis is the product of my own work and that any contribution made to the research by others, with whom I have worked at The University of Sydney or elsewhere, is explicitly acknowledged in the thesis.

I also declare that this thesis is the product of my own work, except to the extent that assistance from others in the project's design and conception or in style, presentation and linguistic expression is acknowledged.

Signature _____

Huma Bilal

June 2022

Abstract

Bulk metallic glasses (BMGs) can be engineered to exhibit a rare combination of strength and toughness that is difficult to achieve by other materials. These properties make them favourable for a diverse range of engineering applications, including transportation, aerospace, biomedical devices, and customised consumer products. However, their disordered amorphous structure does not support deformation by dislocation movement. Instead, catastrophic failure can happen when relatively few shear bands localise, invoking brittle fracture. Their fracture toughness can be engineered to achieve high values, but deformation localisation around a single shear band could risk failure. Such unreliable behaviour has limited their industrial development as structural materials. It is necessary to improve our understanding of their microstructure-property-processing relationship to engineer resilient BMGs. However, it is not yet clear how to quantitatively link microstructural features to processing and mechanical properties in BMGs. This is fundamental because of the difficulties in quantifying the chemical and geometric aspects of their amorphous structure. It is this challenge that this thesis seeks to tackle.

Improved strength and ductility are important properties for enabling the commercial use of BMGs. There is increasing consensus that shear band multiplication enhances plastic deformation in these materials. Therefore, a goal of thermomechanical processing is to create microstructures that enable rejuvenation of the BMG atomic structure. Microstructural heterogeneities that facilitate multiple shear band initiation provide an effective strategy to prevent shear localisation. The ultimate goal, therefore, is to understand the links between their glassy structure and the optimisation of their mechanical properties. Advanced diffraction, microscopy and simulation studies have already advanced many critical attributes of the microstructure of BMGs, and these are reviewed herein. It is clear that resolution limitations and other technical constraints have limited our ability to access a thorough characterisation of the chemical and structural information of BMGs. Structural characterisation becomes especially complicated with quaternary, quinary and other higher-order BMGs. A comprehensive quantification process for evaluating microstructure-property-processing evolution is not yet available.

The aim of this thesis was to quantitatively analyse the structural features contributing to local hardness variations in thermomechanically processed zirconium (Zr)-based BMGs. Advanced atom probe tomography (APT) techniques were used to observe structural and chemical changes in these BMGs. APT generates extensive data for quantitative analyses at the atomic-scale and in 3D. Yet, there is a paucity of APT studies of BMGs', largely because of the complexity associated with the tomographic reconstruction and the data analysis in amorphous materials.

The operational parameters for APT were optimised and tested for robust data outcomes. An approach to the reconstruction was validated and the phenomenon of clustered evaporation, prevalent in APT studies of BMGs, was investigated in detail. A clear basis for discriminating signal from noise/artefacts was established and was named "peak-based ranging". Additionally, an ab-initio molecular dynamic (AIMD) simulation was used to simulate the atomistic distribution in a Zr-based BMG. Solute-rich clusters were observed in the simulated BMG. APT cluster analysis was used extensively and shown to be effective in the characterisation of nanoscale heterogeneities in the BMG microstructure. Similar regions were earlier discovered in the simulated data. This established a platform for a direct comparison of the experimental and simulation studies. The chemical composition of the nanoscale heterogeneities was roughly $Zr_{27}Cu_{29}Al_{21}Ni_{19}Nb_4$ (at. %) in $Zr_{63.96}Cu_{13.36}Ni_{10.29}Al_{11.04}Nb_{1.25}$ (at. %), and $Zr_{22}Cu_{29}Al_{17}Ni_{23}Ti_9$ (at. %) in $Zr_{52.5}Cu_{17.9}Ni_{14.6}Al_{10}Ti_5$ (at. %). Their chemistry was experimentally reported herein for the first time.

APT cluster analysis revealed the nature of the solute-rich clusters observed in the regions of locally high and low hardness, respectively, in the Zr-based BMGs. The sizes, number densities, and volume fractions of the atomic clusters were correlated to the material's local softening. The cluster sizes ranged from six atoms to a few hundred atoms, corresponding to the short-range order (SRO) and medium-range order (MRO) length scales and a threshold devised to distinguish between them based on size (number of atoms). Clusters observed in APT assigned as MRO regions were found synonymous to the shear band nucleation zones. These APT clusters were correlated with the corresponding results from transmission electron microscopy (TEM). The APT results complemented the TEM results by providing new information on the chemistry, volume fractions and the number densities of these nanoscale heterogeneities.

Beyond the novel methodological rigor introduced here, the findings provide a new, independent validation of the inverse correlation between local hardness and size of the MRO regions. Moreover, the work enables an assessment of the chemical composition of these regions, providing a novel handle on the quest for understanding the relationships between the microstructure, properties, and processing in BMGs.

Acknowledgements

If someone claims that a PhD is one person's work, it would be an understatement because it involves tremendous input from the supervisors and fellow researchers. Without the invaluable contribution from them, the research work is nothing but a hollow domain. It takes a whole team to build a PhD. Undertaking a PhD is not an easy task; the journey is long and hard, but it ultimately pays off in the form of one of the most rewarding and enlightening experiences one can get. The research work and a complete psychological and mental transformation make it an important achievement in academic education. There are many people whom I want to thank for their help and support during this PhD work.

First and foremost, I would like to acknowledge my supervisor Prof Simon P. Ringer, for the tremendous encouragement and belief in my research work over the past years. It has been an absolute privilege working with him, and he has been a true inspiration for me. Having a supervisor like him was a real blessing, especially amidst the pandemic. He knows how to steer the attention of a researcher towards crucial yet straightforward details. His phrase, “find the simple approach”, has been served as a beacon during complicated situations. I can't thank him enough. I specifically remember a crucial point during my research where it seemed as if I had reached a dead-end. It was his polite and supportive attitude that kept me going. For this, I am grateful to him for life.

Similarly, I would like to extend my gratitude to my co-supervisors, Dr Anna V. Ceguerra and Dr Keita Nomoto, who have become good friends now. Anna is like a research encyclopedia who had her doors always open for me. I have learnt many skills from her, and I appreciate her always being available to bounce ideas off and discuss work, among other things - it has been a blast! Dr Keita Nomoto is another important academic in my research journey. I have no words to explain the level of support he has provided me. He is the most humble and hardworking individual; I have ever seen in my life. He knows so much, yet he never flaunts his knowledge. He has enormously guided me and helped me to polish my work both technically and linguistically. I wish him the very best for his future as he deserves much success.

Additionally, I would like to acknowledge the collaboration with the University of New South Wales (UNSW) team comprising Prof Jamie Jay Kruzic, A/Prof Bernd Gludovatz and Dr Bosong Li. Their contribution towards this project is highly acknowledged, especially their time and valuable suggestions via regular group meetings. The UNSW also provided the material. Prof Jamie Jay Kruzic and A/Prof Bernd Gludovatz helped improve the shape of the research, whereas Dr Bosong Li carried out the microhardness testing in this study along with beneficial research conversations. Partial funding for this work from the ARC (No. DP180101393) is gratefully acknowledged.

A special thanks to the administrative, scientific and technical support from the staff and students at the School of Aerospace, Mechanical and Mechatronic Engineering (AMME), Sydney Microscopy and Microanalysis (SMM) and Microscopy Australia (MA) at the University of Sydney. Prof Julie Cairney's peaceful nature has provided a friendly environment in SMM, and I commend her for creating a positive and cooperative atmosphere for new researchers in the Madsen building. Dr Vijay Bhatia has similar qualities, who often feel like an unofficial supervisor with his enthusiasm for a good quality research environment. I am also grateful to Dr Takanori Sato for the atom probe knowledge facilitated to me by him. I am grateful for the help and technical support of Ashalatha Indiradevi Kamalasanan Pillai, Ingrid McCarroll, Katja Eder, Limei Yang, Mathew Foley, Mehdi Eizadjou, and Jacob Byrnes.

Another special appreciation goes out to William Davids, who was particularly supportive with learning and support for computer coding – I could not have done it without him. If I could, I would write his name with golden ink as he has been a good friend and supportive colleague since our very first meeting. A person whom you can count on, day in day out. Thank you for being such a lovely human being, Will! I have learnt a lot from you, and I wish you the very best of luck in future in the research field. I do not doubt that you will ace it. Another special mention must be given to Chim (Qi Wang), a close friend and colleague, the whole way through. Other honourable mentions are Apurv Yadav, Bryan Lim, Han Mai, Mengwei He, and other PhD fellows.

I am also very appreciative to Drs: Carl Sui, Andrew Breen, Hansheng Chen, Suqin Zhu, Steven Moody, Jiangtao Qu and Daniel Haley for fruitful discussions and support over the past several years. I would also like to acknowledge the wider atom probe community for their support and encouragement towards PhD students such as myself. In particular, I would like to thank Eric Strennen, Brian Geiser for their support on technical questions regarding the atom probe. Their timely support helped me stay persistent with my research even during COVID. I would also like to thank the folks at CAMECA®.

Finally, I would like to thank my friends and family. A special thank you goes to my husband, Muhammad Bilal, who stood by me throughout this entire time and put up with my obnoxious behaviours from time to time during my PhD. My adorable twins, Zain and Ayan were extremely understanding during this time. I love you both very much, and I can't say thank you enough for your unconditional love and support towards me. A huge thanks to my siblings, especially Ayesha Jaffar and Uzma Hammad, who constantly reminded me of my strengths. To my father, Muhammad Anwar Chaudhary, you are the best dad in the whole wide world. My mom, Fehmida Anwar is not alive but mom! You have been with me the whole time, and thanks for raising me to stand on my own. I thank all my family and friends for their encouragement and support throughout this PhD journey. Even if I have missed any names, you guys are in my heart and mind all the time. Thank you all.

Table of Contents

List of Figures:

List of Tables

List of Abbreviations

APT	Atom Probe Tomography
BMG	Bulk Metallic Glass
HPT	High Pressure Torsion
HR	Hard Region
ICP-AES	Inductively Coupled Plasma Atomic Emission Spectroscopy
MRO	Medium Range Order
NBED	Nano Beam Electron Diffraction
ROI	Region of Interest
SAED	Selective Area Electron Diffraction
SR	Soft Region
SRO	Short Range Order
STZ	Shear Transformation Zones
TC	Thermally Cycled
TEM	Transmission Electron Microscopy
VP	Voronoi Polyhedra
XRD	X-ray Diffraction

PART I

Introductory Chapters
(Chapter 1-4)

1 INTRODUCTION

1.1 Overview

Scientists are in constant search of modified materials that could exhibit combined properties of typical solid-state materials, i.e., plastics, ceramics and metals. Metallic glasses are one such example with thermoplastic formability of plastics, and strength and toughness like metallic alloys [1]. Like all materials, there exist challenges to their practical use, like balancing their strength, plasticity, and their stability under applied stresses. Since their discovery, scientists have been continuously trying to improve and stabilise the physical and mechanical properties of metallic glasses. This is of significant technological importance and interest, given their remarkable mechanical properties. For example, BMGs are considered potential structural materials due to their higher tensile yield strength of ~5 GPa and elastic strain of up to 2% [2-4], but require a clear understanding of the microstructure-property-processing relationship.

As materials scientists, we seek to understand the nature of a material's microstructure, which governs the material's structural and functional properties. However, unlike other metallic alloys, the internal structure of metallic glasses does not possess long-range order and is therefore referred to as amorphous or glassy. The absence of periodic order disables representing their atomic structure through the Bravais lattice unit cells, such as face centred-, body centred- cubic or other crystal structures. Their amorphous atomic structure is the source of great challenges in defining their microstructural attributes. The quantitative assessment of these attributes is essential for the purpose of establishing relationships between microstructure, processing, and properties. Such relationships, so prevalent in the field of materials science and engineering, are a crucial enabler for industrial scale materials technology.

It is a well-established approach that a metallic glass's behaviour can be transformed from brittle to ductile by different thermomechanical processes [5-7]. These processes, in turn, enhance structural heterogeneities that are commonly referred to as hard and soft regions inside the metallic glass structure [6]. The shear band localisation is supressed by the size and dispersion of these regions, facilitating multiple shear bands. However, if the number density of the heterogeneities is too high, this can adversely affect the ductility of the glass [8]. This situation invites a thorough investigation into the chemical and structural characteristics of these local regions. This would also assist in the design of new metallic glasses with enhanced properties e.g., plasticity and fracture toughness. Characterising the structure and chemistry of these regions is the primary goal of this thesis.

Advanced microscopy and diffraction techniques have already contributed much to the analysis of the atomic-scale structure of metallic glasses [9-12]. However, the lack of repeatable structural motifs that produce strong signals in scattering experiments with e.g., electrons, X-rays or neutrons, coupled with the multi-length scale challenges which span from the atomic-scale to the scale of heterogeneities, which is the tens of microns; all conspire to impose limits on what can be achieved using the 2D technique. The 2D approach does not always reveal an accurate picture, as demonstrated in Figure 1.1. This limitation was a primary motivation behind opting 3D microscopy for BMG analysis.

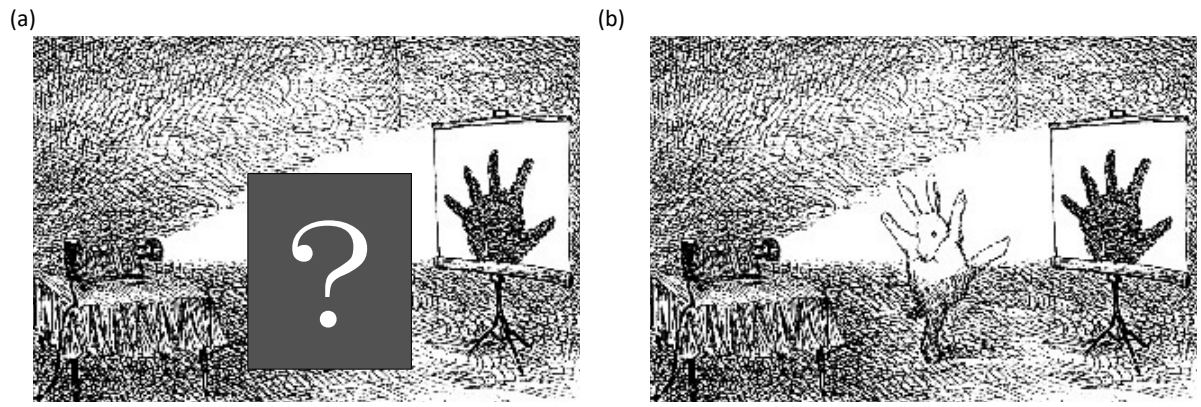

Figure 1.1: The incapability of 2D projection is illustrated by (a) observing the object only through its 2D projection and (b) the contrast between the actual image and its projection (John O' Brien; © 1991 The New Yorker, reproduced from [13]).

The advent of state-of-the-art 3D microscopy techniques such as electron tomography and atom probe tomography (APT), offer new opportunities in the characterisation of metallic glasses. This study applied APT to study the structure and, most importantly, the chemistry of the aforementioned local heterogeneities within the metallic glass microstructure. The emphasis was to explore and understand their microstructural evolution with local hardness variations. It was intended that such linkages will contribute to overcoming the hurdles in commercialising these materials for large-scale applications, by designing a reliable and repeatable metallic glass structure, in future. Thus, a metallic glass could be quantitatively analysed based on local heterogeneities for quality control assessment, in the same way diffraction data is used to assess crystalline materials. APT is not commonly considered for quantifying the local heterogeneities in homogeneous/monolithic metallic glasses as it has its challenges. This is because there are uncertainties around how the field evaporation process operate in the case of metallic glasses [14]. Indeed, the limited work in this field was the primary reason for me to pursue it further, and the following quotation from a famous physicist helped me stay persistent during my research journey:

> "*Study hard what interests you the most, in the most undisciplined, irrelevant and original manner possible."* —— Feynman, R. [15]

This thesis presents a new assessment framework that provides clear criteria for the utilisation of the analytical capabilities of APT for the atomistic characterisation of metallic glasses. This study is focused on zirconium (Zr)-based metallic glasses, which are widely studied and so much reference data is available. Their cost-effectiveness and relatively higher fracture toughness properties have also attracted technological interests. The goal was to quantitatively analyse the heterogeneities within these metallic glasses as a step towards more comprehensive microstructure-property-process relationship.

1.2 Thesis Outline

Below are brief descriptions of the various chapters of this thesis:

In Chapter 2, a brief literature review of the history, properties, potential applications, and limitations of the metallic glasses, is presented. The different thermomechanical processes are discussed, along with their impact on metallic glass structure. Afterwards, various theories are reviewed that are developed to explain the structural configurations of the metallic glasses, over the course of time. Relevant theories related to these structural configurations and deformation mechanism are discussed in some detail. Subsequently, the different characterisation techniques used by researchers are described, along with their various strengths and limitations in analysing the microstructure of metallic glasses.

A summary is presented, highlighting significant features for investigating the Zr-based metallic glasses, gaps in knowledge, and the potential for APT in the analysis of metallic glasses. These lead the readers to Chapter 3, where primary aims and scope of this thesis are summarised.

The materials and methods employed in the thesis are discussed in Chapter 4. This chapter is subdivided into different sections detailing the materials, sample preparation processes, characterisation techniques used in the research such as, transmission electron microscopy (TEM), APT, and computer simulation. Particular emphasis is given to the APT experimental operation, reconstruction strategy, and cluster analysis approaches. This overview of the experimental procedure sets the scene for the more detailed methodology development set out in later chapters.

Chapter 5 and the subsequent chapters present the experimental results and ensuring discussions. Chapter 5 deals with the computer simulation of a specific Zr-based metallic glass (Vitreloy-105) for pre-assessment of its structural and chemical features. Partial pair distribution function, Voronoi polyhedral analysis, co-ordination number and local chemical order analyses are employed for structural characterisation of the simulated metallic glasses. At the end of this chapter, a basic APT cluster analysis approach is applied to the simulation, to assess the feasibility of APT utilisation in generating benchmark structural characterisation of Zr-based metallic glasses.

Chapter 6 addresses the limitations and uncertainties in the application of APT to metallic glasses. Here, we establish a methodology for selecting APT operating parameters for the analysis of metallic glasses via both quantitative and qualitative factors. Other significant issues in the APT analysis of glasses such as, ranging style for mass spectra peaks and the non-uniform field evaporation phenomenon in metallic glasses, are also discussed. The broader application of this methodology in analysing specific elemental proportions within a metallic glass is demonstrated. This chapter concludes with a summary about the impact of different experimental parameters on the assessment of the structure and chemistry of metallic glasses, and an outlook on the application of APT to the characterisation of metallic glasses.

Chapter 7 analyses the composition of both thermally cycled and high-pressure torsion deformed Zr-based metallic glasses, in local variable hardness regions, by employing the methodology developed in the previous chapter. This step is performed to assess whether the hardness variations in the various local regions are linked with the bulk composition variation or not.

Chapter 8 presents the solute-specific cluster analysis for the locally variable hardness regions of the thermally cycled Zr-based metallic glass. The clusters are quantified based on their sizes, number densities, and volume fractions. The parameters are then compared between local regions of the metallic glasses for any structural variations. Moreover, the chemical compositions of these clusters and their surrounding matrix are considered in detail.

Chapter 9 demonstrates the solute-specific cluster analysis between the locally variable hardness regions of the high-pressure torsion Zr-based metallic glass and its fractured surface. The influence of the permanent deformation on the changes in the solute-rich clusters is analysed through such comparison. This approach was used to investigate possible relationship between these clusters and the material's plastic deformation.

Chapter 10 combines the APT study with the TEM study and summarises the similarities and differences of the two techniques. The results are then discussed, to effectively present an overview of local heterogeneities within the Zr-based metallic glasses.

Finally, Chapter 11 presents the overall summary of the results and conclusions. It also highlights a few of the future work possibilities. Appendices contain supporting information, published works and a list of presentations during this PhD candidature.

2 LITERATURE REVIEW

2.1 Why Metallic Glasses?

Metallic glasses are a type of advanced material that exhibit the strength of metals and the formability of plastics [1]. Their strength, hardness and high resistance to corrosion make them a potential candidate for numerous industrial applications and thus popular among researchers [16].

Metallic glasses are non-crystalline solids formed by melting metallic and/or non-metallic elements together and cooling them rapidly below their glassy temperature (Tg). Rapid quenching from the molten state is needed to freeze the amorphous structure quickly, preventing an equilibrium crystalline structure from forming. A schematic of the glass forming process is shown in Figure 2.1. Metallic glasses (<100 μm- metallic ribbons) were initially reported in 1960 by Pol Duwez et al. [17] at Caltech (USA), using an $Au_{75}Si_{25}$ binary system. The size of earlier metallic glasses was limited due to the cooling rate limitations (10^6 Ks^{-1}) [18]. The resulting metallic glass was brittle and highly unstable at room temperature.

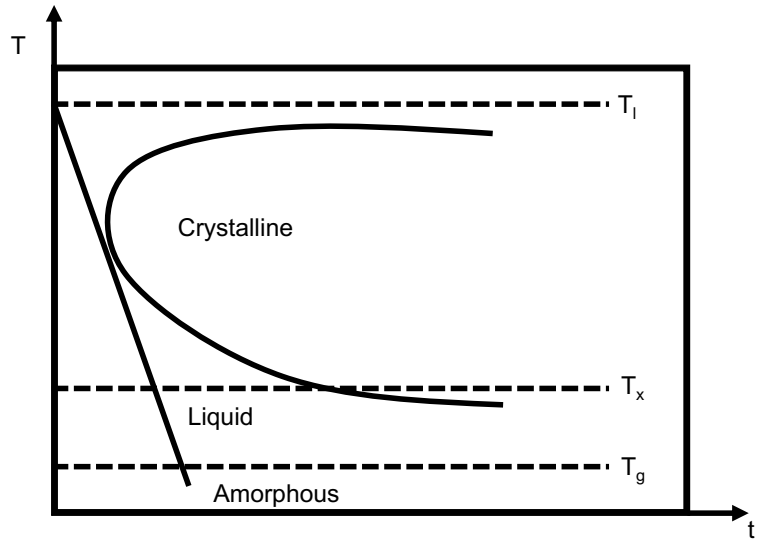

Figure 2.1:Time temperature transformation (TTT) schematic demonstrating amorphous metallic glass formation with a fast-cooling rate to prevent crystallisation. Here, T_l, T_x T_g denotes liquid, crystallisation, and glass transition temperatures, respectively (reprinted from [19]).

2.1.1 Development of Bulk Metallic Glasses

Metallic glasses transitioned to bulk metallic glasses (BMGs) during the 1970s-1980s, with ternary compositions and slower quenching rates. A BMG is a metallic glass with the smallest dimension greater than one millimetre (mm) [6]. However, it should be noted that throughout the thesis, the terms metallic glasses and BMGs, will be used synonymously.

Heavy metals like Pd, Pt or Au were initially used with Si for manufacturing BMGs. Several metallic glasses were discovered with a cooling rate up to 100 Ks^{-1} in 1990 [20, 21]. The slower quenching was made possible by adding multiple elements. Variable sized atomic species restricted crystallisation by limiting the rearrangement of multiple atomic species in proper order, forming a densely packed random structure inside the BMGs [7]. It was easily possible to produce large-sized (> 1cm) BMGs by that time [6].

Most of the atomic pairs in a BMG have negative mixing enthalpies [22]. However, it was later realised that adding at least one element-pair with a positive enthalpy of mixing could improve their glass-forming ability, e.g., Ni-Cu (3.6 $kJmol^{-1}$) bond pair addition [23]. The transition from metallic glasses to BMGs, with the increase in the critical casting thickness, is shown in Figure 2.2.

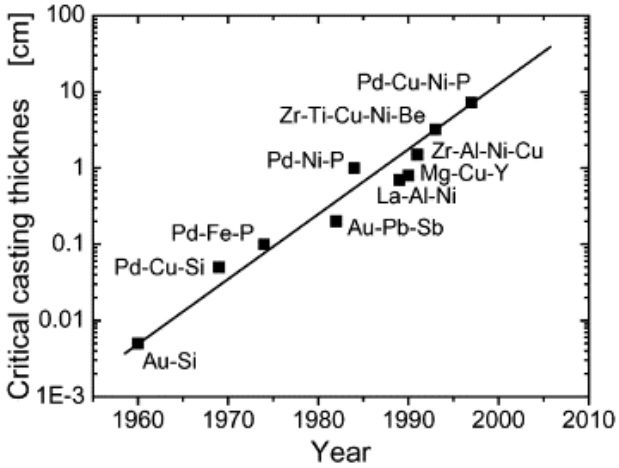

Figure 2.2: History of metallic glass formation in the first 40 years with critical casting thickness variations (reprinted from [1]).

The discovery of BMGs with relatively inexpensive elements came around the same time (1990s). Many quaternary and quinary BMGs were manufactured with inexpensive elements such as Zr, Mg, Fe etc. The first Zr-based BMG was named Vitreloy-1, with the composition $Zr_{41.2}Ti_{13.8}Cu_{12.5}Ni_{10.0}Be_{22.5}$ (at. %) [24]. Two of the early compositions for Zr-based BMGs with larger sizes (>10 mm) are presented in Table 2.1. These BMGs exhibited remarkable physical and mechanical properties [6]. The BMGs typically exhibit better mechanical, chemical, and magnetic properties than the corresponding crystalline alloys due to the absence of grain boundaries and crystalline defects in their amorphous structure.

Table 2.1: Summary of earlier Zr-based BMGs with sizes > 10 mm.

#	Composition	Critical Size D_c (mm)	Processing	Year	Reference
1	$Zr_{41.2}Ti_{13.8}Cu_{12.5}Ni_{10}Be_{22.5}$	14	Copper mould casting	1993	[24]
2	$Zr_{65}Al_{7.5}Ni_{10}Cu_{17.5}$	16	Water quenching	1993	[21]

2.2 Mechanical Properties of Zr-based BMGs

Out of all the properties, the fracture toughness of BMGs is the most significant mechanical property. Their fracture toughness is higher than many metals and metallic alloys (Figure 2.3). Demetriou [25] discovered a highly damage-tolerant BMG, Pd-Ag-P-Si-Ge. This discovery further boosted the aim of having different BMGs with good fracture toughness. However, cost-effectiveness is another crucial component for industrial applications. Research is underway on attaining good toughness properties in relatively cheaper BMGs [26]. Zr-based BMGs are an excellent candidate in this context. Their cost-effectiveness, corrosion resistance and good biocompatibility make them feasible for several applications, including their use as structural materials [27, 28].

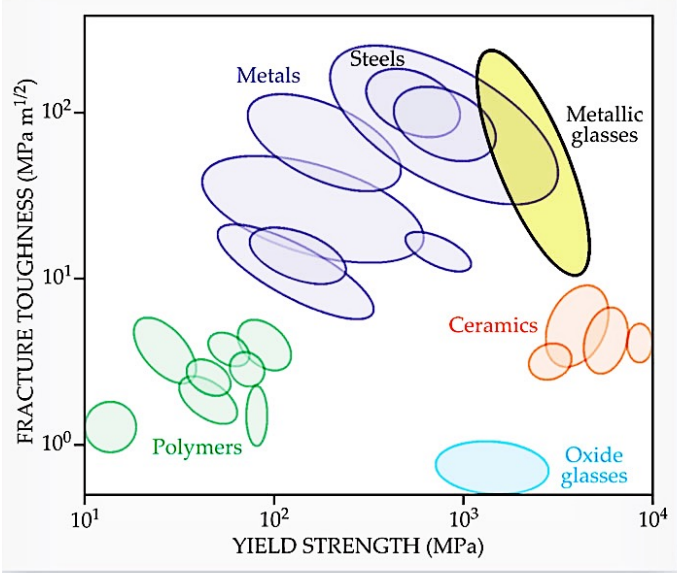

Figure 2.3: Ashby plot of fracture toughness of various materials compared to yield strength (reprinted from[29]).

Zr-based BMGs exhibit a good combination of high yield strength (~1-5 GPa) and relatively higher fracture toughness with an elastic strain limit of about 2% [6]. Their bending flexural strength is about 3-3.9 GPa, which is more than twice compared to Zr- or Ti- crystalline alloys [30]. The fracture surface of metallic glasses makes ~45° angle along the tensile loading axis, which is the property of a tensile material. Although metallic glasses do not exhibit enormous tensile elongation, their fracture surface does not pose a 90° angle relative to the tensile loading axis like brittle material, indicating their ductile behaviour.

Good bending ductility was observed in thin metallic ribbons with numerous shear bands formation near the deformation region [31, 32]. However, the properties in BMGs are size-dependent. Therefore, good bending ductility can only be achieved up to a certain critical thickness and may approach zero beyond it. Similarly, during the compression test, the plastic strain rate can reach as high as 80% when the combined specimen's height and shear band instability index has a particular value ($\lambda_{critical}$) [33]. Beyond this limit, the sample exhibits similar fracture surface characteristics as during the tensile test. However, there is no universally accepted model to predict when loss of ductility and shear band localisation could happen. The unpredictable nature of shear band localisation is the cause of catastrophic failure in metallic glasses, especially those with brittle nature. It is a severe limitation to their use as structural materials.

Despite their excellent bending ductility (Figure 2.4 a,c), their tensile elongation is limited to less than 1% or even zero due to the shear band localisation in some cases (Figure 2.4.b,d).

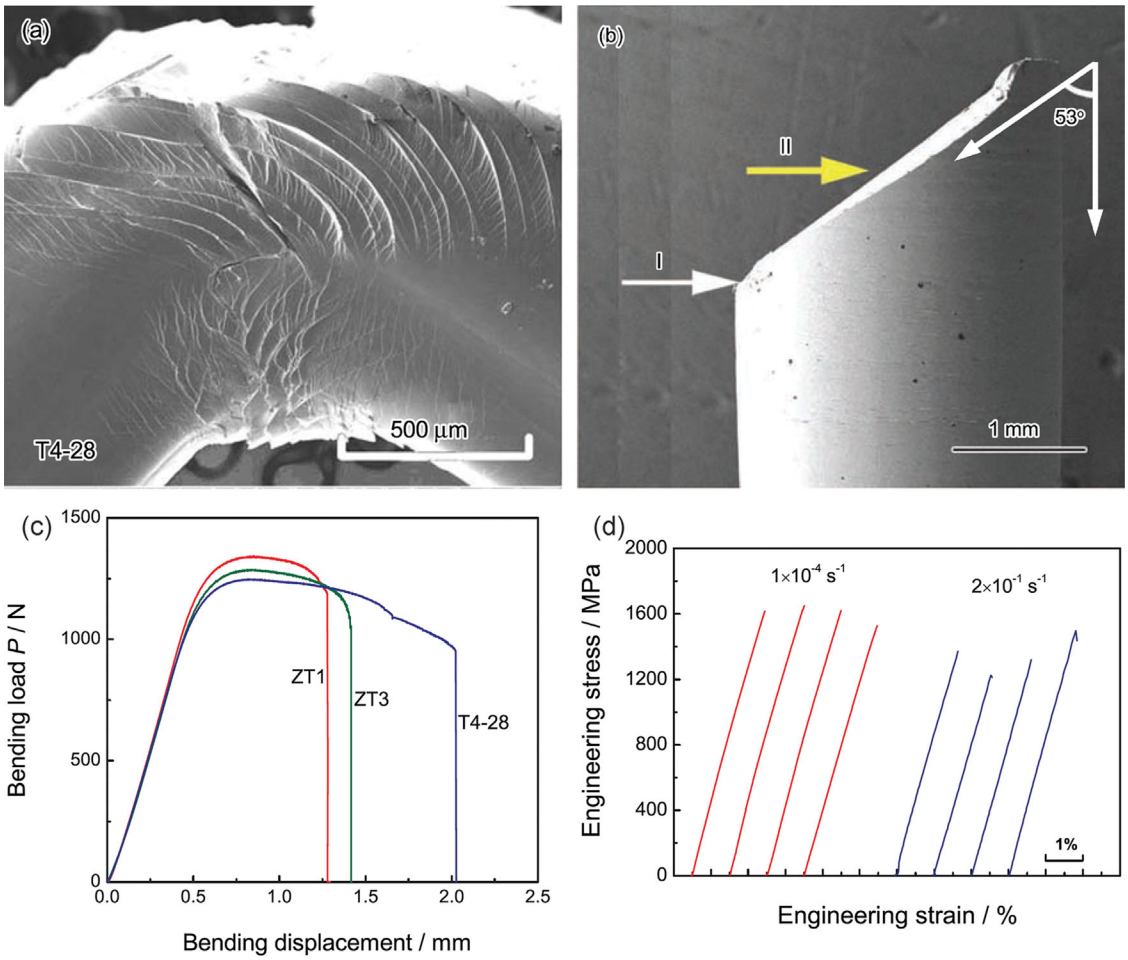

Figure 2.4: Differences observed between tensile and bending behaviours in BMGs: a) multiple shear bands observed in the bending for $Zr_{63.47}Ti_{4.53}Cu_{23}Al_9$ (T4-28), (b) tensile failure demonstrating shear band localisation in ZT1 ($Zr_{61}Ti_2Cu_{25}Al_{12}$), (c) extensive bending ductility shown by both compositions and (d) tensile stress-strain curve for ZT1 showing zero tensile elongation (reprinted from [34]).

Zr-based BMGs, with moderate to high fracture toughness, compete well with metallic alloys. Their ductile nature distributes stresses by forming multiple shear bands restricting their propagation to cause a fracture. Such metallic glasses can be used in engineering applications similarly to metallic alloys after controlling their immediate fracture risk. Hence, the critical feature to optimise physical properties in metallic glasses is restricting shear band localisation [35, 36].

2.3 Applications of BMGs

BMGs are suitable for numerous engineering applications. Their reliability in extremely cold environments makes them favourable for making space rover vehicle micro-gears where other metals become brittle [37, 38]. Metallic glasses thin films are used in making conical spring-type line actuators and on-chip micro-variable inductors [39, 40]. Their thermoplastic formability makes them a material of choice for manufacturing complex shapes [41].

BMGs are applied on surfaces as a scratch-resistant coating due to their higher hardness, e.g., Ti-based BMG's protective coating is used on the computer's memory stick' casings [42]. Similarly W-based metallic glass films can replace industrially used TiN coatings [43]. BMGs are also used for prosthetics and bone implants [44], and for coating over low-corrosion resistance materials such as carbon and low-alloy steels, due to their higher corrosion resistance [45]. Their higher hardness and wear resistance make them good material for surgical instruments like scalpels [46] and dental implants [47].

Most BMGs, especially Fe-based BMGs, exhibit soft magnetic properties with low magnetic hysteresis curves and eddy current losses, making them suitable for microelectromechanical systems (MEMs) [41]. Moreover, Fe-based ferromagnets are primarily used for power transformer core lamination and provide 30% energy savings. Their electrical resistivity is three times higher than the corresponding crystalline metal [43].

Zr-based BMGs exhibit plasticity for easier moulding yet steel-like hardness and strength [48]. Liquidmetal® is a commercial manufacturing company for Zr-based BMGs that supplies these BMGs for research and various industrial applications [48-50], as shown in Figure 2.5. Zr-based BMGs make customised springs and locking mechanisms, brackets, and hinges. These are also used for making pressure sensors and load cells capable of enduring harsh environmental conditions [48]. Zr-based BMGs have good acoustics, making them applicable in audio instruments [49]. These are also used for making sunglasses and other wearables due to their high surface finish and wear resistance [49]. Moreover, contrary to crystalline alloys, their higher surface finish reduces cost by avoiding additional polishing. The colliding objects made from crystalline metals experience a loss of energy as some of the collision energy is absorbed by the material with a low restitution coefficient [51]. On the other hand, Zr-BMGs are a good fit for making golf club heads [30] and tennis racket string-net due to their high coefficient of restitution [49].

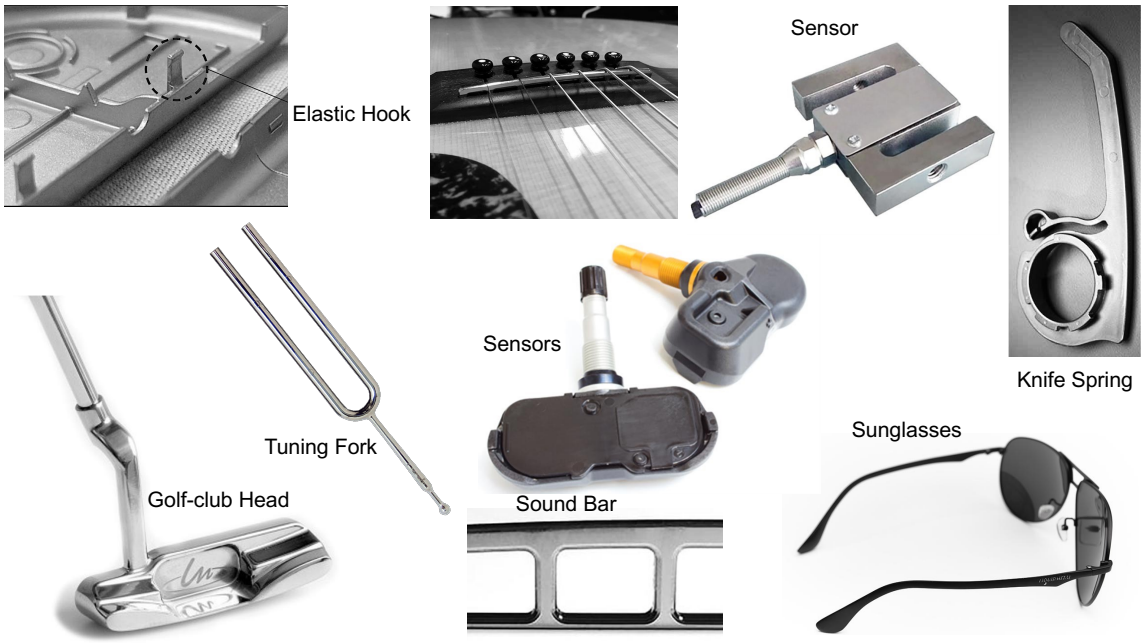

Figure 2.5: Examples of the current applications of Zr-based BMGs (reprinted from [48-50]).

Their wide range of applications motivates scientists and researchers to keep exploring this field. It is expected that BMGs will soon be feasible for large-scale industrial applications, considering the rapid progress in this field.

2.4 Thermomechanical Processing and Property Evolution

Different thermomechanical processes such as; annealing, thermal cycling, cold rolling, high-pressure torsion etc., are used in optimising the properties for engineering applications. Unlike crystalline metals, metallic glasses exist in diverse structural states, exhibiting a broad spectrum of physical, mechanical, and thermodynamic properties. Their structure can be modified to brittle or ductile by structural relaxation or rejuvenation, respectively [7, 12]. The details of some of the thermomechanical processes relevant to this study are discussed in the following sub-sections.

2.4.1 Structural Relaxation by Sub-T_g Annealing

Sub-T_g annealing is used for reducing the size and volume of "free volume" sites in metallic glasses by structural relaxation. It transforms the metallic glass structure into a denser state. The presence of free volume initiates the plastic flow during deformation; annealing is used to deprive deformation sources by free volume annihilation. A sub-T_g annealed sample would be starved of free volume and would be less deformable. The resistance to deformation caused by sub-T_g annealing comes with the expense of loss of ductility. It has been experimentally observed that annealing reduces the bending ductility in metallic glasses [52-54]. However, studies have shown that ductility in the annealed sample can be rejuvenated by inhomogeneous thermal or mechanical deformation processes [55].

2.4.2 Rejuvenation by Thermal Cycling

In thermal cycling, a metallic glass sample is immersed in boiling hot water and subsequently into liquid nitrogen for a certain number of cycles of a given duration. The mismatched thermal expansion causes local stresses inside the glassy structure, creating local structural heterogeneities, and there is much discussion about the potential to modify any locally hard and soft regions [6, 56]. Soft areas are preferred regions for the start of deformation, so the initiation of shear bands happens there. In contrast, hard regions obstruct shear bands propagation to prevent catastrophic failure by branching them out [6]. Microhardness mapping showed that the thermally cycled sample had more inhomogeneous hardness regions and an overall softening effect [56], as shown in Figure 2.6. Thermal cycling requires an initial inhomogeneous metallic glass structure, it cannot be performed on the fully relaxed annealed sample [57]. Therefore, it is advantageous to use thermal cycling in conjunction with high-pressure torsion, cold rolling or imprinting deformation processes for increased heterogeneity effect.

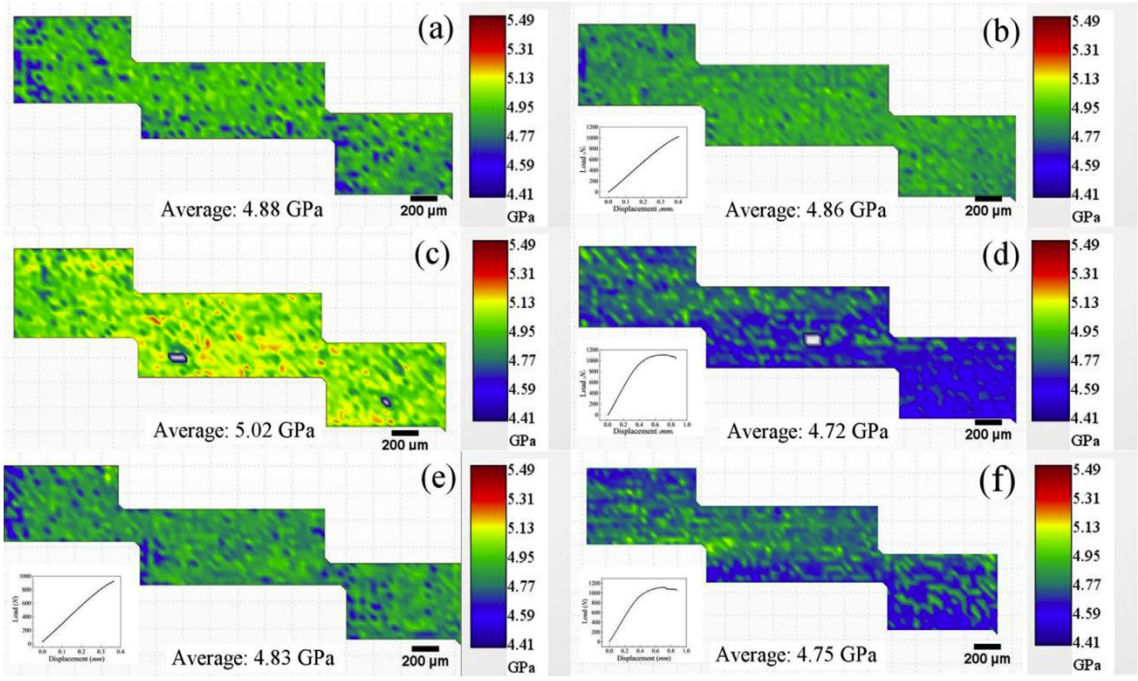

Figure 2.6: Vickers microhardness map from the cross- sections of beams for (a) before and (b) after thermal cycling for a thermally-cycled specimen with 170 cycles (TC-170) with relatively low toughness, (c) before and (d) after thermal cycling for a TC-170 specimen with relatively high toughness, (e) TC-120, a low toughness specimen. (f) TC-120, a high toughness specimen (reprinted from [56]).

2.4.3 Rejuvenation by High-Pressure Torsion

In the past, mechanical properties of crystalline alloys were modified using severe plastic deformation (SPD) techniques to manipulate grain sizes in alloys, following the Hall-Petch relation [55, 58]. High-pressure torsion (HPT) – one of the SPD techniques, is also used in metallic glasses [59]. In HPT, compressive force and torsion straining are applied on a cylindrically shaped sample for multiple rotations. The high-level straining optimises metallic glass structure by enhancing atomic-scale heterogeneities and free volume. Thus, a rejuvenated metallic glass exhibits significantly enhanced mechanical properties than its initial as-cast state [60-62].

Many researchers have tailored mechanical and structural properties in BMGs, by applying thermo-mechanical processing techniques [56, 63-66]. However, a comprehensive structure-property relationship requires in-depth structural information.

2.5 Theoretical Models Defining the Structure of BMGs

The atomic structure of metallic glasses is composed of short-range order (SRO) and medium-range order (MRO) structural units [9, 67]. Local structural and/or chemical interactions are referred to as SRO, whereas the local atomic order beyond nearest neighbours is called MRO [68]. The chemical interactions within various types of SROs and MROs are stronger but are relatively weaker among each other, restricting long-range order [69].

Over time, many theoretical models have been proposed for predicting BMGs' internal structure. The most acceptable of those, and the most relevant to the present work, are briefly described below.

2.5.1 Dense Random Packing of Hard Spheres (DRPHS)

This theory was initially proposed for explaining structure in liquids by Bernal et al. [70], in 1959. It was later adopted by Cohen and Turnbull [71], to describe the metastable glassy state of liquids. According to this model, atoms were randomly stacked without a particular order within the material. The dense packing allowed no space equal to or greater than the size of the rigid atoms [12]. The configuration was suggested for five different polyhedral geometries (Bernal polyhedron). It was proposed that all or some of them co-exist to avoid long-range order [72]. The empty central spacings in the Bernal polyhedron were called Bernal's canonical holes and are shown in Figure 2.7.

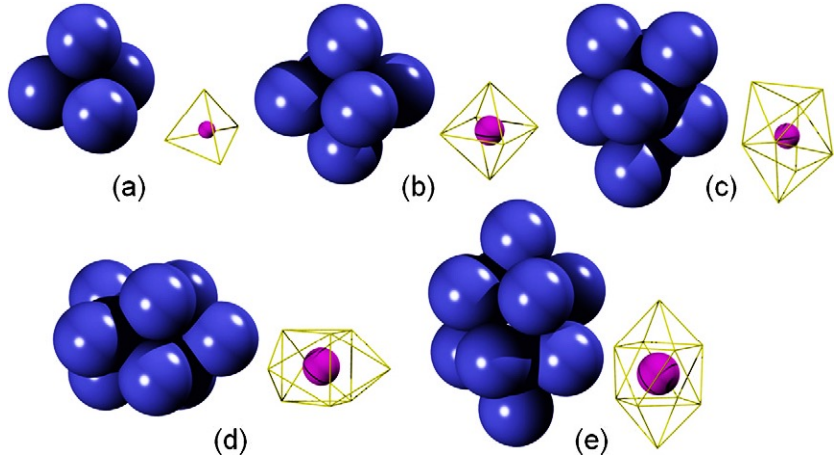

Figure 2.7: Bernal's canonical holes for a)- tetrahedron, b)-octahedron, c)-tetragonal dodecahedron, d)- trigonal prism and e)-Archimedean antiprism. The left side image shows hard-sphere packing in each image, and the right side image shows the Bernal hole in the centre (reprinted from [12]).

This model satisfied the fundamental criteria of describing metallic glass structure due to the following reasons:

- The configuration satisfied the requirement of minimum energy state. Additional energy was required for transforming this structure into the most space-efficient ordered structure (fcc/hcp).

- The packing density of a glassy structure should be lower than the theoretical packing density of the crystal due to its random packing. The fractional packing density of 0.637 was reported for a monoatomic glassy alloy – smaller than the crystalline packing density of 0.74 [73].

- This model resulted in isotropic atomic packing at macroscale as there were no preferred orientations or periodic ordering, thus applicable to all metallic glasses.

This model did not consider the chemical effects among atomic species and is only applicable to monoatomic metallic glasses and few binary metallic glasses with atoms of comparable atomic sizes [74]. Many binary and multi-element BMGs cannot be explained satisfactorily through the DRPHS model. Its lack of chemical consideration and oversimplification present an incomplete picture of their glassy structure. Nonetheless, the hard-sphere model is referred back and forth for partially justifying their microstructure[75, 76].

2.5.2 Polytetrahedral Packing Model

The polytetrahedral packing model was introduced by Frank and Kasper in which many coordination polyhedra (Z8, Z9,…, Z16) were designed for describing the atomic arrangement in complex alloys through triangulated coordination shells [76], as shown in Figure 2.8.

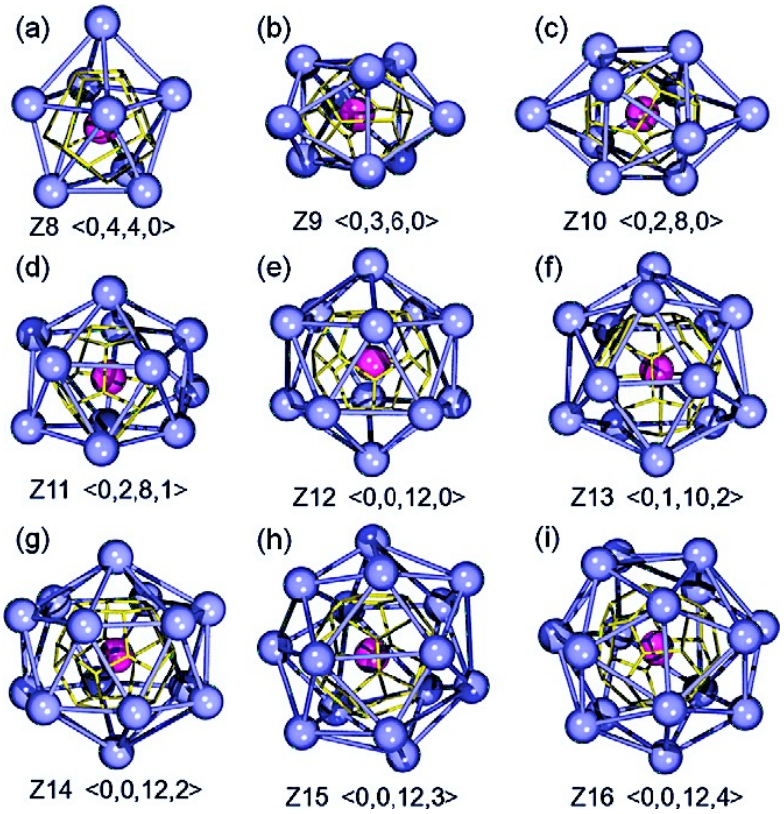

Figure 2.8: Frank-Kasper Polyhedra with polytetrahedral packing. The pink-coloured central atom has a yellow-edged Voronoi cell (reprinted from [12]).

The frustration in 3D polytetrahedral packing was reduced by incorporating disclinations and mismatched bond lengths in the packing. It was a necessary inclusion due to the presence of mismatched atomic sizes and bond lengths inside complex structures. The radial bond lengths can be longer or shorter, but the triangulated coordination shell should have equal edges, as per this model. Therefore, the general formula of $2n_4 + n_5 = 12$ (n_4 = number of tetrahedrons, n_5 = number of pentagons) must be followed, and the resulting packing is called polytetrahedral packing [12]. Nelson and Spaepen [77] later picked up the idea, and they validated the presence of polytetrahedral packing in liquids, metallic glasses, complex alloys and quasi-crystals, by providing a systematic review on experimental and simulation studies.

2.5.3 Stereochemical Model

In the stereochemical model, Gaskell [78] suggested that the metallic glasses contain distinct order in their nearest neighbour shell, making SROs similar to their crystalline counterparts. The discriminating feature is the MRO in amorphous alloys because the chemical SROs exists in both crystalline and amorphous materials. However, some degree of randomness persists in the amorphous structure at a larger length scale, preventing long-range order. This model explained the SRO structure of Ni-P metallic glasses, which was identical to the unit cell of Ni_3P crystalline compound [79]. Although it successfully described the metal-metalloid metallic glasses in general, it was later reported that the glassy structure could have more than one SROs, which may or may not resemble the unit cell in their corresponding crystals [80, 81].

The idea of solute-solute avoidance and the presence of strong chemical order in the stereochemical model was somewhat confirmed by another study [82]. Since this thesis is not about metal-metalloid metallic glasses, it will not be discussed further. The reason behind its mention is to highlight the possibility of co-existing chemical and structural SROs in metallic glasses.

2.5.4 Efficient Cluster Packing Model

The ECP model presented a meaningful approach, initially perceived by Miracle et al. [83], and widely accepted in the BMG community. This model explained the extended structure at the MRO scale while honouring the previous theories about metallic glass structure.

In this model, solute-centred clusters were assumed as the primary contributor to explaining BMG structure – an idea backed by many simulation studies [84-86]. While developing this model, two basic assumptions were made: 1)- the sphere-like shape of solute-centred clusters and 2)- a systematic arrangement of these clusters to create a densely packed unit cell structure, extending to a limited length scale. The concept of a unit cell helped correlate the atomic structure with crystallographic terminology. The dense packing favoured either face-centred cubic (fcc) or hexagonal close-packed (hcp) like unit cell structure along the MRO length scale.

It was proposed that a metallic glass can have only three topologically distinct solute species. The solutes were classified based on their relative radii ratio (R*) with the solvent (Ω) atom. The solute species were called primary (α), secondary (β), and tertiary (γ) in descending order of their R* magnitude [83]. The α-clusters occupied the vertices of a pseudo-fcc-structure, whereas β- and γ-solutes covered octahedral and tetrahedral sites. An illustration of this model is shown in Figure 2.9. The solute-centred clusters were assumed to be surrounded by solvent atoms in the first coordination shell [87]. The significance of the ECP model is that any multi-component BMG can be arranged as a pseudo-quaternary Ω-α-β-γ BMG based on their sizes. For example, a Zr-Cu-Al-Ti-Ni metallic glass will be a pseudo ternary amorphous alloy with Ti (146 pm), Al (143 pm) as α-, and Cu (127 pm), Ni (128 pm) as β-solutes, as per their radii sizes [87].

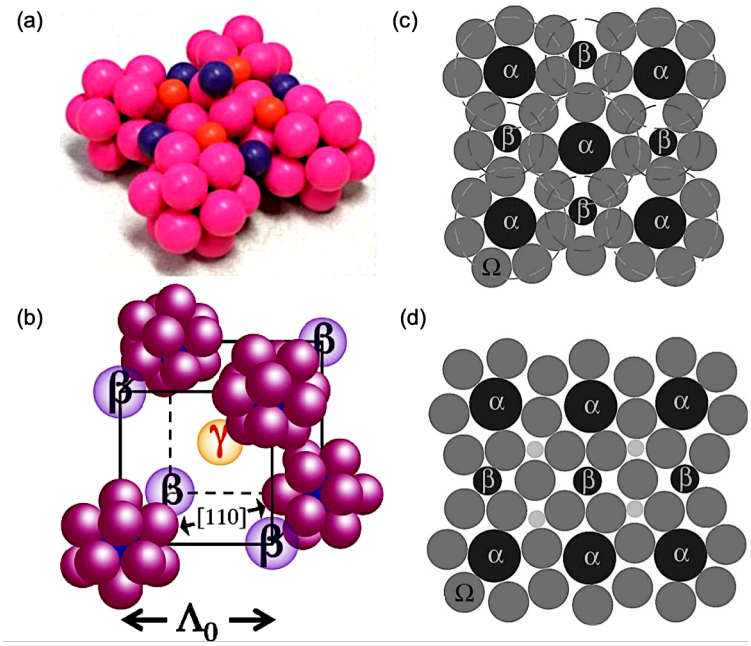

Figure 2.9: Efficient cluster packing (ECP) model showing (a) a three-dimensional cluster unit of the ECP model with γ as tertiary solute and is shown in orange colour, (b) reduced cluster unit cell showing β-octahedral and γ-tetrahedral sites, (c) two-dimensional representation of the (100) plane of fcc-unit cell, with α as primary solute, β as secondary solute and Ω as a solvent, and (d) two-dimensional representation of the (110) plane of fcc-unit cell, with α as primary, β as secondary, γ as tertiary solutes and Ω as a solvent (reprinted from [83, 88]).

The solute-centred clusters were joined together in the second nearest neighbour shell by face sharing (FS), edge-sharing (ES) or vortex sharing (VS), forming MRO clusters [87]. Interestingly, this model accepts the presence of different structural constraints within metallic glasses – explaining the co-existence of randomness, SROs, and MROs. The lack of orientational order introduced a strain factor among the clusters, limiting their interaction to a few cluster diameters (~1-2 nm) and prohibiting long-range order. However, the packing at all length scales should be dense to conform to the relative density of the respective crystalline alloy [87].

The ECP model has been successfully verified against a wide range of, Ca-, Fe-, Zr-based, and other BMGs [87]. However, this model does not consider the chemical strain contributions of constituting elements toward the stability of metallic glasses [89]. The atomic species play a critical role in creating heterogeneities, observed in the BMG's microstructure. Thus, there is a scope for improvement in this basic model for detailed structural analysis of BMGs. Nonetheless, the general framework of this model is verified for its application in quantitative SRO- and MRO- analysis [90] – validating its relevance to the glassy structure.

2.5.5 Modified Efficient Cluster Packing Model

Wang et al. [89] modified the ECP model by introducing negative enthalpy of mixing in the basic model. He inherited the same arbitrary fcc-structure for demonstrating the efficient packing as in the ECP model. However, instead of using relative sizes for classifying solutes, their relative negative enthalpies of mixing were considered. The modified model can be explained by a pseudo ternary (Ω-α-β) alloy, selecting solute species with decreasing order of their enthalpies of mixing with the solvent (Ω), from α to β. This preference was favourable due to a stronger chemical interaction between primary solute and solvent (α-Ω) for reducing the system's energy. The α-centred and β-centred clusters were alternatively joined where β-centred clusters sat at the interstitial sites of the fcc-like structure, as shown in Figure 2.10.

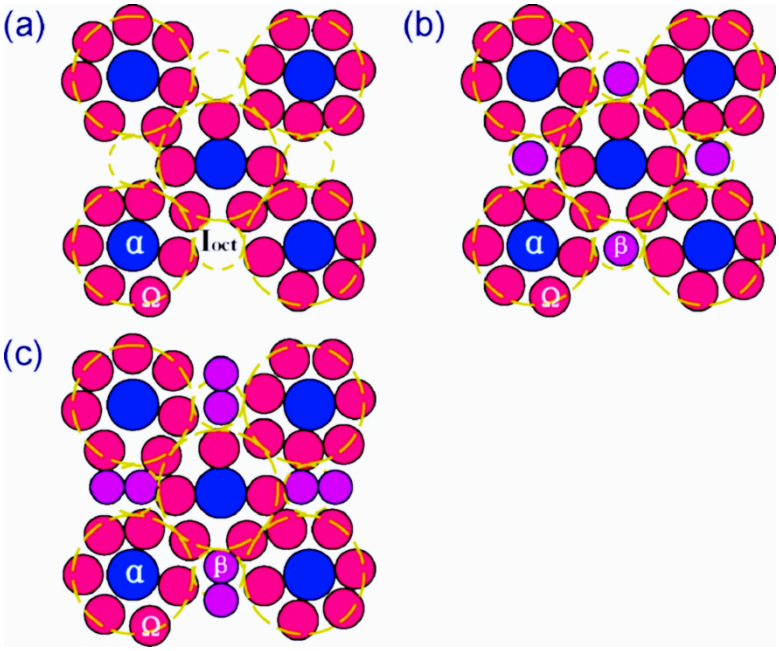

Figure 2.10: The modified ECP model showing (100) plane with fcc dense packing of α-centred clusters. The cluster octahedral interstitial sites (I_{oct}) are (a) empty, (b) filled with one β atom and (c) filled with two β atoms. The solvent atoms (Ω) are shown as pink, α atoms as blue and β atoms as violet spheres (reprinted from [89]).

β concentration was critical in defining the structure of clusters. In the absence of tertiary solute (γ), β can occupy the tetrahedral sites partially or entirely, depending on the concentration of β-solute inside the metallic glass. Another crucial feature of this model was that only those solute species with atomic radii within ±2% and zero or close to zero enthalpies of mixing were considered equivalent [89].

Although this model theoretically covered the basic ECP model's discrepancies, it overlooked some technical considerations. For example, while explaining a Zr-Al-Ni-Cu BMG, it was simplified to Zr-Al-(Cu-Ni) for considering pseudo-Ω-α-β amorphous alloy. However, Cu and Ni should not be considered together since they have a positive mixing enthalpy and may create some heterogeneities inside the atomic structure [91]. Similarly, it is difficult to hold efficient packing if the primary solute size is smaller than the secondary solute size, as seen in the example of the Fe-(B, C)-Mo system (~7% discrepancy) [89]. Therefore, careful consideration of both relative radii size and enthalpy of mixing is required for analysing the atomic structure of metallic glasses.

2.5.6 Micro-Crystallite Model

Bragg et al. [92] initially came up with the micro-crystallite model and described that the basic structure of metals/metallic alloys is comprised of grains and grain boundaries. This model was later used by Bagley et al. [93] to explain the internal structure of metallic glasses, where small grains were arranged randomly in a disordered manner preventing long-range order, as shown in Figure 2.11. Although this model theoretically explained some metallic glasses, but was not backed by much experimental evidence [94, 95]. It was found impossible to determine the atomic arrangement in the surroundings of these grains, especially if the grains are small, as their boundary would occupy too much volume [96]. Therefore, it was not considered further for metallic glass structure

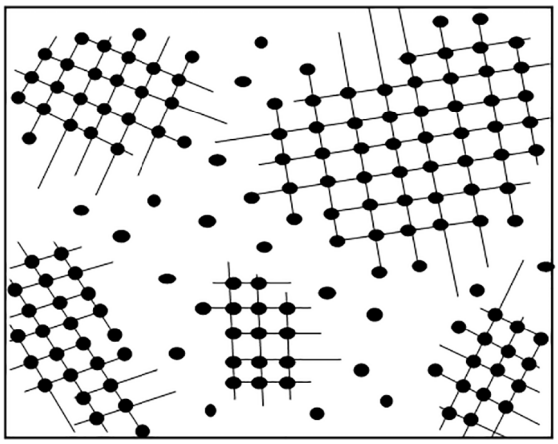

Figure 2.11: Schematic of the micro-crystallite model (reprinted from [96]).

2.5.7 Free Volume Theory

Cohen and Turnbull introduced the concept of free volume to explain diffusivity in the liquid state of metallic glasses [97-99]. Later, Spaepen [100] modified this theory to explain the deformation and plastic flow in metallic glasses. Since then, it has been referred back and forth to describe the structure of metallic glasses [101-103].

Spaepen suggested that some free volume pockets exist inside the amorphous structure, facilitating microscopic plasticity by allowing atomic level jumps [100], as shown in Figure 2.12. The logical explanation behind the free volume presence inside the glassy structure was its fast-quenching process which locked some of the "gaps" inside it. These gaps were called free volume, making the metallic glass volume slightly higher than its crystalline counterpart.

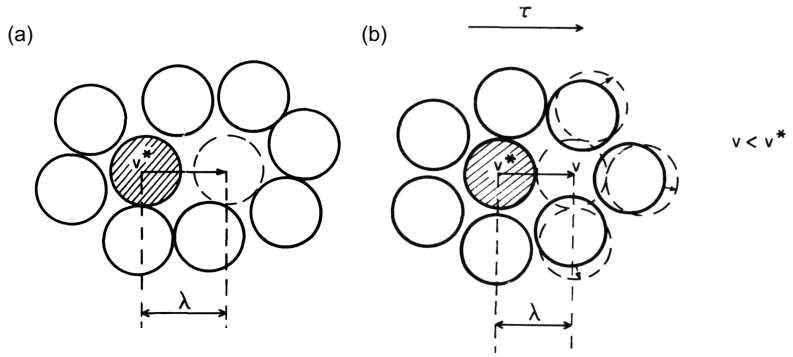

Figure 2.12: Schematic illustrating (a) atomic jump of length λ, (b) and creation of free volume under shear force τ. Here, v^* is the size of the effective hard sphere (reprinted from [100]).

Unlike Van der Waal liquids, the concept of free volume partially explained the structure of metallic glasses [104]. It reflected upon half of the story about what is happening inside metallic glasses, alongside other mechanisms. Despite its limitations, the creation and annihilation of free volume are commonly considered for explaining BMGs' dynamics under external stimuli [100], as described in Section 2.4. However, its meaning should not be considered literally as it is more of a phenomenological approach for describing complex glassy structures.

The basic free volume model was modified and experimentally validated by Argon [105], in 1979. He specified the atomic jump as a flow event caused by rearranging a group of atoms instead of a single atom. This theory was further developed by Falk [96, 102, 106] using a mathematical model as shear transformation zone (STZ) theory.

2.5.8 Discussion – Structural Models

Researchers have successfully resolved significant issues concerning the metallic glass structure with the help of the theories mentioned above. However, many aspects of the microstructure require further work. This section will discuss these models, considering their critical details and discrepancies.

Random packing of hard spheres initially helped understand the basic structural model of BMGs. However, it failed to provide a general description of MRO, observed experimentally in various metallic glasses, with the requirement of the atomic sizes of the constituent elements to be different.

The ECP model provided a common consensus about efficient space-filling with SRO- and MRO-clusters inside the glassy structure. It determined a topological basis for explaining the MRO clusters inside the metallic glass structure. It was also reported in the ECP model that the preferred solute-solute interaction could hinder the solute-solvent bonding in the first coordination shell [87]. Thus, although the generalised description of monolithic metallic glasses suggested homogeneous dispersion of constituent elements, the possibility of local solute-solute interaction is probable. The ECP model presented the crystal-like order of the MRO clusters in BMGs. Another school of thought proposed the icosahedral packing of clusters at the MRO level [82]. However, it is difficult to suggest which concept better represents the structural symmetry at the MRO scale in BMGs.

Modification of the ECP model, by adding negative enthalpy of mixing, strengthened the thermodynamical aspect of the MRO packing. Although mixing enthalpy consideration was a critical factor and improved the glass-forming ability (GFA) composition formula, the basic ECP model was much better in describing the structural basics of metallic glasses. Such as, the larger solute radii clusters would accommodate smaller ones, yet the opposite is not feasible [89].

Micro-crystallite theory presented a very naïve concept, yet it highlighted a very critical approach. Since the initiation of clusters within BMGs is not a random but rather chemically favourable phenomenon, based on the enthalpies of mixing and interactions between atomic pairs of different species. The nucleation of these clusters could begin at various points in the supercooled state inside the metallic liquid, transforming it into tightly bound SRO- or MRO-clusters in the glassy state MROs. The 'as is' glassy structure would be unrelaxed and would carry high volume and energy around SRO- and MRO-clusters within its structure, lacking long-range order [96, 107]. Based on this concept, the vicinity around these clusters is equally important, making it a 'favourable region.' Thus, if this region has a similar proportion of the interacted species as of the clusters, then it could interconnect with the nearby clusters, increasing their sizes under external stimuli.

The widely agreed approach regarding BMGs' microstructure suggests the coexistence of various coordination polyhedra [12]. The lack of long-range order in metallic glasses optimises nearest neighbour interactions for efficient cluster packing [73, 83, 108]. It was suggested that bond length and atomic arrangement in SROs of metallic glasses are in better order than the corresponding crystals, since the BMG's SROs do not undergo atomic redistribution for establishing long-range order. This provision results in relatively lower energetics in BMGs compared to the competing crystal [109].

The chemical influence of atomic species inside the glassy structure is an important factor that was not considered adequately while designing most metallic glass models. There are various types of SROs and MROs inside metallic glasses. The "instant freeze" during the transformation from glassy liquid to solid is responsible for the atomic scale heterogeneities within BMGs. Their relative fractions and distributions are primarily the determining factors of their physical characteristics. Therefore, it is recommended to extract as much statistical information about metallic glass structure as possible [12].

2.6 Deformation in Metallic Glasses

The technological imperative to improve the plasticity of metallic glasses has motivated researchers to understand the physical process of the dynamics and rheology behind plastic deformation at room temperature [110]. A few basic models to describe these behaviour are: 1)- deformation through free volume theory by Cohen and Turnbull [97] and Spaepen [100, 111], 2)- STZ theory by Argon [112], 3)-and co-operative shear model (CSM) by Johnson and Samwer [113] and Falk and Langer [102].

The free volume theory is a simplistic approach that many researchers considered for explaining the deformation process in metallic glasses. Spaepen [100] modified this theory to explain the deformation and plastic flow in metallic glasses under various degrees of external stimuli. However, its application in explaining metallic glass deformation is questionable [114]. The primary reason is the smaller fraction of free volume in metallic glasses (~10%) compared to 80 % of the average atomic volume in the case of Van der Waal liquids [115].

Argon [112] modified the free volume approach, stating that plastic deformation initiated from the collective motion of a group of atoms rather than individual atoms. The initiation of the shear bands occurs at multiple places simultaneously by the distribution of the shear transformation in specific atomic clusters. Those atomic clusters were located at the sites of larger free volume. The relative sliding between atomic clusters and free volume inside the metallic glass created 'internal flow units.' These internal flow units aggregated to form STZs [116]. Although STZs favour free volume sites, the required free volume size was less than 80% of the average atomic volume due to the dynamic nature of the surrounding atoms [105]. In the ECP model, absence of atomic species at the tetrahedral or octahedral vertices would create nano-voids in MRO clusters. Additional gaps/free volume could be linked to the boundaries of different SRO- and MRO-clusters due to different symmetries. The atoms with lower coordination numbers were considered the favourable clusters for STZs [117]. As per Cohen and Grest [118], their range of percolation ranged from 0.198 to 0.246. An STZ comprised about 30 atoms with an average size of about 0.48 nm^3 [119]. These regions' local stiffness and stability are relatively lower with more significant free volume sites [120]. These local regions are commonly called "liquid-like regions," as anelastic atomic rearrangement is easier in these regions. However, this term is defined differently among researchers, and it is sometimes confusing to consider these regions as liquid-like. Instead, STZs or soft regions are rather appropriate terms to refer to these regions, for understanding deformation in metallic glasses.

The transition of monolithic BMGs from brittle to ductile BMGs was reported by introducing deformation-induced structural heterogeneities with higher densities [5, 121-124]. HPT, thermal cycling and other thermo-mechanical processes introduced heterogeneities known as soft spots (soft regions), causing improvement in plasticity without significantly impacting the average structure of the BMGs [125].

Both dynamic regions and higher density regions were jointly considered in the co-operative shearing model (CSM). It was stated that shearing happened due to the co-operative motion of the atomic clusters and the free volume [126]. The combined effect of densely packed clusters and dilute vicinity generated two types of defect densities inside the metallic glass structure: 1)-free volume (dilute surroundings), 2)- anti-free volume (dense clusters). The dilation effect was earlier linked with the shearing process. However, it was recently reported that the shearing process results from the mutual impact of the free volume and anti-free volume site instead of dilation [104]. Moreover, their opposite nature resulted in minor or no variation in the average atomic density of the BMGs. The fraction of local density defects (free-volume and anti-free volume sites) was ~ 0.243, based on transformation strain calculations [104, 127]. Improved compressive plasticity of cold-rolled $Ti_{40}Zr_{25}Be_{18}Cu_9Ni_8$ BMG was observed by Park et al. [128] with about 14.5 % enhanced plastic strain magnitude. The plastic flow was facilitated by the mutual effect of the deformed softened regions and undeformed hard regions in the modified microstructure [128].

Wang et al. [129] found that the interface between soft and hard regions inside metallic glasses acted as STZ nucleation sites. It was predicted that the ductile BMG comprised homogeneous distribution of soft regions or STZ fertile sites, causing multiple shear bands nucleation. The localisation of these regions inside brittle BMGs created a single shear band, limiting plastic deformation [129]. The function of soft regions in plastic deformation and the effect of their distribution is shown in Figure 2.13. The STZs originated primarily from the soft regions, which evolved into shear bands upon further loading. The hard regions acted as barriers to hinder the shear bands propagation [5].

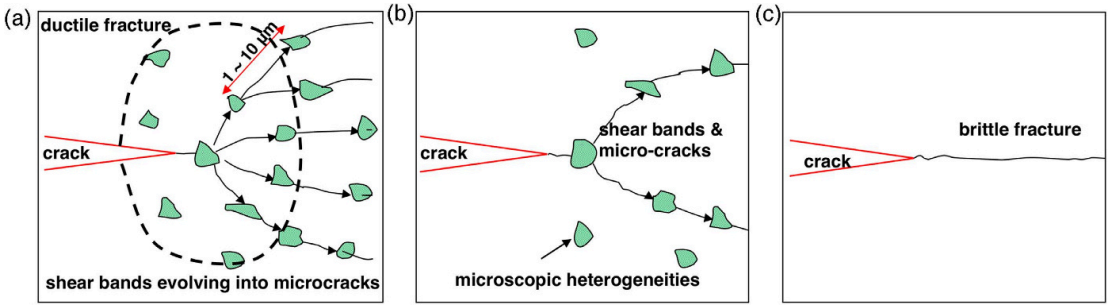

Figure 2.13: Schematic model showing ductile-to-brittle behaviour. Pre-existing defects or shear initiating zones (green colour) in (a) the as-cast sample, (b) moderately relaxed sample, and (c) completely relaxed samples. The microscopic heterogeneity density manages the ductile or brittle fracture behaviour in metallic glasses (reprinted from [130]).

The composition of soft regions was proposed to be widely different from the matrix, and these regions were considered the initiation spots for plastic strain [131]. Another study confirmed chemical heterogeneities stating that shear bands have amorphous regions with different compositions, free volume and internal stresses compared to the amorphous structure of the surrounding matrix [132]. Therefore, the chemistry, structure or both could be different in the soft regions compared to the surrounding matrix.

2.7 Characterisation Techniques

The microstructure of a material plays a vital role in its macroscopic properties. The secret to tailoring materials' mechanical and functional properties lies within their atomic- and sub-atomic-scale structural arrangements and their manipulation [133].

The use of experimental techniques for the microstructural analysis of metallic glasses is particularly complicated due to the absence of long-range order and their isotropic nature. The SRO- and MRO-clusters are considered as the main structural components of a BMG, which can topologically and/or chemically differ from each other. The absence of long-range periodicity makes it more important to obtain statistically significant structural information for revealing the microstructure-property relationship. The typical structural factors used for characterisation are; size, morphology, composition and volume fraction of SRO/MRO regions [18]. Various characterisation techniques for the microstructural analysis of BMGs, are briefly discussed in the following sub-sections, including thermal, diffraction, 2D and 3D techniques.

2.7.1 Thermal Techniques

Differential scanning calorimetry (DSC) profiles analyse enthalpies from glassy to supercooled and crystallisation states. This technique is mainly used for analysing the BMGs' glass-forming ability (GFA) through the difference between glass transition temperature (T_g), liquidus temperature (T_l) and crystallisation temperature (T_x). The more significant the difference between Tg and T_x, the better is its GFA. DSC can reveal indirect structural information like two-step crystallisation, as shown in Figure 2.14. However, it cannot provide specified structural information like presence of different phases or atomic rearrangement during the transition.

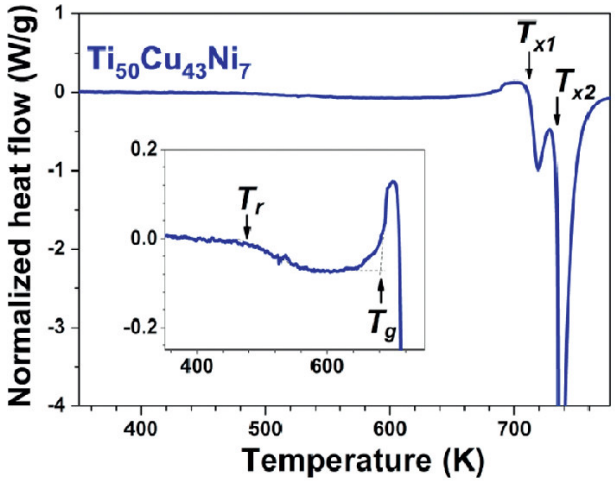

Figure 2.14: DSC profile of the as-cast $Ti_{50}Cu_{43}Ni_7$ ribbon at 30 K/min heating rate, T_{x1} and T_{x2} shows the onset of the two-step crystallisation process. The inset shows T_r and T_g are the onset of the relaxation process and the glass transition temperature, respectively (reprinted from [134]).

2.7.2 X-ray Diffraction

X-ray diffraction (XRD) is a powerful technique that utilises diffracted X-rays from the atomic planes of a material to quantify its crystalline features [135]. XRD is frequently employed in metallic glasses to confirm the absence of crystalline features, validating their amorphous nature. The outcome appears as a broad diffused Bragg peak. This technique has also helped analyse secondary crystalline phases of the BMG matrix composites [136]. High energy synchrotron XRD helps observe BMGs' structural evolution from amorphous to various crystallisation states. The crystallisation process is studied either under the isothermal or isochronal state [137]. Figure 2.15 shows the transformed crystalline phases used to indirectly predict the possible SROs/MROs inside the amorphous structure.

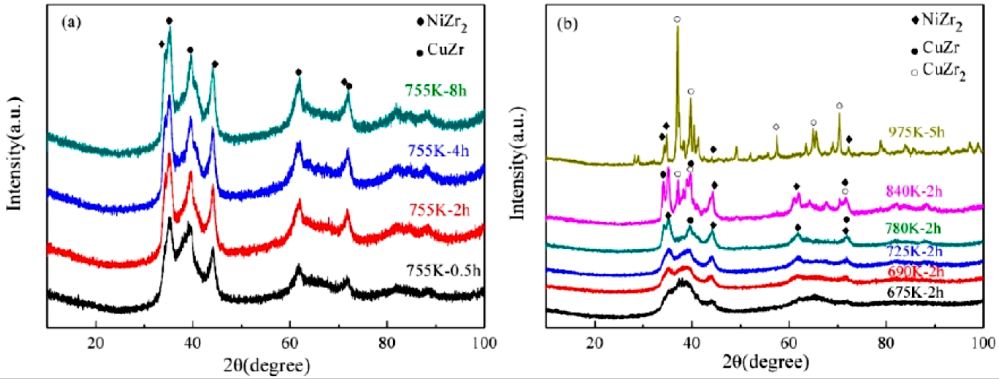

Figure 2.15: XRD pattern of Vitreloy-105 after isothermal annealing at different temperatures (reprinted from [138]

Extended X-ray absorption fine structure (EXAFS) is an advanced characterisation technique where extended regions of X-rays provide intense radiation sources to reveal information about interatomic bonding and chemical correlation. It helps analyse each element separately through its distributions and nearest neighbour analysis, as each type of atom has specific X-ray absorption based on its unique spectral location [139]. This technique was used in conjunction with the ab-initio molecular dynamics (AIMD) to reveal the atomic structure of $Cu_{45}Zr_{45}Ag_{10}$ metallic glass [140]. The limitations of this technique are twofold: 1)- partial pair distribution functions (PDFs) require EXAFS measurements for every element, which makes it complicated to use for quaternary and quinary elements, and 2)- the reliable results from this technique are limited to the nearest neighbour shells – providing information about SROs only [12]. Neutron diffraction is another technique frequently used to analyse SROs by PDF analysis [141].

Although XRD is a powerful technique, its implication for the structural analysis of metallic glass has certain limitations, especially for multi-component systems. It is challenging to extract the chemical identities of all alloying elements. Although, such information can be extracted from the partial radial distribution functions (RDFs) [142]. However, extracting information from all the partial RDFs experimentally is extremely difficult, especially for a multi-component system. Furthermore, partial RDFs provide average radial distances of the neighbouring atoms instead of the actual information about their positions and chemistry. Thus, the information about an averaged structure could be secured but not specific to the heterogeneities inside the BMGs.

2.7.3 Transmission Electron Microscopy (TEM)

TEM is another powerful technique for atomic-scale structural analysis through 2D projected imaging. The high energy electron beam can reveal crucial details about complex structures and chemistry. Recently, Yang et al. [90] have applied atomic electron tomography, where they have combined 2D TEM images at various tilt angles to create a 3D tomographic reconstruction of multi-element metallic glass particles. This new advancement opens a new avenue for effectively exploring metallic glass structures.

TEM offers various analysis techniques to explore the structural and chemical information about phases, precipitates, grains boundaries and other significant features in materials. Electron energy loss spectroscopy (EELS) and energy-dispersive X-ray spectroscopy (EDXS) in TEM are potential tools for extracting the chemical information of materials. However, the visualisation of elemental species is challenging for homogeneous samples, especially for topologically similar elements. Although the strength of its lateral resolution is high, its depth resolution is much lower, making it difficult to determine specific atomic species in different structural layers [143].

TEM analysis and sample preparation processes require high-level expertise from its users; otherwise, certain artefacts like oxidation, crystallisation, and phase changes, may cause ambiguous outcomes [144]. It is undoubtedly one of the most sophisticated microscopy techniques for characterising materials at the nanoscale. However, one should be very careful in implementing this energy-intensive technique for the atomic structure analysis of metallic glasses due to their metastable state. Atomic resolution can be achieved by high-angle annular dark-field (HAADF) imaging in conjunction with scanning TEM (STEM) [145-147]. However, this approach provides a feasible compositional solution to only dilute binary alloys [146, 148]. Advanced TEM techniques specific to the BMG structure analysis are described in the following sub-sections.

2.7.3.1 Selected Area Electron Diffraction (SAED)

The SAED patterns (Figure 2.16) are used for finding the structure-function and pair distribution functions (PDFs). The observed PDF peaks assess nearest neighbour distributions inside the glassy structure [9]. The information obtained through this method is limited to four/five nearest neighbour distances only. A PDF is the average sum of all the partial PDFs of the binary elemental combinations, which can reveal generalised information only for higher-order multi-element BMGs. SAED patterns are used for spotting any fluctuation in average atomic volume by comparing BMGs of similar compositions [126].

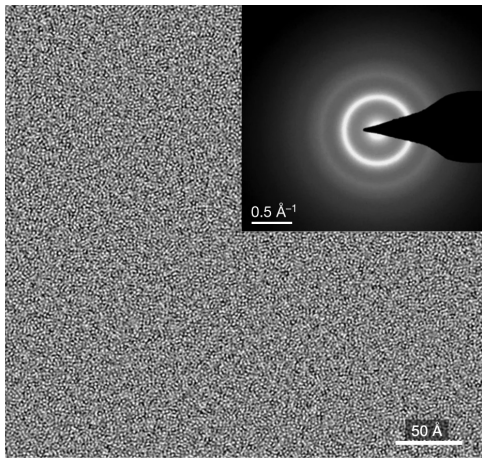

Figure 2.16: High-resolution transmission electron micrograph and SAED pattern (inset) of a BMG sample (reprinted from [9]).

2.7.3.2 Fluctuation Electron Microscopy

Fluctuation electron microscopy (FEM) is applied for MRO changes (~1 nm) [149], as shown in Figure 2.17. Nanometre sized near-parallel electron beams are swept across the sample surface, and the resulting scattering intensities are measured through nano-beam electron diffraction (NBED) patterns [12]. The NBED patterns are then statistically evaluated to measure the MRO sizes [150]. Structural information of MRO clusters in BMGs can be examined using this technique [9, 151].

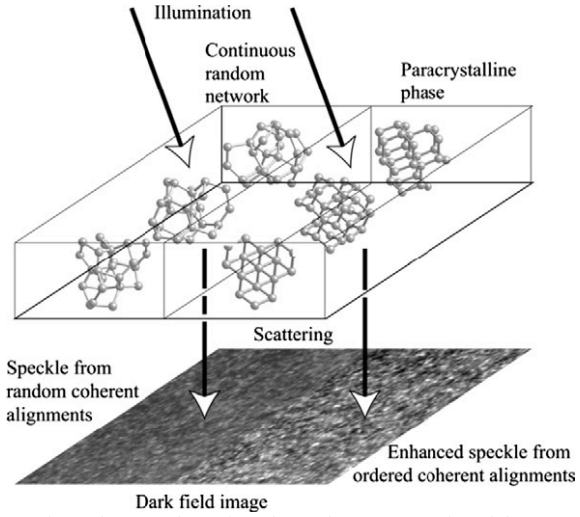

Figure 2.17: A simplified demonstration of MRO detection through FEM (reprinted from [152]).

These characterisation techniques provide instrumental information about the metallic glass structure. However, TEM's limitations to in-depth resolution and distinguishing topologically similar species confine its application. Its correlation with other advanced 3D techniques, such as APT, is required for detailed structural and chemical information about metallic glass structures.

2.7.4 APT

As earlier discussed in Section 2.5, both structural and chemical information about SROs/MROs is required to completely understand metallic glasses' internal structure. Therefore, characterisation techniques with a broader range of analytical ability are required to discern structural heterogeneities from the atomic scale to the sub-nanoscale. APT is an invaluable technique for investigating chemical heterogeneities with a near atomic-scale resolution at various size scales [153, 154]. It is a destructive technique that reconstructs a 3D tomographic image from the real-time atomic positions in materials by the field evaporation process.

In this technique, a needle-shaped specimen is used where the atoms are systematically ionised and evaporated from the specimen's apex by either high voltage- or laser-pulsing under ultra-high vacuum and cryogenic conditions. Laser pulsing is also called thermal pulsing as field evaporation occurs in this mode by instantaneous increment in temperature. The basic working principle of laser-pulsed APT is shown in Figure 2.18. APT can capture millions of ions from the material specimen during a single run. The evaporated ions are then projected on a position-sensitive imaging detector. Their travel time from the specimen surface to the detector is converted to their respective mass-to-charge ratios. The sequence of projections for each pulsing helps transform a 3D tomographic reconstruction. This instrument has generally ~ 0.3 nm spatial resolution [155, 156] and greater than 500 m/Δm mass resolution at full-width-at-half -maximum (FWHM) [157] for a standard sample such as crystalline Si. APT can chemically identify each atom in the reconstruction with a higher mass and spatial resolution, and 3D imaging helps visualise real-time elemental distributions within materials.

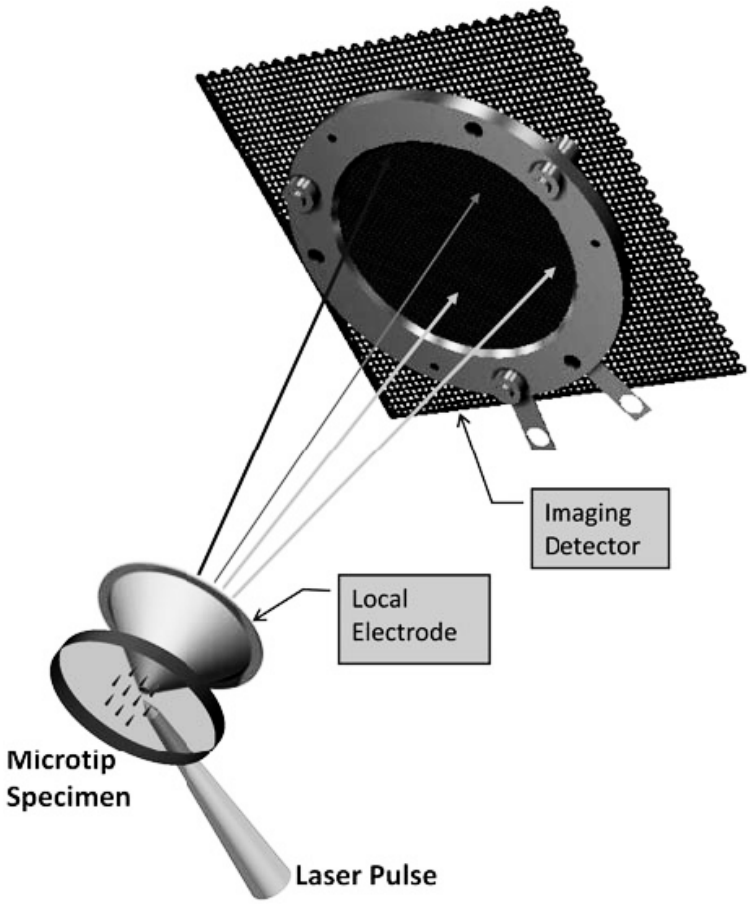

Figure 2.18: Schematic for depicting the basic principle for laser pulsing in APT using Si specimen (reprinted from [158]).

Before the advent of APT, its predecessor, 'atom probe field ion microscopy (APFIM)', was used for studying the non-random distribution of solute species inside the metallic glasses by Miller et al.[154, 159] and local concentration variations. In the early 90s, the Markov chain analysis of the APFIM data for Zr-based BMGs of various compositions ($Zr_{55}Al_{10}Ni_5Cu_{30}$, $Zr_{57}Nb_5Al_{10}Cu_{15.4}Ni_{12.6}$, $Zr_{52.5}Ti_5Al_{10}Cu_{17.9}Ni_{14.6}$) revealed significant levels of short-range chemical ordering around Al [154]. Dieter et al. [160] employed a 1D concentration profile using a fixed number of atomic blocks to detect nanometre scale clusters in Al-based metallic glasses and discovered Ni-rich clusters, as shown in Figure 2.19.

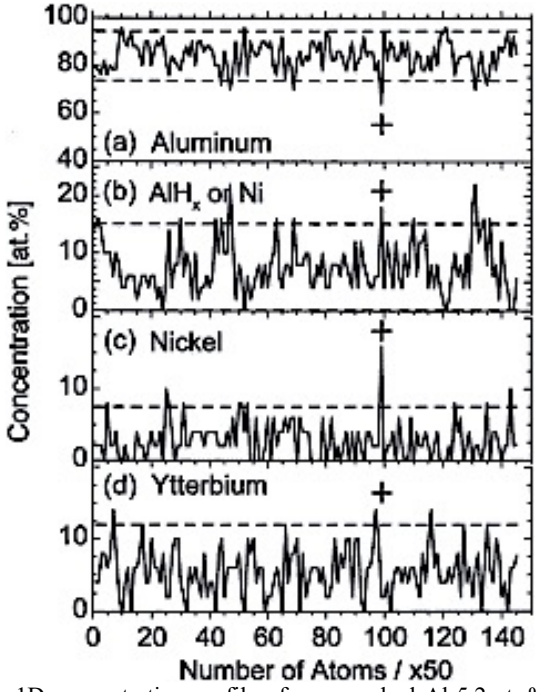

Figure 2.19: Ni-rich cluster (+) in 1D concentration profile of as-quenched Al-5.2 at. % Ni- 6.8 at. % Yb metallic glass (reprinted from [160]).

APFIM progressed to APT with technological advancement, exhibiting enhanced field of view and data acquiring abilities. The latest straight flight path local electrode APT can collect bigger data comprising millions of evaporated ions from a single experiment. Each atom has a set of 11 data points containing information about its position in the form of x, y, z coordinates, mass-to-charge ratio, time-of-flight and other parameters [155]. The primary emphasis has shifted towards selecting a sophisticated data mining approach and extracting helpful information from such extensive data.

2.7.4.1 APT Characterisation Techniques

Following are some typical data analysis approaches for APT data:

- 1D concentration Profile
- Iso-surfaces
- Distribution Analysis
- Nearest Neighbour (NN) Analysis
- Cluster Analysis

A brief overview of these methods and their application in metallic glasses are summarised in Table 2.2.

Table 2.2:Summary of data analysis techniques in APT using Cameca ® built-in algorithms.

#	Analysis Technique	Procedure and Details	Metallic Glass Applications	Additional Comments
1-	1D-Concentration Depth Profile and Proxigrams	The 1D concentration profile is usually analysed along the z-axis (depth of reconstruction). In the 1D-concentration profile, a cylindrical-shaped region of interest (ROI) is generally chosen from the centre of a reconstruction. The centre of the reconstruction is selected for avoiding trajectory aberration or edge effects. The1D concentration profile help analysing any fluctuations in atomic species. If the concentration of selected atomic specie is not uniform the ROI, it would indicate atomic-scale heterogeneity. A proxigram is like a 1D-concentration profile, where instead of analysis along some axis of reconstruction, the proxigram calculates the concentration profile along the selected region of interest (ROI).	Microstructure-property relationship was successfully observed through APT with the help of 1D-concentration depth profiles and proximity histograms in various phase-separated metallic glasses [161-164]. Gd-enriched regions were observed in the $Cu_{46}Zr_{47-x}Al_7Gd_x$ APT data and were successfully correlated with the magnetic property enhancement by Mattern et al. [163], as shown in Figure 2.21. The early spinodal decomposition was investigated by observing the size and compositional fluctuations in the Gd-rich clusters. The APT study of the amorphous $Nd_{58}Fe_{30}Al_{10}Dy_2$ clarified the mysterious coercivity mechanism inside this alloy, which was under debate for quite a while [165]. Another important APT application is microstructural evolution during the amorphous state to early-stage crystallisation. APT study of the as-quenched, annealed and partially crystallisecrystallised$i_{13.5}B_9Nb_3$ metallic glass demonstrated that Cu clusters were developed before the nucleation of α-Fe crystals and worked as activation sites for α-Fe nucleation[166].	Compositional profiles are primarily appropriate for relatively larger-sized microstructural features like interfaces or precipitates [155] It is not helpful for monolithic metallic glasses.

2-	Iso-Surface Analysis	Iso concentration surfaces display the spatial distribution of the elements inside a material. These surfaces visually represent the elemental fluctuation in the 3D reconstruction based on a concentration threshold value. The selection of this threshold value is arbitrary to a certain extent since the concentration continuously varies between clusters and matrix. One or more elements in their atomic or ionic state can be selected to generate these iso-surfaces in a multi-element material sample. These iso-surfaces can identify microstructural features, such as phase separation, nanocrystals, and solute clusters.	Various researchers carried the microstructural characterisation of metallic glasses through iso-concentration surfaces [161-163, 165, 167, 168]. An example of such representation is shown in Figure 2.20. The composition of each iso-surface was taken from its mass spectrum. The sizes of these nano features were obtained by averaging the size of each iso-surface through visual inspection, which is rather a qualitative approach [162].	The possibility of human error is quite likely in this approach, especially in selecting the threshold value for creating iso-surfaces and estimating the average size of the features.
3-	Distribution Analysis	The distribution analyses showcase the presence of significant solute clustering [155]. The APT data is first divided into 3D bins called voxels, either of	Significant solute clusters in BMGs were confirmed through APT distribution analyses [173, 174].	The selection of voxel sizes is crucial in detecting the features of interest [175].

		similar size or containing the same number of atoms. A frequency histogram is obtained by dividing the APT data into 3D bins (voxels), either fixed size or number of atoms. The frequency plot specifies solutes' quantity within each voxel. A comparison of the experimental and binomial distribution (random data) decides the significance of solute clustering in the material based on the chi-squared (χ^2) test [169-172].		If the voxel size is too large, the identity of clustering will be lost. On the other hand, if the voxel size is too small, too much fluctuation in the random data will neglect the evidence of clustering. Researchers are striving to resolve the voxel sizing issue [176], yet it remains as a limitation of this approach. Since it distributes the data into several blocks, it does not provide accurate information about the scale at which clustering happens.
4-	Nearest Neighbour (NN) Distribution	This method determines the frequency histogram of distances of the target solute species from their nearest neighbours. It identifies clustering if the atoms of the clustering species tend to get closer to each other than other atomic species.	Shariq et al. [142, 173] used APT for the atomic pair correlations in a monolithic ternary metallic glass, using NN-distribution analysis on the APT data. The mean of the Gaussian fit of the NN distribution was considered as an average value of the pair distances.	Its application is limited to ternary metallic glasses only due to increased complexity for quaternary and higher-order multi-element BMGs.

		Randomised data is considered for comparison by conserving the atomic positions and randomly shuffling the ion identities while preserving their bulk composition. The left shift of the experimental curve compared to the randomised data confirms solute-clustering. This analysis can be employed to observe 1st, 2nd, and 3rd to higher-order NN distribution [155].	Six different pair correlations were analysed and compared with respective RDFs obtained from other techniques [142].	
5-	Cluster Analysis	It is APT's unique ability to identify fine-scale clustering, which is otherwise indistinguishable through other characterisations. This will be thoroughly discussed in the following section.	It has not been applied for metallic glasses yet. This will be thoroughly discussed in the following section.	Cluster analysis is APT's unique ability to identify fine-scale clustering, otherwise indistinguishable using other characterisation techniques. APT can provide chemical information from very fine-scale clusters to larger scales clusters. Cluster analysis is a frequently used approach applied to many materials due to its ability to reveal useful information about materials' processing and physical properties [177-184].

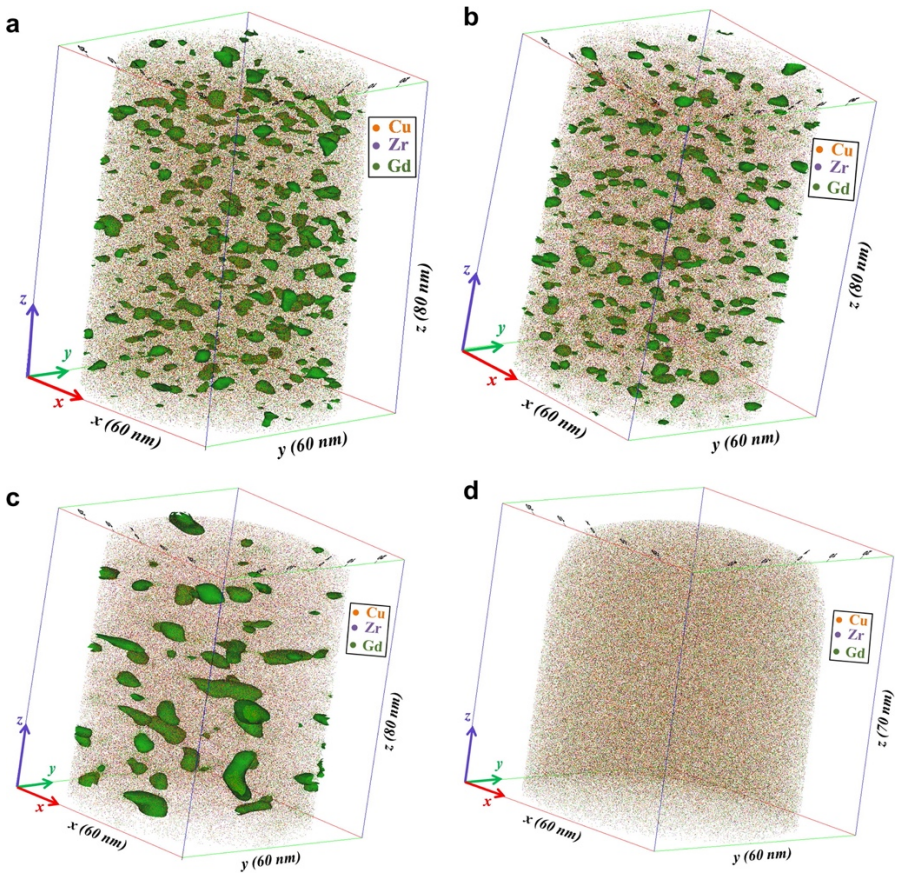

Figure 2.20: Iso-concentration surfaces are drawn in green for clusters/nanocrystals, (a) $Cu_{50}Zr_{45}Gd_5$ BMG in the as-quenched state with Gd enriched clusters (7 at. % Gd iso-surface), (b) annealed at 673 K for 10 min with Gd-rich clusters (11 at. % Gd iso-surface, (c) annealed at 723 K for 10 min with Gd enriched nanocrystals (14 at. % Gd iso-surface, (d) a homogeneous distribution without iso-surface (reprinted from [162]).

APT has been previously used for visualising microstructural features such as solute clustering and phase separation in metallic glasses. It has also helped in determining the local chemistry around the solute species. What is rather challenging is to analyse structural features in the homogeneous reconstruction of amorphous structures. The cluster analysis is a unique and dynamic tool that has been successfully considered for observing different cluster sizes and bigger precipitates in alloys [177, 178, 185]. Thus, a similar approach may likely be applied to extract such information from amorphous materials. If successfully applied, cluster analysis can provide invaluable information about the structure and chemistry all at once.

2.7.4.2 Cluster Analysis – an Overview

This section summarises the contribution of researchers toward APT clustering process development and its classification. A specific group of atoms closer to each other than its surrounding solid solution is called a cluster in APT. Atomic clustering may happen inside a randomly distributed solid solution as an artifact of the field evaporation process. However, if a material specimen exhibits more clustering than expected, it can be conveniently considered as the material's intrinsic microstructural feature. In that case, clustering will be further studied for its impact on other physical properties. A particular element can undergo individual or co-clustering in a multi-component material.

APT cluster analysis is based on the following steps [186];

Step 1: Identify the solute species that are expected in a cluster.

Step 2: Select maximum separation distance d_{max} – a threshold value within which clustering is expected.

Step 3: Use a recursive algorithm to identify groups of atoms within a specified distance.

Step 4: Select the minimum size of cluster N_{min}; atomic groups larger than the minimum size will be termed clusters or precipitates.

Out of the parameter mentioned above, d_{max} is particularly important because too big or too small a value can cause the excess or depleted population of the clusters, respectively. The most crucial consideration for d_{max} selection is that the resultant clusters should be significant, i.e., clusters beyond randomly distributed data. Once the cluster analysis algorithm is complete, the resulting data is refined for obtaining information about number density, volume fraction, morphology, composition etc.

Many cluster analysis methods have been developed over the past decade. The most common of which are as follows:

- 3D Markov Field (3DMF) [187]
- Delaunay tessellation method [188]
- Maximum separation method [189-191]
- Density-based scanning algorithm (DBSCAN) [191, 192]
- Core-linkage algorithm [191]

The most common cluster finding techniques, specifically related to the work in this thesis, are briefly discussed below.

2.7.4.2.1 Maximum Separation Method

It is the most common approach for larger clusters [189]. The clustered and non-clustered atoms were filtered by scanning all the solute atoms based on their first nearest neighbours. It is a highly localised approach and is usually considered for large scale clusters and precipitates only [191].

2.7.4.2.2 DBSCAN- Density-based Clustering Algorithm

The density-based clustering approach is an extended version of the maximum separation algorithm. The atoms were deemed 'core atoms' with a sufficiently higher density of similar or different solute atoms in their proximity (DBSCAN or KNN algorithm) [186]. An additional parameter, K (the order), was introduced in this algorithm for defining the order of the higher density nearest neighbour (NN) region (>1 nearest neighbour). The minimum cluster size was K+1 in this case. The addition of another step further iterated this technique. The additional step included two parameters, 'L' and '$d_{erosion}$' [186]. Unlike the max separation algorithm, it was possible to ignore local density fluctuation caused by the field evaporation process through higher-order NN selection.

2.7.4.2.3 Core-Linkage Algorithm

This algorithm used two independent steps for cluster analysis. In the first step, only the core atoms were identified, and this step was performed using either maximum separation or the DBSCAN algorithm. In the second step, linkage of any nearby atoms with the core atoms was applied if the distance was less than 'd_{link}.' The introduction of d_{link} provided flexibility to the cluster finding mechanism for sensibly selecting fine-scale clusters with better precision. However, proper selection of these parameters was a crucial task for the success of this analysis [191]. The average density values and necessary ad-hoc data can be used for specifying clustering parameters in crystalline structures, making it particularly feasible for crystalline alloys.

A summary of the cluster analysis techniques is represented in Figure 2.21. The DBSCAN and core-linkage approach have similar results and are equally popular. The sensitivity associated with approximating d_{link} value limits its application in metallic glasses, which makes DBSCAN method a better choice for cluster analysis of BMGs.

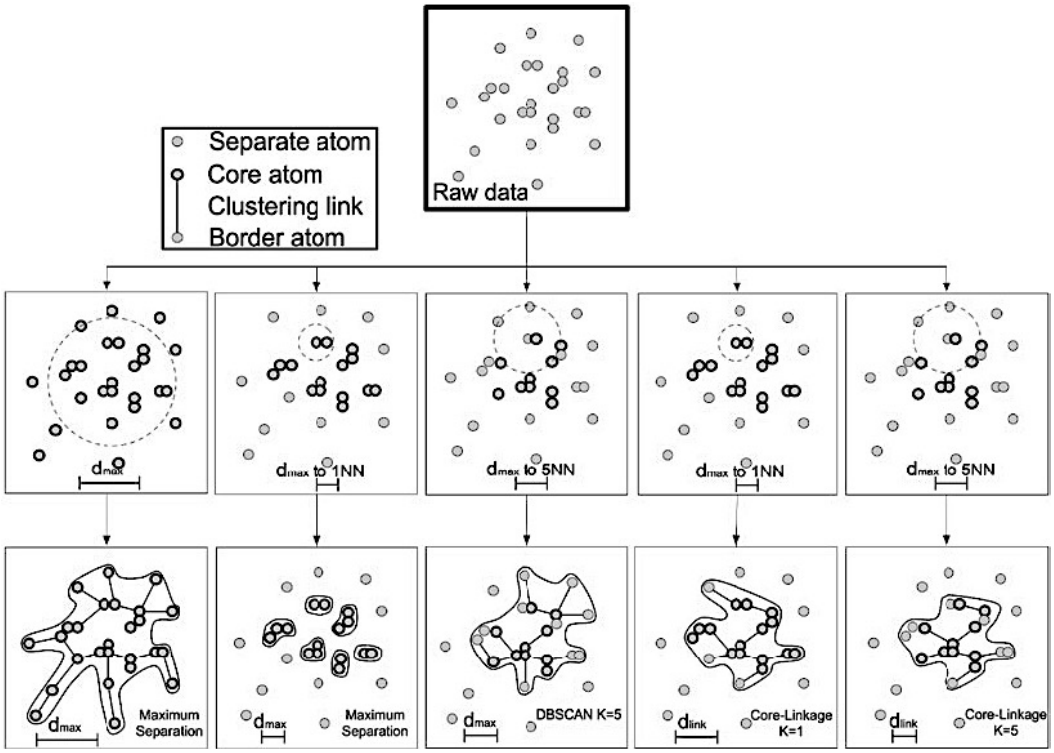

Figure 2.21: Comparison of the clustering algorithms (reprinted from [191]).

2.7.4.3 Limitations of APT

It may appear as if APT is a miraculous tool that can unravel structural aspects of any material without a problem. APT has its limitations as mentioned in the following sub-sections.

2.7.4.3.1 Spatial Resolution Limitation

The performance of any instrument can be assessed by the knowledge of its spatial resolution, which is generally a fixed local measurement. Contrarily, APT's spatial resolution is a relative term that can fluctuate by the specimen type, reconstruction shortcomings or both [158]. It is because the APT specimen itself acts as the primary optic of the microscope.

The operating conditions should be modified relative to the corresponding testing material. The optimisation studies on oxides, carbides, and other materials helped acquire better outcomes from their APT experiments [193-198]. A gap is observed concerning a thorough optimisation of BMGs for APT experiments. Although, Shariq and Mattern [167] reported the effect of APT experimental parameters' optimisation on better yielding of yttrium in $Ni_{66}Nb_{17}Y_{17}$ (at. %) alloy system [193]. Similarly, Zemp et al. [199] recorded the improvement in composition and data quality with variation in specimen temperature for $Cu_{45}Zr_{45}Ag_{10}$ amorphous alloy. However, a wide range of errors in composition was observed for atomic species in most BMGs, as shown in Table 2.3. A comprehensive study of the BMGs is required to quantitatively observe the effect of all APT experimental parameters on their data yield and quality.

Table 2.3: Absolute error in the APT composition of various BMGs [193].

References	Nominal Composition (at. %)	APT Composition (at. %)	Absolute Error (at. %)
Zhang et al. [200]	$Al_{88}Ni_7Sm_4Cu_1$	$Al_{88.37}Ni_{8.21}Sm_{2.57}Cu_{0.85}$	0.15-1.43
Hirotsu et al. [68]	$Pd_{40}Ni_{40}P_{20}$	$Pd_{40}Ni_{38}P_{22}$	0.00-2.00
Miller et al. [201]	$Fe_{61}Y_2Zr_8Co_6Al_1Mo_7B_{15}$	$Fe_{65.75}Y_{2.05}Zr_{7.1}Co_{3.6}Al_{1.5}Mo_{8.8}B_{11.2}$	0.05-4.75
Shariq & Mattern [167]	$Ni_{66}Nb_{17}Y_{17}$	$Ni_{67}Nb_{17.9}Y_{15.2}$	0.90-1.80
Mattern et al. [163]	$Cu_{46}Zr_{40}Al_7Gd_7$	$Cu_{46.1}Zr_{41.6}Al_{7.5}Gd_{4.8}$	0.10-2.20
Han et al. [161]	$Zr_{48}Gd_5Co_{28}Al_{16}$, $Zr_{46}Gd_{10}Co_{28}Al_{16}$	$Zr_{51}Gd_5Co_{27}Al_{17}$, $Zr_{46}Gd_{10}Co_{27}Al_{17}$	0.00-3.00, 0.00-1.00
Zemp et al. [199]	$Cu_{45}Zr_{45}Ag_{10}$	$Cu_{45.4}Zr_{44.9}Ag_{9.8}$	0.10-0.60
Sarker et al. [174]	$Ni_{42}Nb_{28}Zr_{30}$	$Ni_{41.97}Nb_{26.05}Zr_{31.98}$	0.03-1.98
Yuan et al. [202]	$Co_{47.36}Fe_{20.30}B_{21.79}Si_{5.07}Nb_{4.98}Cu_{0.47}$	$Co_{43.50}Fe_{22.71}B_{20.94}Si_{6.73}Nb_{5.59}Cu_{0.47}$	0.03-3.80

Other primary factors that adversely affect the spatial resolution are detector limitation, reconstruction shortcomings, local magnification, trajectory aberration at poles, zone lines and grain boundaries [155, 158, 203]. Moreover, spatial accuracy is relatively reduced in laser pulsing since the temperature of the specimen apex is raised for a short duration (100-500 ps) to facilitate field evaporation. Voltage pulsing is favoured for spatial accuracy, yet it is not favourable for non-conductive BMGs. In those cases, the signal-to-noise ratio is the preferred metric to determine the data quality. Overall, the quality vs. yield is a constant trade-off in APT operations.

2.7.4.3.2 Mass Resolution Limitation

An APT mass spectrum is based on the mass-to-charge ratio (m/n), where the mass cannot be separated from the charge state. The difficulty arises due to the similar m/n ratio of multiple elements, which creates the problem of mass spectrum peak overlap. The most common cases of peak overlaps for Zr-based BMG are: $^{62}Ni^{2+}/^{93}Nb^{3+}$, $^{63}Ni^{2+}/^{94.5}Zr^{3+}$ as well as $^{64}Ni^{2+}/^{96}Zr^{3+}$, and Zr^{2+}/ZrH^{+}, Nb^{2+}/ZrH^{+}.

Artefacts such as; hydride/oxide formation and thermal tails following the rear-end of mass spectrum peaks can severely degrade the mass spectrum and the compositional analysis. Oxide formation is caused by specimen exposure to air after preparation, whereas hydride formation results from the interaction of evaporated ions from the specimen surface with chamber gases. Thermal tails are delayed signals of the respective peaks. The delayed signals may occur due to ions bouncing off the chamber walls, dissociating molecular ions into atomic ions before hitting the detector, or ions evaporating after the pulse [155, 204]. These artefacts should be reduced to a maximum extent for better compositional analysis.

2.7.4.3.3 Multiple Ions

Molecular ions commonly appear in the analysis of various multi-component materials. Although, the detection of multiple ions is no longer a problem due to advancements in technology. However, it is generally recommended to optimise experimental parameters to avoid a higher proportion of multiple ions in APT data [155]. Multiple ions should be decomposed into constituent atomic ions before thorough data analysis.

2.7.4.3.4 Reconstruction Error

The local magnification effect due to field variation in different phases of materials and inappropriate selection of reconstruction parameters are common sources of reconstruction errors. Reconstruction calibration should be undertaken whenever possible [154, 158, 203]. Local magnification and thermal effects can cause trajectory aberration, due to which the lateral resolution will be compromised. These effects mostly appear around zone lines, poles, and grain boundaries. Although the field evaporation process of BMGs does not comprise zone lines or poles due to its amorphous nature, its operation under thermal pulsing may cause some limitations to correct reconstruction. Scientists are constantly working on improving the quality of this state-of-the-art instrument. Recently, the new flight path technology by CAMECA has improved the detector efficiency to ~ 80 % in LEAP 5000 XS [205]. The detector efficiency was limited to ~ 57 % for earlier instruments [206].

2.7.4.4 Clustered Evaporation

Clustered evaporation is an artifact that appears particular for metallic glasses. The field evaporation of metallic glasses is a stochastic process that exhibits a non-uniform evaporation phenomenon called clustered evaporation. An example of it is shown in Figure 2.22. Since the main principle of tomographic reconstruction in APT requires uniform layer-by-layer evaporation, the non-uniform evaporation of spatially correlated events from the tip apex reduces its depth resolution. Despite this limitation, APT has been used to extract valuable information about phase separation, shear bands, and nanocrystals in metallic glasses, as evidenced by the literature [164, 165, 207-209]. Interestingly, as suggested by Haley et al. [14] and Zemp et al. [199], clustered evaporation may be intrinsically linked to the microstructural features of metallic glass and requires more study to investigate whether and how this phenomenon contains useful signals from the microstructure.

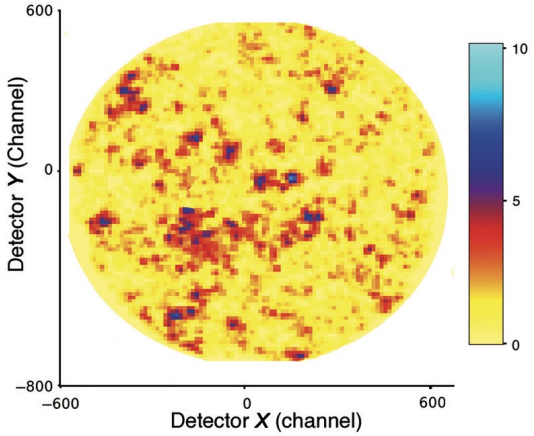

Figure 2.22: Detector hitmap showing clustered evaporation in $Mg_{65}Cu_{25}Y_{10}$ BMG (reprinted from [14]).

2.7.5 Computational Characterisation – Molecular Dynamics Simulation

Computer simulation, particularly molecular dynamics (MD) simulation, is an effective tool for analysing different internal mechanisms, which are otherwise difficult to analyse through experimental methods, such as the local interactions in super-cooled and near glass-forming states. It is also helpful in visualising the 3D microstructure of glassy alloys. Computer simulation has been extensively used for analysing the microstructure-property relationship in materials [210].

However, some constraints must be considered while considering computer simulation. Firstly, the size of the supercell for simulation studies. Due to high computing costs and time restraints, the supercell can only have ~500 atoms for ab-initio molecular dynamics (AIMD) simulation and ~5000 atoms for Reverse Monte Carlo (RMC) simulations. Secondly, a relatively faster cooling time is applied during computer simulation, which is not achievable by actual laboratory experiments. Despite advanced simulation techniques, the structural characterisation of quinary BMGs is still challenging due to multi-element constraints and disordered structures. MD simulation is reasonably valuable for obtaining chemical and structural information [211-214].

2.8 Discussion– Zr-based Metallic Glasses

Zr based metallic glasses are the most famous group of BMGs due to their unique structural characteristics, availability to be prepared in larger sizes and cost-effective production. The most studied Zr-based BMG group is represented as Zr-(Ti, Nb)-(Cu, Ni)-Al [12]. This group is not considered a lean-solute group, as solutes contribute towards ~ 40-50% of the total composition. Although it is one of the most extensively studied groups, its glassy structure has not been fully understood. Structural complexity arises from the number of elements within a metallic glass – increasing the likelihood of chemical heterogeneity due to variable chemical affinity between different element pairs [12]. Even a homogeneous metallic glass exhibits local heterogeneity at the atomic scale. The structure of Zr-based BMGs contains considerable structural variations from atomic to sub-nanometre scales [2, 140, 215]. The types of chemical bonding, positive and negative atomic stresses, and the effect of variations in compositions of Zr-based metallic glasses are possible factors making it difficult to explain their structure via a unified theory. Following are several limitations that knock down their selection as preferable industrial materials.

- The presence of multiple elements in the quaternary, quinary and higher-order BMGs makes their structural analysis difficult by the conventional characterisation techniques. For example, analysing an n-component BMG would require characterising n(n+1)/2 individual pair correlations [216].

- The strain localisation [217-219] and thermal softening [220] of Zr-based BMGs at room temperature make them highly unreliable for structural applications [100, 221].

- The microstructural modifications inside the glassy structure significantly influence their mechanical behaviour under applied stresses [216]. Complete understanding of their deformation mechanism is difficult due to subtle changes in their composition and/or structure with deformation. The effect of external force on the microstructure of metallic glasses requires more research [216].

- Thermo-mechanical deformation processes have reportedly improved the plasticity of Zr-based BMGs by introducing structural heterogeneities [6, 7, 12]. However, the structural and, most essentially, the chemical information about these heterogeneities are little known. A complete understanding of these structural perturbations is required to learn about the deformation mechanism and develop a deformation theory for metallic glasses [222, 223].

It is essential to mitigate these limitations to take full advantage of these advanced materials. The main structural aspects from the information obtained about the structure of Zr-based BMGs are summarised in the following sub-sections.

2.8.1 Elemental Contribution and Effects:

It was reported that the combined effect of topologically similar elements dramatically enhances the glass stability compared to using a higher proportion of a single element, e.g., (Cu, Ni) and (Ti, Al) in Zr-based [224]. The chemical effect of topologically similar species cannot be neglected as it holds specific significance, the details of which are yet to be explored [87]. In this context, the ECP model is a somewhat generalised approach, demonstrating the BMG structure on average.

The toughness of Zr-based BMGs was increased by increased Zr content and decreased Al and Ni proportions [26]. It was reported that the increased Zr proportion reduced the fraction of full icosahedral clusters in Zr-(Cu, Ag)-Al BMG. It enhanced the plasticity of the metallic glass by providing more fertile sites, facilitating the plastic flow and shear strain [225]. Minor additions of Al reportedly increased the shear transformation sites in $Zr_{47.5}Cu_{47.5}Al_5$ BMG [129]. Al-addition increased local structural heterogeneity by increasing the population of both hard and soft regions inside the metallic glass.

The elements with positive enthalpy of mixing tend to avoid each other and may cause phase separation in some cases [163, 167, 174]. For example, Cu-rich and Ag-rich nanometre-scale amorphous domains were observed in $Zr_{43}Cu_{43}Ag_7Al_7$ BMG in 3DAP [226]. It was implied that bond pairs with positive mixing enthalpy might cause phase separation or local ordering through micro-alloying [227]. Similarly, it was determined that the regions enriched with Ni-Cu pairs demonstrated different order compared to the amorphous matrix [227], majorly comprising icosahedral ordering.

Chemical Mixing enthalpy (ΔH^{chem}) was applied to observe the chemical affinity between the atomic species [228] by the following relation:

$$\Delta H^{chem} = \sum_{\substack{i=1 \\ i \neq j}}^{3} 4\Delta H_{AB}^{mix} c_i c_j \tag{2.1}$$

The enthalpies of mixing (ΔH_{AB}^{mix}) between binary combinations of the alloying elements and their relative concentrations (c_i, c_j) were used for finding the chemical mixing enthalpy of a BMG through the Miedema's model [26]. This equation may provide a generalised value for mixing enthalpies, yet the real interactions may vary from system to system.

2.8.2 Short and Medium Range Order (SROs/MROs)

The presence of SRO/MRO clusters was initially reported through the simulation studies [211, 229]. It was found that different atoms start forming complex clusters inside the melt with distinct SROs, well before their glass transition state [12, 230]. It was confirmed by the viscosity measurements where the viscosity of the metallic glass-melt was only a few orders lesser than its glassy state. It is quite contrary to a crystalline alloy where the melt's viscosity is three to four times lower in magnitude than the corresponding viscosity of the metallic glass.

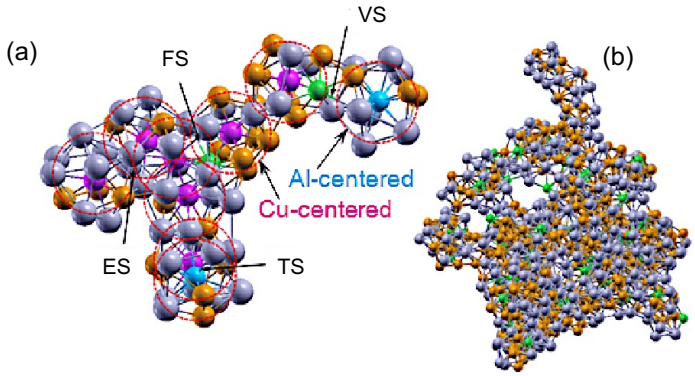

Figure 2.23: A demonstration of network of clusters, leading to SRO- and MRO- clusters (depending on their length scale), (a) 9 interconnected Al-centred (blue) and Cu-centred (pink) full icosahedra clusters, joined by vertex sharing (VS), edge sharing (ES), face sharing (FS) or tetrahedra sharing (TS), (b) MRO cluster (~2 nm in size) inside $Cu_{46}Zr_{47}Al_7$ (reprinted from [211]).

A wide range of structural and/or topological SRO/MRO clusters may exit inside the multi-component Zr-based BMGs, creating a heterogeneous structure, as shown in Figure 2.23. It is due to the presence of various sized solutes with different chemical interactions among each other and Zr (solvent).

2.8.3 Heterogeneities in Zr-based BMGs

The heterogeneities inside the metallic glasses play a crucial role towards the physical properties of BMGs [221]. A two-phase glassy structure was reported to have dark (Ni-rich) and light (Cu-rich) regions, with variable local hardness in Zr-Cu-Ni-Al alloy [231], as shown in Figure 2.24. It was determined that the Cu-rich region had lower hardness (soft region) than the Ni-rich region. One specific reason was the presence of nanocrystals inside the Cu-rich region.

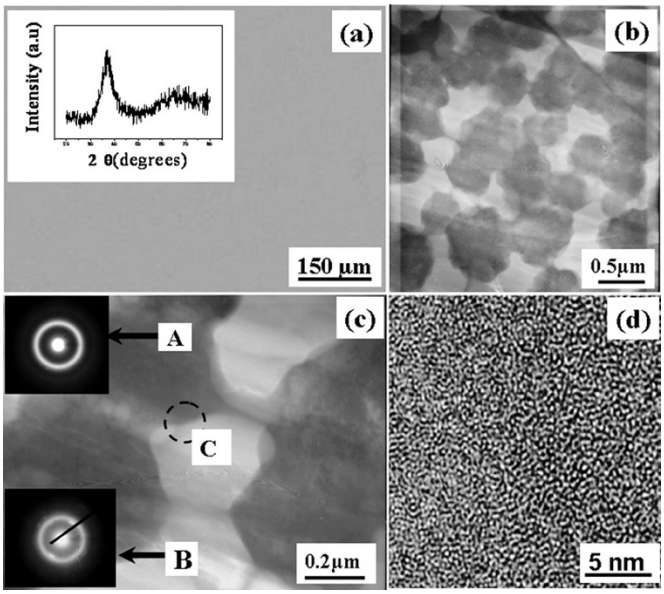

Figure 2.24: (a) SEM image with XRD pattern (inset), (b, c) TEM bright field images with 'A' showing the dark region, 'B' the light region and 'C' the mix of A and B, and (d) HREM image of Zr-Cu-Al-Ni BMG. (reprinted from [231]).

Even if the heterogeneities are not as significant as to form a two-phase matrix, small-scale local heterogeneities exist at the atomic scale [8]. These local variations either come from chemical combinations of constituent elements, e.g., Zr-Ni and Ni-Nb regions in $Ni_{60}Nb_{40-x}Zr_x$ [91] or distinct topological orders [232, 233]. The SRO/MRO clusters are considered the intermetallic phases' precursors, which ultimately transforms into nanocrystals/crystalline phases inside the metallic glasses [234]. Partial crystallisation is a way of analysing glassy structures through their intermetallic compounds [30, 166, 234, 235]. For example, Ni-centred clusters showed reduced bond length with Zr atoms than the sum of their atomic radii, in Zr-Ni-Al BMG [235]. The shorter bond length was due to the covalent bonding with strong hybridisation of Ni-d orbital and Zr-d orbital [235]. On the other hand, Al in Al-centred clusters showed metallic bonding with s,p-electrons. Kasper polyhedral for Al-centred clusters and prism-like Zr-centred and Ni-centred clusters (Figure *2.25*) were observed in the BMG structure. The intermetallic compounds: Zr_6Al_2Ni, ZrNiAl and ZrNi, reportedly contained similar basic structure as of the clusters in the respective BMG.

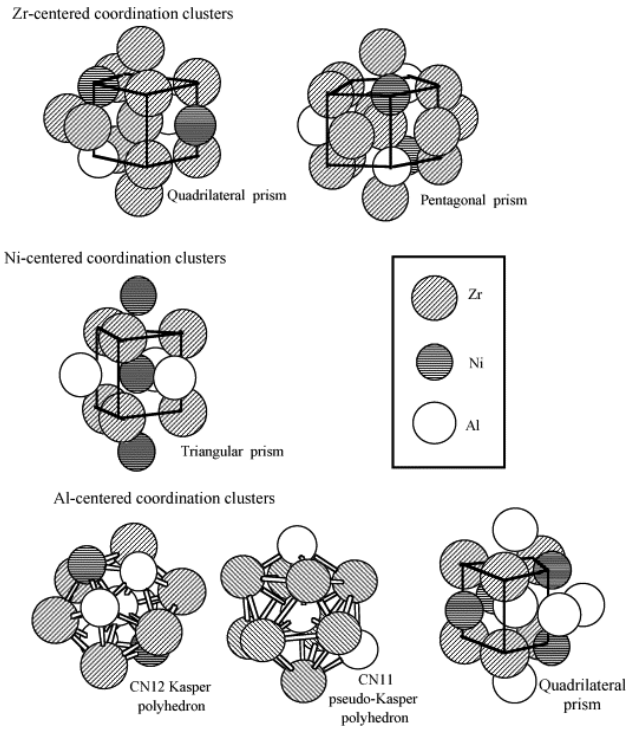

Figure 2.25: Different types of Zr-centred, Al centred and Ni-centred clusters in Zr-Ni-Al BMG (reprinted from [235]).

Partial crystallisation is an indirect method for understanding the microstructure of BMGs because it demonstrates the evolved structural feature after heating. Although it can predict the possible chemical and structural features inside the glassy structure, it cannot confirm the origin of those heterogeneities, originally existing inside the structure without direct experimental evidence.

It was reported that $Zr_{53.8}Cu_{31.6}Al_{7.6}Ag_{7.0}$ BMG with higher compressive plasticity did not show any microstructural or chemical heterogeneity when analysed through TEM, three-dimensional atom probe (3DAP) and anomalous small-angle X-ray scattering techniques [225]. The improved plasticity was linked to an increased proportion of Zr in $Zr_{53.8}Cu_{31.6}Al_{7.6}Ag_{7.0}$ compared to $Zr_{46}Cu_{37.6}Al_{8.0}Ag_{8.4}$. However, the pieces of evidence confirming the absence of microstructural heterogeneity are not strong enough. Identifying microstructural heterogeneities through small-angle X-ray scattering is quite impossible, especially of lower proportions. Furthermore, analysing these features from TEM and 3DAP requires sensitive analytical approaches, like NBED patterns and cluster analysis, respectively. It is impossible to abandon the presence of structural heterogeneities without testing through delicate analysis tools.

2.8.4 Solute-Centred Clusters:

It was observed that the structural analysis of Zr based BMGs in terms of pseudo-ternary metallic glasses (Zr-α(Al, Ti)-β(Ni, Cu)) by the ECP model (Section 2.5.4), is a useful and simplified approach [236]. A wide range of experimental studies quantitatively validated this model [87, 90, 236]. For example, high energy x-ray and neutron diffraction experiments confirmed short-range chemical ordering (SRO) around the α- (Ti, Al) and β- (Cu, Ni) solutes, as per the ECP model [236]. The random distribution of elements in Vitreloy-105 ($Zr_{52.5}Cu_{17.9}Al_{10}Ni_{14.6}Ti_5$) would expect 7 solvent atoms (Zr) in the first coordination shell. Whereas 11.8 solvent atoms (Zr) were observed experimentally [236] – indicating chemical SRO.

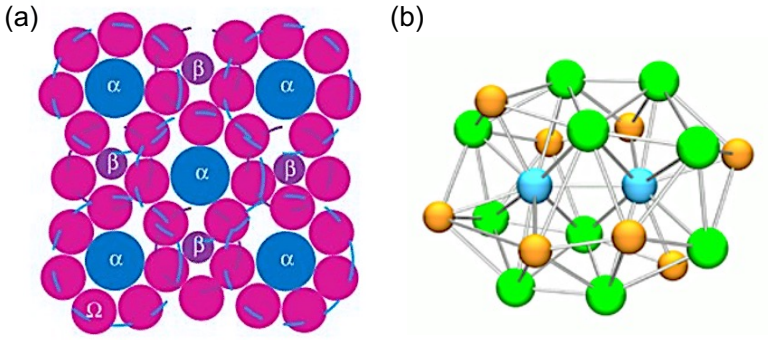

Figure 2.26: Example of solute clusters; (a) interpenetrating solute-centred clusters representation of α (blue), β (purple) solutes surrounded by Ω (pink) solvent, based on ECP model [87], (b) interpenetrating cluster with paired Ag-atoms (blue) in the centre, surrounded by Cu (bronze) and Zr (green) atoms in $Cu_{45}Zr_{45}Ag_{10}$ BMG [140], (reprinted from [87] and [140]).

It is widely agreed that solute-centred clusters are the fundamental building blocks in metallic glasses [69, 83, 86, 87, 237]. However, due to the higher proportion of solutes in the Zr-based BMGs, complete solute-solute avoidance is not possible, and the presence of interpenetrating solute-based clusters is rather likely [12]. In such cases, the solute clusters are surrounded by other solute atoms instead of solvent alone, as shown in Figure 2.26 (b). Either way, considering solute clusters in determining the metallic glass structure is a mutually accepted approach in the research community.

2.8.5 Types of MROs in Zr-based BMGs

The presence of various chemical and/or structural SRO clusters is a known trait of a metallic glass structure. These clusters may arrange themselves to form different MRO clusters, acquiring improved packing efficiency, lower energy and maximised stability [12, 238]. The coexistence of different structural MRO clusters was reported by Hwang et al. [232], where experimental data confirmed the presence of both the icosahedral and the fcc-like MRO clusters in ZrCuAl BMG.

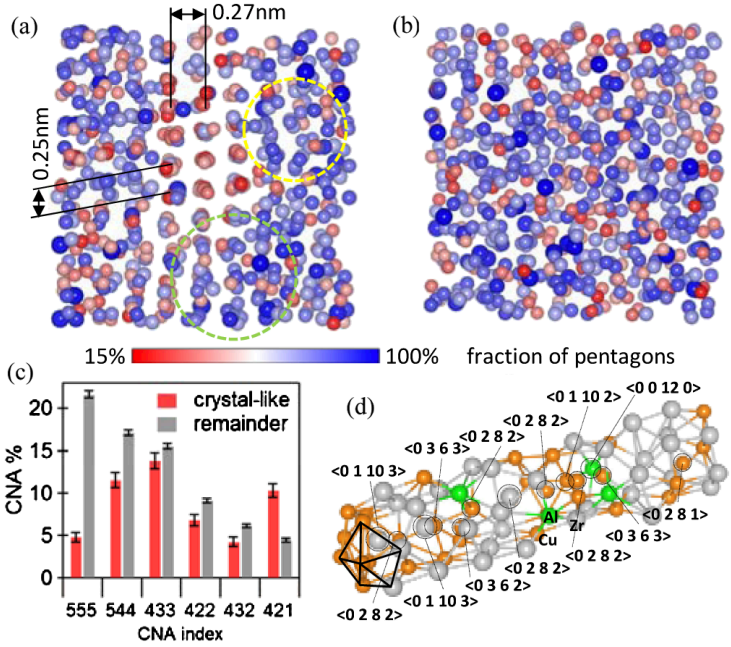

Figure 2.27: (a) A region from the simulated annealed structure of $Zr_{50}Cu_{45}Al_5$ BMG showing the crystal-like supercluster with dashed circles, (b) a same sized region from the embedded atom model. (c) Common neighbour analysis (CNA) indices of the crystal-like and other supercluster in the annealed model. (d) One of the dashed circles from (a) is expanded to show chain icosahedral supercluster. Al (green), Cu (bronze), and Zr (grey) atoms are shown in (d) (reprinted from [232]).

Researchers reported modified deformation behaviour in metallic glasses due to multiple shear bands created from the hindrance of hard icosahedral clusters while percolating soft crystal-like clusters [233, 239]. Yang et al. [90] found the crystal-like MRO clusters with an average size of ~2-2.4 nm in the glassy nanoparticles. A similarity between these MRO clusters and the STZs was observed based on their average sizes [12, 100, 105]. The ordered clusters were also observed in other amorphous alloys by TEM through high contrast lattice fringes and nano-beam electron diffraction images [240].

2.9 Summary

In this literature review, the unique characteristics of BMGs were discussed in Sections 2.1 to 2.3. Different methods to enhance their mechanical properties by structural rejuvenation were introduced in Section 2.4, followed by various structural models and deformation theories about their atomic structures (Sections 2.5, 2.6). Different characterisation techniques and their limitations were considered in Section 2.7. Eventually, the significant structural features of Zr-based BMGs were presented in Section 2.8. This literature review highlighted a few of the unanswered questions that are crucial to linking the microstructure-property-processing relationship in metallic glasses. The mechanical properties of BMGs such as, fracture

toughness, hardness, and plasticity, depend on the optimisation of deformation mechanism (Section 2.6). Therefore, it is critical to explore atomic to the sub-atomic level structural features, contributing towards modified deformation behaviour in BMGs.

The chemical influence of different elements on the properties of BMGs is a significant aspect that requires thorough understanding. The slightest compositional variation of the atomic species significantly affects their properties, especially their compressive plasticity. On the other hand, similar sized atomic species in multi-element metallic glasses make it difficult to experimentally evaluate their chemistry due to resolution limitations in many microscopy and diffraction studies (Section 2.7). The structural profiles are solved on an average scale, yet much information is still required at the atomic or near-atomic scale for a complete structural understanding.

It was observed that the data mining tools in APT could be worthwhile in extracting the chemical and structural information about structural heterogeneities to help understand the microstructure- property relationship in metallic glasses. The field of APT is least explored by researchers for analysing structural features in homogeneous BMGs. Given its success in many non-metallic materials, its utilisation for obtaining beneficial chemical and microstructural information for metallic glasses is an exciting avenue for research. However, the technique has certain limitations, particularly while considering BMGs. APT – with careful considerations of its constraints and by optimising its working conditions, certainly overshadows its limitations. Its ability to discern topologically similar atomic species is undoubtedly one of its most vital features.

In summary, the following limitations were found after the literature review:

1) The absence of long-range order in BMGs makes their structural characterisation difficult through a single structural model, as described in Section 2.5.

2) The chemical contribution of topologically similar elements is challenging. Although several studies have been conducted, the similar atomic sized species in BMGs make it difficult to identify their contribution to property variations. Only the average structural chemistry is observed in most cases due to the technical limitations of various characterisation techniques, as discussed in Section 2.7.

3) Microstructural analysis of BMGs through APT is not straightforward. In Section 2.7.4, the discussion on APT introduced the idea of BMGs' characterisation through this 3D microscopy technique. This approach seemed feasible due to its high atomic resolution for resolving the chemical identities of almost all the related species within the BMGs. However, as mentioned in Section 2.7.4.3, there are certain limitations to the use of APT, especially clustered evaporation and optimised operating conditions. These limitations should be addressed to obtain a valuable APT outcome.

4) The chemical origin of the structural heterogeneities found in BMGs contributing towards plastic deformation is unknown (Section 2.6, Section 2.8.3). Even a monolithic BMG contains local heterogeneities. However, it is not evident among the scientific community whether these local structural variations are chemically, structurally, or jointly different from the remaining BMG structure. Quantifying these structural features is a prerequisite for understanding their microstructure-property-processing relationship and designing future BMGs for advanced applications.

3 AIMS AND SCOPE OF THESIS

This thesis aims to study the microstructural features responsible for local hardness variations in Zr-based BMGs, with particular attention to their chemistry. APT methodologies were critically examined in search of protocols that delivered information of known precision. Atomic-scale chemical and structural information, that could contribute to microstructure-property relationship in multi-element Zr-based BMGs, was the ultimate goal.

The previous chapter outlined the significant role of structural heterogeneities towards enhanced mechanical properties (Section 2.4). As was discussed, considerable uncertainty in the chemical, topological and structural details of these heterogeneities remain (Sections 2.6, 2.8.3). A detailed understanding about these distinct features is necessary to regulate ductility and fracture toughness in these materials. The particular limits of electron microscopy and diffraction techniques towards the complete characterisation of these local heterogeneities were discussed in the previous chapter. It remains an attractive possibility to resolve such microstructural issues via APT – a significant opportunity that this thesis sought to investigate. Therefore, the specific aims and scope of this research were as follows:

Aim #1: To assess the nature of structural and chemical heterogeneities in Zr-based BMG through computational simulation.

Scope: An atomic-scale structural model of the Zr-based BMG was generated via simulation. This was used as an input to a clustering analysis, using typical APT clustering analysis protocols, to gain insights into the atomic-scale structural and chemical variations within the BMG (Chapter 5).

Aim#2: To develop a methodology for the quantitative and qualitative assessment of the BMG microstructure by APT.

Scope: Particular attention was given to carefully devising a methodology for robust composition and data quality by systematic evaluation of APT experimental parameters. The optimised method was then applied on to various Zr-based BMGs, for assessing possible compositional fluctuations across their variable local hardness regions (Chapters 6, 7).

Aim #3: To investigate the distinctive features inside the various regions of high and low hardness by APT.

Scope: The APT data was used to characterise the significant atomic-scale structural features in BMGs via primary structural parameters like size, chemistry, number densities and volume fractions across different hardness regions. Two of the compositions of Zr-based BMGs ($Zr_{52.5}Cu_{17.9}Ni_{14.6}Al_{10}Ti_5$ and $Zr_{63.78}Cu_{14.72}Ni_{10}Al_{10}Nb_{1.5}$ (at. %)) were considered for possible differences or similarities in variable hardness regions. The distinct structural features and their surrounding matrix were evaluated for any chemical variations (Chapters 8, 9).

Aim #4: To correlate the APT data with available TEM results to explore the microstructure-property relationships.

Scope: The BMG data obtained through the APT technique was correlated with the available TEM results for validating its relative competence. The approach behind this correlative study was to gain maximum information from the strengths of both methods in attaining a comprehensive analysis of the material's atomic structure (Chapter 10).

Whilst the development of an atomistic model is beyond the scope of this study, a thorough understanding of BMG local structure and its evolutions with local hardness variations was pursued. The implication of the work is its importance in tailoring ductility and plastic deformation to enhance fracture toughness, which is a critical attribute required for the practical application of these advanced materials.

4 MATERIALS AND METHODOLOGY

4.1 Materials

The work reported in this thesis was obtained using the following materials and processes.

4.1.1 Materials: Composition, Processes and Reference Mechanical Properties

The following three Zr-based BMGs were used in the present study:

- $Zr_{63.78}Cu_{14.72}Ni_{10}Al_{10}Nb_{1.5}$ (at. %) BMG
- $Zr_{52.5}Cu_{18}Ni_{14.5}Al_{10}Ti_5$ (at. %) BMG
- $Zr_{59.3}Cu_{28.8}Nb_{1.5}Al_{10.4}$ (at. %) BMG

Their processing history is briefly described in the following sections.

4.1.1.1 Thermally Cycled Zr-based BMGs

The master alloy was arc-melted in a Ti-gettered high purity Ar (99.99%) atmosphere using 99.99 % pure elements (Zr, Cu, Al, Ni) with 18.5 % (Zr-Nb). The BMG samples were prepared in collaboration with Shenzen University, China. For compositional homogeneity, the master alloys were re-melted at least four times. These were then cast by injecting homogeneous master alloys into a copper mould in Ar (99.999%) environment. Moulded plates of dimensions $2 \times 4 \times 55$ mm^3 were manufactured by injection moulding into a copper mould using 99.999 % pure Ar gas, as reported in detail by Xie et al. [241]. The resulting composition was $Zr_{63.78}Cu_{14.72}Ni_{10}Al_{10}Nb_{1.5}$ (at. %). The rectangular beams were then annealed at a temperature of 473 K (below T_g=645 K) for 10 min in a flowing high purity nitrogen atmosphere for relieving residual stresses. Thermal cycling was conducted by alternatingly immersing samples into liquid nitrogen and boiling water for 1 minute each, for 70 cycles and 120 cycles to create 'TC2' and 'TC3' samples. Further details about the material and thermo-cycling procedure can be found in previous studies [56, 193].

Two bulk samples (TC2 and TC3) of thermally cycled BMG were used in this study. TC2 was mainly used for the methodology and basic parametric studies of the BMG. The microstructural analysis to compare hard and soft regions was conducted on the TC3 sample.

4.1.1.2 High-Pressure Torsion (HPT) Vitreloy 105 BMG

The HPT samples of $Zr_{52.5}Cu_{18}Ni_{14.5}Al_{10}Ti_5$ (at. %), commonly known as Vitreloy 105, were prepared from research-grade plates of 30 × 30 × 2.3 mm^3 dimensions. The samples were procured from Liquidmetal Technologies, USA. A disc of about 8 mm diameter and ~1 mm thickness was cut by wire electrical discharge machining. It was then annealed at 630 K for 2 hours. Subsequently, it was HPT deformed at a deformation rate of 0.2 rotations per minute at room temperature and hydrostatic pressure of ~ 7.6 GPa for one rotation. These plates were then cut into beams with 2 × 4 × 20 mm^3 dimensions for fracture toughness test. The fractured sample in this study was taken from the fractured surface.

4.1.1.3 3D-Printed AMZ4 BMG

$Zr_{59.3}Cu_{28.8}Nb_{1.5}Al_{10.4}$ (at. %) BMG, formerly known as AMZ4, was processed from selective laser melting (SLM) using an EOS M290 with a 400 W Yb-fibre laser. The printed material was produced using commercially available amorphous AMZ4 powder of 10-45 μm particle diameter (from a collaborator in Heraeus, Germany). The BMG specimen was printed using a classic electrooptical system (EOS) rotating stripe pattern (67° scan rotation between each layer) and a 20 μm layer thickness, as detailed in [242]. A specimen with dimensions of 10 × 10 × 18 mm^3 was fabricated, with the longest dimension corresponding to the build direction.

4.1.2 Nominal Composition of Materials

The compositions of all the materials were quantitatively acquired through inductively coupled plasma atomic emission spectroscopy (ICP-AES) per ISO/IEC 17025 standards, are shown in Table 4.1 (wt. %) and Table 4.2 (at. %).

Table 4.1: ICP-AES compositions of Zr-based BMGs under study in wt. %.

Materials	Elements					
	Zr	Cu	Al	Ni	Ti	Nb
TC2	75.6	11.0	3.86	7.83	0.05	1.51
TC3	75.1	11.2	3.95	7.86	0.01	1.54
Vitreloy 105	66.6	13.8	3.94	11.8	3.45	0.12
AMZ4	71.2	22.7	3.94	<0.01	0.02	1.99

Table 4.2: ICP-AES compositions of Zr-based BMGs under study in at. %.

Materials	Elements					
	Zr	Cu	Al	Ni	Ti	Nb
TC2	63.96	13.36	11.04	10.30	0.08	1.25
TC3	63.49	13.59	11.29	10.33	0.02	1.28
Vit 105	53.38	15.88	10.68	14.70	5.27	0.09
AMZ4	59.78	27.36	11.18	0.00	0.03	1.64

4.1.3 Fracture Toughness of Materials

The single edge notched bending (SENB) test was conducted to obtain the fracture toughness of the BMG samples (Model 8872, Instron Corporation, Norwood, MA, USA). The nominal dimensions of $2 \times 4 \times 20$ mm^3 nominal dimensions were used for all the samples. The samples were ground to a smooth surface and polished to 0.05 mm surface finish. A 15 mm loading span, with a 5 kN load cell and a constant displacement rate of 0.83 μm^{-1} [56].

Table 4.3:K_Q and K_J, representing the fracture toughness values due to dimension limitations. The latter is based on J-integral.

Sample Name/Type	K_Q (MPa√m)	J (KJ/m^2)	K_J (MPa√m)
AC (As Cast)	55 (15)	33 (16)	55 (15)
TC-2 (70 cycles)	82 (16)	203 (140)	132 (51)
TC-3 (120 cycles)	76 (22)	146 (88)	115 (35)
HPT-02 (Vitreloy 105)	(14.7)	-	-

*Data of AC was taken from Ref [241], whereas TC-70 and TC-120 was taken from Ref [56]. The p-values for K_Q and K_J were 0.028 and 0.019, respectively.

4.1.4 Microhardness Maps of Materials

Vickers microhardness mappings were created on the polished cross-sections of the BMG samples that were cut parallel to the fracture surface. Microhardness mapping was performed with a 0.05 kg load and a dwell time of 10 s, using Durascan-80, Struers, USA. To avoid the interference between the indentations, a spacing of 40 μm was used between each indentation. The mapping revealed a microstructure of hard and soft domains (~63–105 μm) in the BMG [56].

Nanoindentation was tested on one of the BMG samples. However, the hardness map did not significantly change compared to the results of Vickers microhardness mapping. Therefore, Vickers microhardness mapping was chosen instead for mapping larger area with the hard and soft domains in the as-cast BMGs and their transition with thermomechanical processing. The statistical testing confirmed that the thermal cycling heterogeneously softened the hard domains while the soft domains remained apparently unchanged [56].

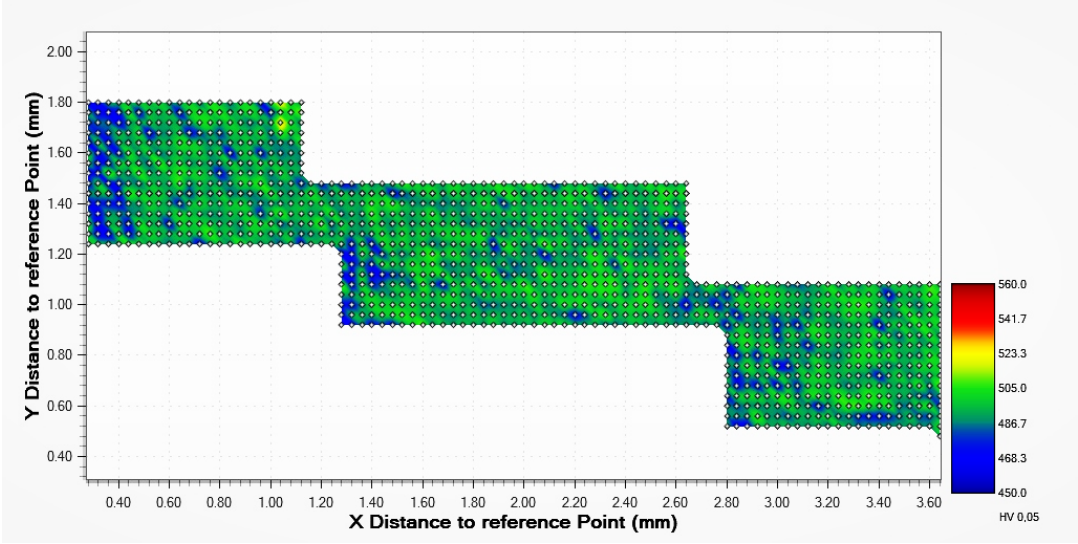

Figure 4.1: Hardness map of thermally cycled (TC3) $Zr_{63.78}Cu_{14.72}Ni_{10}Al_{10}Nb_{1.5}$ BMG.

The hardness maps of the samples used in this study are shown in Figure 4.1, Figure 4.2, and Figure 4.3 for TC, HPT, and HPT-fractured samples, respectively. The blue regions representing the relatively lower local hardness values, will be referred to as "soft regions." The green and red regions will be considered as "hard regions," throughout this dissertation.

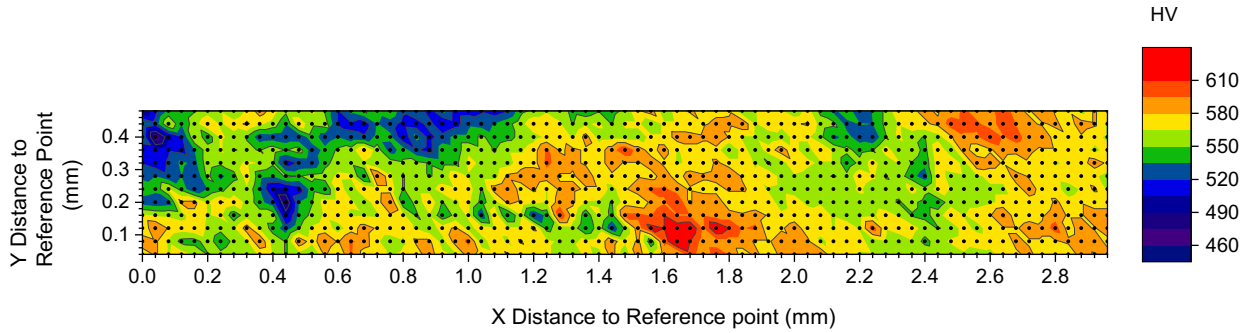

Figure 4.2: Hardness map of high-pressure torsion (HPT) $Zr_{52.5}Cu_{18}Ni_{14.5}Al_{10}Ti_5$ (Vireloy-105) BMG for the analysis of hard and soft regions.

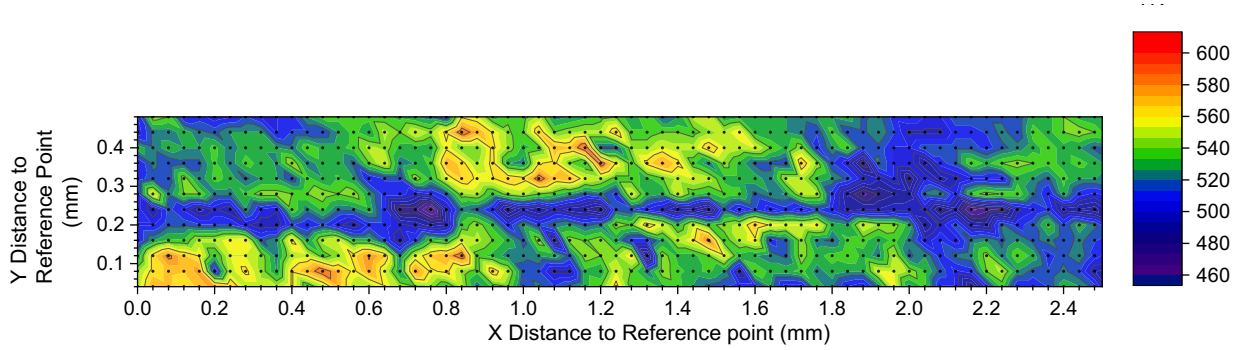

Figure 4.3: Hardness map of high-pressure torsion (HPT) $Zr_{52.5}Cu_{18}Ni_{14.5}Al_{10}Ti_5$ (Vitreloy 105) BMG for the analysis of fractured region.

4.2 Sample Preparation – Scanning Electron Microscopy

The samples of the TC- and HPT- BMGs were prepared through the dual beam focussed ion beam – scanning electron microscope (FIB-SEM). Further details are described in the following sub-sections.

4.2.1 Site Specific Analysis – Material Extraction

The samples were extracted from specific sites, i.e., the hard, soft, and fractured regions of the BMGs. The microhardness maps shown in Section 4.1.4, were used for the site-specific hard and soft regions' analysis. The plastic zone radius of each indent was found to be about 10-13 μm [243-245]. The samples were extracted away from the plastic zones of the surrounding indents, for both the TEM and APT experiments, as shown in Figure 4.4a.

4.2.2 Specimen Preparation – TEM Experiment

TEM specimens were prepared by the standard lift-out procedure [246], using dual beam SEM/FIB. The upper layer was coated with ~1.5 μm Pt layer to prevent from Ga-ion beam. The sample was thinned down to ~10 μm depth, using 30 kV voltage and 50–250 pA current during coarse milling. A 5 kV voltage and 50 pA current was used for fine milling. The electropolished TEM samples were prepared from twinjet electropolishing (TwnuPol-5, Struers, USA), using 10% by volume nitric acid in methanol. The thinning was performed at 20–30 V, with the electrolyte at a temperature of –20 ºC. The ion milled TEM samples were prepared using an Ar-broad ion beam, (PIPS II Gatan, USA). Coarse milling on a polished disc of less than 100 μm thickness was performed at energies of 3–5 keV and at milling angles of ± 4º–6º, whereas it was fine milled at 1 keV and milling angles of ± 4º.

4.2.3 Specimen Preparation – APT Experiment

APT tips were prepared using a Zeiss Auriga FIB-SEM with a Kleindiek micromanipulator system. The specimen holder was inserted into a dual beam FIB-SEM. The lift-out method was based on a two-stage sample preparation process [247]. The first stage involved lifting-out a rectangular ROI. A sharp atom probe needle was prepared from the rectangular ROI by annular milling. The process comprised of the following steps:

- A 1.2 μm protective Pt-layer was deposited on the 2.5 × 20 μm^2 rectangular region of interest (ROI), to protect it from Ga-ion beam.

- In the first stage, angular milling was applied for the lift-out process. In the first step, ~6 × 32 μm^2 or 10 × 32 μm^2 rectangular slot was cut, with the depth of ~7-8 μm and at a tilt angle of 33º-35º. The slot was about 4 μm away from the ROI. This step is called "coarse rectangle milling."

- Another rectangular region of similar dimensions, was milled on the other side of the ROI, after rotating the specimen to 180º.

- In the next step, a fine rectangular slot of 10 × 32 μm^2 dimensions, was milled on either side of the ROI, covering ~0.5 μm region from the ROI.

- The fine rectangular slot was re-milled to avoid re-deposition and potential ion damage to the sample. The details are summarised in Table 4.4.

Table 4.4: The detailed specifications for lift-out milling of the rectangular piece for APT sample preparation.

Type of Cutting Slot	Slot Dimensions (μm^2)	Tilt Angle	Operating Conditions	Depth (μm)
Coarse rectangle	32 × 10	33°-35°	30 kV voltage, 15 nA current	7-8
Fine Rectangle	32 × 4	33°-35°	30 kV voltage, 2.5 nA current	7-8

- After that, one side of the rectangular ROI was cut free.

- The Kleindiek micromanipulator (lift-out probe) was attached to the centre of this cut side with Pt deposit. Once the micromanipulator was properly attached to the ROI rectangular piece, the final side was milled to remove linking with specimen.

- Micromanipulator along with the lift-out piece was removed from the specimen. The rectangular piece was then cut into four or five 2 × 2 μm^2 squared long pieces which were separately attached on the electropolished tungsten (W) grid posts through Pt-deposition. The entire process is illustrated in Figure 4.4.

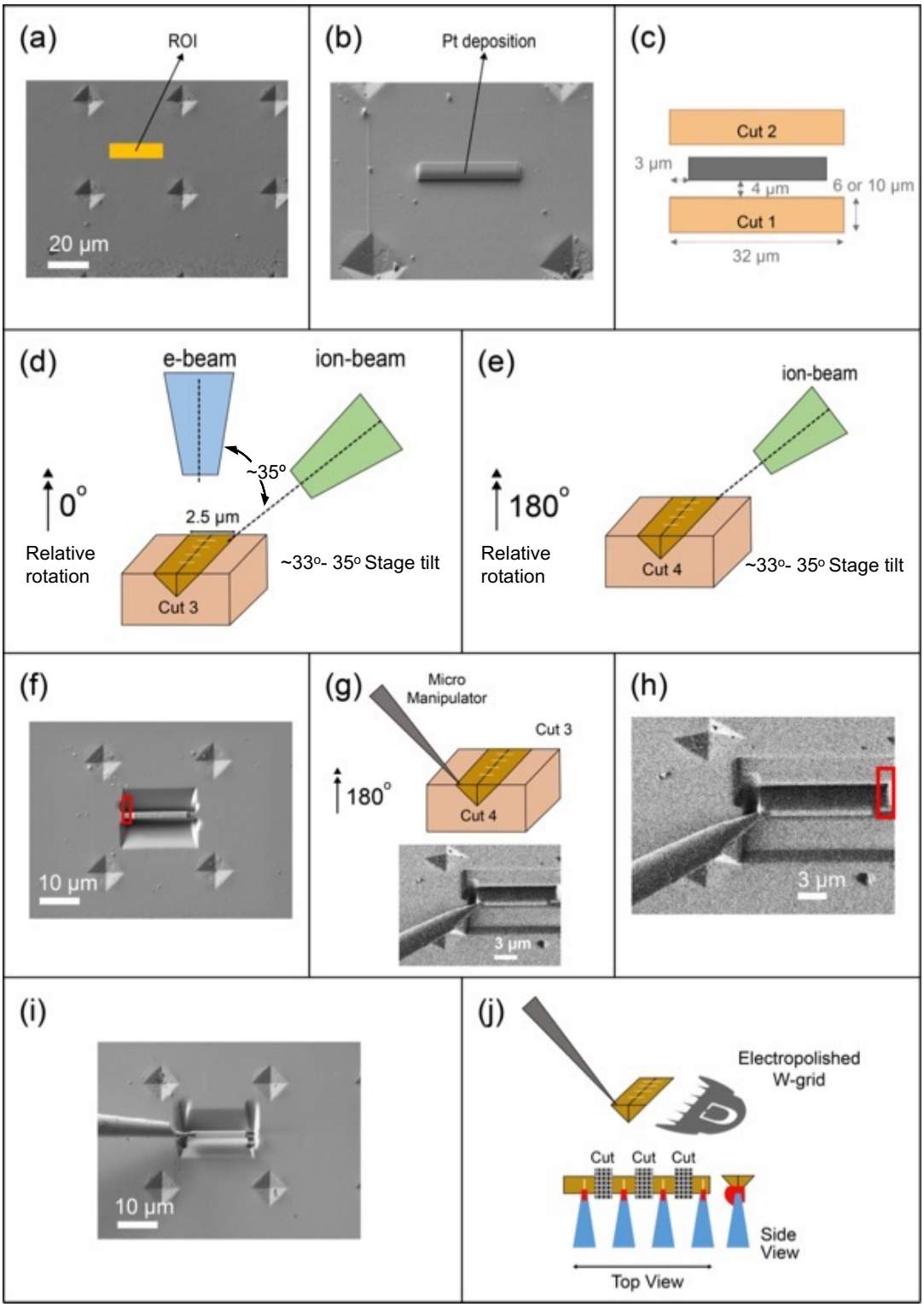

Figure 4.4: Major steps detailing the FIB lift-out process for site-specific atom probe tips preparation: (a) A rectangular region of interest (ROI) is selected between four indent from the bulk material. (b) Pt deposition is applied on the rectangular site first by electron-beam and then through ion-beam, with a total thickness of 1.5 µm, for surface protection. (c) Rough cuts are applied on either side of the ROI (coarse milling). (d, e) Fine cut (#3 and #4) finalised the ROI in the desired shape. (f) One side of the ROI is removed from the bulk sample. (g,h,i) Micromanipulator is attached to the ROI, other side of the ROI is removed from the bulk sample and micromanipulator is carefully retracted with the lift-out. (j)) The lift-out bar is attached to the supporting posts of the electro-polished tungsten grid.

- The square-shaped lift-out attachments were annular milled in the second stage.

- Both rough and fine annular milling involved multiple rounds of milling and the typical values used in this study are listed in Table 4.5. The process is illustrated in Figure 4.5. The tips were milled to an apex diameter of about 40-65 nm, measured through voltage estimation of APT reconstruction algorithm.

Table 4.5: The details of the parameters for annular milling of the APT sample.

Step #	Operating Conditions	Dwell time (μs), pattern overlapping	Circular Milling Slot Inner-Diameter (μm)
Coarse Annular Milling			
1	30 kV voltage, 1 nA or 500 pA current.	500, 10%	2
2-4	30 kV voltage, 250 pA current	500, 10%	1
		300, 10%	0.5
		300, 10%	0.3
Fine Milling-Pt removal			
5	10 kV voltage, 50 pA current	100, 10%	0.3
6	5 kV voltage and 50 pA current.	20, 10%	0.3

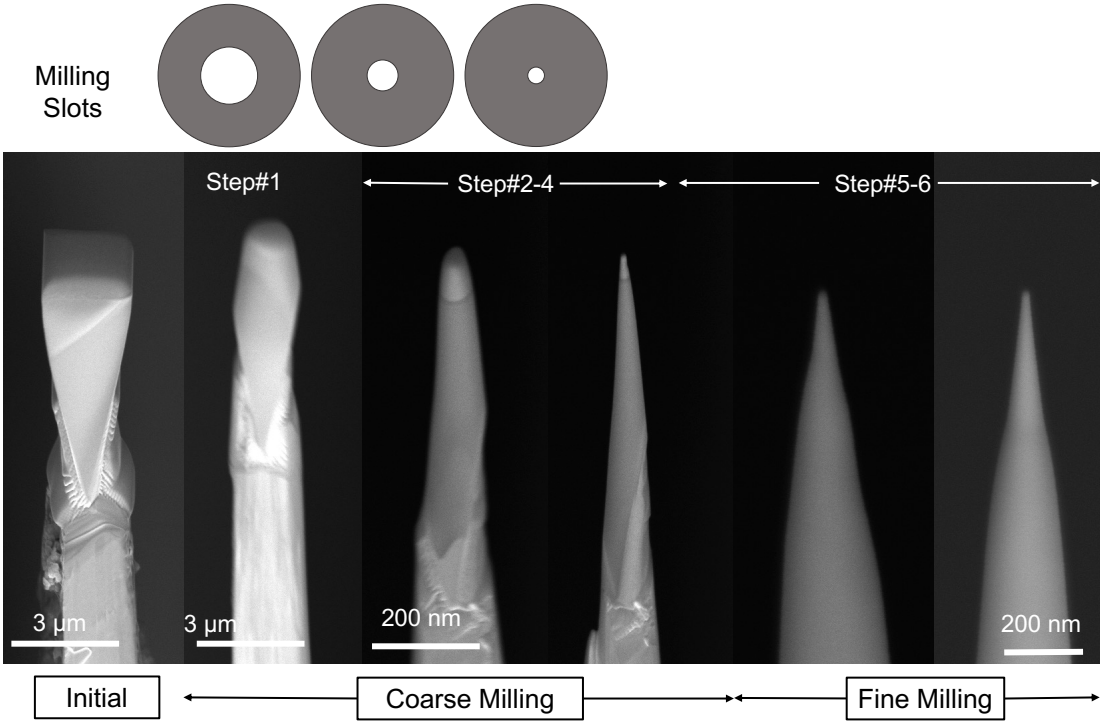

Figure 4.5: Stages of annular milling from start to end. Annular milling is used to create a needle shaped tip – a final cleaning mill at low kV is also used to remove the ion damaged layer.

4.3 BMG Sample Characterisation – TEM

A JEM-2200FS (JEOL, Japan) TEM was used for studying the microstructure of the BMG specimens. The machine was operated at 200 kV with an in-column Ω-filter and a Gatan Rio CMOS camera. The thickness of the electron diffracted area was 29 ± 5 nm, which was measured using an energy filtered TEM function in DigitalMicrograph™ (Gatan, USA).

The probability of finding an atom at a distance 'r' from a central atom at the sub-nanometre scale, was found using the pair distribution functions (PDFs). A selected area aperture of 10 μm and entrance aperture of 120 μm was used for SAED patterns. The SAED patterns were acquired at the magnification of 10^5 with an exposure time of 2s and using an energy slit of 5 eV. These diffraction patterns were collected from an area of ~200 nm. The signal was obtained from both the ordered clusters and the less ordered matrix. An in-house developed software named EDP2PDF was applied to extract an azimuthally integrated diffraction pattern (AIDP) from the SAED pattern, as detailed in Ref. [248]. The AIDP was then converted to the structure function (SF) and the PDF. The background was almost entirely eliminated by a sensitive nonlinear iterative peak clipping algorithm [249]. The PDFs were calculated from the inverse Fourier transform of the structure function.

The MRO analysis was carried out by NBED patterns and fluctuation electron microscopy. A condenser aperture of 40 μm diameter was used for the NBED experiments. In the TEM image mode, the nanometre sized electron beam diameter was measured using a CMOS camera at the magnification of 1.2 million. The electron beam diameter was varied from 0.7–1.6 nm. The Bragg-active volume fraction ($A_{hkl}\phi$) was calculated using the sample thickness of 30 nm, the material's density of 52 atoms/nm^3 for $Zr_{63.78}Cu_{14.72}Ni_{10}Al_{10}Nb_{1.5}$ (at. %), and 56 atoms/nm^3 for $Zr_{52.5}Cu_{17.9}Ni_{14.6}Al_{10}Ti_5$ (at. %). The nanobeam diameters of 1.9 nm, 2.2 nm, and 2.4 nm were used for $A_{hkl}\phi$ calculation.

4.4 Atom Probe Tomography (APT)

APT is an invaluable three-dimensional visualisation technique which is highly sensitive to accurate elemental identification of individual atoms with near atomic resolution. It is particularly reliable in differentiating the elements with similar atomic numbers; a trait which is difficult to acquire through other microscopy techniques. Therefore, it is a powerful tool for analysing solute distribution for microstructural characterisation of materials. The reader is directed to look into the books by Gault et al. [155], Miller and Forbes [203], Larson et al. [158] and other several review papers [161, 250-252], for the historical evolution and detailed information regarding the instrumentation, sample preparation and further applications.

In this section, the first part describes an overview of the basic principle and operation of the APT. The second part deals with the data reconstruction process and various reconstruction parameters. The third part is about the data analysis techniques especially the process of cluster analysis. The details of acquiring random APT data are also discussed. In the end, the statistical approach is described for observing the significance of the clusters.

4.4.1 Working Principle and Operation – APT

APT is a destructive technique in which high electric field is applied to field evaporate the atoms from the needle-shaped tip of the specimen. The needle-shape sample is used for facilitating the evaporation process, and the specimen is kept under high vacuum pressure at cryogenic temperature throughout the process. A schematic of the APT, illustrating its basic principle, is shown in Figure 4.6.

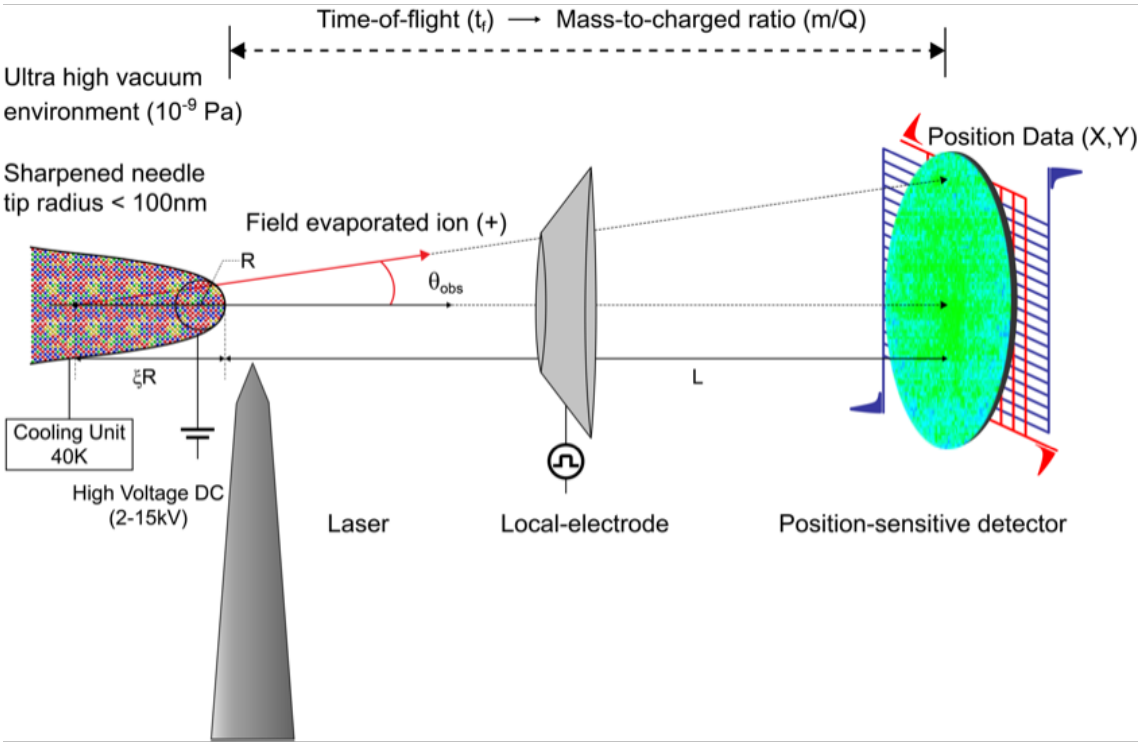

Figure 4.6: Basic working operation of APT (modified from [253]).

The basic operation of an APT includes the following details:

- The voltage is applied between a negatively biased APT tip and a counter electrode [154, 158, 254]. The presence of local electrode enables reconstructions with larger field-of-view (FOV). High energy laser light is absorbed by the specimen, per pico-second rate, which drastically increases the tip apex temperature during the pulse and ions start evaporating from the tip. The thermal energy then dissipates down the shank between the pulse.

- Once the laser pulse is applied, the positively charged ions within the FOV of the local electrode, pass through the aperture of the local electrode and flow towards the micro-channel plates (MCPs). The MCPs then convert these ions into the cascade of electrons for amplifying their signals. The electron clouds hit a position-sensitive delay-line detector, which comprises of two or three conductive lines, which then determines their lateral impact positions with a precision of ~0.2 mm.

- The ion coordinates and their sequence of evaporation is used to construct the three-dimensional (3D) imaging, based on their x, y (lateral) and z (depth) positions in the original specimen. The time-of-flight (TOF) of each ion, is the time recorded from the point of it leaving the specimen apex to the point of it hitting the detector, using a high-speed digital timing system. The mass-to-charge ratio (m/n) is calculated from the TOF by the following equations:

$$neV \approx \frac{1}{2} m \frac{d^2}{t^2} \tag{4.1}$$

$$\frac{m}{n} \approx 2eV \frac{t^2}{d^2} \tag{4.2}$$

Where;
n = charge state
e = elementary unit of charge
V = applied voltage
t = time between the laser-pulse and the detection
d = flight path length

The TOF spectrum is then converted to the mass spectrum by the help of eq. (4.2). The 3D image is constructed based on the above information and by the help of reconstruction algorithm [95-97], which will be detailed in the later section.

The straight flight path Local Electrode Atom Probe (LEAP) 4000 XSi™, manufactured by CAMECA Science and Metrology Solutions, was used in the current work (Figure 4.7). The APT experiments were performed by using the laser-pulsed mode and a 355 nm wavelength UV laser. After the atom probe tips were prepared, following the approach mentioned in Section 4.2.3, these were loaded in the load lock chamber of LEAP 4000XSiTM, which were further taken to the analysis chamber after achieving the low enough vacuum (~10-8 Torr). The vacuum in the analysis chamber was kept at <10-11 Torr. A tip was then positioned in front of the local electrode which is located several mm away from it. The positioning and alignment of the tip was controlled through the stage controls, by the help of optical cameras at the front and rare side of the stage. Further alignment was adjusted by opening the laser aperture and manually aligning the laser beam at the apex of the APT sample tip.

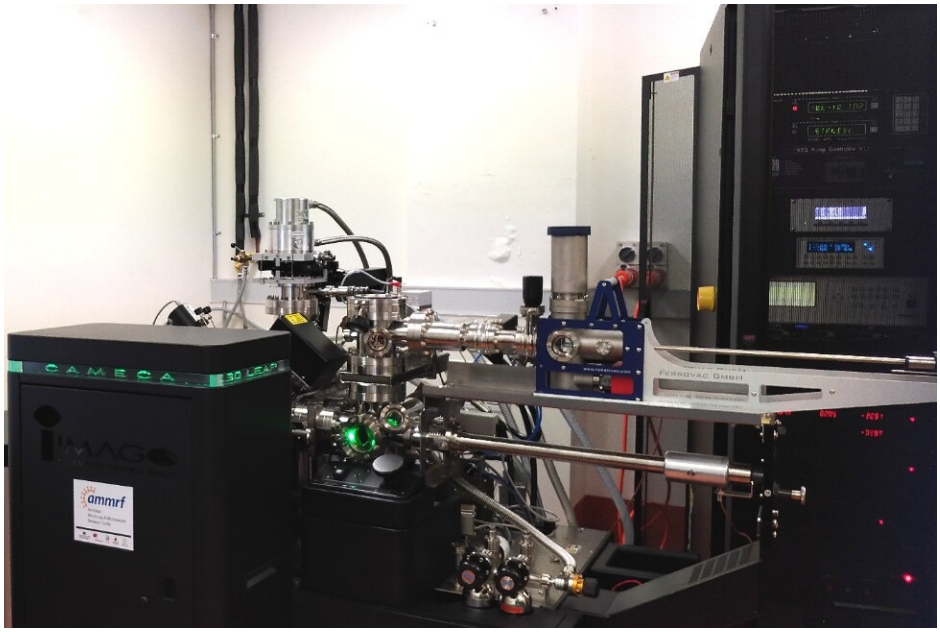

Figure 4.7: The CAMECA LEAP 4000 XSi with laser pulsing capability in the University of Sydney.

Once the APT tip was roughly aligned to the local electrode, appropriate operating conditions were selected for the operation. The parameters such as; temperature, laser energy, pulse repetition rate, maximum voltage and maximum number of ions collected, were considered at that moment. The APT experiment was started once the analysis chambers reached the appropriate level of pressure and cryogenic temperature. Fine adjustments in positioning were made after the APT tip reaching adequate evaporation conditions. The rule for the APT tip alignment in this study was such that 2/3 of the detector should be filled with the evaporation ions and the evaporated ions image centre should be aligned with the detector's centre. The data quality was assessed for preliminary analysis, from the emerging mass spectrum and detector-hit map. The mass peak ranging was customised based on the information about the constituting elements and their subsequent identification on the emerging mass spectrum.

The experimental quality, yield and fracture rate of the specimen depends on the material of the specimen and proper selection of experimental parameters. Regrettably, there is no universal rule for appropriate parameters selection. Optimal parameter selection is usually a heuristic process. The author has therefore developed and implemented a methodology for the selection of adequate experimental parameters that has provided a robust yield and high-quality data outcome. The details of the methodology will be discussed in chapter 6. Nonetheless, the summary of the selected experimental parameters is shown in Table 4.6.

Table 4.6: A summary of the APT experimental parameters that were used to produce good quality data for subsequent chemical and structural analysis.

Experimental parameters	$Zr_{63.78}Cu_{14.72}Ni_{10}Al_{10}Nb_{1.5}$ (at. %)	$Zr_{52.5}Cu_{18}Ni_{14.5}Al_{10}Ti_5$ (at. %)	$Zr_{59.3}Cu_{28.8}Nb_{1.5}Al_{10.4}$ (at. %)
Specimen temperature	40 K		
Laser pulse energy	100 pJ	75 pJ	75 pJ
Pulse frequency	160 kHz		
Detection rate	6%	3%	3%

4.4.2 Reconstruction Procedure of APT Data Used in This Work

The reconstruction of the APT data was carried out by Integrated Visualisation and Analysis Software (IVAS)® 3.6.8. The reconstruction process was based on seven discrete steps. The details of which are as follows:

1. In the step#1, the IVAS® software window showed the basic details about the specimen ID, date of acquisition, operating parameters, and detector event classes (single, multiple, partial and total hits).

2. The second step contained multiple windows for checking the voltage curve, background noise (ppm/ nsec), etc. versus ion sequence. The smooth region under the voltage curve was selected. The corresponding background history was checked to make sure of lower noise intervention. Initial 0.5–1 M ions were discarded to avoid sudden changes in voltage and any fluctuation in the start of the experiment.

3. In the next step, the area in the detector hit map was selected. The selected area should be circular on detector event histogram.

4. Voltage and bowl corrections were made on the mass spectrum of the selected ions through an automatic sequence, in the time-of-flight (TOF) correction step.

5. In the mass calibration step, the known peaks of certain species were selected and identified in the mass spectrum calibration step. The purpose of this step was to calibrate the experimentally found mass spectrum using theoretically known masses from the periodic table. In this work, Al^{+}, Zr_{92}^{2+} and Cu_{65}^{+} peaks were selected first for mass spectrum fitting, then Al^{2+}, Zr_{93}^{3+} and Ni_{58}^{2+} peaks were selected using the same fitting process for repeating the same process. The two-step process was performed to accomplish proper calibrate for every mass spectrum.

6. A range file was selected in the next step for ranging the mass spectrum. Every peak, except hydrogen peaks, was assigned to a particular ionic specie with an appropriate m/n peak width. Different ranging methods included full-width-half-maximum, full-width-nine-tenth-maximum and background-to-background peak ranging [255-257]. Unfortunately, there is no universal peak ranging strategy, and the application of different ranging methods affects the robustness of the reconstructed data from user to user. A customised and easy to use ranging approach (peak-based ranging) was used throughout the current study for maintaining the quality and robustness of the APT reconstructed data. Further details of the ranging approach are available in Section 6.1.1.

7. In the last step, certain reconstruction parameters were selected to finalise the reconstruction. The details of those parameters and their selection procedure are described in the next section.

4.4.3 Tomographic Reconstruction Parameters Used in This Work

Three categories of the reconstruction parameters are available:

Instrument Parameters

- Detector Efficiency
- Image Compression Factor (ICF)
- Field factor (k_f)
- Reconstruction centre (bowl and voltage correction)

Material Parameters

- Evaporation field of the primary element (F)
- Element specific atomic volume

Specimen Parameters

- Initial voltage, V or initial tip radius
- Voltage-based radius evolution ($r = V/k_fF$), or shank-angle based radius evolution

The accuracy of the reconstructed APT data depends on the successful implementation of all the steps especially the final step where the reconstruction parameters are chosen. The detector efficiency of the instruments at the University of Sydney had previously been determined to be ~57% [258] and was applied into the reconstruction algorithm. Unfortunately, pole structure on the desorption images was not available due to the amorphous nature of the Zr-based BMGs. Therefore, the ICF (ξ) and field factor (k_f) were determined using the method described by Loi et al.[259], by the following equations:

$$\xi = (c_1 D + c_2)T + c_3 D + c_4 \tag{4.3}$$

$$k_f = \left(1 - \frac{1}{c_1 V + c_2}\right)\xi^3 - e^{-(c_3 V + c_4)} + c_5 \tag{4.4}$$

Where:

D= Electrode aperture diameter (50 μm for the present study).
T= Distance between the specimen tip and the aperture (45 μm for the present case).

The values of the constants are as follows:

Constants	ξ	k_f
c_1	9.286×10^{-6}	0.3721
c_2	5.589×10^{-3}	1.303
c_3	5.589×10^{-3}	0.2767
c_4	1.499	3.422
c_5	-	0.067

ξ = 1.5 from eq. (4.3) and k_f = 3.5 was obtained from eq. (4.4). Similarly, an average evaporation field of 29 V/nm was used. It was calculated based on the evaporation field of the main element (Zr) and other solute elements with evaporation field higher than the main element, by the following relation [193]:

$$F = \sum (X_{(1-X_{Cu+Ni+Nb})}.F_{Zr} + X_{Cu}.F_{Cu} + X_{Ni}.F_{Ni} + X_{Nb}.F_{Nb}) \quad (4.5)$$

Where:

F= Evaporation field

X= Molar fraction

The evaporation field values of the elements in $Zr_{63.96}Cu_{13.36}Ni_{10.29}Al_{11.04}Nb_{1.25}$ (at. %) BMG, were 28, 30, 35, 19, and 37 V/nm respectively. The apex diameter was estimated based on voltage-curve for 3D reconstruction.

4.4.4 Clustered Evaporation

A particular concern in applying a field emission technique, such as APT to BMGs, is the uncertainty in the details of its field evaporation process. In crystalline materials, there exist discrete atomic ledges and terraces that serve to perturbate the local field intensity of the specimen tip such that the field evaporation occurs in a way that can be precisely controlled to achieve atomic layer-by-layer analyses [193]. The situation in BMGs is obviously different [14] and referred to as "clustered evaporation", which is the occurrence of localised high field regions that are usually clearly visible in field evaporation images and are indicative of a non-uniform evaporation sequence. An important consequence of all this is that the assumptions underpinning the usual reconstruction algorithms in APT are grossly invalidated. A close investigation of this phenomenon and its effect on the reconstructed data is crucial to discern the extent of damage on the APT outcome, if any.

The maximum separation method (MSM) for cluster analysis [181] was applied to interrogate this phenomenon. The primary distinction between the clustered evaporation regions and other parts of the reconstruction is that these regions are of higher density, so the distances between the atoms will be relatively less than the surrounding atoms. K^{th} order was selected for nearest neighbour (KNN) distributions. A term 'r_{max}' was used to describe the distance between 'K' atoms in the reconstruction.

Different K^{th} order distributions were generated from K=1 to 10. The Gaussian model of these distributions revealed two curves. The first curve with relatively lower r_{max} values represented clustered evaporation region, whereas the higher r_{max} value region was subsequently considered as the matrix. The Gaussian model was fitted in a way that the aggregate of two curves in each bin would exhibit the total frequency for that bin. A MATLAB™ script prepared by The University of Sydney's graduate student (William Davids) was used for this purpose. 500 bins were selected for this analysis and the intercept between these two Gaussian curves was used as cut-off r_{max}.

A thorough examination of the different KNN distribution revealed that the point of intersection between curve-1 and curve-2 was changing with the increase of K^{th} order (Figure 4.8). This variation was not similar for all the datasets. It suggested that the shape and size of the tip likely affected the rate of clustered evaporation. Thus, the order was not a constant number among different datasets. A different approach was considered instead for consistent selection of the order. Thus, the minimum order K, with which the peak of curve-1 and curve-2 were at the opposite sides of the intersection point, was selected. In this way, there was a clear difference between clustered region and the matrix, as shown in Figure 4.8b, unlike Figure 4.8a. The values of the KNN were, $3 \leq KNN \leq 5$, for all the datasets in the present study. It should be noted that since all the elements equally participated in the clustered evaporation process, therefore, all the elements, including solvent (Zr), were selected in the clustered evaporation investigation process.

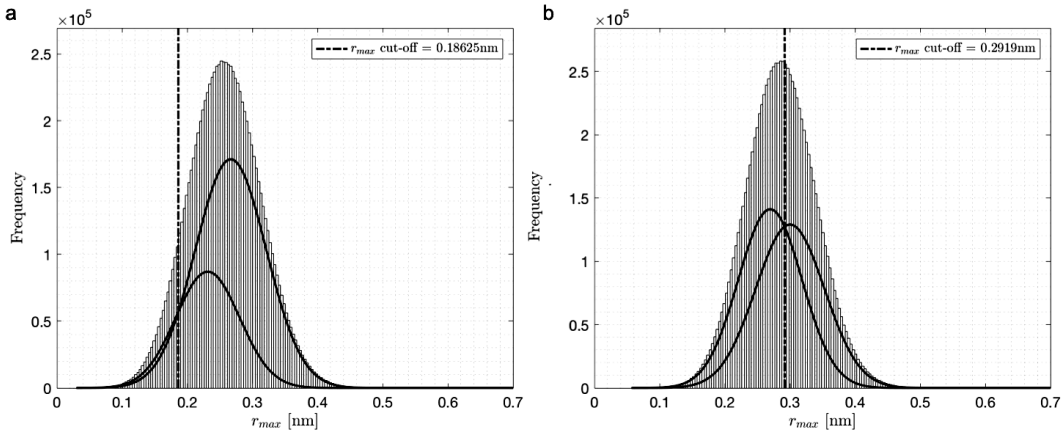

Figure 4.8: Comparison between (a) 3NN and (b) 4NN distribution.

4.4.5 Data Analysis Techniques

A 3D reconstructed APT data for HPT-Zr-based BMG is shown in Figure 4.9, as an example. The 3D reconstructions of the whole data and its individual elements were separately shown. It was observed that all the elements were homogeneously distributed. The possible presence or absence of structural features could not be determined unless investigated thoroughly.

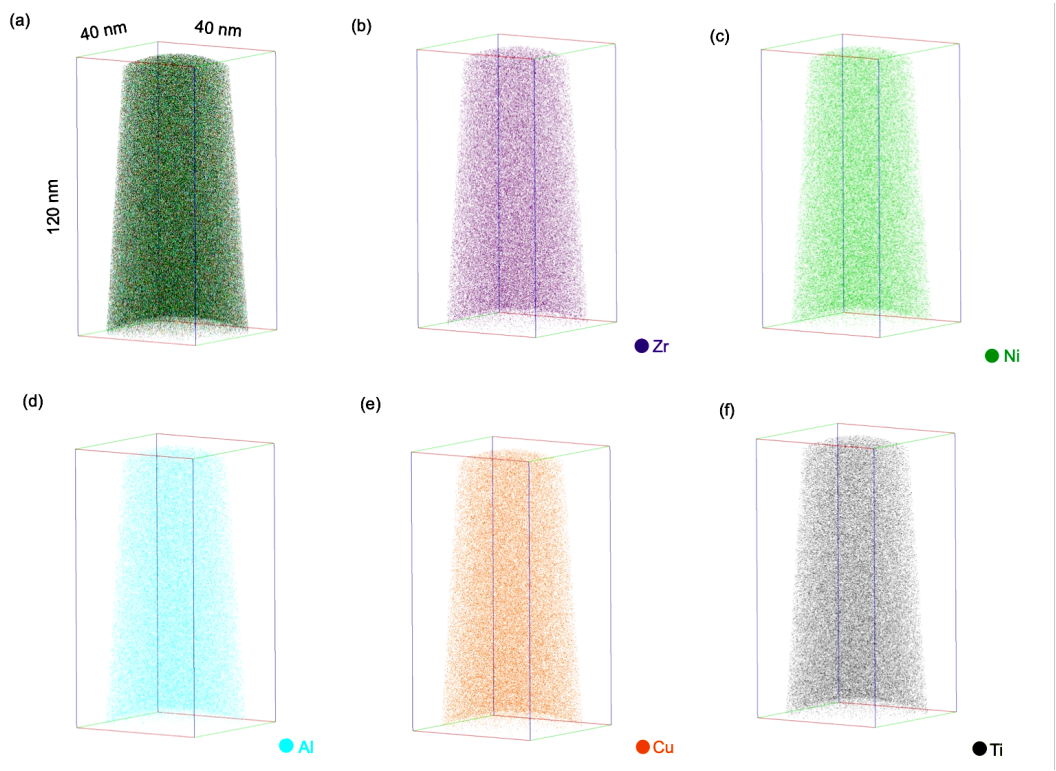

Figure 4.9: 3D reconstruction of one of the soft regions of HPT-Vitreloy-105 BMG (sample ID: R18-59799) showing (a) bulk, (b) Zr, (c) Ni, (d) Al, (e) Cu and (f) Ti.

IVAS cluster analysis algorithm was used as a data mining tool for further analysis of the APT data. This data mining tool helped explore the chemical clusters based on their sizes. Careful selection of parameters is important for appropriate outcome of cluster analysis. The primary parameters of the process are detailed in Table 4.7.

Table 4.7: Main parameters of the IVAS cluster analysis algorithm.

Parameter	Description
d_{max} (nm)	Maximum cluster separation distance.
Order (ions)	The order of atoms to be selected for investigating the clusters with distance d_{max}.
N_{min} (ions)	Minimum number of atoms to be part of the cluster

The literature is filled with a diverse range of parameter selection methodologies for precipitates, nanocrystals, or clusters inside the data [177, 186, 191, 260]. The correct selection of parameter selection primarily depends on the nature of the data.

4.4.5.1 Heuristic Approach for Cluster Analysis – KNN Cluster Analysis

As discussed in Section 2.7.4.2.1, the maximum separation cluster finding algorithm with 1st nearest neighbour (1NN) distances is a very localised approach. Intrinsic uncertainties in the field evaporation of amorphous materials suggest that this analysis, in its intended form, will be too sensitive towards the local density fluctuations.

A heuristic density-based cluster finding algorithm (DBSCAN or KNN maximum separation with K > 1) by Marceau et. al [177], was used instead. It is similar to max separation algorithm with NN higher than 1. The basic principle of its operation is illustrated in Figure 4.10.

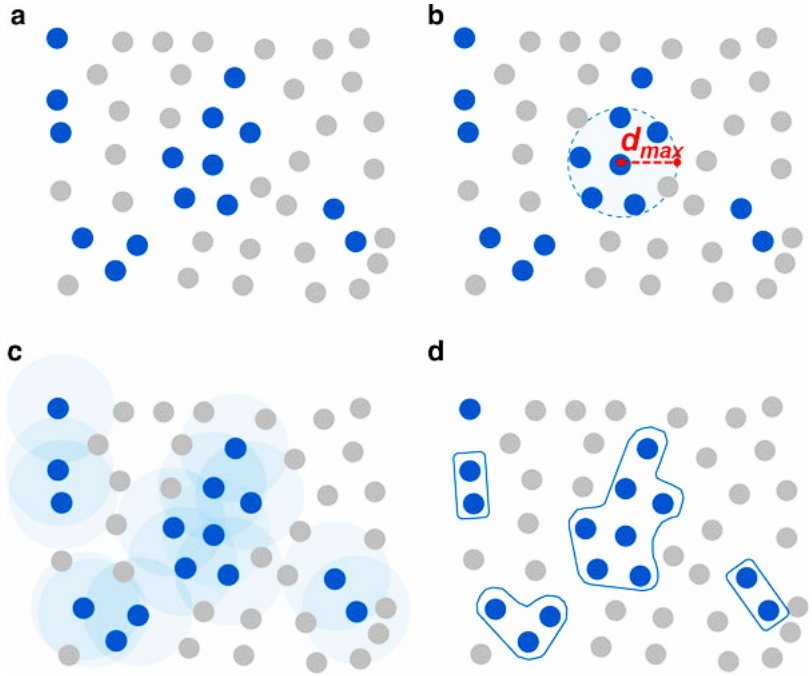

Figure 4.10: Schematic representation of the steps for 5-KNN cluster analysis: (a) A system with blue atoms as solutes and grey atoms as solvent, (b) sphere of radius d_{max} is drawn around one of the solute atoms, (c) d_{max} applied on all the solute atoms, (d) all the atoms are selected as a cluster if the sphere of one blue solute atom overlaps with another (reprinted from [155]).

This approach demonstrated distinct difference between experimental and random results with 5NN than lesser NNs for different hardness regions of Zr-based BMGs (Figure 4.11). Thus, 5NN was selected for cluster analysis. The nearest neighbour (NN) distance distributions for the experimental and random data were compared and d_{max} was selected as the distance of largest difference between the experimental and random.

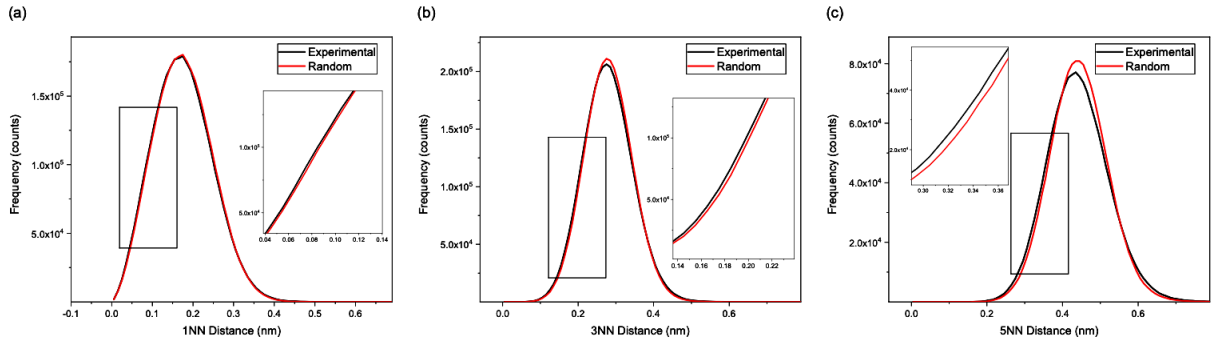

Figure 4.11: Nearest neighbour (NN) histogram for (a) 1NN, (b) 3NN and (c) 5NN for both experimental and random dataset. The insets are demonstrating the difference between the experimental and the random data for the left side of the curve.

Once the cluster analysis algorithm was applied on the experimental APT data, its outcome was saved as a .csv file. The reconstruction files of clusters and the residual matrix were saved in the .pos file format. There were three columns representing cluster size in the .csv file. The titles of these columns were; solute atoms, ranged atoms, and total atoms, respectively. The solutes atoms column represented the ranged solute atoms inside each cluster, the ranged column showed the sum of solutes and solvent atoms. On the other hand, the total atoms column counted all atoms, including impurities. The column of "ranged atoms" was selected for the cluster size consideration here, since it showed the total number of correctly ranged atoms including solutes and solvent for each cluster.

4.4.5.2 Cluster Analysis Parameters Used in this Work

The order (K) was taken as 5, based on the NN selection in the previous section. N_{min} was selected as 6 atoms, as the minimum cluster size to be equal to K+1. The distance parameter, d_{max}, was selected through the NN frequency histogram, as the distance with the largest difference between experimental and random data [177]. Al, Cu, Ni and Nb were selected for TC- $Zr_{63.78}Cu_{14.72}Ni_{10}Al_{10}Nb_{1.5}$ (at. %), whereas Al, Cu, Ni and Ti were chosen for HPT- $Zr_{52.5}Cu_{18}Ni_{14.5}Al_{10}Ti_5$ (at. %), as clustering solutes of Zr-based BMGs in the present study.

The number density of the clusters in different regions was calculated by the following relation:

$$Number\ Density\ of\ clusters = \frac{Total\ \text{count}\ of\ clusters\ \text{for}\ each\ \text{cluster}\ size}{Volume\ of\ the\ reconstruction\ (cm^3)} \quad (4.6)$$

In order to compare the APT cluster sizes with other microscopy techniques, the clusters were converted to linear measurements, such as diameter or radius of the clusters. The clusters were assumed spherical and the size conversion was obtained by the following equations:

$$N_v = \frac{(N_{cluster}/0.57)}{v_{cluster}} \quad (4.7)$$

Where:

N_v = Number density of a cluster
$N_{cluster}$ = Number of atoms in a cluster
$v_{cluster}$ = Volume of a cluster

The constant of 0.57 was added to account for intrinsic limited detector efficiency (57%) of atom probe [178]. Moreover, the volume and number density of a clusters were found by the following relations:

$$v_{cluster} = \frac{4}{3}\pi\left(\frac{d}{2}\right)^3 \tag{4.8}$$

$$N_v = \frac{\sum(X_{Zr}.\rho_{Zr} + X_{Cu}.\rho_{Cu} + X_{Al}.\rho_{Al} + X_{Ni}.\rho_{Ni} + X_{Ti}.\rho_{Ti})N_A}{\sum(X_{Zr}.m_{Zr} + X_{Cu}.m_{Cu} + X_{Al}.m_{Al} + X_{Ni}.m_{Ni} + X_{Ti}.m_{Ti})N_A}\ 10^{-21} nm^3 \tag{4.9}$$

Where:

d = diameter of a cluster (nm)
X = molar fraction of the elements inside a cluster
ρ = atomic density of the element (g/nm^3)
N_A = Avogadro's number (6.022×10^{23} atoms/mol)
m = molar mass of the elements inside the cluster (g/mol)

After substituting N_v and $v_{cluster}$ from eq. (4.8) and eq. (4.9), eq. (4.7) will be transformed as follows:

$$\frac{\sum(X_{Zr}.\rho_{Zr} + X_{Cu}.\rho_{Cu} + X_{Al}.\rho_{Al} + X_{Ni}.\rho_{Ni} + X_{Ti}.\rho_{Ti})N_A}{\sum(X_{Zr}.m_{Zr} + X_{Cu}.m_{Cu} + X_{Al}.m_{Al} + X_{Ni}.m_{Ni} + X_{Ti}.m_{Ti})N_A}\ 10^{-21} = \frac{(N_{cluster}/0.57)}{\frac{4}{3}\pi\left(\frac{d}{2}\right)^3} \tag{4.10}$$

$$d = \left(\frac{(Number\ of\ atoms\ in\ a\ cluster/0.57)}{numebr\ density\ of\ a\ cluster} \times \frac{6}{\pi}\right)^{1/3} \tag{4.11}$$

4.4.5.3 Morphology of the Clusters

The morphology of the clusters was calculated from the oblateness and aspect ratio of the best-fitted ellipsoid of every cluster [155, 261]. Three parameters from the cluster analysis .csv file were used; 'extent_x ranged', 'extent_y ranged' and 'extent_z ranged.' Out of these three, the largest was named as 'L_1', 2nd largest as 'L_2', and the smallest as 'L_3.' The oblateness and aspect ratio were calculated by the following relations:

$$Oblateness = {}^{L_3}/_{L_2} \tag{4.12}$$

$$Aspect\ ratio = {}^{L_2}/_{L_1} \tag{4.13}$$

Each morphology map was divided into four quadrants: disc, sphere, lath, and rod. An example of it is shown in Figure 4.12.

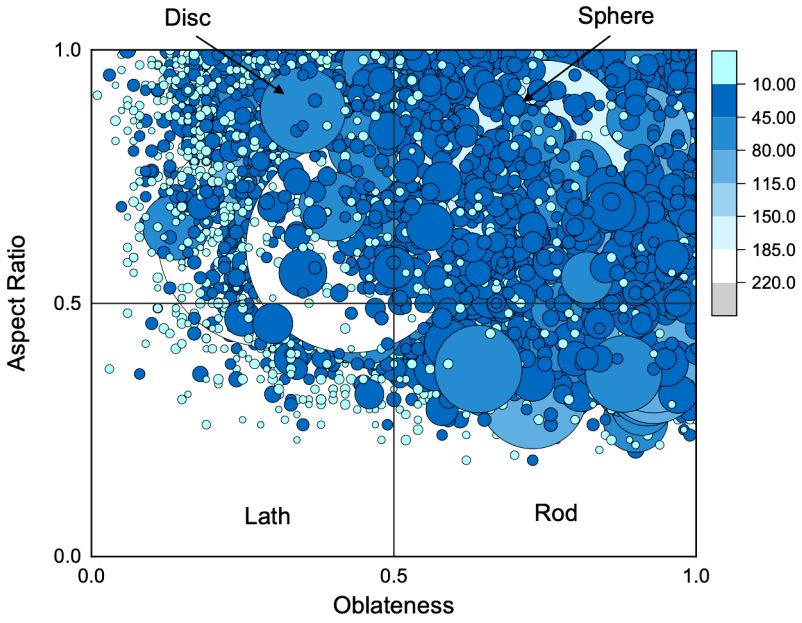

Figure 4.12: Morphology map sample for the clusters in Zr-based BMGs.

4.4.5.4 Statistical Analysis Methods – Random vs Non-Random

The randomly labelled dataset is a random comparator of the actual experimental data, where the identities of the elements are randomised while the concentration of each species is kept constant. A comparison between the observed and random datasets was made to confirm presence of clusters inside experimental data beyond what would be found in a random distribution. A MATLAB™ program, developed by Dr. Anna V. Ceguerra from The University of Sydney, was used for this comparison. The random labelled datasets were used from time to time in the present study for the comparison of clusters' number densities in actual and randomly distributed APT data.

4.4.6 Statistical Analysis Methods – Level of Heterogeneity of Clustering

The level of heterogeneity is a robust statistical analysis to clearly distinguish the experimental APT data from random distribution. It was used to quantify the spatial heterogeneity of solutes in the experimental data beyond accidental/ random variations.

Parametric statistical tests such as chi-squared test and Z-test were reportedly used in the past for comparing experimental and random data [262-264]. However, these tests were unable to discern previously reported nanoscale clustering [262, 264, 265]. An important reason invalidating their use for APT datasets was that in many cases the data was not normally distributed. Since the parametric tests work on normally distributed data whereas non-parametric statistical tests do not hold such requirement, non-parametric testing was selected for the current study.

In the present case, a goodness-of-fit-type statistic, called the level of heterogeneity (LH*), was considered for the statistical measurements. It was primarily used for the comparison between experimental and random distribution of nearest-neighbor distances [266]. A MATLAB™ script prepared by The University of Sydney's PhD student (William Davids) was used for this purpose. This comparison was made using more than 200 random labelled datasets. The level of heterogeneity (LH*) was calculated by the following relation [266]:

$$LH^* = \int_{\mathrm{d}} \left|\hat{G}(\mathrm{d}) - \bar{G}^*(\mathrm{d})\right| d\mathrm{d} \tag{4.14}$$

Where:

d = nearest neighbour distance,
$\hat{G}(\mathrm{d})$ = experimental G function,
$\bar{G}^*(\mathrm{d})$ = random G function.

The LH distribution was applied on the leading edge of the distribution curve as it contained the atoms with smaller inter-distances; hence the primary clustering information. In the case of clustering, the leading edge of the experimental distribution curve will be ahead of the random distribution. There are three ways to show such variation, as depicted in Figure 4.13.

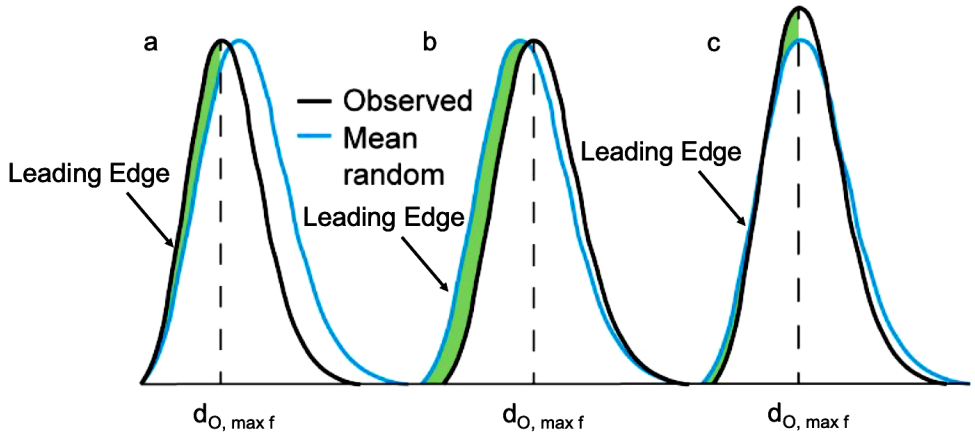

Figure 4.13: Three types of differences between the experimental and random distributions in APT data, (a) distribution confirming $LELH^*_{pos}$, (b) distribution confirming $LELH^*_{neg}$,(c) distribution to be interpreted through both $LELH^*_{pos}$ and $LELH^*_{neg}$.

Accordingly, eq. (4.14) was replaced by two test statistics for positive or negative area differences denoted as $LELH^*_{pos}$ and $LELH^*_{neg}$, respectively. These test statistics were defined as follows;

$$LELH^*_{pos} = \int_0^{\mathrm{d}_{O,max\,f}} \hat{G}(\mathrm{d}_i) - \bar{G}^*(\mathrm{d}_i)\, dw, \;\; \text{for } \hat{G}(\mathrm{d}_i) - \bar{G}^*(\mathrm{d}_i) > 0 \tag{4.15}$$

$$LELH^*_{neg} = \int_0^{\mathrm{d}_{O,max\,f}} \hat{G}(\mathrm{d}_i) - \bar{G}^*(\mathrm{d}_i)\, dw, \;\; \text{for } \hat{G}(\mathrm{d}_i) - \bar{G}^*(\mathrm{d}_i) < 0 \tag{4.16}$$

Where:

$d_{O,max\ f}$= d-value corresponding to the maximum frequency of the observed NN distribution,
w_i = cumulative distribution function (cdf) value at bin i.

The extension of LH* distribution using eq. (4.15) and eq. (4.16) was used for describing both circumstances: whether solutes were closer or father apart from each other, respectively, compared to the random distribution. The p-value for both $LELH^*_{pos}$ and $LELH^*_{neg}$ was 0.05. As an example, the role of $LELH^*_{neg}$ was to confirm the leading-edge position shifted to the right. If p-value of $LELH^*_{neg}$ was lower than 0.05, the inter-solute distance would be larger than what would be expected in a random distribution. The compiled outcome of all the solutes was demonstrated as a checkerboard pattern; an example of which is shown in Figure 4.14. The description of the symbols is summarised in Table 4.8.

Table 4.8: Summary of the LH* symbols and their descriptions.

Symbol	Description
▵	Solute distribution is non-random, and they are closer together than expected from a random distribution.
▼	Solute distribution is non-random, and they are further apart than expected from a random distribution.
☆ ○ ●	Solute distribution is non-random, but the NN distribution leading edge does not indicate how.

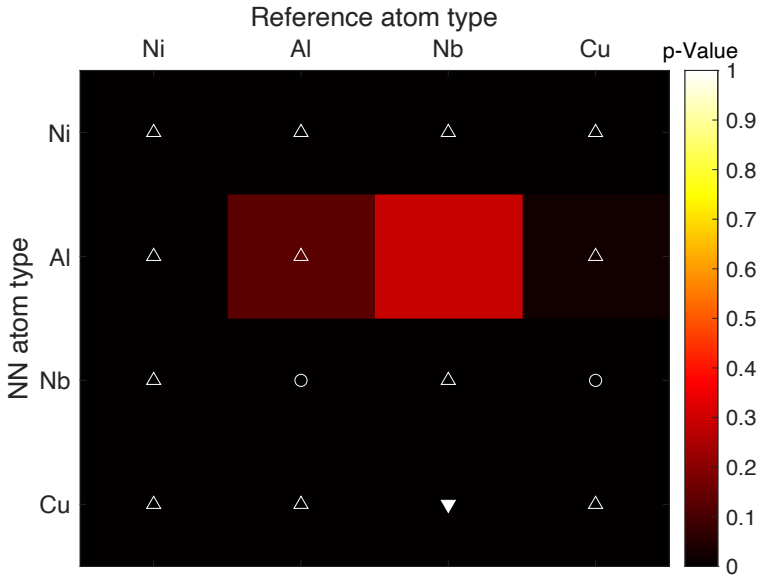

Figure 4.14: LH* checkerboard pattern final image of thermally cycled Zr-based BMG. (Sample ID:R18-59581).

4.5 Structural Characterisation using Molecular Dynamics

The molecular dynamics simulation was considered to obtain preliminary structural information about the Vitreloy-105 BMG, before the experimental APT analysis. The ab initio molecular dynamics (AIMD) calculations based on density functional theory (DFT) were used to investigate the local atomic structure of BMG by using the projector augmented wave (PAW) method [267] as implemented in the Vienna ab-initio simulation package (VASP) [268-270]. The electronic exchange correlation was treated using the generalised gradient approximation (GGA) utilising the Perdew-Burke-Ernzerhof functional [271]. The AIMD experiments were carried out in the canonical (NVT) ensembles using Nosé thermostats to control temperature. Outer electron wave functions were expanded using a plane-wave basis set with the kinetic energy cut-off of 400 eV. Only Γ point was used for sampling the Brillouin zone. The atomic relaxation force tolerance was 0.01 eV/Å. The valence electrons were $4s^2 4p^6 4d^2 5s^2$ for Zr, $3d^{10} 4s^1$ for Cu, $3d^8 4s^2$ for Ni, $3s^2 3p^1$ for Al, and $3d^2 4s^2$ for Ti.

The nominal composition of the 500-atom AIMD model was Zr(262) Cu(90)Ni(73)Al(50)Ti(25) which was similar to the experimental concentration used, i.e., $Zr_{52.5}Cu_{17.9}Ni_{14.6}Al_{10}Ti_5$ (at. %). Correspondingly, a cubic supercell with a lattice constant of 20.78Å was developed by using the experimental density of the BMG (56 atoms/nm^3). A timestep of 2 fs was used for all AIMD simulations.

The ensemble was firstly equilibrated at 3000 K, that was well above the melting temperature (~1078 K) of the considered alloy. After being relaxed for 10 ps, the alloy was sequentially quenched to 1000 K and 300 K, at a cooling rate of 2×10^{12} K/s to produce amorphous structures. At each temperature, at least 5000 configurations were applied for sampling. For the PDF analysis, the final well-equilibrium 500 configurations were used.

For the DFT differential charge density analysis, the AIMD derived amorphous structure was relaxed at 300K to release the internal stress by optimising the cell through the conjugated gradient algorithm. Here the plane-wave cut-off and K-point samples were changed to 500 eV and $6 \times 6 \times 6$, respectively.

The AIMD-based super cell was the replica of experimental as-cast sample. This information was used to explore basic microstructural features inside the glassy structure and understanding the co-existence of multiple atomic species inside the BMG. The structural aspects of the BMG were determined using various parameters such as PDFs, Voronoi polyhedra and co-ordination numbers. The chemical short-range ordering calculations were considered for the understanding about the chemical bonding between the constituent species. The following sub-sections describe the different analysis techniques applied for the characterisation of the simulated BMG data.

4.5.1 AIMD-PDF Analysis

The pair correlation function (PCF) commonly referred to as 'g(r),' was implemented to describe the distribution of atoms in a thin shell at a radius 'r' from an arbitrary atom in the material. It was used for studying the details of the system. The PCF was calculated by summing the number of atoms found at a given distance in all directions from a particular atom by the following relation:

$$g(r) = \frac{dN/N}{dV/V} = \frac{1}{4\pi r^2}\frac{1}{N_\rho}\sum_{i=j}^{N}\sum_{j\neq i}^{N}\langle\delta(r - |r_i - r_j|)\rangle \quad (4.17)$$

Where:

r = Radial distance
ρ = Average density of the entire material
N = Number of atoms
V= Volume of the super-cell

Furthermore, the pair distribution function (PDF) between two elements A and B, was calculated by the following relation:

$$g_{AB}(r) = \frac{1}{4\pi r^2}\frac{1}{\rho N_A N_B}\sum_{i\in A}\sum_{j\in B, j\neq i}^{N}\langle\delta(r - |\boldsymbol{r}_i - \boldsymbol{r}_j|)\rangle \quad (4.18)$$

4.5.2 Voronoi Polyhedral Analysis

The Voronoi polyhedral analysis was performed on the AIMD super cell to acquire the topological information of the BMG. The Voronoi tessellation method [272] was considered which divided the 3D space of the super cell into sub-cells centred by each atom. In this method, the planes of each sub-cells were drawn through bisecting bond pairs of the central atom with the neighbouring atoms. The sub-cells were called Voronoi cell. The atoms sharing a common cell surface were considered nearest neighbours. A Voronoi cell is commonly labelled by the Voronoi index, to describe the symmetry and arrangement of neighbouring atoms around the central atoms. The Voronoi index convention uses four number vectors e.g., $<i_3, i_4, i_5, i_6>$. Here, i_3, i_4, i_5, i_6 denotes the number of triangles, quadrangles, pentagons, and hexagons, respectively, in a Voronoi polyhedron. For the present study, a cut-off value was applied for the bisection between different atomic species. The cut-off value for an atomic pair was the corresponding minimum value of the partial pair correlation function's (PCF) first peak.

4.5.3 Co-ordination Number

The bond pair analysis was carried out as follows: The atomic pairs were classified based on three aspects: 1)- whether the atoms in a pair were neighbours or not? 2)- the number of neighbouring atoms common to both atoms of the respective pair, 3)- and the maximum number of bonding between the neighbouring atoms. The neighbouring criterion was based on the cut-off value, which was similar to PCF's first peak minima, for each bond pair. This information was used to calculate the co-ordination number (CNs) from each central atom and its neighbouring atoms.

4.5.4 Chemical Short-Range Order

The local chemical order is essential to evaluate the structural variations. The chemical short-range order was obtained through the experimental partial CNs around all the elements in the BMG, by the following equations [273];

$$\alpha_{ij} = 1 - \frac{CN_{ij}}{(x_j CN_i)} \text{ for } i \neq j \tag{4.19}$$

Where;

x_j= Atomic fraction of j-element
CN_{ij}= Partial coordination number of j in i.
CN_i= Total partial coordination number of i.

In eq. (4.19), a negative value represented the short-range order, a positive value showed clustering, whereas a '0' value denoted a random distribution.

α_{ij} and α_{ii} are dependent, therefore:

$$(1 - x_i)\alpha_{ij} = -x_i\alpha_{ii} \tag{4.20}$$

For eq. (4.20), if $\alpha_{ii} < 0$, this shows local clustering of solute 'i', and if $\alpha_{ii} > 0$, then there exists chemical short-range ordering around the element 'i.'

PART II

Result and Discussion
Chapters
(Chapter 5-11)

5 AB-INITIO MOLECULAR DYNAMICS (AIMD) MODEL OF VITRELOY-105

This work was done in collaboration with two senior research associates: Dr Xiangyuan (Carl) Cui, from the School of Aerospace, Mechanical and Mechatronic Engineering at The University of Sydney, and Dr Chunguang Tang from the College of Science at The Australian National University, Australia. These researchers provided the author with the Ab-Initio Molecular Dynamics (AIMD) simulation and Voronoi Tessellation method data for the $Zr_{52.5}Cu_{17.9}Ni_{14.6}Al_{10}Ti_5$ (Vitreloy-105), respectively, and the author conducted the detailed analysis. The details about the AIMD simulation and the Voronoi analysis were documented in Section 1.1. Voronoi tessellation analysis was considered for extracting structural information, such as partial co-ordination numbers (CNs) and different co-ordination polyhedra inside the BMG.

This chapter aims to provide a preliminary evaluation of the internal structure of the Vitreloy-105, based on which the detailed analysis will be carried out through APT. Partial pair distribution functions (PDFs), Voronoi polyhedra (VPs), partial CNs were explored to target the specific features contributing to atomic-scale chemical and/or structural heterogeneities within the BMG. The tendency to form solute-based clusters was assessed via APT cluster analysis of the simulated data.

5.1 Partial Pair Distribution Function Analysis

Partial pair distribution functions (PDFs) were used to analyse the individual and mutual bond pairs of all the elements inside the simulated Vitreloy-105 BMG, and a total of 15 bond pairs were analysed. The purpose of this analysis was to look for bond pairs that experienced bond lengthening or bond shortening relative to their theoretical bond pair distances. The theoretical bond pair distance was calculated by adding the atomic radii of the contributing elements, and the first peak position of the partial PDF was considered as the experimental bond pair distance.

The experimental and theoretical bond pair distances were examined at 300 K and 1000 K temperatures, to observe their variations while transitioning from supercooled state (1000 K) to the glassy state (300 K), as shown in Table 5.1. The differences were made easier to comprehend by grouping Ni, Cu as "β-solutes," and Al, Ti as "α-solutes," due to their similar topology. Zr-Al bond pair intensity was dominated by the β-Al bond pairs from liquid to glassy state (Table 5.1). Overall, the peak intensities of Zr-α and Zr-β bond pairs were still relatively high, indicating higher likelihood of Zr presence in the first co-ordination shell of the solute elements inside the Vitreloy-105.

Table 5.1: Bond pair order based on the height of the partial PDFs' first peak at 300 K, showing the experimental bond pair lengths compared to the theoretical bond lengths, at 300 K and 1000 K.

#	Bond Pair at 300 K	Height of 1st-Peak at 300 K	Theoretical Bond Length at 300 K (Å)	Experimental Bond Length at 300 K (Å)	Difference at 300 K (Theoretical-Experimental)	Height of 1st-Peak at 1000 K	Theoretical Bond Length at 1000 K (Å)	Experimental Bond Length at 1000 K (Å)	Difference at 1000 K (Theoretical-Experimental)
1	Ni-Al	6.30	2.71	2.47	0.24	4.21	2.71	2.46	0.25
2	Ni-Ti	5.80	2.74	2.42	0.32	3.9	2.74	2.45	0.29
3	Al-Cu	5.80	2.70	2.54	0.16	3.9	2.7	2.49	0.21
4	Zr-Al	5.78	3.01	2.91	0.1	4.34	3.01	2.93	0.08
5	Al-Ti	5.75	2.89	2.80	0.09	4.11	2.89	2.84	0.05
6	Zr-Cu	5.02	2.85	2.77	0.08	3.81	2.85	2.75	0.1
7	Zr-Ni	4.60	2.86	2.64	0.22	3.65	2.86	2.63	0.23
8	Zr-Ti	4.59	3.04	3.02	0.02	3.46	3.04	2.93	0.11
9	Ni-Cu	4.57	2.55	2.52	0.03	3.33	2.55	2.48	0.07
10	Cu-Cu	4.20	2.54	2.51	0.03	2.87	2.54	2.49	0.05
11	Ti-Ti	3.78	2.92	2.74	0.18	2.66	2.92	2.67	0.25
12	Cu-Ti	3.46	2.73	2.59	0.14	3.17	2.73	2.55	0.18
13	Zr-Zr	2.95	3.16	3.11	0.05	2.99	3.16	3.08	0.08
14	Al-Al	2.74	2.86	2.83	0.03	2.17	2.86	2.72	0.14
15	Ni-Ni	2.65	2.56	2.48	0.08	1.63	2.56	2.5	0.06

A particular comparison between the theoretical and experimental bond pairs (Table 5.1) revealed that the Ni-X bond pair distance decreased the most when the bonding element (X) was either Al, Ti, or Zr. Cu on the other hand, did not show similar level of bond shortening with Al, Ti and Zr as observed for Ni, despite Ni and Cu being topologically similar. It was noticed that the Zr-Zr bond pair distance decreased the most, compared to its theoretical bond distance (~19%), indicating the tendency of efficient packing, due to its abundance in the BMG. The bond pair distance was increased for Al-Al, Ti-Ti bond pairs, showing that Al and Ti were not favoured in their respective first co-ordination shell.

The total and partial PDFs of the individual elements are shown in Figure 5.1, whereas Figure 5.2 represents the partial PDFs of unlike-elements bond pairs, in the glassy state. Similar shape of the total PDF and Zr-Zr partial PDF was observed due to it higher abundance in the Vitreloy-105. The second peak of Ni-Ni PDF was almost similar to its first peak (Figure 5.1c), indicating Ni to Ni avoidance in the nearest neighbour shell. The relatively higher probability of Ni's existence around other elements appeared to suppress Ni-Ni interaction.

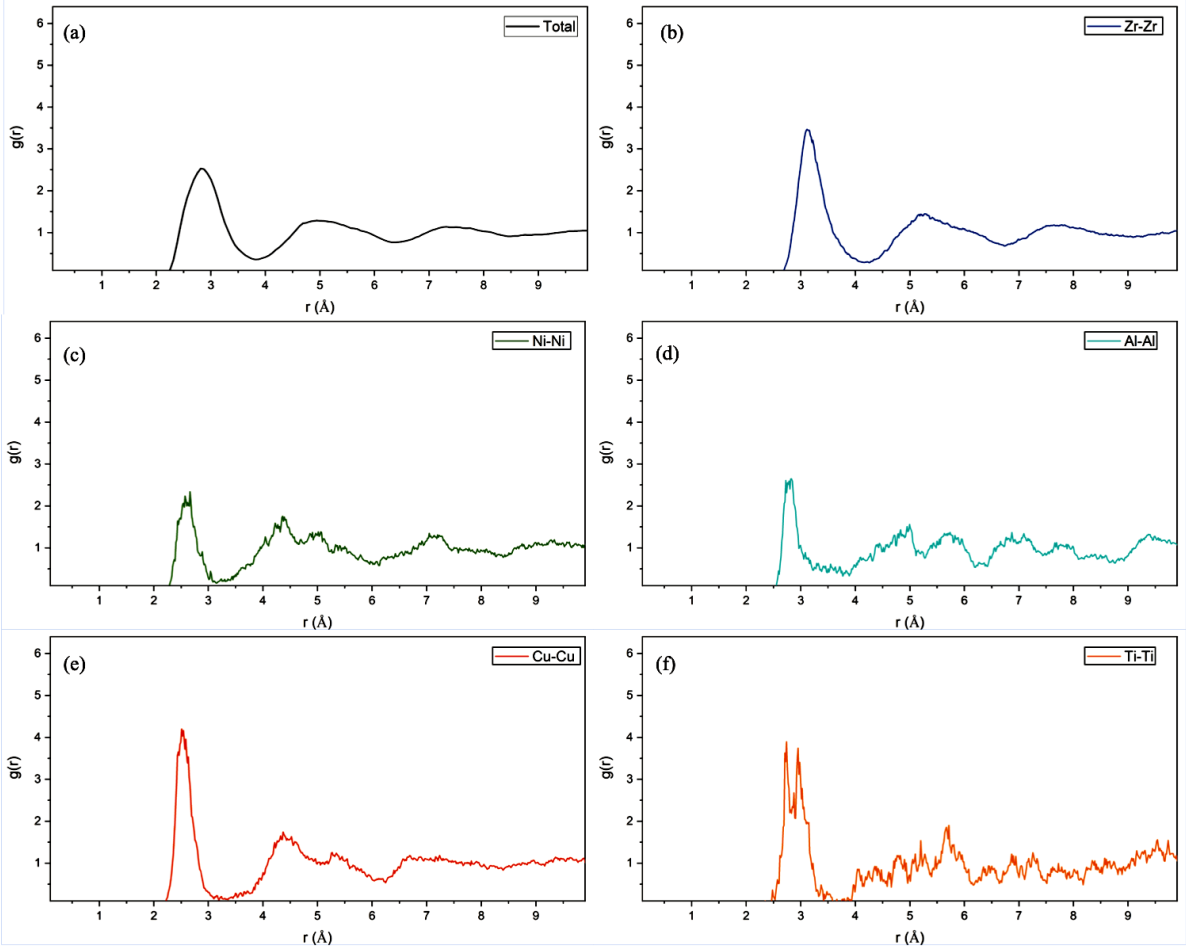

Figure 5.1: (a) Total pair distribution function, and (b-f) partial radial distribution functions of X-X of Vitreloy-105 at 300 K, where X=Zr (purple), Ni (green), Al (cyan), Cu (red), Ti (orange).

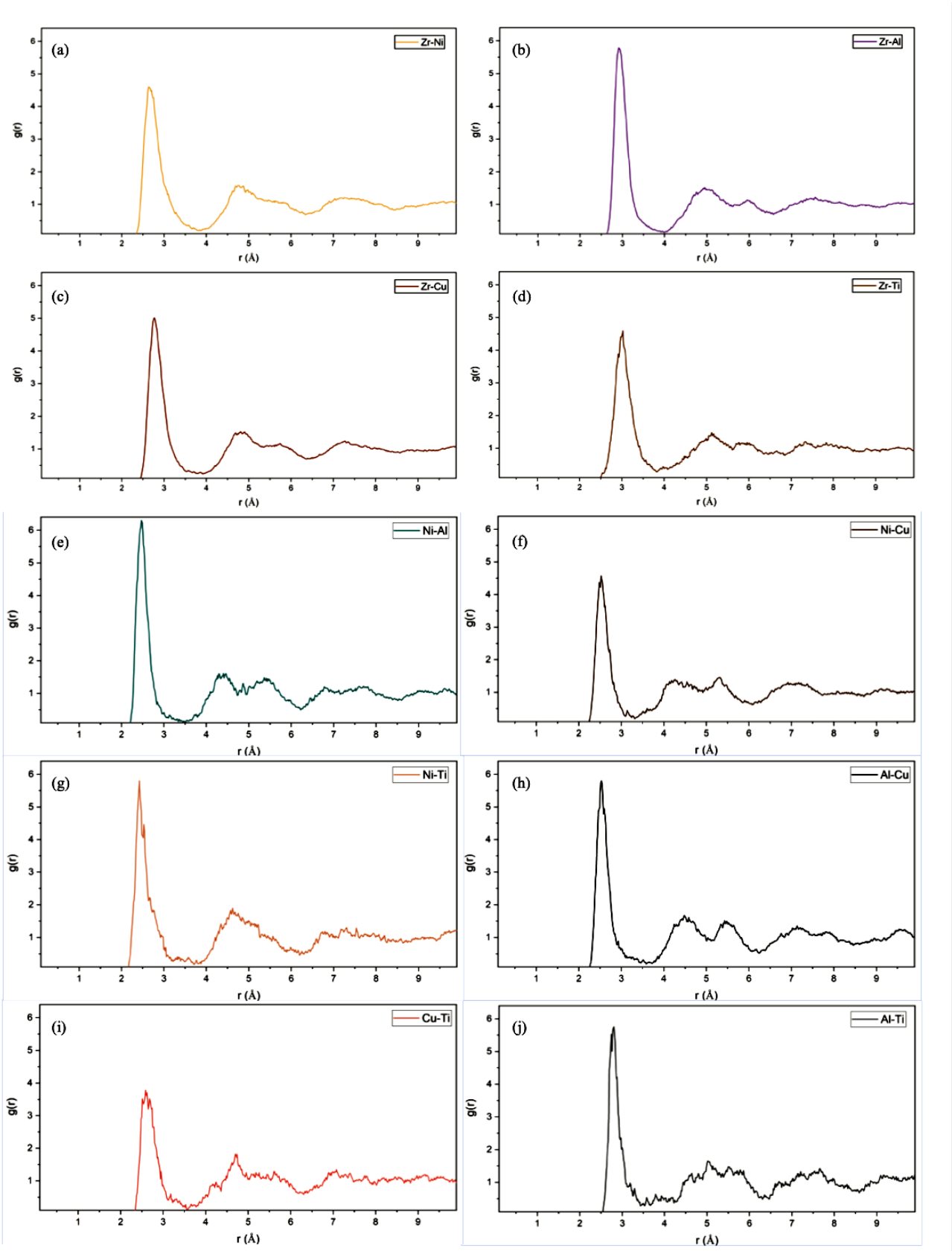

Figure 5.2: Partial pair distribution functions g(r) for, (a) Zr-Ni, (b) Zr-Al, (c) Zr-Cu, (d) Zr-Ti , (e) Ni-Al, (f) Ni-Cu, (g) Ni-Ti, (h) Al-Cu, (i) Cu-Ti, and (j) Al-Ti, in Vitreloy-105 at 300 K.

The behaviour of Zr with all the solute elements (Ni, Al, Cu, Ti) was found similar, as shown in Figure 5.2 (a-d). The first peak intensity in the partial PDFs of Ni with Al, Ti was observed relatively higher than the partial PDFs of Cu-Al and Cu-Ti, respectively.

The individual pairs avoidance and preferred interactions with other elements will be analysed through the differential charge distribution of the elements inside the BMG in the following section.

5.2 Differential Charge Distribution Analysis

This section analyses the differential charge distribution around all the elements inside the simulated Vitreloy-105, as shown in Figure 5.3. It was obtained by comparing the valence electron of an isolated atom to the valence electrons of all the atoms inside the simulated system. The charge around Ni was positive, so Ni tended to give away electrons to its neighbouring elements. In contrast, most Al atoms received electrons. The electro-positivity of Cu was comparatively less than Ni; therefore, the extent of bond length shortening observed between Cu and Al was lesser than between Ni and Al, in section 5. On the other hand, the electronegativity values of most Zr atoms were similar to the Al atoms, their heavier nuclei provided a screening effect rendering valence electrons highly localised and isotropic. Moreover, since the concentration of Ti was comparatively lower in the present glassy structure, its distribution was not analysed in detail. The aim of this analysis was to briefly explain the varied bonding behaviour of topologically similar elements inside a material due to their various chemical affinities [82, 274]. The detailed investigation of the electronic structure is, however, beyond the scope of this study.

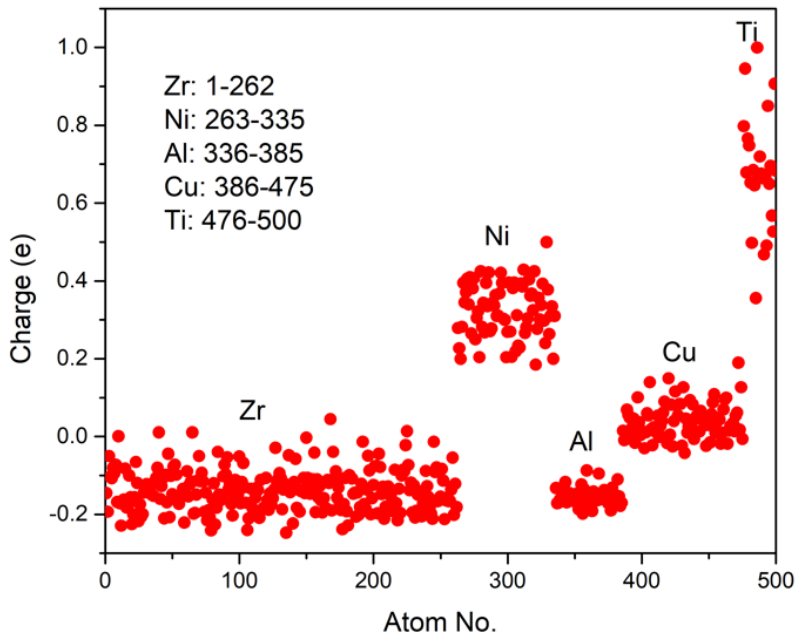

Figure 5.3: Differential charge distribution chart of Vitreloy-105 demonstrating the charge against their assigned atom numbers in the supercell of Vitreloy-105.

5.3 Voronoi Polyhedra Analysis

In this section, Voronoi tessellation analysis was used further to analyse the local atomic structure of the BMG. It is a sophisticated approach in which different clusters are denoted with Voronoi index <n_3, n_4, n_5, n_6, …n_i >, where 'i' represents the number of edges in a Voronoi Polyhedron [272]. Thus, n_3 would represent the number of triangles, n_4 tetragonal, n_5 pentagonal, and so, in a Voronoi polyhedron. The primary focus was given to the Voronoi polyhedra (VPs) analysis of the Vitreloy-105 at 300 K temperature. In the foregoing analysis, Zr was defined as 'solvent', and all other species as 'solute.'

The top ten solute-centred Voronoi polyhedra are shown in Figure 5.4. There were more than 100 types of solute-centred VPs and ~312 Zr-centred VPs, but the fraction of most of them was less than 5%; such a diverse range implied the amorphous nature of the BMG. Out of all the elements, the highest fraction (19.2%) of VP with <0,3,6,4> Voronoi index was observed for Al. Its second-highest fraction (12.3%) was for <0,0,12,0> polyhedra, which is commonly referred to as full icosahedra (FI), whereas the third highest (7.6%) fraction appeared for <0,2,8,2> VP. Two other polyhedra with indices <0,1,10,2> and <0,3,6,5>, had larger than 5% fraction. The details of the top three Ni-centred VPs were; 13.0 % of <0,2,8,1>, 11.3 % of <0,3,6,1> and 9.8% of <0,3,6,3> VPs (Figure *5.4*a). Six different co-ordination polyhedra had a larger than 5% fraction for Ni, and FI (5%) was also one of them.

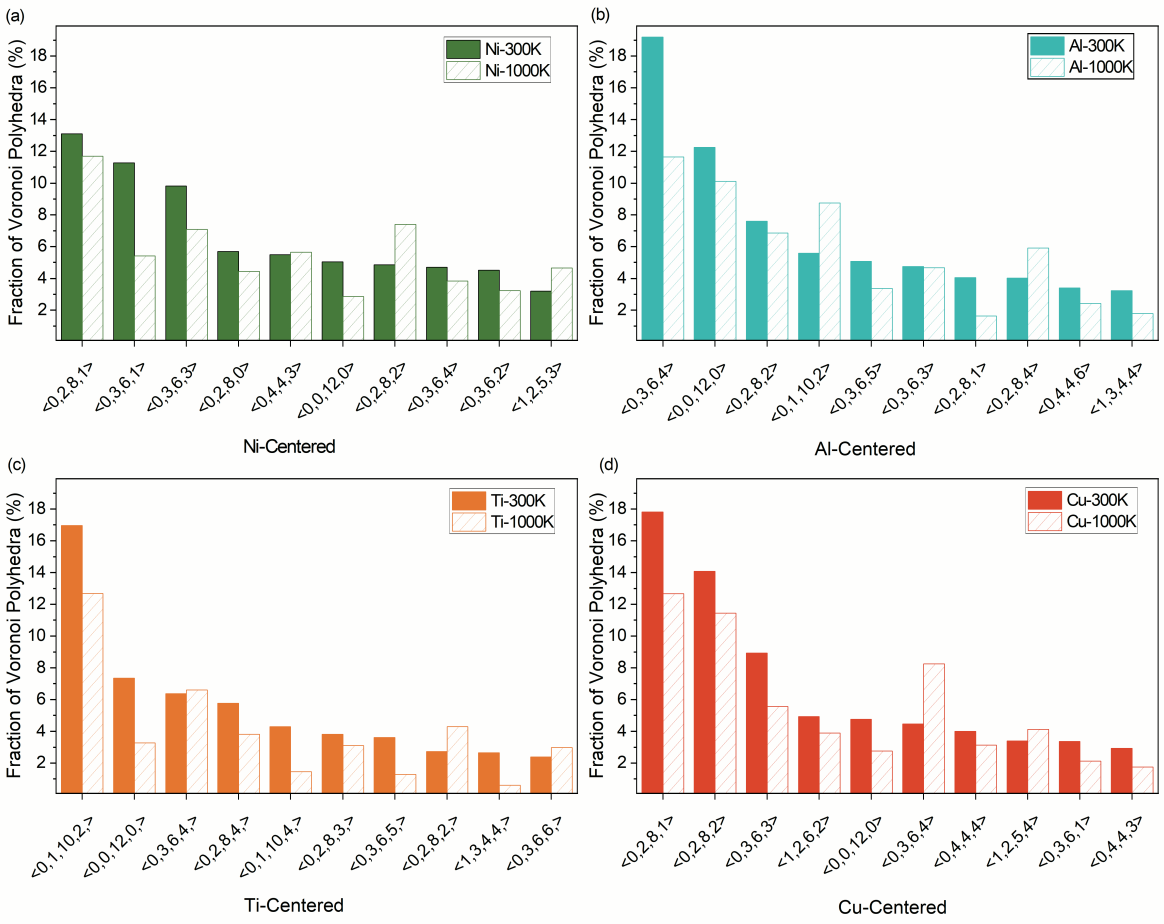

Figure 5.4: Fractions of top-ten (a) Ni-centred, (b) Al-centred, (c) Ti-centred and (d) Cu-centred Voronoi polyhedra in Vitreloy-105.

In the case of Cu, three prominent polyhedra included 17.8% of <0,2,8,1>, 14.1% of <0,2,8,2>, and 8.9% of <0,3,6,3>. All three polyhedra were common to either Al- or Ni-centred polyhedra with >5% fraction. A larger difference in the fractions of the Ti-centred polyhedra was observed between its first VP (<0,1,10,12>) with 15.2%, and the second VP (<0,0,12,0>) with 8.2%. There were a total of four different VPs of Ti with a fraction larger than 5%. Interestingly, the top three Ti-co-ordination polyhedra were also common in the top ten Ni- or Al-centred VPs. Thus topologically, there were some similarities observed in the co-ordination polyhedra of different solute species. For Zr-centred polyhedra, the <02,8,5>, <0,2,8,6>, <0,1,10,4>, <0,1,10,5> VPs were the most populous than others, with fractions of 7.8%, 7.2%, 6.2% and 5.2%, respectively, as shown in Figure 5.5. Compared to the liquid state (1000 K), an increased fraction of VPs was observed at the glassy state (300 K) for all the elements inside Vitreloy-105, due to the glassy state being more stable than the supercooled state.

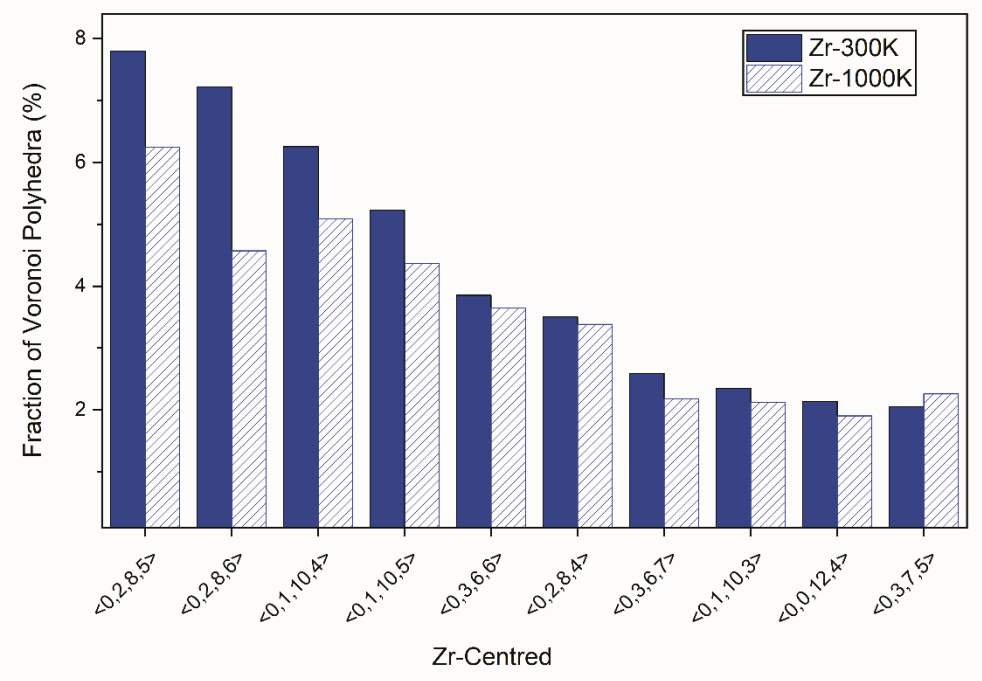

Figure 5.5: Fractions of top-ten Zr-centred Voronoi polyhedra in Vitreloy-105.

Various VPs were organised into different categories for better comparison between the liquid and the glassy state. The most populated VPs inside the Vitreloy-105 were indexed by; <0,1,10,x>, <0,2,8,x>, <0,3,6,x>, <0,4,4,x>, <0,5,2,x> and <0,0,12,0>. Thus, 'x' denoted variable numbers from 0 to 8 and, in some cases, up to 11 for this BMG. As stated earlier, <0,0,12,0> is commonly referred to as, "full icosahedron (FI)," because it comprises of twelve 5-edge polygons. Moreover, <0,2,8,x> and <0,1,10,x> were called as “distorted icosahedra”, due to populous five-fold rotational symmetry found in these polyhedra [275-277]. Therefore, the whole group with Voronoi indices, <0,0,12,0>, <0,1,10,x>, <0, 2, 8,x> was referred to as “icosahedral-like”. Similarly, VPs with Voronoi index of <0,4,4,x> and <0,5,2,x> were called "crystal-like" due to their four-fold and six-fold rotational symmetry alike crystallographic rotational symmetries [278], with a higher number of tetragonal and hexagonal polygons. Additionally, the VPs of <0,6,0,8> index, was considered as bcc-like polyhedra [279], whereas <0,12,0,0> index corresponded to fcc- or hcp-like polyhedra [280]. Therefore, these were also considered in the crystal-like group.

The polyhedra of Voronoi indices between the icosahedral-like and crystal-like with Voronoi index of <0,3,6,x> were considered as a "mixed" group[275]. This classification was particularly useful in squeezing a broad distribution of VPs into fewer convenient groups. These groups covered about 57% to 67% of the total fraction of the VPs' population.

The distribution of Zr-centred polyhedra at 300 K and 1000 K based on the above-classified group is shown in Figure 5.6. The fraction of the icosahedral-like group spiked the most during the transition from liquid to a glassy state. A small increase in the mixed and crystal-like group was also recorded. However, a minimal fraction of FI was spotted in the liquid state, which further reduced while transitioning to the glassy state.

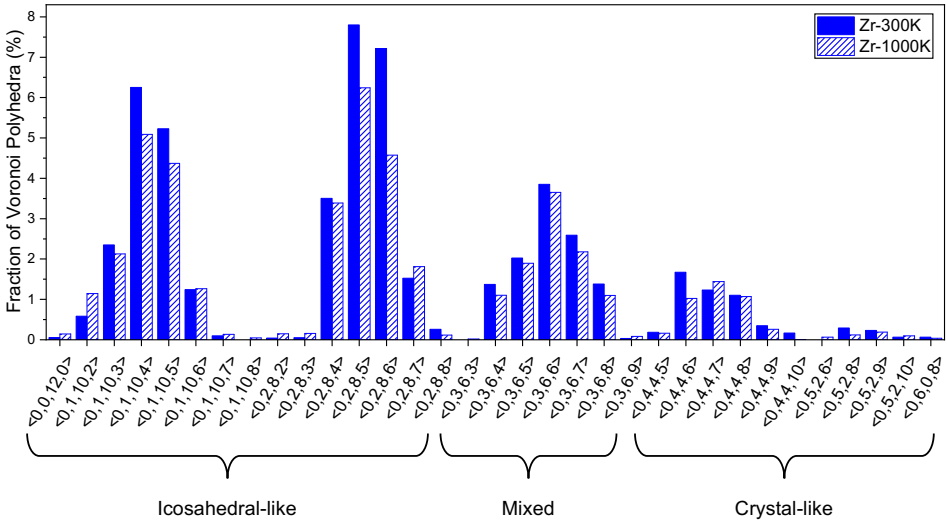

Figure 5.6: Fractions of icosahedral-like, mixed- and crystal-like Zr-centred Voronoi polyhedra in Vitreloy-105.

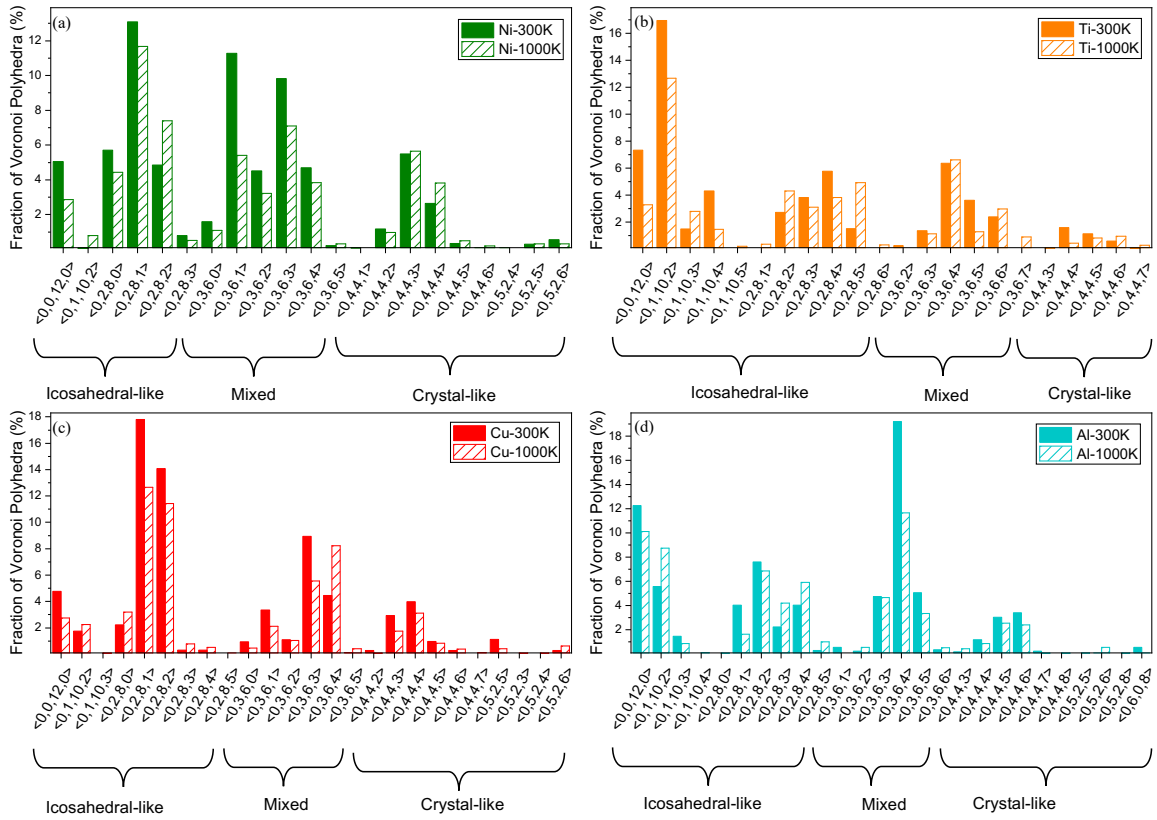

Figure 5.7: Fractions of icosahedral-like, mixed- and crystal-like Voronoi polyhedra in (a) Ni, (b) Ti, (c) Cu, and (d) Al inside Vitreloy-105.

The effect of change in temperature on the VP of the solute species (Ni, Cu, Al, Ti) was observed (Figure 5.7). Mixed-type VPs increased the most in Ni- and Al-centred polyhedra, with a simultaneous increase of 11.12% and 9.38% while transitioning to the glassy state. Different fractions of full icosahedra (FI) with Voronoi index of <0,0,12,0> were also observed around all solute-species; 5.0% in Ni, 12.3 % in Al, 4.8% in Cu, and 7.4 % in Ti, and 0.05% of FI existed in Zr. About 3.2% fraction of FI in the simulated metallic glass structure was observed in total, as shown in Figure 5.8. Although, Ti and Al were topologically alike, the trend in the transition of Ti VPs resembled Cu- centred VPs instead.

The fraction of crystal-like polyhedra was 10.8% in Ni, 8.7% in Al, 10% in Cu, 3.3% in Ti, and 5.4% in Zr. The crystal-like VPs with a total 7.2 % fraction demonstrated a different polyhedral class than the FI, with four-fold and six-fold symmetry instead of the five-fold symmetry. Overall results for simulated Vitreloy-105 were; 36.9% icosahedral-like polyhedra, 7.2% crystal-like polyhedra, 17.7% of the mixed-group, and 45.6% of other polyhedra with less than 2% fraction of each, as shown in Figure 5.8.

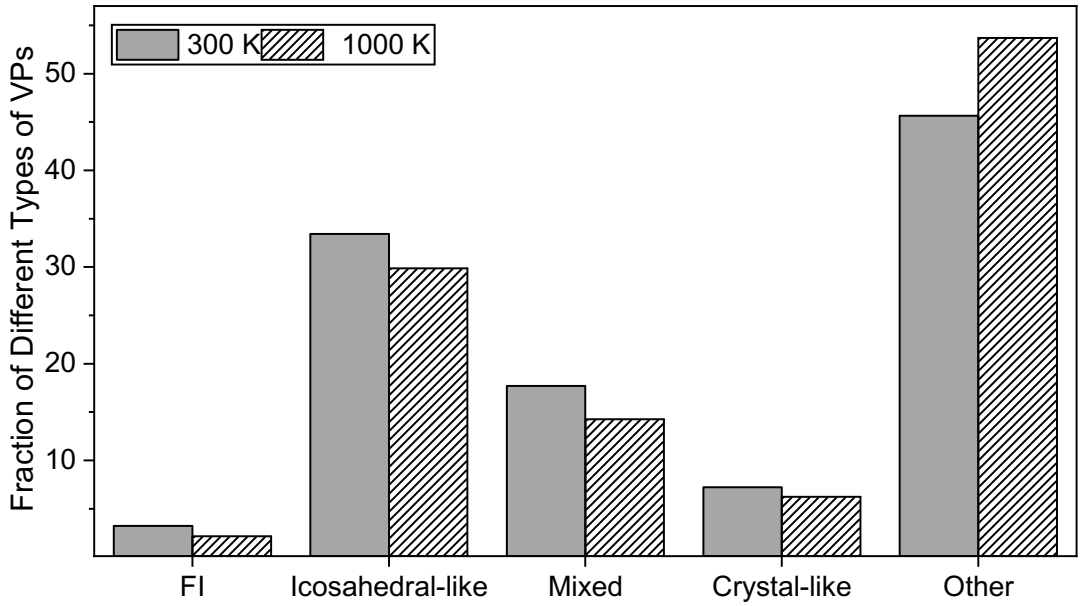

Figure 5.8: Summary of different co-ordination polyhedra of Vitreloy-105 at 300 K.

The sum of the Voronoi index was used to obtain the respective co-ordination number (CN) of different polyhedra inside the BMG. The total distribution of VPs based on their CNs is shown in Figure 5.9. It was noticed that there was no single dominant co-ordination polyhedron inside the simulated Vitreloy-105, and the distribution was quite diverse, ranging from VPs with CN=10 to CN=18, highlighting the complexity of the metallic glass structure with multiple elements.

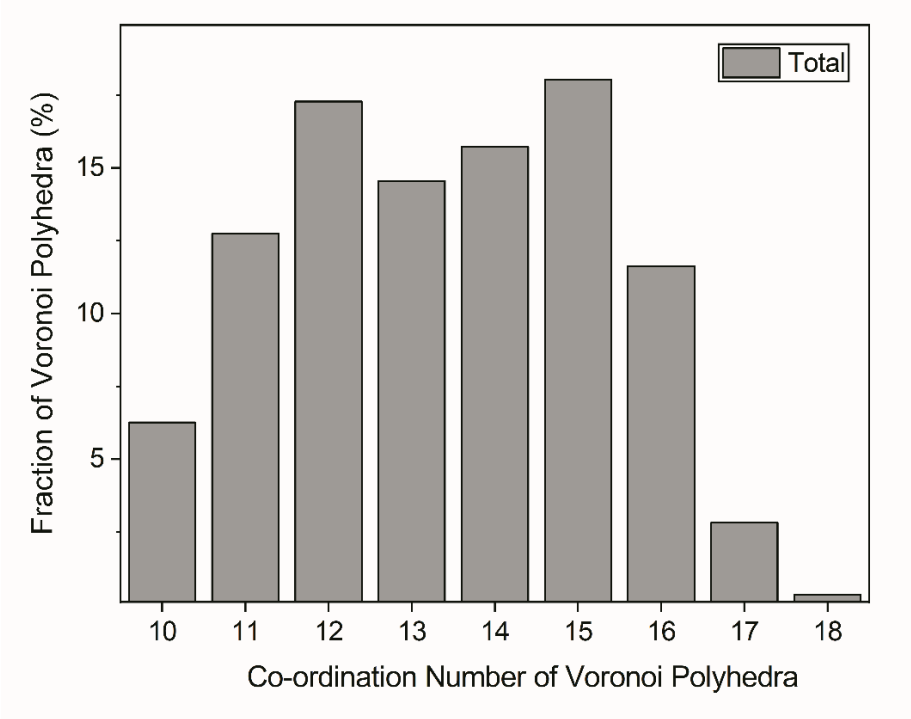

Figure 5.9: Summary of total Voronoi polyhedra in Vitreloy-105 based on their co-ordination number.

5.4 Co-ordination Number and Local Chemical Order

The theoretical CN of each element within the BMG was calculated based on its effective size ratio. The effective size ratio is the ratio of the atomic radii of solute to the solvent atoms [87]. The experimental CN was obtained through the Voronoi polyhedra analysis, where the width of the first peak of the partial PDFs was used as the cut-off value. The values of the experimental partial CNs and the effective size ratio, along with the corresponding theoretical CNs, are shown in Table 5.2. The experimental partial CNs were larger than the theoretical CNs, indicating efficient packing among elements in the BMG.

The partial CN of Zr (solvent) around all solute species was more prominent than other elements, as shown in Table 5.2.. It indicated that the solute atoms were surrounded mainly by Zr (>60%) in their first co-ordination shell. However, their co-ordination shells also contained some other elements (24-37%). The presence of elements other than Zr, is not uncommon due to the higher concentration of other solutes inside the simulated Vitreloy-105.

Table 5.2: Experimental and theoretical partial co-ordination numbers (CNs) of the elements in Vitreloy-105 BMG at 300 K.

Refer. Atom	Zr	Ni	Al	Cu	Ti	Total Experimental CNs	Effective Size Ratio	Theoretical CNs
Zr	8.2	1.9	1.5	2.4	0.8	14.8	1	13.34
Ni	7.0	0.7	1.0	1.5	0.5	10.7	0.81	10.13
Al	7.7	1.4	0.7	1.9	0.6	12.2	0.91	12.04
Cu	7.0	1.2	1.0	1.3	0.5	11.0	0.80	10.06
Ti	8.0	1.5	1.2	1.7	0.5	12.8	0.92	12.30

Given the structural variations, local chemical order was evaluated through the experimental partial CNs around all the elements in the BMG. The chemical short-range order parameter (α) shown in Table 5.3, was calculated by the following equations [273];

$$\alpha_{ij} = 1 - \frac{CN_{ij}}{(x_j CN_i)} \text{ for } i \neq j \tag{5.1}$$

Where;
x_j= Atomic fraction of j-element
CN_{ij}= Partial co-ordination number of j in i.
CN_i= Total partial co-ordination number of i.

A negative value indicates chemical short-range ordering, a positive value suggests chemical short-range clustering, and a 'zero' is for the random distribution in the above equation. It should be noted that chemical short-range ordering meant that the respective solute atoms were surrounded by the atoms of other elements. On the other hand, chemical short-range clustering reflected the likely presence of the respective solute atoms than the atoms of other elements in its surroundings. All α_{ij} and α_{ii} are dependent, therefore:

$$\sum x_j \alpha_{ij} = -x_i \alpha_{ii} \tag{5.2}$$

For equation (5.2), if $\alpha_{ii} < 0$, this shows local clustering of solute 'i' whereas if $\alpha_{ii} > 0$, it means that there exists chemical short-range order around the element 'i.' The resulting values of α_{ii} were multiplied by (-1) again, before entering in Table 5.3, to avoid sign confusion between α_{ij} and α_{ii}.

Table 5.3: Short-range order parameter (α_{ij}) values for Zr-, Ni-, Al-, Cu-, Ti- centred VPs in $Zr_{52.5}Cu_{17.9}Ni_{14.6}Al_{10}Ti_5$ (Vitreloy-105) BMG. Color code: blue (short-range ordering), orange (short-range clustering), yellow (random). Prominent chemical short-range order values are shown in bold.

i \ j	Zr	Ni	Al	Cu	Ti
Ni	-0.24	-0.56	0.07	**0.21**	0.01
Al	-0.19	**0.19**	-0.45	**0.15**	0.06
Cu	-0.20	**0.24**	0.06	-0.33	**0.16**
Ti	-0.18	**0.18**	0.10	**0.27**	-0.24

*A negative value indicates chemical short-range ordering, a positive value suggests chemical short-range clustering, and a 'zero' is for the random distribution (-0.05 > random < 0.05).

All the solute elements showed ordering with the solvent (Zr), confirming the presence of Zr in the first co-ordination shell of all the solutes. Similarly, highly negative values were observed for α_{ii} when i= solute elements, indicating a higher degree of alike atoms avoidance in the first co-ordination shell. Positive values for α_{ij} were observed between solutes, predicting chemical short-range clustering while considering the solutes bond pairs.

It was observed that majority of the co-ordination polyhedra of solute species followed the approach of solute-centred clusters presented by the Miracle model [87], where solvent atoms largely surrounded the solutes. Nonetheless, about 10–24% of the Voronoi polyhedra in Vitreloy-105 appeared to have a larger population of solute atoms (> 50%) instead of the solvent. The deviated population of solute polyhedra was separately analysed to observe its possible impact on the mechanical and thermal properties (Table 5.4).

Table 5.4: Experimental partial co-ordination numbers (CNs) of the elements corresponding to the deviated population (10-24%) of polyhedra in simulated Vitreloy-105 BMG, at 300 K.

Refer. Atom	Zr	Ni	Al	Cu	Ti	Total Experimental CNs
Zr	6.8	2.4	2.1	3.0	1.0	15.3
Ni	5.3	1.2	1.2	2.6	1.1	11.3
Al	5.8	2.2	1.2	3.1	0.4	12.7
Cu	5.2	1.8	1.8	2.1	0.8	11.8
Ti	6.2	1.9	1.1	2.9	1.0	13.1

Since 10–24% of the solute-centred clusters showed higher population of solute elements than the solvent, the average co-ordination number of all those co-ordination polyhedra were considered to calculate the specific chemical short-range order parameter (α) for those unusual polyhedra (Table 5.5). In that case, chemical short-range ordering was observed between the solute elements (negative values). On the other hand, the presence of Zr in the surrounding of these solute-rich polyhedra was suppressed (positive values between solutes and Zr). Although, Ni and Cu had a positive enthalpy of mixing, they appeared to surround each other (α_{NiCu}, $\alpha_{CuNi} < 0$). Higher proportion of Ni and Cu was noticed around other solutes and vice versa, in these specific polyhedra (shown with bold numbers).

Table 5.5: Specific short-range order parameter (α_{ij}) values for Zr-, Ni-, Al-, Cu-, Ti- centred VPs with enriched solute atoms in $Zr_{52.5}Cu_{17.9}Ni_{14.6}Al_{10}Ti_5$ (Vitreloy-105) BMG. Color code: blue (short-range ordering), orange (short-range clustering), yellow (random). Prominent chemical short-range order values are shown in bold.

i \ j	Zr	Ni	Al	Cu	Ti
Ni	0.07	-0.64	**-0.16**	**-0.34**	0.01
Al	0.13	**-0.16**	-0.03	**-0.37**	0.31
Cu	0.16	**-0.07**	**-0.52**	0.01	**-0.43**
Ti	0.10	0.01	0.13	**-0.23**	0.52

*A negative value indicates chemical short-range ordering, a positive value suggests chemical short-range clustering, and a 'zero' is for the random distribution (-0.05 > random < 0.05).

It was observed that α-solutes (Al, Ti) as well as β-solutes (Ni, Cu) would tend to deviate from their general behaviour of short-range ordering with Zr, if the proportion of β- and α-solutes was increased, leading to specific solute-ordered polyhedra.

It should be noted that the local chemical analysis presented above was a moderately pseudo-quantitative approach acquired for predicting the chemical interactions among different elements inside this BMG. A thorough quantitative analysis would require including the detailed study on random counter data to declare chemical ordering or clustering with reference to counter random values. However, this approach is too complex and thus outside the scope of the present work and was not considered.

5.5 Cluster Analysis of Simulated Data

As mentioned above, apart from solvent atoms' average structure around solutes, a particular proportion of solute-rich co-ordination polyhedra was also detected around the solutes in this BMG. These features were used for determining the feasibility of the APT cluster analysis in finding the atomic-scale heterogeneities within the BMG. To test the presence of solute-rich clusters, the simulated data was converted to ".pos-format," and the maximum separation method (Section 4.4.4,) was applied for the cluster analysis with a d_{max} value of 0.26 nm and $N_{min} = 3$. A customised random labelling MATLAB program created counter data with a random distribution of all the elements. The randomised data was used to discern significant solute-rich clusters via comparison.

Table 5.6: A comparison between the actual and random labelled files of the AIMD simulated data for the APT cluster analysis.

Characteristics	Actual Simulated Data	Random Labelled
Cluster Size Range (atoms)	3-38 atoms	3-5 atoms
Volume fraction	0.230 ± 0.012	0.060 ± 0.001
Composition	$Cu_{40.3}Al_{20.8}Ni_{27.8}Ti_{11.1}$	$Cu_{41.0}Al_{23.1}Ni_{28.2}Ti_{7.7}$

The random labelled dataset was generated using a generic MATLAB programm where the element identities were randomised while keeping their actual concentrations similar to Vitreloy-105. A comparison of the APT cluster analysis between the existing and randomised dataset is listed in Table 5.6. The largest cluster in the actual data set comprised of 38 atoms, whereas only 5 atoms joined to make the largest cluster of the randomly distributed data. Their volume fraction was the ratio of the aggregated volume occupied by each cluster in a region to the total volume of the supercell. The volume of each cluster was calculated by equation (4.3). The volume fraction of clusters in actual data was significantly different from the randomised data, confirming the unambiguous solute-rich clusters inside the simulated BMG.

5.6 Discussion

The simulated Vitreloy-105 was considered to observe the possible chemical and structural heterogeneities inside the actual BMG. The experimental bond lengths were compared with the theoretical bond lengths (Table 5.1). Most of the bond pair distances of the present study were equivalent to many other experimental studies [211, 281, 282]. The bond pair distances for Ni-Al, Al-Cu, Al-Ti, and Zr-Al, were comparable to the experimental results of Sheng et al. [283]. These comparisons confirmed the validity and relevance of the simulated data.

The first peak width of the total PDF (Figure 5.1a) was ~2.5 Å ≤ r ≤ 3.1 Å, which is very close to the experimental X-ray diffraction and neutron diffraction total PDF results (~2.3 Å ≤ r ≤ 3.6 Å) by Ma et al. [236]. The second peak splitting was observed for most of the elements' bond pairs (Figure 5.1c-e). It signified the characteristic nature of the amorphous materials, commonly observed in the BMGs [275]. The detailed analysis of the partial PDFs revealed bond length shortening in most of the bond pairs, indicating strong chemical interaction between specific atomic pairs. A strong interaction between Ni to, Al and Ti, was observed. Moreover, it was observed that although Ni and Cu are topologically similar due to their similar atomic radii (r_{Ni}=128 pm, r_{Cu}=127 pm), their chemical and electronic behaviour differed. Higher enthalpy of mixing between Ni and Al (-22.3 kJ/mol), Ni and Ti (-34.5 kJ/mol) [284] resulted in relatively higher bond length shortening than Cu-Al (-7.6 kJ/mol) or Cu-Ti (-8.9 kJ/mol), as shown in Figure 5.2.

The sp-d orbital hybridisation effect was slightly higher between Al and Ni than Al and Cu due to the relatively complete d-orbital of Cu. The higher electronegativity difference between Ni and Al was another reason for its bond length shortening (Figure 5.3). The concentration of the elements played an important role, which is why the probability of Ni-Al bonding was higher than Ni-Ti bonding. It was observed that the probability of unlike-bond pairs is higher than the like-bond pairs, in Vitreloy-105.

VP analysis determined that the atomic structure of Vireloy-105 was quite complicated. Unlike the binary metallic glasses, there was no single dominant polyhedron in the simulated BMG. The classification into icosahedral-like, crystal-like and mixed polyhedra covered ~54% of the total structure. The remaining 46% of the glassy structure belonged to other VPs with individual fractions less than 2%. The presence of unique and distinctive icosahedral-like VPs and crystal-like VPs indicated the possible coexistence of different ordered structures, among the disordered polyhedral, inside the metallic glass (Figure 5.6, Figure 5.7).

It was determined by Hwang et al. [232] that crystal-like VPs could join to form a supercluster that favours crystal-like local ordering due to their four-fold and six-fold rotational symmetry. This symmetry contrasts with icosahedral-like VPs that form superclusters with approximate two-fold rotational symmetry. Detailed analysis of the formation of superclusters (MRO) is outside the scope of this work. However, it is suggested that the mutual existence of two different types of superclusters/MROs proposes it as a structural attribute of the present case. This is not an unusual suggestion as many other researchers have previously suggested the coexistence of distinct structural units as well [233, 239, 285]. Following this line of thought, it is further suggested that the crystal-like structural units produces a smaller size than the critical size required for the nucleation into crystals [232]. This sub-critical size effectively suppresses crystallisation as well as contributing towards slow kinetics during the glass transition [286, 287].

The partial co-ordination number based on a cut-off value determined that the first co-ordination shell of all the solute elements averagely comprised of Zr atoms (Table 5.2). However, 10–24 % of the solute-centred polyhedra deviated from the average structure with higher proportion of neighbouring solutes than the solvent (Zr) atoms (Table 5.4). This implied local chemical heterogeneity a requirement for improved glass-forming ability and physical properties in metallic glasses [12, 140, 288].

The present analysis also revealed chemical short-range ordering between Zr and other elements (solutes), as demonstrated in Table 5.3. In contrast, robust chemical short-range ordering between most solute atoms was also observed for 10–24 % solute-enriched polyhedra (Table 5.5). The simulated Vitreloy-105 was further compared with the randomly distributed data through the APT cluster analysis (Table 5.6), confirming the significant presence solute-rich clusters inside the Vitreloy-105. The volume fraction of these clusters was ~23 % which is similar to the proportion (10-24 %) of the solute rich Voronoi polyhedra (Section 5.4). It is inferred that the hardness variations, observed in Section 4.1.4, could be analysed in detail through these solute-rich clusters.

5.7 Summary

AIMD simulation was applied to predict the internal structure of the quinary Vitreloy-105 BMG. The results were generally consistent with previous experimental and simulation studies of various binary and ternary metallic glasses. The present results confirmed a topologically diverse structure with specific icosahedral- and crystal-like structural units, and other less-ordered polyhedra. Moreover, the potential for creating local structural heterogeneities in Vitreloy-105 was assessed using charge distribution and the enthalpy of mixing between different combination of elements. The presence of the solute-rich polyhedra was confirmed by cluster analysis, following typical APT protocols. These solute-rich clusters are suggested to be effective local chemical heterogeneities that will be studies further for investigating the microstructure-property-process relationship in BMGs.

6 DEVELOPMENT OF METHODOLOGY FOR ATOM PROBE ANALYSIS OF ZR-BASED BULK METALLIC GLASSES

APT can reveal valuable information about the chemical composition of a material and other microstructural features at the near-atomic scale and in 3D [289, 290]. As introduced in Chapter 2 (Section 2.7.4), APT provides access to microstructural information that is otherwise difficult to achieve through other microscopy techniques. This feature makes it an appealing technique for analysing BMGs. However, APT has not been used to its full potential for BMGs' due to their unique field evaporation process (Section 1.1.1.1). Moreover, there is no standard process by which the selection of operating parameters for high fidelity APT experiments can be reliably achieved for multi-element BMGs (Section 2.7.4.3.1).

This chapter focuses on bridging these gaps by developing a process methodology for determining optimum experimental parameters for Zr-based BMGs, as well as setting out a workflow for their accurate APT compositional analysis. It is to ensure that the requisite conditions are attained before any attempt to evaluate the microstructure in general, or the much sought-after analyses of chemical short-to-medium range order. The preliminary APT results without optimised conditions were demonstrated at the start of this chapter, followed by the step-by-step process for selecting operating conditions and other prerequisites. The optimised methodology was validated by applying it to the chemical evaluation of a 3D-printed BMG material at the end of this chapter. Most parts of this chapter have been published already [193, 291].

6.1 Preliminary Results: $Zr_{63.96}Cu_{13.36}Ni_{10.29}Al_{11.04}Nb_{1.25}$ (at. %) BMG Composition

This section aims to document the initial measurement of the composition, which was obtained by following the method described in Section 4.4. At the start of the project, a set of operating conditions was selected to learn about the composition of a thermally cycled (TC)-$Zr_{63.96}Cu_{13.36}Ni_{10.29}Al_{11.04}Nb_{1.25}$ (at. %) BMG. These parameters were selected based on the recommendations of the atom probe manager, Dr Takanori Sato, and research associate, Dr Keita Nomoto.

A few APT experiments were carried out using a pulse rate of 250 kHz, 0.5% detection rate, and 30 K temperature, to find appropriate laser energy for the respective BMG. 100 pJ laser energy was chosen due to the uniform evaporation across the APT tip. The APT mass spectra for the respective BMG primarily consisted of Al^{2+}, Al^{+}, AlH^{+}, Ni^{2+}, Ni^{+}, Zr^{3+}, Zr^{2+}, ZrH^{+}, ZrO^{+}, Cu^{+}, Cu^{3+}, Nb^{2+}, Nb^{3+}, and their isotopes, as shown in Figure 6.1. Peak deconvolution was applied for the overlapped peaks: Ni^{2+} and Nb^{3+}, at 31 Da, Ni^{2+} and Zr^{3+} at 31.5 Da and 32 Da, Zr^{2+} and ZrH^{+} at 45.5 Da, 46.0 Da, Nb^{2+} and ZrH^{+} at 46.5 Da. H^{+}, H^{2+} peaks were ignored in the compositional analysis since these peaks appeared due to the ionisation of hydrogen inside the chamber. Hf (<0.01–0.3 at. %) and Ti (0.08 at. %) peaks were also observed in the mass spectra and were ignored as impurities.

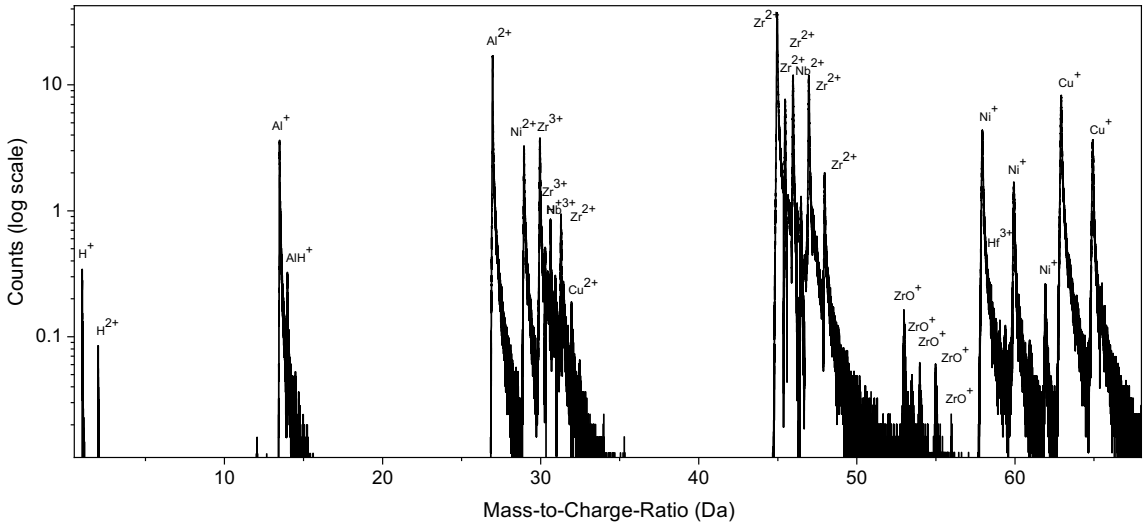

Figure 6.1: Mass spectrum normalised to the highest peak of Zr_{92}^{2+}.

A background-to-background ranging approach [257] was used for ranging the peaks in the mass spectrum. The resulting APT composition was compared with the nominal (ICP-AES) composition, as shown in Table 6.1. The ICP-AES composition was taken as a reference as it offers sufficiently accurate compositional information of the metallic elements in the materials. The comparison resulted in a range of absolute error from 0.49 at. % to 3.21 at. %.

Table 6.1: Comparison between the composition obtained from the atom probe experiment and the ICP-AES composition for TC- Zr-based BMG. The error bars represent the standard error.

	Zr (at. %)	Cu (at. %)	Al (at. %)	Ni (at. %)	Nb (at. %)
ICP-AES Composition	63.96 ± 0.40	13.36 ± 0.18	11.04 ± 0.17	10.29 ± 0.16	1.25 ± 0.06
APT Composition	60.75 ± 0.75	14.55 ± 0.55	10.55 ± 0.35	9.00 ± 0.5	2.50 ± 1.1
Absolute Difference	3.21	1.19	0.49	1.29	1.25

A large difference between the ICP-AES composition and APT composition stresses the importance of optimising operating parameters. These results were used as an initial reference to track the improvement in the APT composition measurements after applying the new methodology for appropriate parameter selection, which is detailed in the next section.

6.2 Methodology for Optimised Operating Conditions

There were three challenges in the APT analysis of $Zr_{63.96}Cu_{13.36}Ni_{10.29}Al_{11.04}Nb_{1.25}$(at. %) BMG. The first was the absence of crystallographic features. Next was a non-uniform field evaporation process. The third was a quinary Zr-based BMG being relatively new to the APT studies. These challenges became the primary motivation behind developing a strategic approach for acquiring accurate APT data from this BMG. Al was the lightest element (evaporation rate = 17 V/nm) and Nb was the heaviest element (evaporation rate = 37 V/nm) in the respective BMG. Special attention was given to selecting a set of operating parameters that could manage elements with contrasting evaporation rates, thus, avoiding preferential evaporation or retention at the APT tip-apex.

The following questions were considered for developing the methodology and assessing the APT data:

1. What assessment criteria should be used for the APT data quality?

2. What is the effect of experimental parameters (pulse rate, temperature, detection rate, and laser energy) on the data quality?

3. Which mass spectrum peak ranging technique in step# 6 of the APT data reconstruction (Section 4.4.2) should be selected? And how can we implement a robust ranging style?

4. How to manage peak overlaps in the mass spectrum, and what element-assignment strategy should be used for the overlapping peak?

5. Is clustered evaporation affected by laser energy?

6. Are there any operating conditions that can avoid clustered evaporation of the BMGs?

7. How do we obtain accurate and reproducible composition from the APT experiment with better data quality?

Following factors can be considered for the APT data quality evaluation:

1. Mass Resolution
2. Signal-to-thermal tail ratio (STTR)
3. Overlapped peak decomposed ratio (OPDR)
4. Composition

6.2.1 Mass Resolution

The mass resolution of the mass spectrum is M/ΔM, where ΔM is the peak width at different peak heights and M is the total mass of the peak. The error governing the mass resolution can be expressed as [155]:

$$\frac{M}{\Delta M} = \frac{1}{\sqrt{(\frac{\sigma\upsilon}{V})^2 + (2\frac{\sigma_{t_{flight}}}{t_{flight}})^2 + (2\frac{\sigma_{L_{flight}}}{L_{flight}})^2}} + f_{pulse}(t_d) \quad (6.1)$$

Where;

V = Applied DC voltage

t_{flight} = The time-of-flight

L_{flight} = The flight distance

f_{pulse}= Pulsing mode

t_d = Time of the departure of the ion from the surface

The values of mass resolution of the representative peak in the mass spectrum at full-width-half-maximum (FWHM) and full-width-at-tenth-maximum (FWTM) can be used for assessing the operating conditions, provided the operating voltages and geometries of the APT tips are similar [155]. In this way, higher values of FWHM and FWTM indicate higher data quality. However, since the mass resolution values can be affected by other factors during laser pulsing, e.g., the illumination conditions of the laser, the direction of polarisation of the laser [155], it alone cannot provide a viable comparison between experiments. Therefore, additional factors should be considered.

6.2.2 Signal-to-Thermal Tail Ratio (STTR)

An important feature in laser-pulsing mode is the thermal tail, appearing beside some of the peaks in the mass spectrum. In the above equation (6.1), where the first term is associated with the standard deviations on the errors in the measurements, the second term, $f_{pulse}(td)$, is the function considering the loss of resolution associated with the pulsing mode and the instant of departure of the ion from the surface. It is the latter term in laser-pulsing which causes an asymmetric peak, referred to as a thermal tail. The delayed evaporation mainly happens during the cooling of the tip apex [155]. Thermal tails are unavoidable, especially for materials with low thermal conductivity, such as Zr-based BMGs. However, their extent can be minimised through the optimisation of the experimental conditions.

The concept of thermal tails was used as an effective comparator in improving APT operating conditions. This approach was applied using the highest peak in the mass spectrum, Zr_{92}^{2+}, which was ranged between 44.85–45.15 Da. The thermal tail associated with that peak was named "TTZr" and was ranged from 45.15–45.35 Da, as shown in Figure 6.2. The ratio of signal counts to the thermal tail counts was termed as "signal-to-the-thermal tail ratio (STTR)." This ratio was considered to assess the size of the adjacent thermal tail such that good quality mass spectra with relatively small thermal tails report higher values of the STTR.

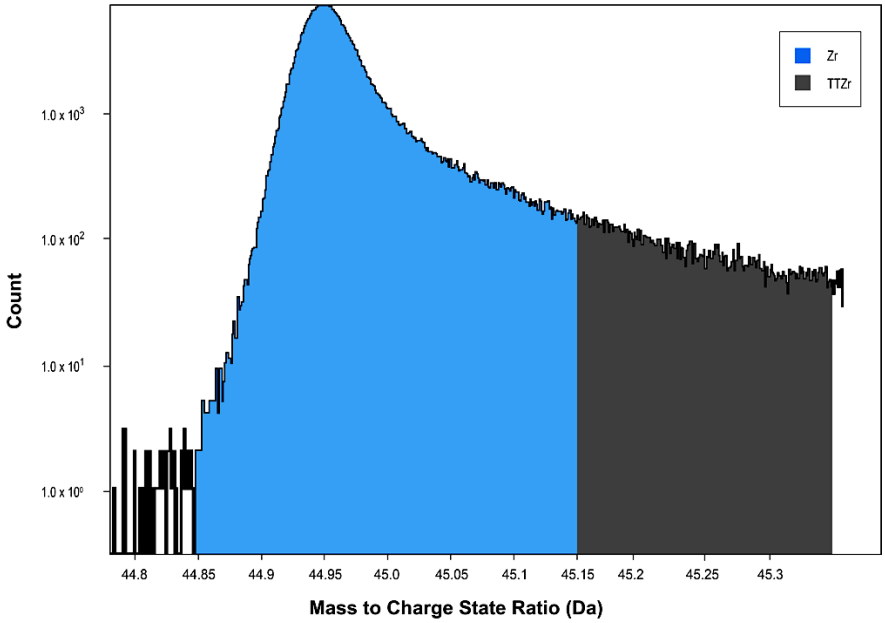

Figure 6.2: Zr_{92}^{2+} peak is illustrated along with its thermal tail.

6.2.3 Overlapped Peak Decomposed Ratio (OPDR (%))

One of the overlapped peaks in the mass spectra of TC-$Zr_{63.96}Cu_{13.36}Ni_{10.29}Al_{11.04}Nb_{1.25}$ BMG was between the ZrH^{+} and Nb^{2+} peaks at 46.27–46.80 Da (Figure 6.3). The correct identification of Nb^{2+} counts within this overlapped peak is important because of its major contribution towards Nb composition (1.25 at. %) in the dataset. Therefore, a data-specific criterion was considered which was the percentage of the ratio of the ZrH^{+} counts to the total backgrounded corrected counts in this peak and was called OPDR (%). The ZrH^{+} counts fluctuated significantly with different sets of APT operating parameters, possibly due to the varied ionisation between Zr^{+} ions and the chamber hydrogen. In any case, the OPDR (%) was conveniently used to check the proportion of ZrH^{+} in the respective peak, where its smaller value represented a reduced interaction with chamber hydrogen and ease in quantifying the data.

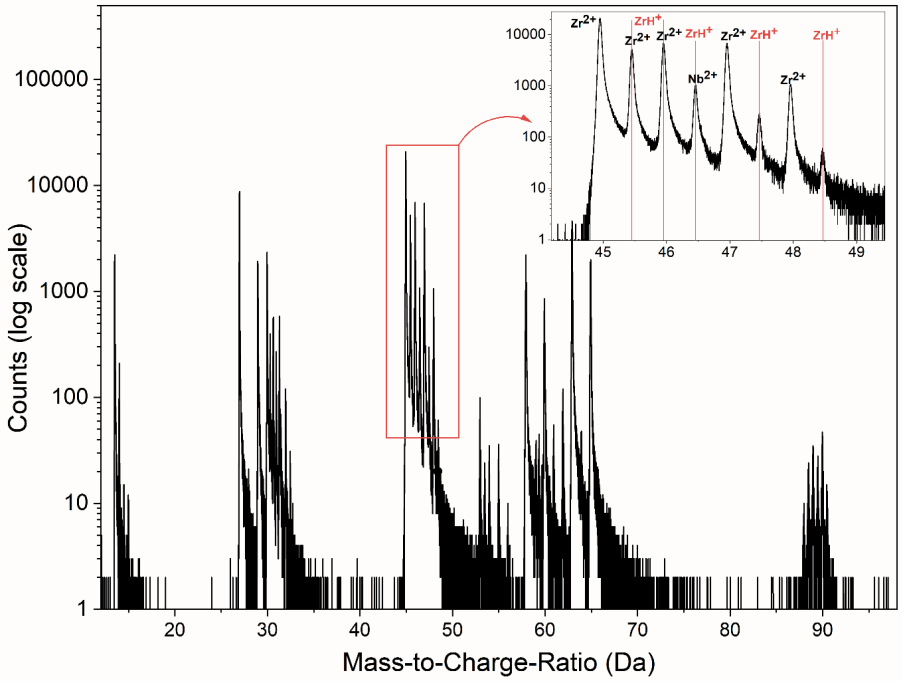

Figure 6.3: Mass spectrum of TC- Zr-Cu-Ni-Al-Nb BMG, inset highlights the overlapped peaks of ZrH^{+} and Nb^{2+} ions (reprinted from [193]).

6.2.4 Composition

The bulk composition obtained through an APT experiment can be taken as another quantifying factor to assess the APT data quality. Those experimental parameters were chosen with which the APT bulk composition was close enough to the ICP-AES composition. The APT composition was obtained after decomposing the overlapped peaks to accurately quantify all the constituent elements inside the BMG.

6.2.5 Ranging Technique: Peak-Based Ranging

The selection of the mass ranging approach significantly impacts the calculated composition and repeatability between different users [292]. Different researchers have used a variety of approaches for mass spectra peak ranging. These include full-width-at-half-maximum (FWHM), full-width-at-nine-tenth maximum [255], and background-to-background ranging [256, 257, 293]. Moreover, the peak shapes can differ between different ionic species, with some having longer thermal tails than others. As mentioned in Section 6.2.2, thermal tails are delayed signals from the associated peaks, but their inclusion in the ranging requires the windowing of relatively broad peaks, diminishing the accuracy of the composition. This is because the area under thermal tail convolutes delayed signals from the respective ion, out-of-sync evaporation of other species, and noise.

Amongst the above-mentioned ranging approaches, FWHM and full-width-nine-tenth maximum are most widely used for estimating phase compositions because of the corresponding higher signal-to-noise ratio [255]. But the restricted peak width selected in these ranging approaches can risk underestimating the ion counts in the analysis of BMGs (Figure 6.4a). Conversely, the background-to-background ranging style unnecessarily broadens the ranged width, increasing the risk of including the out-of-sync counts of other species [155] and thus reducing the accuracy of the composition (Figure 6.4b). There is a need to implement a new ranging style to minimise the issues concerning the above-mentioned peak ranging styles and to provide an easier method. This will create a more consistent compositional outcome.

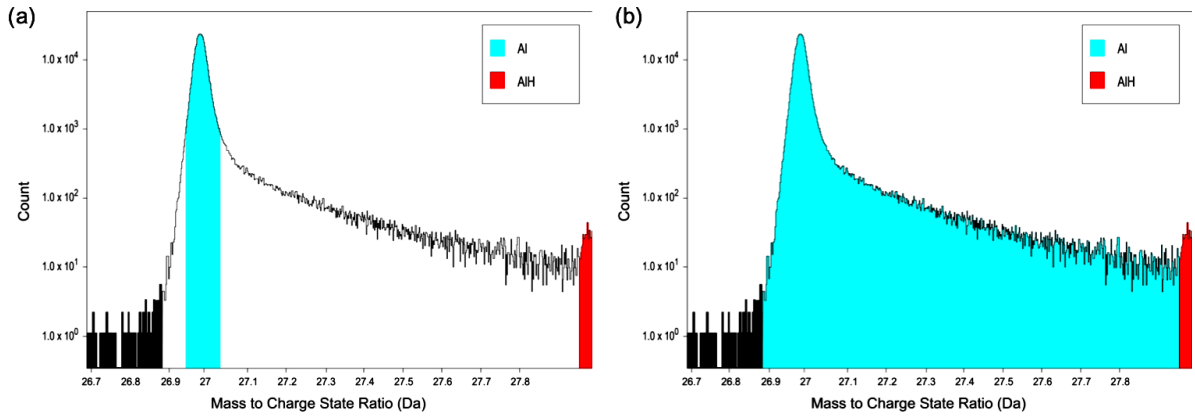

Figure 6.4: Mass spectrum peak ranging style: (a) FWHM ranging style, (b) background-to-background ranging style.

"Peak-based ranging" approach was applied to address this discrepancy, as follows. Peaks not exhibiting thermal tails (symmetrical, Gaussian-type peaks) were ranged where the lower limit is defined by the first channel where signal rises above the noise level, and the upper limit by that channel corresponding to the center of the range being aligned with the apex of the peak (Figure 6.5a). For asymmetric peaks with thermal tails, the width of the whole range deduced by the above procedure was doubled (Figure 6.5b). In this way, a prominent part of the thermal tail was included, and a balance was struck between the desire to retain counts from delayed signals and minimise excess background counts. Multiple peak-widths were selected for asymmetric peaks, before reaching to the double-width mass peak solution. It was found that only double-width peak ranging approach provided minimum at. % error for the respective elements in the APT bulk composition compared to the ICP-AES bulk composition. Peak-based ranging approach will be used in this work from now on.

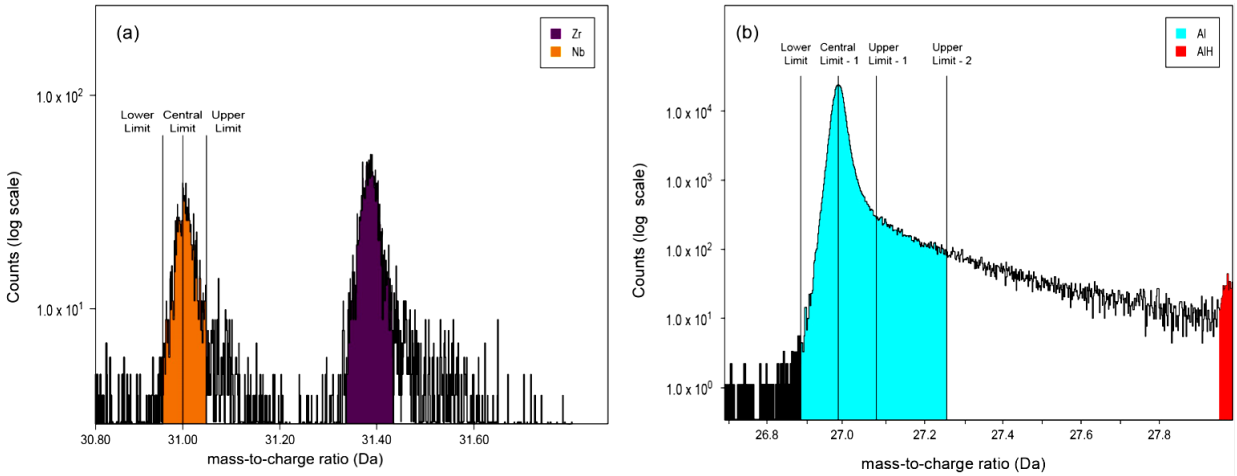

Figure 6.5: Peak-based ranging style for (a) symmetric (Gaussian-shaped) peaks, (b) asymmetric peak (reprinted from [193]).

6.2.6 Effect of Experimental Parameters on the APT Data

Based on the above factors (mass resolution, STTR, OPDR (%) and composition), the influence of each of the experimental parameters was assessed one-by-one, while keeping the others constant. The details are as follows.

6.2.6.1 Effect of Temperature

The influence of temperature was analysed by varying the temperature from 70 K to 25 K. The other parameters used were: 250 kHz pulse rate, 0.5% detection rate, and 100 pJ laser energy. The mass resolution in the form of FWHM and FWTM is displayed in Figure 6.6a. An overall improvement in mass resolution from 70 K to 25 K was observed through the increase in FWHM and FWTM at 45 Da, from 527 to 976.4 and 167 to 418, respectively.

The clear trend of improvement in the mass spectrum quality with decreasing temperature was confirmed for STTR values down to 40 K. Interestingly, the STTR value decreased with a further temperature decrease. Interestingly, the STTR value decreased with a further temperature decrease (Figure 6.6b). The OPDR (%) values increased as the temperature was reduced. On qualitative grounds, relatively higher peaks were observed for the mass spectrum at 40 K compared to 25 K and 70 K, Figure 6.6c. Broader peaks with bigger thermal tails were seen at 70 K, and a higher ZrH^{+} peak at 47.5 Da indicated more hydride formation. The absolute error in the composition was larger for temperature < 40 K, as illustrated in Figure 6.6d.

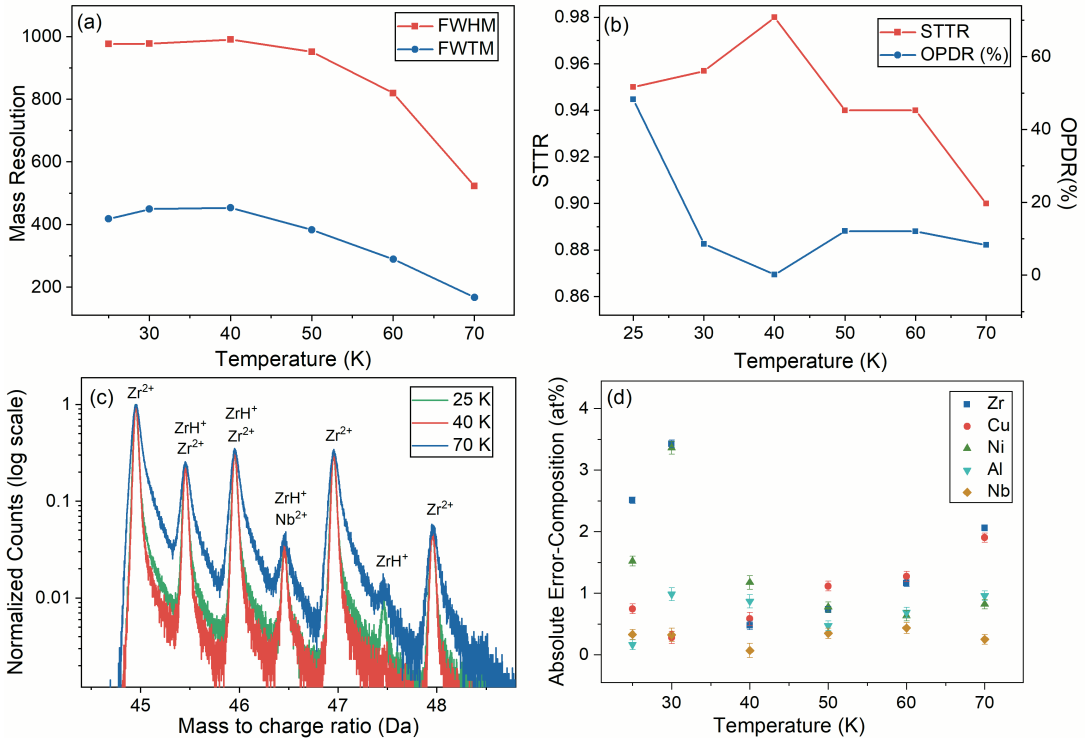

Figure 6.6: Effect of variation of temperature on BMG. (a) Mass Resolution in terms of FWHM and FWTM at 45 Da. (b) STTR and OPDR(%). (c) Mass spectra at different temperatures, where counts are normalised using the highest peak at 45 Da (Zr^{2+}) and (d) the absolute error in the composition (reprinted from [193]).

6.2.6.2 Effect of Pulse Rate

The effect of pulse rate on the compositional accuracy, STTR, OPDR (%), and mass resolution of the Zr-based BMG is demonstrated in Figure 6.7. The error in the composition of Cu was observed to increase with the decrease in pulse rate. However, preference was given to Nb due to its lower concentration (1.25 at. %) inside the BMG. Reducing the pulse rate from 250 kHz to 160 kHz improved its compositional accuracy (Figure 6.7.a). A sharp decline in the STTR was observed with lower pulse rates and larger OPDR (%), indicating increased ZrH^+ counts in the dataset, possibly due to the increase in the ionisation of Zr^+ with chamber hydrogen at lower pulse rates (Figure 6.7c).

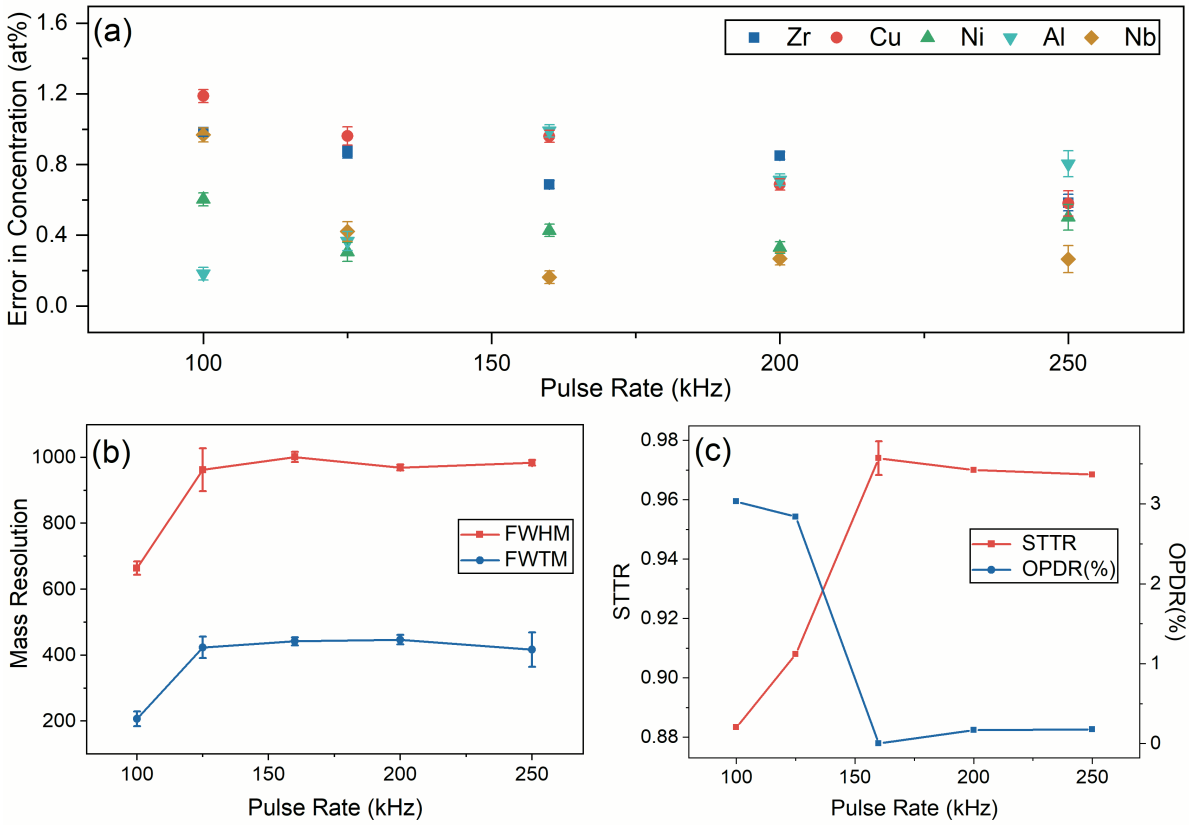

Figure 6.7: Effect of pulse rate on BMG. (a) Absolute error in the composition (b) Mass Resolution in terms of FWHM and FWTM. (c) STTR and OPDR (%), compared to pulse rate variation (reprinted from [193]).

6.2.6.3 Effect of Detection Rate

The detection rate is expressed as the number of detected ions per 100 pulses. Experiments analysing variations in the detection rate were performed in the range between 0.5 % to 6 %. A positive impact on the data outcome was observed with the increase in the detection rate (Figure 6.8). It is, in fact, experimentally challenging to maintain a lower detection rate in the presence of clustered evaporation in this material. Therefore, a relatively larger spread in error was observed at the lowest detection rate of 0.5%, as shown in Figure 6.8c. The OPDR (%) values were minimal (<0.1%), and a slightly improved mass resolution was observed with the increase in detection rate. In addition, a higher detection rate provided faster data acquisition with a better yield for this BMG.

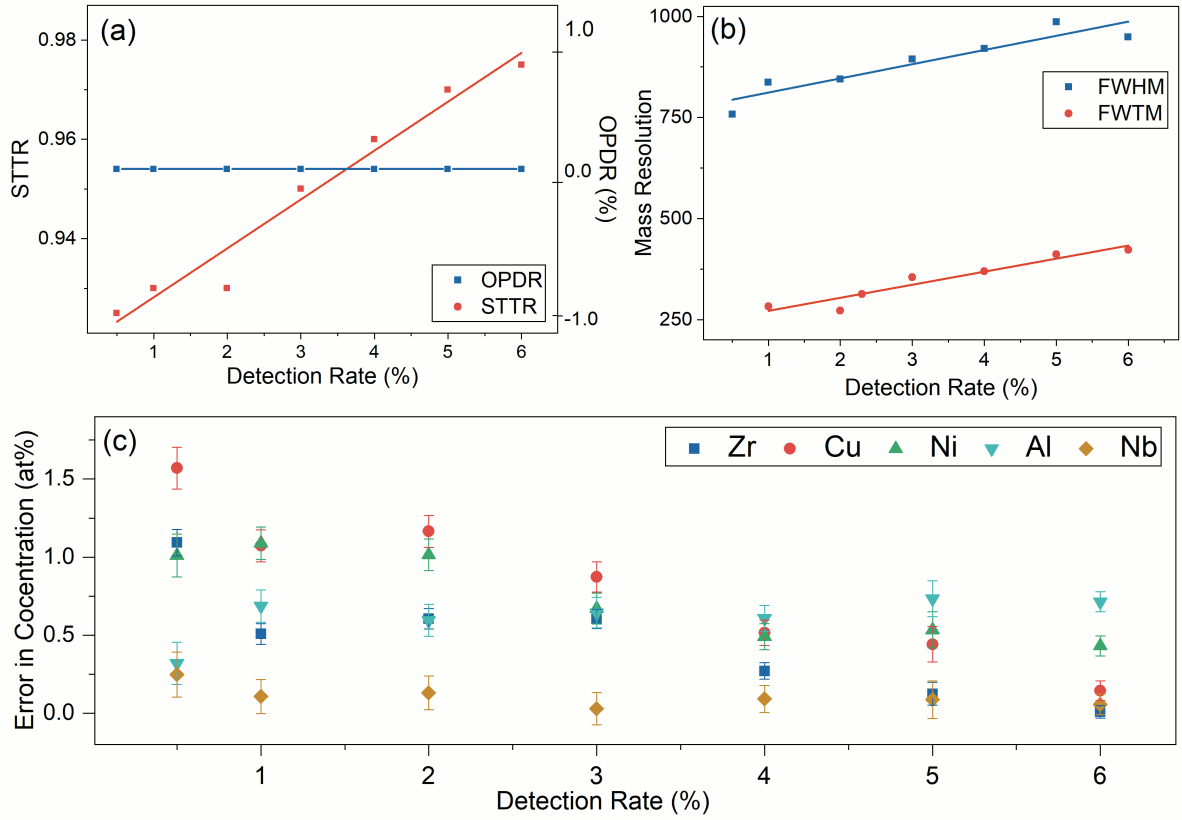

Figure 6.8: Effect of detection rate on BMG. (a) STTR and OPDR (%). (b) Mass Resolution in terms of FWHM and FWTM. (c) Absolute error in the composition, compared to detection rate (reprinted from [193]).

6.2.6.4 Effect of Laser Energy

It is widely agreed that the duration of the thermal excursion arising from a laser pulse in APT can be significantly longer than the duration of the laser pulse itself [195, 294-296]. This can result in a localised heating effect that can degrade the data quality, especially if the heat transfer is not uniform across the tip-apex. In addition, the lower laser energies can cause elements with higher evaporation rates to be preferentially retained at the specimen surface [158]. Therefore, selection of the appropriate laser energy is essential for a successful APT experiment.

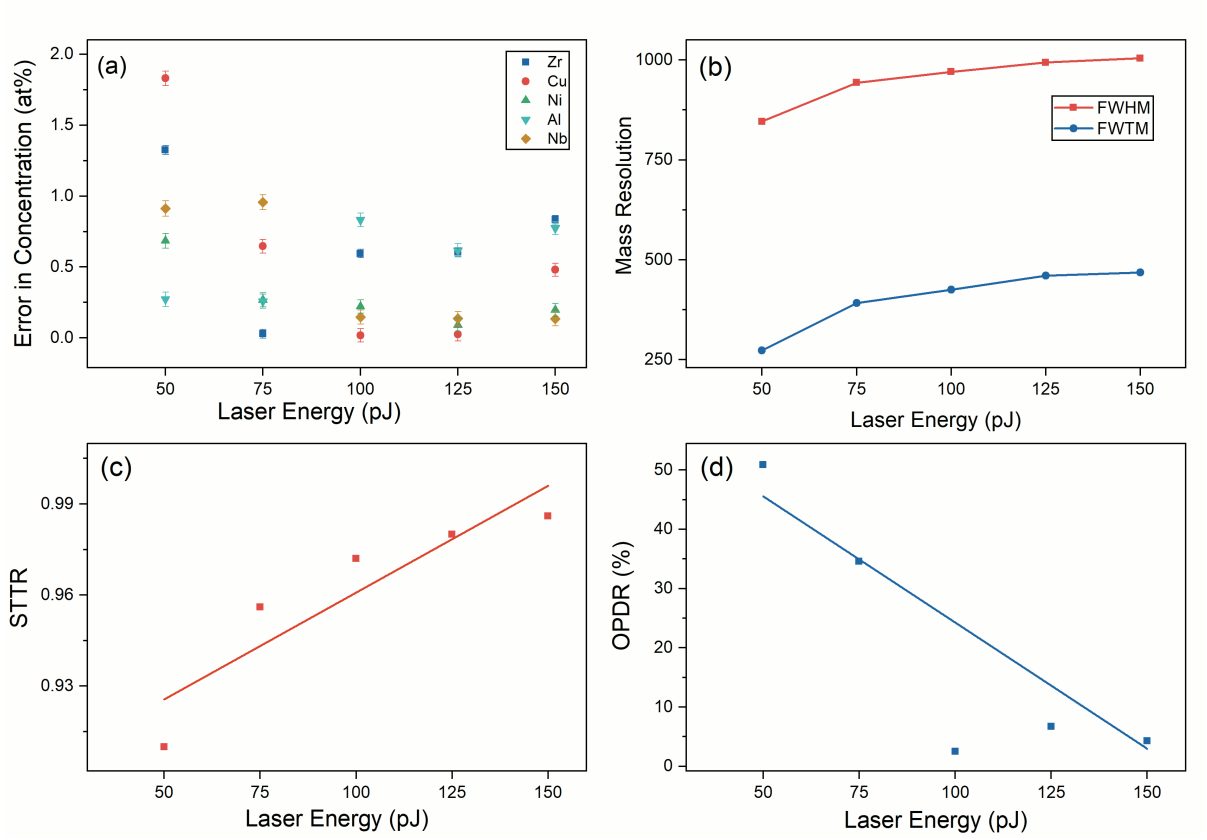

Figure 6.9: Effect of laser energy on BMG. (a) Absolute error in the composition. (b) Mass Resolution in terms of FWHM and FWTM. (c) STTR and OPDR (%), compared to laser energy variations (reprinted from [193]).

The changes in the absolute error of the composition with variations in the laser energy are summarised in Figure 6.9. Higher laser energies up to 150 pJ resulted in higher compositional accuracies for all the elements. Figure 6.9c suggests that the evaporation process has occurred with minimal thermal tails throughout the range. The mass resolution increased significantly when the laser energy rose from 50 pJ to 75 pJ. It was followed by a modest increase above ~75 pJ (Figure 6.9b). Relatively low STTR values were observed at a laser energy of 50 pJ, (Figure 6.9c).

The OPDR (%) was improved from 50% to ~8% with increased laser energy (Figure 6.9d). These results did not include laser energies >150 pJ because this triggered extreme non-uniform field evaporation around the tip, manifesting as artifacts induced by temperature differences across the field desorption map. Interestingly, the error in the composition of all the elements were less than 1 at. % between 100 pJ to 150 pJ.

6.2.7 Effect of Different Ranging Styles

After the optimised experimental parameters selection, the impact of different ranging styles was explored. The purpose of this step was to ensure the chosen peak ranging style as an appropriate one for the Zr-based BMGs. An optimised APT data was collected by running the APT sample of TC-$Zr_{63.96}Cu_{13.36}Ni_{10.29}Al_{11.04}Nb_{1.25}$ BMG under the pulse rate of 160 kHz, 40 K temperature, 6 % detection rate and 100 pJ laser energy.

Different mass spectrum peaks ranging styles were applied on the optimised APT dataset, and the corresponding bulk composition is summarised in Table 6.2. The absolute error in the concentration of Zr, Cu, and Ni was >1 at. % using FWHM peak ranging, and the ranged ion counts covered only two-third of the total detected counts in the dataset. In the background-to-background ranging method, the error was slightly improved. However, <1 at. % composition error with larger ranged ion counts (4.1 M) was obtained with "peak-based ranging" style.

Table 6.2: Absolute error in APT composition compared to ICP-AES composition by different mass spectrum peaks ranging styles.

Ranging Style	Error Zr (at. %)	Error Cu (at. %)	Error Ni (at. %)	Error Al (at. %)	Error Nb (at. %)	Ranged Ion Counts (M)
FWHM	1.43	1.14	1.83	0.63	0.01	3.4
Background-to-Background	0.68	1.35	0.51	0.22	0.16	4.3
Peak Based Ranging	0.03	0.92	0.74	0.17	0.06	4.1

6.2.8 Clustered Evaporation

The APT reconstruction assumes that the process of field evaporation is uniform. The atomic layer-by-layer field evaporation in BMGs, however, is incompatible with the amorphous structure. Instead, a feature of the APT data from BMGs is the clustered evaporation, which diminishes the spatial resolution at the atomic scale [14, 199]. Clustered evaporation refers to the occurrence of localised, high field regions representing non-uniform evaporation sequences, which are usually clearly visible on the field desorption maps. The compositions of the clustered evaporation regions (named the 'clusters' in this chapter) were tested against the residual non-clustered evaporation regions in the APT data. The clusters were identified using maximum separation method (MSM) as detailed in Section 4.4.4, to isolate the clustered evaporation regions from the reconstructed data. The parameters selected were D_{max} = 0.18nm and N_{min} = 5. A 5 nm thin slice perpendicular to the analysis direction is displayed for reconstructed data (Figure 6.10a) and clustered data (Figure 6.10b).

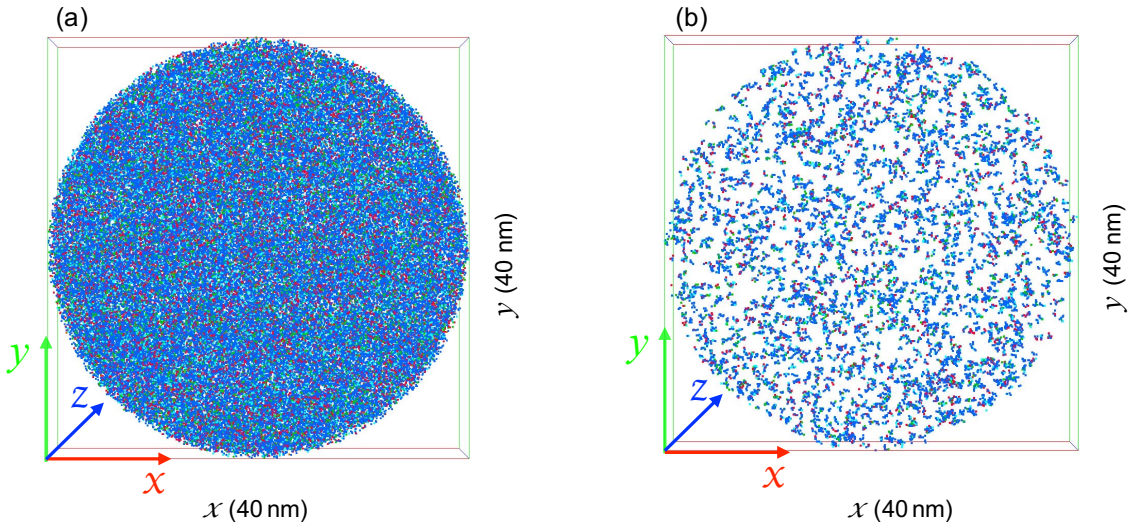

Figure 6.10: 5nm cross section perpendicular to the analysis direction to show (a) reconstructed data, (b) clustered data. Zr [blue], Cu [red], Ni [green], Al [cyan], Nb [mustard] (reprinted from [193]).

The composition of the matrix and the clustered evaporation regions were plotted in Figure 6.11 with reference to the nominal alloy composition from ICP-AES. No significant difference between these compositions was found, as the variations were < 0.56 ± 0.03 at. %.

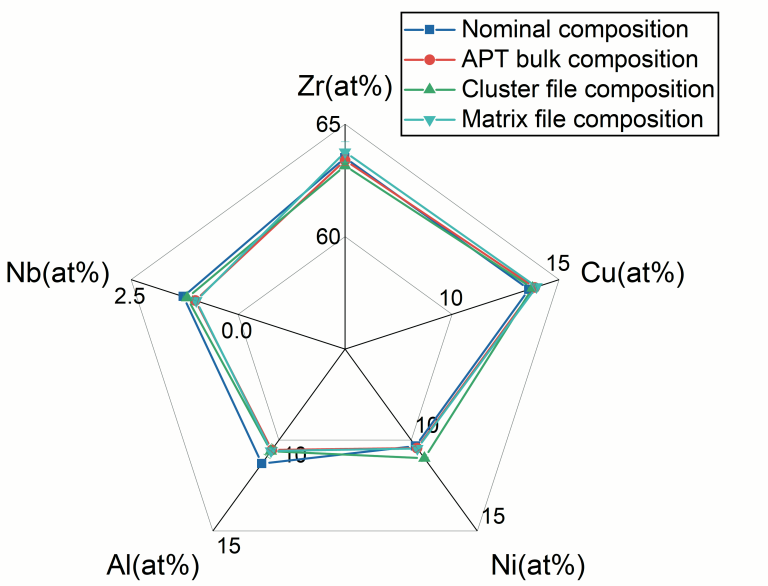

Figure 6.11: Comparison of APT bulk compositions of the overall file for clusters and matrix relative to the actual nominal composition of $Zr_{63.96}Cu_{13.36}Ni_{10.29}Al_{11.04}Nb_{1.25}$ (at. %)(reprinted from [193]).

In order to examine as to whether the clustered evaporation diminishes from the start to the end of the experiment, a cylindrical region of interest (ROI) was extracted from the top of the reconstruction and one from the bottom (Figure 6.12). There were about 10 M ions collected in total, during this APT experiment, and the ROI at the top and bottom had about a similar number of ions (~ 2 M ions).

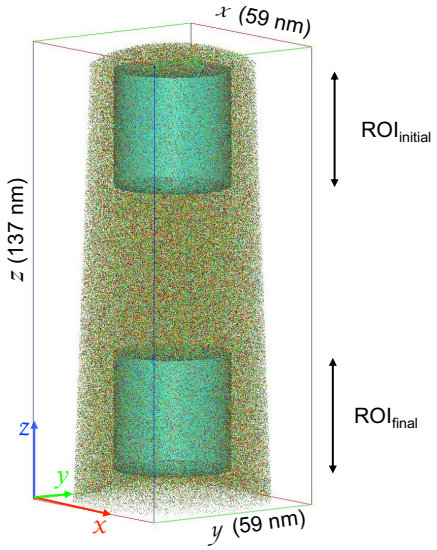

Figure 6.12: Cylindrical ROIs (35 × 35 ×35 nm) at the top ($ROI_{initial}$) and the bottom (ROI_{final}) of the reconstruction, for examining clustered evaporation variation across the overall reconstruction.

The outcome is documented in Table 6.3. The number of clusters in the ROI_{final} are slightly larger than in the $ROI_{initial}$, but this variation does not count for anything because two exactly similar regions can have slightly different number of clusters. The difference between the number densities of the clusters at the start and end of the reconstruction is only 0.01 nm^{-3} which is negligible.

Table 6.3: Details of clustered evaporation at the start and end of the APT reconstruction of Zr-based BMG.

Operating Conditions	ROI	Number of Clusters from the Clustered Evaporation	Volume of the Cylindrical ROI (nm^3)	Number Density of Clusters from the Clustered Evaporation (nm^{-3})
100 pJ laser energy, 160 kHz pulse rate, 40 K temperature, 6 % detection rate	$ROI_{Initial}$ (Start)	39858	33673.95	1.18
	ROI_{Final} (End)	40173	33673.95	1.19

*ROI is the region of interest.

The next step was to understand the effect of laser energy on the clustered evaporation, for which the APT data from a single tip was collected by subsequently applying higher (125 pJ) to lower (75 pJ) laser energy with a step variation of 25 pJ. Another tip was analysed for reverse laser power sequence, i.e., from lower to higher laser energy. The cylindrical ROIs were extracted for cluster analysis of each laser energy from the reconstructed APT tips. The cluster analysis approach as described in Section 4.4.4 was applied. The summary of the results is shown in Table 6.4.

Table 6.4: Comparison of clustered evaporation at various laser energies. The data were collected at 40 K temperature, 160 kHz pulse rate and a detection rate of 6 %.

Order of Application	Laser Energy (pJ)	Number of Clusters from the Clustered Evaporation	Volume of the Cylindrical ROI (nm^3)	Number Density of Clusters from the Clustered Evaporation (nm^{-3})
Descending Order	125	41039	37699.11	1.09
	100	44060	62831.85	0.70
	75	44790	58904.86	0.76
Ascending Order	75	57581	49087.39	1.17
	100	55885	49087.39	1.14
	125	79662	49087.39	1.62

*ROI is the region of interest.

Interestingly, the number density of the clusters is the lowest for 100 pJ laser energy in both cases (descending or ascending). This implies that 100 pJ is an optimum laser energy which can provide accurate APT composition (Figure 6.9) with minimum clustered evaporation (Table 6.4). It is also observed that the changes in clustered evaporation correspond to the respective laser energy but independent of the order at which different laser energies are applied. The order of increase in clusters' number densities as per the laser energies is: 100 pJ < 75 pJ < 125 pJ. Although the clustered evaporation cannot be eliminated, it can be minimised by the appropriate selection of parameters, particularly the laser energy. The fact that clustered evaporation exists, both with the laser-pulsing and with the voltage-pulsing (results not shown here), suggests that clustered evaporation is an intrinsic phenomenon of the BMGs. However, its extent can be augmented by higher laser energies; therefore, the minimum laser energy is recommended out of the optimum range.

6.3 Application of the Optimised Methodology for the Chemical Analysis of AMZ4

This section will showcase the practical application of the developed methodology (Section 6.2). The application was an analysis the oxygen distribution in a 3D printed $Zr_{59.4}Cu_{27.2}Al_{11.2}Nb_{1.6}$ (at. %) (AMZ4) BMG. Selective laser melting (SLM) is one of the many additive manufacturing (AM) processes that create large-scale components from BMGs with flexible geometries. The interrelationship between the AM parameters, the microstructural details, and the local properties, remains a vital research frontier. The compositional variations and oxygen contamination across different layers of the melt and melt-pool boundaries can significantly impact the mechanical performance of the 3D build [297, 298]. The optimised methodology devised above was utilised to analyse oxygen distribution in the AMZ4-BMG sample, and the results are shown in the following section.

6.3.1 Oxygen Distribution in Top and Bottom layers of 3D-Printed AMZ4

The established methodology for parametric selection has helped obtain correct composition across a wide range of Zr-based BMGs, which will be discussed in the following chapter. A particular example is mentioned here, which involves investigating the effect of oxygen distribution at the top, and bottom surface of the melt-pool of a 3D-printed AMZ4 BMG (Figure 6.13). The results have enabled a better understanding of the oxygen distribution, which can be benefited by avoiding high oxygen content areas from the 3D build.

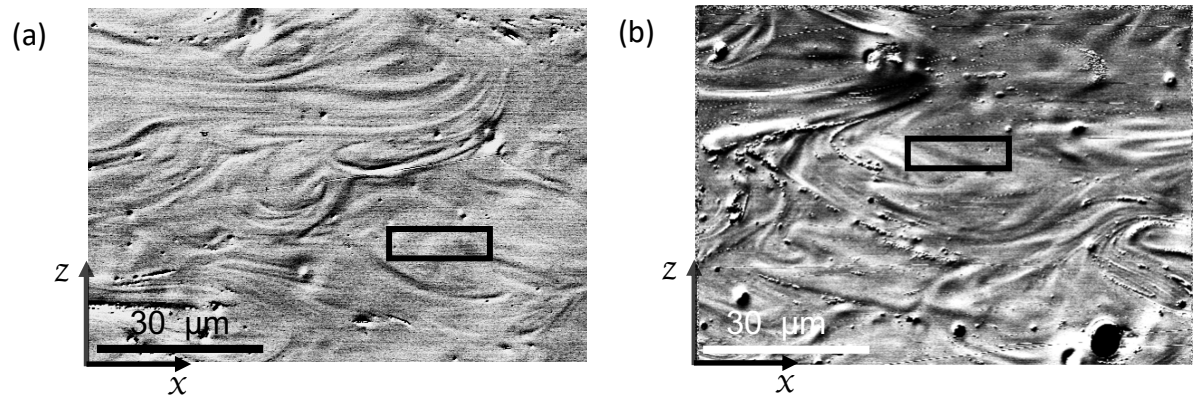

Figure 6.13: Backscattered electron micrograph of the chemically etched cross-section showing (a) the top and (b) the bottom layer of the melt-pool. The rectangles are drawn to highlight the centre of the melt pool.

The APT samples (two each) were prepared from the centre of the melt-pool; one from the top and the other from the bottom layer of the 3D-build. Their lift-out process is detailed in Section 4.2.1. A light element analysis in accordance with ISO 4491-4 standards showed that the AMZ4-BMG bulk sample contains 1271± 41 $\mu g.g^{-1}$ (0.60 ± 0.02 at. %) of oxygen. However, the oxygen distribution across the build layers was unknown.

The APT experimental conditions were (1) pulse rate of 160 kHz, (2) 40 K temperature, (3) 3 % detection rate and (4) 75 pJ laser energy, for the analysis of AMZ4-BMG samples. This was obtained by following a methodology with the goal of optimising the combination of parameters, by checking against some known quantities such as nominal composition, STTR, mass resolution and OPDR (Section 6.2). These parameters were then applied to obtain the APT bulk composition for the top and bottom layers, and the results are shown in Table 6.5.

Table 6.5: The average APT composition of the top and bottom layers of 3D-printed AMZ4-BMG. The samples are taken from the centre of the melt-pool of both layers.

Regions \ Elements		Zr (at. %)	Cu (at. %)	Al (at. %)	Nb (at. %)	O (at. %)
ICP-AES Composition	Actual Composition	59.44 ± 0.38	27.21 ± 0.26	11.12 ± 0.17	1.63 ± 0.06	0.60 ± 0.02
Top Layer	Average	60.21 ± 0.42	27.58 ± 0.20	10.53 ± 0.12	1.09 ± 0.12	0.59 ± 0.02
	Difference with Actual	0.77 ± 0.18	0.37 ± 0.17	0.59 ± 0.12	0.54 ± 0.1	0.01 ± 0.00
Bottom Layer	Average	58.48 ± 0.33	28.89 ± 0.09	10.97 ± 0.29	1.19 ± 0.03	0.47 ± 0.01
	Difference with Actual	0.96±0.19	1.68±0.24	0.15±0.23	0.44±0.05	0.13±0.02

*Compositions are shown with standard deviations.

It appears that the centre of the melt-pool at the top layer has more oxygen content (0.59 at. %) than the bottom layer (0.47 at. %). This preliminary analysis suggests that the oxygen distribution is not uniform across different build layers, and the top layer accumulates more oxygen than the bottom layer (Figure 6.14).

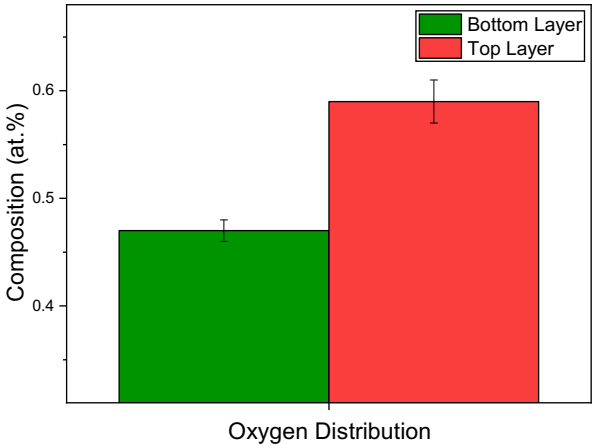

Figure 6.14: Oxygen distribution at the top and bottom layer of the 3D-printed AMZ4 BMG.

A detailed analysis considering the edges of the melt-pool from the top, middle and bottom layers of the build would resolve the oxygen contamination response inside the 3D-build. This type of understanding is vital for improving the BMG's 3D-printing production quality. However, such a detailed study is outside the scope of this thesis and will not be discussed further. Nonetheless, this example has rightfully indicated the broad implication of the developed methodology.

6.4 Discussion

The purpose behind the methodology development was to explore the APT operational parameters. On one hand, the parameters should provide reasonably precise APT compositions. On the other hand, the methodology should result in simple/reproducible high-quality data for further BMG analyses. Due to the nature of this chapter, results were partly discussed alongside for leading the procedure forward. In this section, a brief discussion is given of the main aspects that contributed to the development of a methodology for the optimum selection of the APT experimental parameters of the BMG. The data was evaluated both qualitatively and quantitatively by the help of several factors such as: mass resolution, STTR, OPDR (%) and bulk composition. The reproducibility in the measurement of the bulk composition was ensured by employing a customised peak-based ranging style (Section 6.2.5) for ranging the peaks in the mass spectrum of the APT experiments. The effect of each of the operating conditions on the data quality and the obtained compositions have been discussed in the following sub-sections.

6.4.1 Effect of Temperature

The data quality was assessed in terms of mass resolution, STTR and OPDR. A higher mass resolution was observed at lower temperatures (Figure 6.6a). The values of the FWHM and FWTM improved when the temperature was decreased from 70 K to 40 K, accompanied by a slight decline with a further reduction in temperature. This observation was consistent with lower base temperatures reducing surface diffusion and supporting more rapid cooling after the thermal pulse [158]. The peaks in the mass spectrum at 40 K were more discrete (Figure 6.6c), confirming better field evaporation of the individual elements at this temperature. A similar mass spectrum was observed at 25 K, but the higher prevalence for hydride formation was observed at this temperature that ultimately reduced the STTR values.

Nb was the most dilute specie with a concentration of ~1.25 at. % in the observed BMG and was therefore considered primary in the compositional analysis. The error in Nb concentration varied from ~0.07 at. % to 0.44 at. %, with temperature variations. The overlap of ZrH^{+} peak with Nb^{2+} peak at 46.5 Da was the crucial factor upsetting Nb estimation (Figure 6.3). The fluctuation in ZrH^{+} counts was observed due to the varying interaction between the chamber hydrogen and the Zr^{2+} ions at different temperatures (OPDR (%), as shown in Figure 6.6b). Ni and Zr also exhibited more significant errors at the lower temperatures (< 40 K). The evaporation field of hydrides of an element is generally 10–20% lower than its pure state [299], the preferential evaporation of ZrH^{+} (Figure 6.6b) at lower temperatures have apparently caused an overestimation to Zr concentration. Whereas the higher field evaporation rate of Ni (35 V/nm) may have caused error in Ni concentration due to possible preferential retention. These effects were reduced between 40 K to 50 K temperature for all the constituent elements, with range of error in the composition to less than 1.5%, thus making it an ideal temperature range for this material.

6.4.2 Effect of Pulse Rate

The data quality varied little for pulse rates greater than 150 kHz (Figure 6.7). A degraded mass resolution and a decline in the STTR values at higher pulse rates indicated that the heavier species like, Zr and Nb, require longer times-of-flight. However, extremely low pulse rates can introduce the risk of preferential evaporation of elements exhibiting lower evaporation fields. If this occurs, these ions could go undetected, introducing errors in the composition. This was supposedly the case for Cu ions as in Figure 6.7a, at 100 kHz.

In the pure elemental state, the theoretical evaporation field values for each species in this quinary BMG are as follows: Al (19 $V.nm^{-1}$), Zr (28 $V.nm^{-1}$), Cu (30 $V.nm^{-1}$), Ni (35 $V.nm^{-1}$), Nb (37 $V.nm^{-1}$) [155]. Yet, the actual evaporative field of the species in a complex multi-component alloy will be different from that in the elemental state. Noting that the Cu composition was most affected by the pulse rate, it was perceived to be an example of preferential evaporation, notwithstanding that Cu was not the lowest field evaporator in this alloy.

Unlike in voltage-pulsed APT, a key consideration in selecting the pulse rate in laser pulsing is the minimum rate with which the evaporation of all ions in a material is detectable within a single pulse window under all acquisition voltages [158]. It minimises the base temperature offset effect from lasing and avoids the wrap-around effect in heavier ions requiring longer times-of-flight (TOF) [155, 158]. The changes in the pulse rate had relatively little effect on the compositional error range for frequencies between 250 kHz to 125 kHz (Figure 6.7a). Based on this approach, either 125 kHz or 160 kHz could be chosen. However, since Nb concentration error was increased with 125 kHz, 160 kHz pulse rate was preferred for this BMG.

6.4.3 Effect of Detection Rate

The data quality was improved with the increase in detection rate (Figure 6.8a, b). There was no change in ZrH^+ ion counts with the change in detection rate (Figure 6.8a), at constant temperature, laser energy and pulse rate. The compositional error was not strongly affected by this increase either. Focusing on the most dilute specie in the alloy, a more accurate Nb concentration was attained at detection rates between 3–6%, as shown in Figure 6.8c. A higher detection rate is preferred unless the material is subject to poor yield (easy rupture) or multi-hits issues [155]. Thus, based on the results, a higher detection rate was recommended for this material, since its sample showed high yield and low proportion of multiple hits (< 25% in all cases).

6.4.4 Effect of Laser Energy

In terms of the effects of laser energy, it is noteworthy that the range of compositional error for all species increased as the laser energy decreased, Figure 6.9a. It was attributed to the insufficient evaporation of certain species of this BMG at lower laser energies. More accurate concentrations were achieved in the range of 100 pJ–150 pJ. Moreover, increase in the laser energy (Figure 6.9) increased the STTR and mass resolution as well (Figure 6.9 b-d).

It is noteworthy that the effects of base temperature variations were more substantial (Figure 6.6) due to a higher pulse rate than the effects of laser energy (Figure 6.9) observed at a lower pulse rate. This is due to increased thermal pulsing effect at higher pulse rates. From the results, it was found that temperature and laser energy had the most influence on the APT compositions.

6.4.5 Effect of Ranging Style on APT Composition

"Peak-based ranging" style proved to be the best technique to range the BMG and provided the most accurate APT composition. It was easier to apply when compared with the FWHM or background-to-background ranging techniques (Table 6.2). More ions with accurate element identifications were shown under each peak via peak-based ranging, which is advantageous for precise advanced microstructural and chemical analyses. Thus, the peak-based mass spectrum ranging style was effectively employed for a robust compositional outcome.

6.4.6 Clustered Evaporation Effect

The clustered evaporation phenomenon was analysed for its possible effects on the APT composition and the data quality. This analysis confirmed that the clustered evaporation regions in this alloy did not occur as a result of a significant variation in local composition (Figure 6.1). Therefore, the clustered evaporation does not affect the detection of individual elements of this BMG and had no adverse effect on the compositional analysis [193]. This finding was broadly consistent with the homogeneous composition outcome of $Cu_{45}Zr_{45}Ag_{10}$ BMG reported by Zemp et al. [199]. Given that it was observed in a five-component BMG, it is speculated to be a general result, relative to clustered evaporation, in BMGs. It suggested that something other than the local compositional variations caused local changes in the bond strength resulting clustered evaporation effect in the BMGs.

An APT tip with 10 M ions was evaluated for any fluctuations in the clustered evaporation at the start and end of the experiment. It was found that the difference between the number density of the clusters at the top and bottom of the tip was negligible (0.01 nm^{-3}). This additional experiment confirmed the inevitable presence of the clustered evaporation that exist uniformly throughout the reconstruction. Another set of experiments was conducted where a range of laser energies was applied in ascending and descending orders, to observe any changes in the clusters' magnitude. Interestingly, the number density of the clusters was found the lowest for 100 pJ laser energy in both cases (descending or ascending) as shown in Table 6.4. This implied 100 pJ laser energy as an optimum laser energy for accurate APT composition (Figure 6.9) as well as minimum clustered evaporation. It was also observed that the changes in clustered evaporation were relative to the respective laser energy, yet independent of the order at which different laser energies were applied. The order of increase in clusters' number densities as per the laser energies was: 100 pJ < 75 pJ < 125 pJ. Thus, the clustered evaporation cannot be eliminated, it can be minimised by the appropriate selection of parameters, particularly the laser energy. The fact that clustered evaporation existed, both with the laser-pulsing and with the voltage-pulsing (results not shown here), confirmed its existence as an intrinsic phenomenon in the BMGs. However, its extent can be augmented by higher laser energies; therefore, the minimum laser energy was recommended out of the optimum range.

Eventually, the methodology was tested by applying it to a 3D-printed BMG material (AMZ4). The results provided comparable composition (Table 6.5) and proved beneficial in understanding the oxygen concentration between the top and bottom layer of the 3D-build (Figure 6.14).

6.5 Summary

A step-by-step approach was effectively developed for the appropriate selection of APT operating parameters. The error in the APT composition without optimised parameters was up to 3.21 at. %, which was dramatically reduced to < 1 at. % for the constituent elements. The data quality was enhanced by implementing a customised ranging style, optimised operating parameters and minimising the amount of clustered evaporation regions. The methodology developed in this chapter can be implemented for APT compositional analysis of any BMG, and guarantees optimised data for further chemical and microstructural analyses.

In the context of the questions listed in section 6.1, this chapter is summarised in Table 6.6, as follows;

Table 6.6: Summary of response for the questions presented in the chapter.

#	Questions	Response	Comments
1	What is the effect of pulse rate, temperature, detection rate and laser energy on the data quality?	Completed	The experimental parameters significantly affected the resultant APT data quality.
1a	Effect of temperature		The temperature had the most significant effect on the laser-pulsed atom probe, and lower temperatures were recommended. However, too low a temperature was avoided to suppress hydride formation.
1b	Effect of Pulse rate		The optimised pulse rate in laser-pulsing was the minimum pulse rate that could adequately evaporate all constituting elements. A higher pulse rate was avoided to reduce overheating the tip apex.
1c	Effect of detection rate		Higher detection rate was considered for the appropriate value providing compositional accuracy relative to its nominal composition.
1d	Effect of laser energy		The lower end of the optimum laser energies provided uniform evaporation as per the field desorption maps and efficient APT composition.

2	What criteria should be used for the assessment of data quality?	Completed	The data quality should be quantitatively assessed using more than one factors. The following factors were successfully utilised for quantitative and qualitative evaluation of the APT results. 1)- Mass Resolution 2)-STTR 3)-OPDR (%) 4)- Composition
3	Which mass spectrum peak ranging technique (FWHM, background to background and others etc.) should be selected, and how can we implement a robust ranging style?	Completed	Peak-based ranging style was found the most efficient for the Zr-based BMGs in the present study for the efficient and robust outcome.
4	How to manage peak overlaps in the mass spectrum and assigning a strategy for the overlapped peak?	Completed	IVAS 3.6.8/ AP Suite 6.0 decomposition algorithm can be used for peak decomposition. For overlapped peaks, the peak was assigned to the element with the higher contribution in that peak. However, care must be taken in case the element contributions are very similar.
5	Is the clustered evaporation affected by laser energy?	Yes	Higher laser energy increased the clustered evaporation.
6	Are there any operating conditions that can avoid clustered evaporation of the BMGs?	No	The clustered evaporation was found inevitable in the BMGs. It will occur no matter what laser energy or voltage pulsing is applied. However, with the improved data quality and the efficient APT compositions, further microstructural analysis was expected. The clustered evaporation was ignored in that case due to its uniform distribution and no adverse effect on constituent elements' detection.
7	How to obtain the accurate and reproducible composition from the APT experiments with better data quality?	Completed	It is possible to have a robust APT composition by employing the modified set of operational conditions and the same ranging style across different datasets.

7 COMPOSITIONAL ANALYSIS OF ZR- BASED BMGS

This chapter aims to inquire whether the bulk compositions of the local regions are similar or different in various Zr-based BMGs. Firstly, hard and soft regions (names based on local hardness values) of the TC-$Zr_{63.49}Cu_{13.59}Ni_{10.32}Al_{11.29}Nb_{1.28}$ (at. %) BMG were assessed for the compositional variations. This followed by the compositional evaluation of hard, soft and fractured regions of the HPT-$Zr_{52.5}Cu_{17.9}Ni_{14.6}Al_{10}Ti_5$ (at. %) (Vitreloy-105) BMG. The fractured region of HPT-Vitreloy-105 underwent fracture by a three-point bend test (Section 4.1.1.2).

7.1 Compositional Analysis of TC-Zr-Based Bulk Metallic Glass

The average hardness value was ~493 HV for the TC-Zr-based BMG. The average hardness values of its hard and soft regions were 503 ± 1.41 HV and 477 ± 3.85 HV, respectively. The local hardness values were obtained through the micro-indentation process, detailed in Section 4.1.4. The hardness difference between soft and hard regions was ~26 ± 4 HV (Section 4.1.4). Throughout the thesis, the terms 'soft' and 'hard' are meant for relatively lower and higher hardness values. It was proposed that the local regions' chemical and/or structural changes are responsible for the local hardness variations. However, nothing can be stated with conviction without experimental evidence. Three samples from each region were extracted for their chemical assessment via APT.

7.1.1 Reconstruction

The APT experiments were carried out using 100 pJ laser energy, 160 kHz pulse repetition rate, and a 6% detection rate in the LEAP 4000 XSi at a cryogenic temperature of 40 K. The experiments were conducted under the pressure of ~10^{-11} Torr in the analysis chamber. The details about selecting the experimental parameters for TC-Zr-based BMG have been mentioned in the previous chapter (Chapter 6). At least 5M ions of each sample were collected during the reconstruction process. ~2M ions were cropped from the smooth voltage region. The 3D reconstruction was obtained by following the step-by-step process detailed in Section 4.4.2. The size of the dataset (number of ions) was kept similar for all the samples. The reconstruction of one of the hard and soft region samples is shown in Figure 7.1 and Figure 7.2, respectively. The distribution of each element is separately demonstrated; Zr (purple), Cu (orange), Ni (green), Al (Cyan), and Nb (grey). The qualitative comparison between the reconstructions of hard and soft regions revealed no difference. The distribution of all elements appeared homogeneous by simple inspection in both areas. More detailed statistical analysis was undertaken for small-scale perturbations and is reported in the later section.

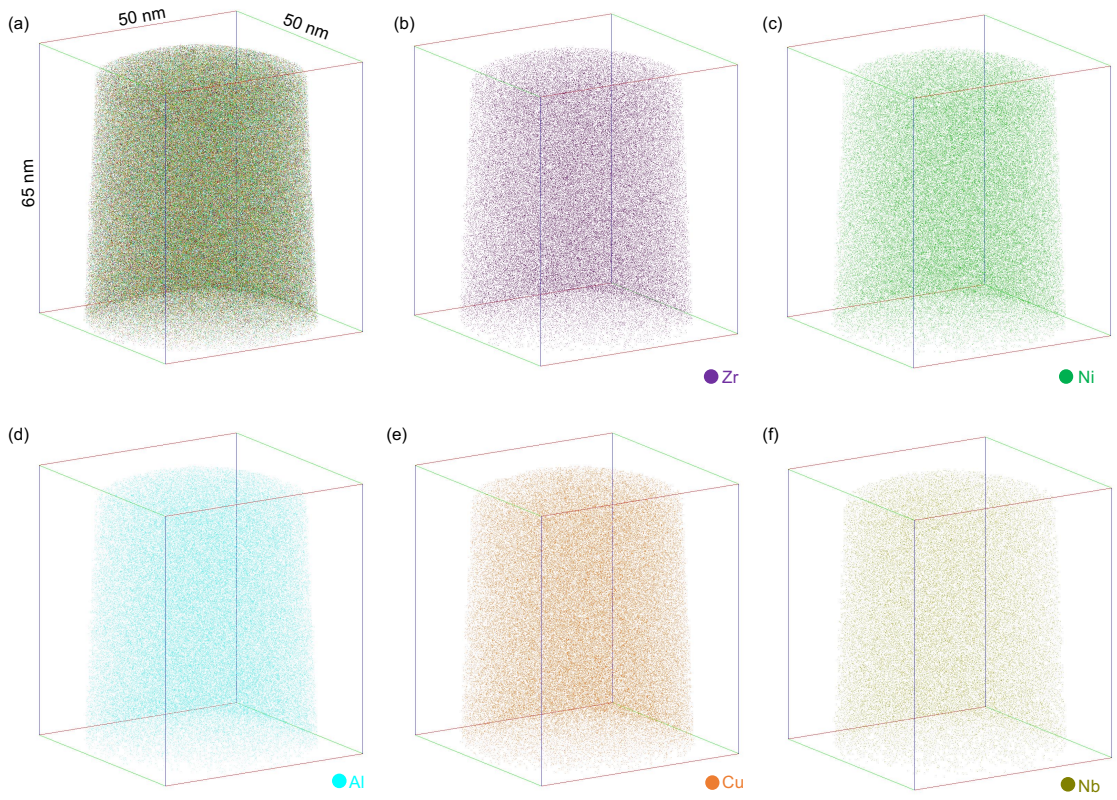

Figure 7.1: 3D-APT reconstruction of a hard region sample (sample ID: R18-59567) of TC-$Zr_{63.78}Cu_{14.72}Ni_{10}Al_{10}Nb_{1.5}$ BMG. (a) Bulk, (b) Zr, (c) Ni, (d) Al, (e) Cu and (f) Nb reconstructions.

7.1.2 Bulk Composition of the Hard and Soft Regions

The average composition of three samples from each region was considered for the comparison. The hydrogen peaks were not ranged in the APT mass spectrum. Hf was present as an impurity in the sample; therefore, the sum of at. % of Zr, Cu, Al, Ni, and Nb was less than 100 at. %. The standard deviation values were mentioned with the average composition values to show the deviation among different samples in each local area. The respective concentration of each element was calculated by decomposing their overlapped peaks using IVAS 3.6.8 decomposition algorithm.

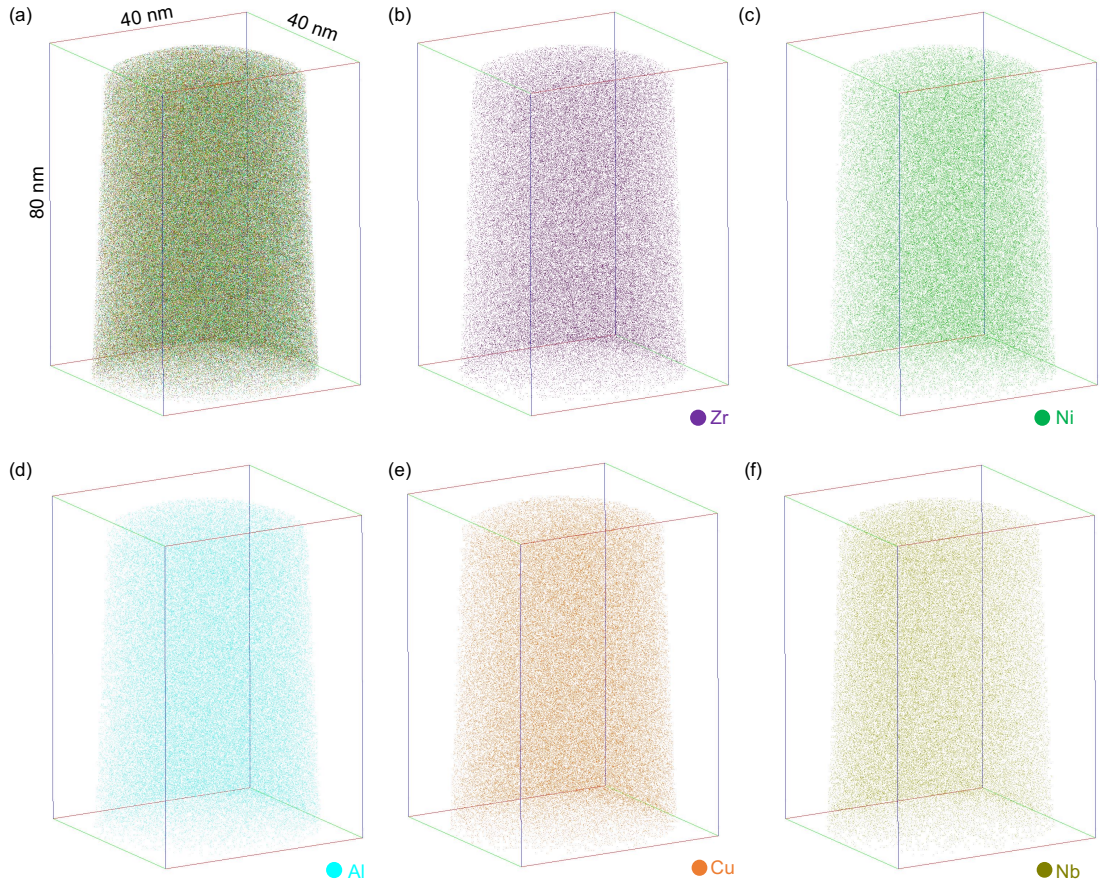

Figure 7.2: 3D-APT reconstruction of a soft region sample (sample ID: R18-59479) of TC-$Zr_{63.78}Cu_{14.72}Ni_{10}Al_{10}Nb_{1.5}$ BMG. (a) Bulk, (b) Zr, (c) Ni, (d) Al, (e) Cu and (f) Nb reconstructions.

The bulk compositions of all samples are shown in Figure 7.3. A slight deviation existed in the concentrations of each element around different samples. Yet, no significant difference was observed in both regions. Cu was slightly lower in one of the soft regions, but the other two samples showed a relatively similar concentration as the hard regions.

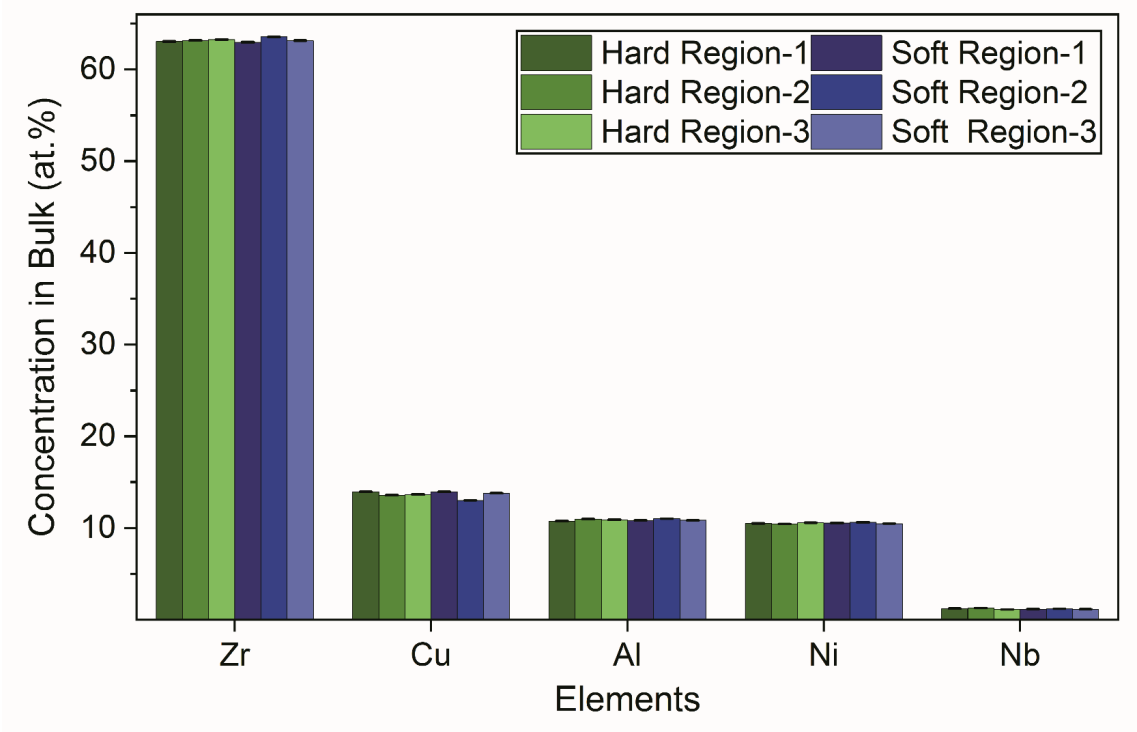

Figure 7.3: Bulk composition of all the hard and soft regions samples of TC-$Zr_{63.78}Cu_{14.72}Ni_{10}Al_{10}Nb_{1.5}$ BMG.

The average compositions of each element with their standard deviation are shown in Table 7.1 and Figure 7.4. The percentage compositions of all the elements were found similar and conveniently lying within the standard deviation values of both regions. The average bulk compositions were compared with the ICP-AES composition of the $Zr_{52.5}Cu_{17.9}Ni_{14.6}Al_{10}Ti_5$ BMG (Table 7.1). The difference was less than 0.5 at. % for all the elements.

Table 7.1: Average bulk composition of the hard and soft region and their difference with the actual composition of TC-$Zr_{63.49}Cu_{13.59}Ni_{10.32}Al_{11.29}Nb_{1.28}$ BMG.

Region \ Elements (at. %)		Zr (at. %)	Cu (at. %)	Al (at. %)	Ni (at. %)	Nb (at. %)
ICP-AES Composition	Actual Composition	63.49	13.59	11.29	10.32	1.28
Hard Region	Average	63.16±0.11	13.74±0.18	10.88±0.11	10.51±0.07	1.21±0.08
	Difference with Actual	0.33±0.11	0.15±0.18	0.41±0.11	0.19±0.07	0.07±0.08
Soft Region	Average	63.26±0.31	13.60±0.62	10.90±0.51	10.60±0.07	1.18±0.09
	Difference with Actual	0.23±0.31	0.01±0.62	0.39±0.51	0.28±0.07	0.10±0.09

**The equation $\sigma_c = \sqrt{c(1-c)/N}$ was used for calculating the standard error for each element, with N being the total number of atoms.*

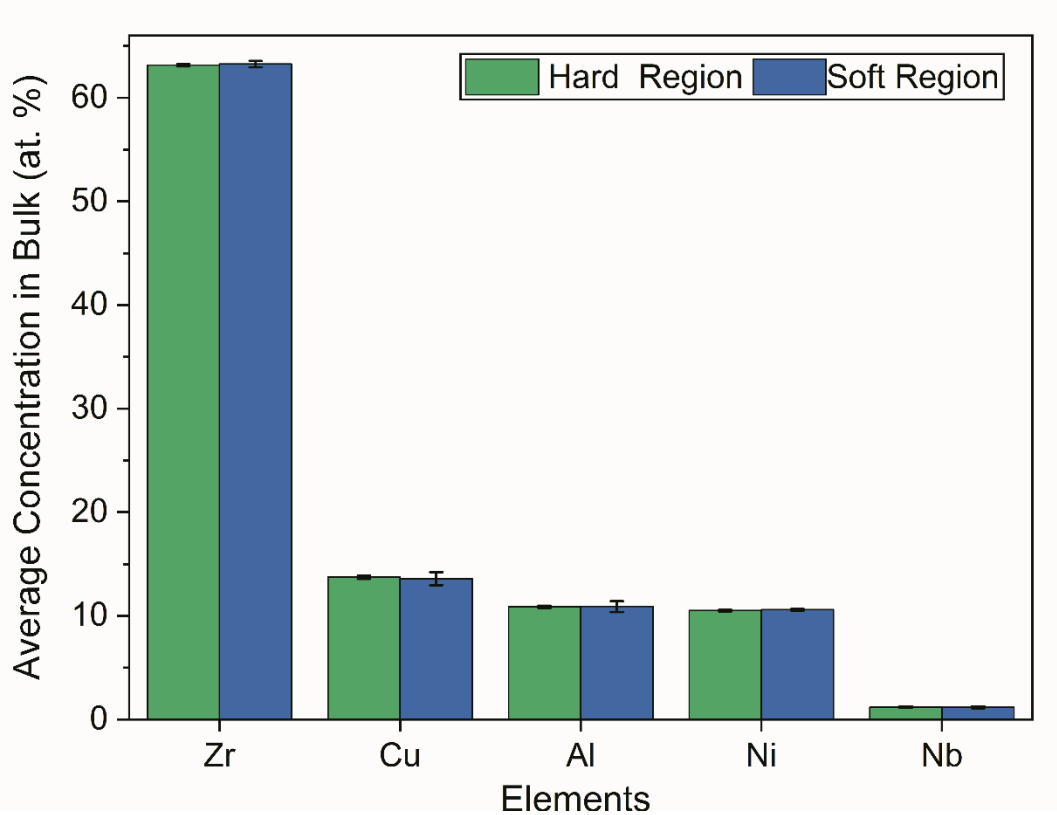

Figure 7.4: Average bulk composition of the hard and soft regions of $Zr_{63.78}Cu_{14.72}Ni_{10}Al_{10}Nb_{1.5}$ BMG.

7.2 Compositional Analysis of HPT-Zr-based BMG.

This section presents the results of the bulk compositions in the hard, soft, and fractured regions for the HPT Vitreloy-105. The average hardness values of the HPT samples were ~564 HV and ~526 HV. The later one was used for three-point bending fracture test. The hardness difference between soft and hard regions was ~93 ± 3 HV, which was more prominent than the above-mentioned TC-$Zr_{63.49}Cu_{13.59}Ni_{10.32}Al_{11.29}Nb_{1.28}$ BMG. Another Zr-based BMG with different composition and processing method was analysed due to two reasons: 1) Vitreloy-105 is a commercially available BMG, its results can be directly compared with the literature and 2) A fractured region was included in the compositional analysis to observe the effect of severe plastic deformation on the overall composition.

7.2.1 Reconstruction

For the APT experiments of Vitreloy-105, 75 pJ laser energy, 160 kHz pulse repetition rate, and 3% detection rate were applied. These values were based on the methodology developed in Chapter 6. It is noteworthy that APT experimental parameters were different from the one used for the TC-$Zr_{63.49}Cu_{13.59}Ni_{10.32}Al_{11.29}Nb_{1.28}$ BMG, possibly due to the presence of Ti instead of Nb and different concentrations of other elements. Each experiment was carried out using the LEAP 4000 XSi at a cryogenic temperature of 40 K and under a pressure of ~10^{-11} Torr. The reconstruction process and the data size were similar, as mentioned in the Section 4.4.2. The 3D reconstruction of one of the fractured regions is shown in Figure 7.5. The distribution of Zr (purple), Cu (orange), Ni (green), Al (Cyan), and Ti (grey) can be observed in this image. The distribution of all the elements was homogeneous and was similar for the hard and soft regions (not shown).

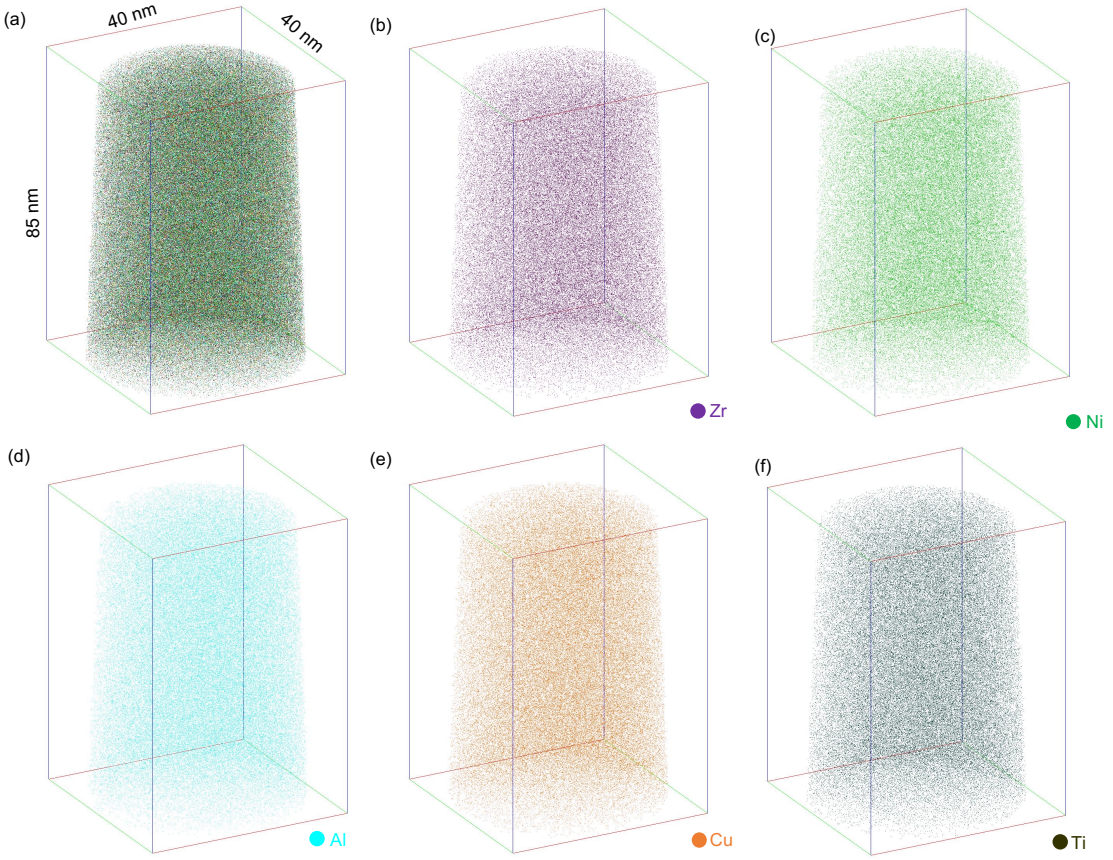

Figure 7.5: 3D-APT reconstruction of a fractured region sample (sample ID: R18-60075) of Vitreloy-105 BMG. (a) Bulk, (b) Zr, (c) Ni, (d) Al, (e) Cu and (f) Ti reconstruction.

7.2.2 Bulk Composition of the Hard, Soft, and Fractured Regions

The bulk compositions of all the samples are shown in Figure 7.6. There were no significant variations in the concentrations of the elements in different regions. Slight fluctuations in the bulk compositions of all the samples existed, yet no noticeable difference was spotted among samples.

Table 7.2: Average bulk composition of the hard and soft region and their difference with the actual composition of HPT-Vitreloy-105 BMG.

Region	Elements (at. %)	Zr (at. %)	Cu (at. %)	Al (at. %)	Ni (at. %)	Ti (at. %)
ICP-AES Composition	(Actual Composition)	53.38	15.88	10.68	14.70	5.27
Hard Region	Average	52.60±0.34	16.73±0.35	10.32±0.48	15.17±0.24	5.19±0.21
	Difference with Actual	0.78±0.34	0.85±0.35	0.36±0.48	0.47±0.24	0.08±0.21
Soft Region	Average	52.34±0.46	16.73±0.78	10.38±0.13	14.82±0.32	5.24±0.11
	Difference with Actual	1.04±0.46	0.85±0.78	0.30±0.13	0.12±0.32	0.03±0.11
Fractured Region	Average	52.56±0.19	17.05±0.24	10.19±0.11	14.96±0.09	5.24±0.10
	Difference with Actual	0.82±0.19	1.17±0.24	0.49±0.11	0.26±0.09	0.03±0.10

**The equation $\sigma_c = \sqrt{c(1-c)/N}$ was used for calculating the standard error for each element, with N being the total number of atoms.*

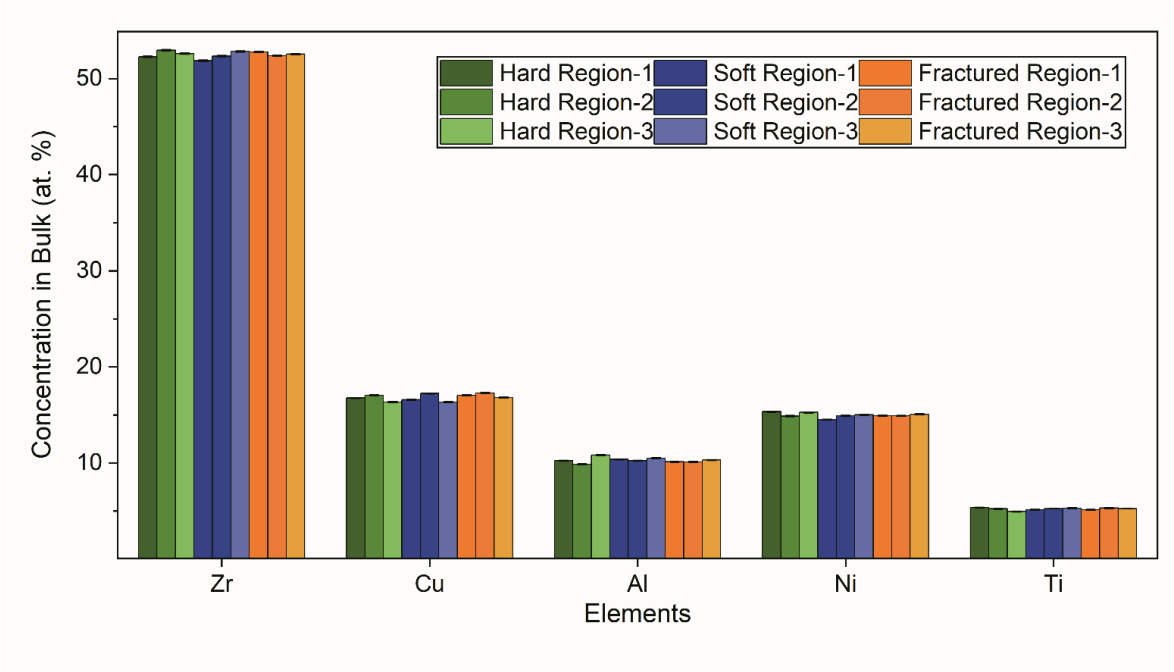

Figure 7.6: Bulk composition of all the hard and soft regions samples of Vitreloy-105 BMG.

Similar results were obtained when the average compositions of different regions were compared, as shown in Figure 7.7 and Table 7.2. Table 7.2 presents the bulk composition of each element with its standard deviation. The average bulk composition values of the hard, soft, and fractured regions were observed to be within the standard deviations of each other. The APT bulk composition of each region was quite accurate with <1.2 at. % error from the ICP-AES composition of the Vitreloy-105 BMG (Table 7.2).

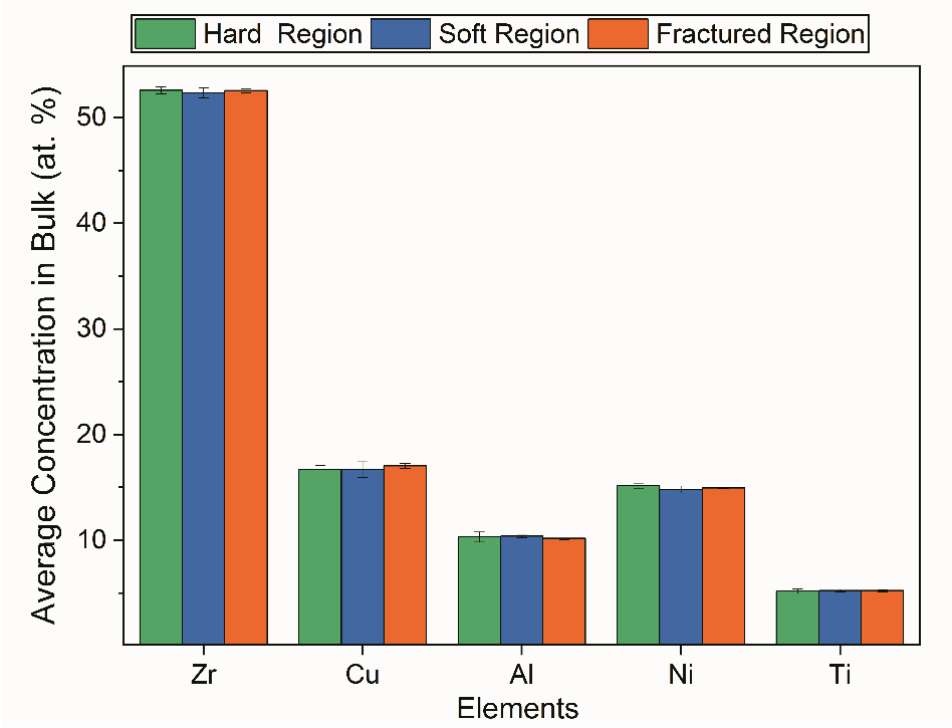

Figure 7.7: Average bulk composition of the hard and soft regions of Vitreloy-105 BMG.

7.3 Possibility of Solute-Based Clusters

The following section will evaluate the feasibility of the APT cluster analysis for assessing any regional perturbations. APT clustering approach identifies densely packed solute-based clusters. Minor density variations likely exist in a randomly distributed APT data due to the nature of the field evaporation process. The data was checked for non-random solute clustering. The spatial heterogeneity of the solute elements beyond randomness was statistically evaluated using the LH^* checkerboard pattern, as detailed in section 4.4.6. About 1000 randomly labelled datasets were used for comparing the degree of randomness in each APT dataset by analysing the bond-pair distance between solute atoms (Cu, Ni, Al, Nb for TC- and Cu, Ni, Al, Ti for HPT Vitreloy-105 BMG . The randomly labelled datasets were acquired through simulation by randomly labelling the atoms in the dataset as the solute elements while keeping their concentration similar to their actual concentrations. Moreover, the reason for choosing a larger number of randomly labelled datasets was to improve the preciseness of the comparison. The results of both the BMGs are presented in the following sub-sections.

7.3.1 Statistical Analysis of TC-$Zr_{63.49}Cu_{13.59}Ni_{10.32}Al_{11.29}Nb_{1.28}$ BMG

In this section, the level of heterogeneity (LH*) checkerboard statistical analysis (Section 4.4.6) was used for the significance of solute-rich clusters in the experimental data by comparing with ~1000 random data. The LH^* checkerboard pattern results for TC-$Zr_{63.49}Cu_{13.59}Ni_{10.32}Al_{11.29}Nb_{1.28}$ BMG are shown in Figure 7.8 and Figure 7.9, for one of the hard and soft regions, respectively. The upward triangles show clustering, indicating the distance reduced distance between the reference and the neighbouring solute atom than its random counterpart, and vice versa (segregation) for downward triangles. The dark colour indicates the higher significance of the outcome, with dark red indicating the result with $p < 0.05$. The checkerboard pattern is useful for observing clustering or segregation in every solute pair all at once.

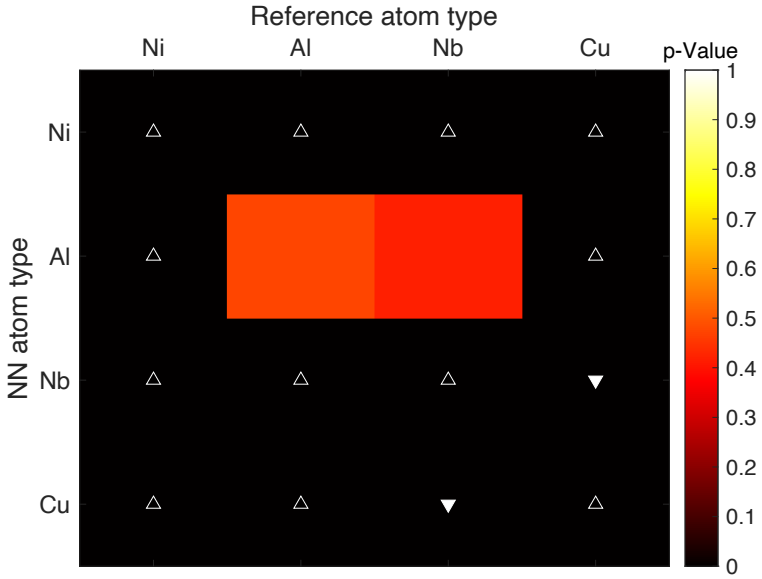

Figure 7.8: LH stat for one of the hard regions (sample ID: R18-59492) of TC-$Zr_{63.49}Cu_{13.59}Ni_{10.32}Al_{11.29}Nb_{1.28}$ BMG. Upward triangles determine the distance between solute-solute pair is decreasing, downward triangle is used if the pair distance is increasing. The darker value means that the outcome is non-random with a 95% confidence level ($p < 0.05$).

Most solute pairs in the hard regions (Figure 7.8) showed significant clustering among solute elements (upward triangles). Conversely, Cu-Nb bonding showed segregation (downward triangles). The trend between Al-Al and Nb-Al was not very significant (p~0.4-0.5) and were not considered in the analysis. Overall, the majority trend was leaning towards solute clustering in all hard region samples.

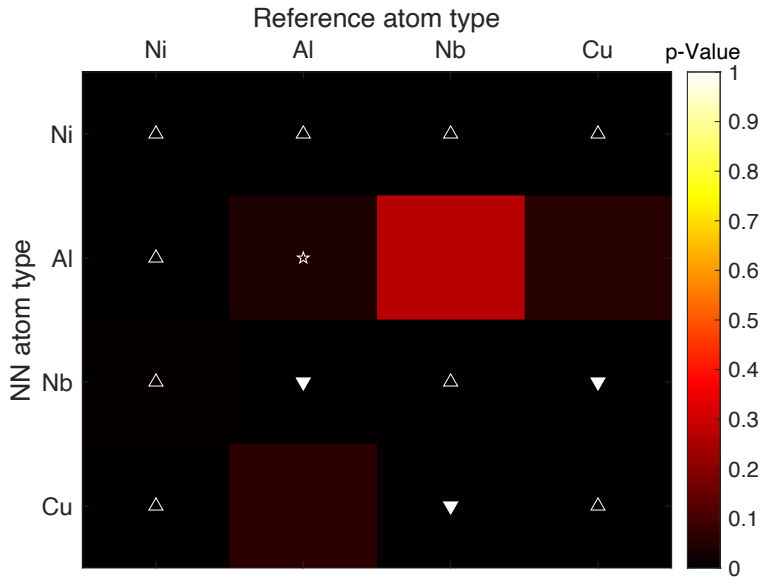

Figure 7.9: LH stat for one of the soft regions (sample ID: R18-59584) of $Zr_{63.49}Cu_{13.59}Ni_{10.32}Al_{11.29}Nb_{1.28}$ BMG. Upward triangles determine that the distance between solute-solute pair is decreasing, downward triangle means that the pair distance is increasing, star means non-random distribution without further information. The darker value means that the outcome is non-random with a 95% confidence level.

The majority of solute-pair distances were significantly non-random ($p < 0.05$) in soft regions, as shown in Figure 7.9. The tendency of solute clustering was higher in most of the solute pairs. Just like the hard regions, the Cu-Nb pair showed segregation (downward triangle ~ solute pair distance increases). Al-Nb pair also demonstrated segregation (downward triangles), a unique feature of soft regions. Al-Al, Nb-Al, Cu-Al, and Al-Cu solute pair distances could not be included in the analysis due to their lower p-value.

7.3.2 Statistical Analysis of HPT Vitreloy-105 BMG

The LH* checkerboard pattern for different HPT Vitreloy-105 are shown in Figure 7.10, Figure 7.11, and Figure 7.12. All the solute species demonstrated clustering with a 95% confidence level ($p < 0.05$) in the hard region, as shown in Figure 7.10. Similar results were obtained for other samples of the hard regions (Appendix 0A).

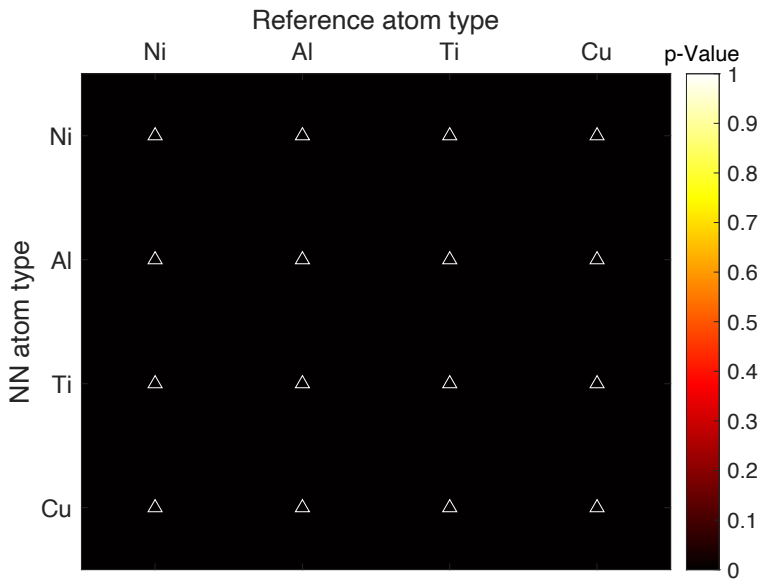

Figure 7.10: LH stat for one of the hard regions (sample ID: R18-59875) of Vitreloy-105 BMG. Upward triangles determine that the distance between the solute-solute pair decreases, and the darker value means that the outcome is non-random ($p < 0.05$).

The soft (Figure 7.11) and the fractured (Figure 7.12) regions showed a similar trend as the hard region.

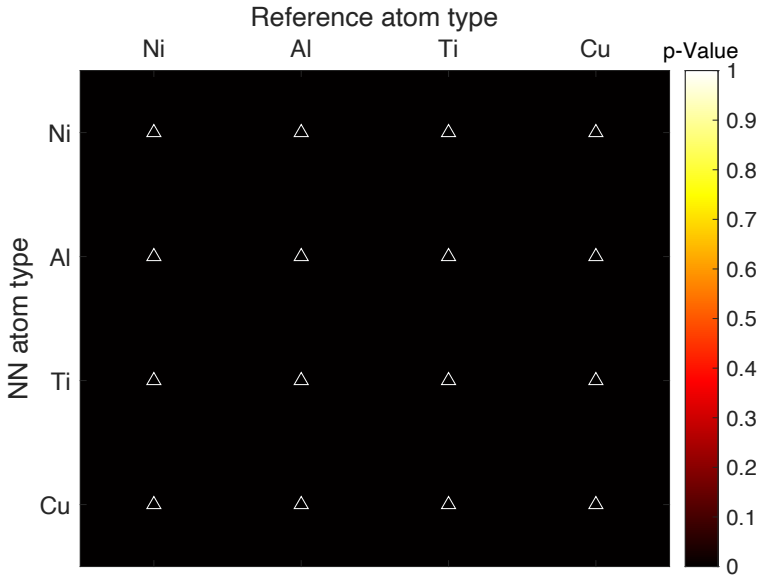

Figure 7.11: LH stat for one of the soft regions (sample ID: R18-60190). Upward triangles determine that the distance between the solute-solute pair decreases, and the darker value means that the outcome is non-random ($p < 0.05$).

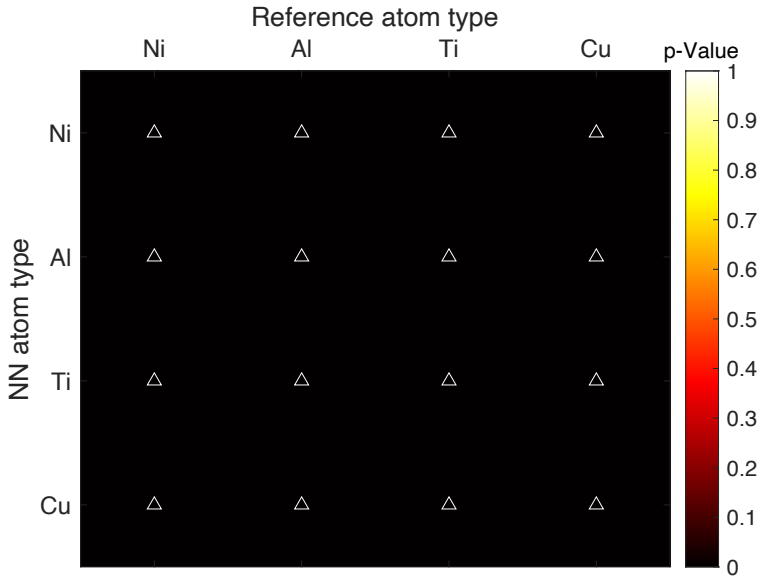

Figure 7.12: LH stat for one of the fractured regions (sample ID: R18-59900). Upward triangles determine that the distance between the solute-solute pair decreases, and the darker value means that the outcome is non-random ($p<0.05$).

7.4 Discussion

APT compositional analysis was used to compare the compositions between various regions in different BMGs. The following results were obtained.

- The APT compositional analysis revealed that the percentage compositions of all the constituent elements were similar in the local hard and soft regions of TC-$Zr_{63.49}Cu_{13.59}Ni_{10.32}Al_{11.29}Nb_{1.28}$ BMG. Any differences in elemental concentrations were within the standard deviation values of both regions (Table 7.1).

- No significant difference was observed in the composition of the various regions in the Vitreloy-105 (Figure 7.7, Table 7.2).

- The APT composition was comparable to ICP-AES composition for both BMGs (Table 7.1, Table 7.2).

The compositional variations within different regions of the BMGs were earlier thought of, causing the local hardness variations (Chapter 3). However, it was confirmed that the bulk compositions remained same in all the local regions of the TC-$Zr_{63.78}Cu_{14.72}Ni_{10}Al_{10}Nb_{1.5}$ BMG and Vitreloy-105, despite the region's local hardness variation and/or severe plastic deformation. Moreover, the effectiveness of the APT compositional analysis was confirmed since the compositions were very close to the ICP-AES composition (<1.2 at. % error).

As the possibility of compositional variation has been ruled out, local hardness variations in Zr-based BMGs appeared to be associated with the local structural variations instead. These micron-scale local regions did not show any visible precipitates or phase separations (Figure 7.1, Figure 7.2, Figure 7.5), yet the structural variations could belong to sub-atomic scale features. It should be noted that any atomic or sub-atomic scale heterogeneities cannot be detected through "by-eye inspection," and a sophisticated statistical analysis is required for

their evidence. A non-parametric test (LH-checkerboard) was applied to confirm the non-random distribution of the constituent elements in the local regions of BMGs, as a pre-requisite of the APT cluster analysis. The significance of each solute pair outcome was measured based on the colour, with dark red pointing towards $p < 0.05$ (95% confidence level). Some of the solute pairs distances increased (segregation) compared to the random datasets (Cu-Nb in Figure 7.8,Figure 7.9, Al-Nb in Figure 7.9). However, the differences between hard and soft regions were not emphasised using the checkerboard patterns since all the solute pairs could not be included due to their lower p-values. This test was considered for overall clustering/segregation/random tendency only.

Typically, solute clustering was observed in most solute pairs in all regions of the TC-$Zr_{63.78}Cu_{14.72}Ni_{10}Al_{10}Nb_{1.5}$ BMG and Vitreloy-105. These statistical results highlighted the clustering behaviour of the solute distribution beyond what would be expected in the random distribution in both hard and soft regions. Thus, the APT clustering approach can be applied to explore possible differences in clusters of different regions for variable hardness attribution.

7.5 Summary

The compositional analysis of TC-$Zr_{63.49}Cu_{13.59}Ni_{10.32}Al_{11.29}Nb_{1.28}$ BMG and HPT-$Zr_{52.5}Cu_{17.9}Ni_{14.6}Al_{10}Ti_5$ BMG was successfully carried out. The APT compositional analyses revealed that the bulk compositions of the local regions are not accounted for their local hardness variation or severe plastic deformation. It was proposed that the local property variations are likely connected with the local structural variations. Moreover, the statistical results confirmed the possibility of solute clustering in the local hardness regions of both BMGs. Thus, APT cluster analysis can be used for observing the local microstructure-property-processing relationship.

8 MICROSTRUCTURAL ANALYSIS OF THERMALLY CYCLED ZR-BASED BULK METALLIC GLASS

This chapter focuses on the microstructural features behind the local hardness variations in the TC-$Zr_{63.49}Cu_{13.59}Ni_{10.32}Al_{11.29}Nb_{1.28}$ (at. %) BMG. The possibility of chemical fluctuations causing hardness variation has already been ruled out by earlier examination of variable hardness regions within this BMG (Chapter 7). It was noticed as a common characteristic of Zr-based BMGs despite their compositions or processing conditions. The presence of sub-atomic level perturbations in the form of solute-rich clusters has been observed through the simulation studies of Zr-based BMG (Chapter 5), as well as in the previous chapter (Section 7.3). A hypothesis is made here that solute-rich clusters are responsible for the local hardness variations inside the Zr-based BMGs. This chapter will test this hypothesis by atomic-scale structural analysis of these clusters in TC-Zr-based BMG.

8.1 Atom Probe Tomography (APT)

The hard and soft regions of the TC-Zr-based BMG were analysed through APT. This powerful technique is employed due to its excellent ability in exploring nano-structural features inside the material and their quantitative description. The average hardness values of the hard and soft regions of the TC Zr-based BMG were 503 ± 1.41 HV and 477 ± 3.85 HV, respectively. The local hardness values were obtained through the micro-indentation process, detailed in Section 4.1.4. The atom probe sample preparation and experimental details are described in Sections 4.2.3 and Section 4.4. The experimental data were investigated in detail for local chemical and structural variations throughout the chapter. The results are discussed and summarised at the end of this chapter.

8.1.1 APT Cluster Analysis

The solute-rich clusters inside the APT experimental data of TC-Zr-based BMG were analysed using IVAS 3.6.8 cluster analysis approach. Some irregularities in the cluster sizes were observed within each region due to the amorphous nature of this material. More than one sample was considered to specify the regional fluctuations in cluster sizes and number densities. Any variations beyond the region's variability were determined as the possible difference between local hardness regions. Three hard and soft region samples were selected for the cluster analyses.

The cluster analysis of the APT data was performed using a density-based scanning algorithm (DBSCAN). The 5NN heuristic method was used with N_{min}= 6 atoms, solutes= Cu, Al, Ni, and Nb (Section 4.4.5.2). The raw and clustered data comparison suggested that the matrix comprised a few un-clustered solute atoms (Figure 8.1, Figure 8.2).

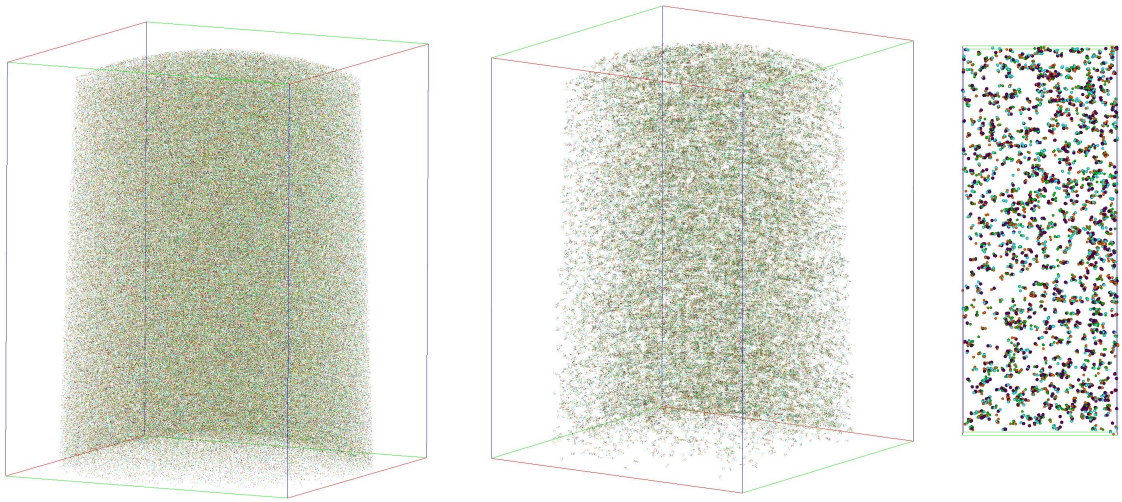

(a) (b) (c)

Figure 8.1: 3D APT reconstructions (dimensions 59 × 59 × 137 nm) of HPT deformed BMG-hard region (502 ± 2.82 Hv). (a) Raw data. (b) Clustered data. (c) 2.5 × 24 × 60 nm clustered region with atoms as spheres. (Purple = Zr atoms, Orange = Cu atoms, Cyan = Al atoms, Green = Ni atoms, Brown = Nb atoms).

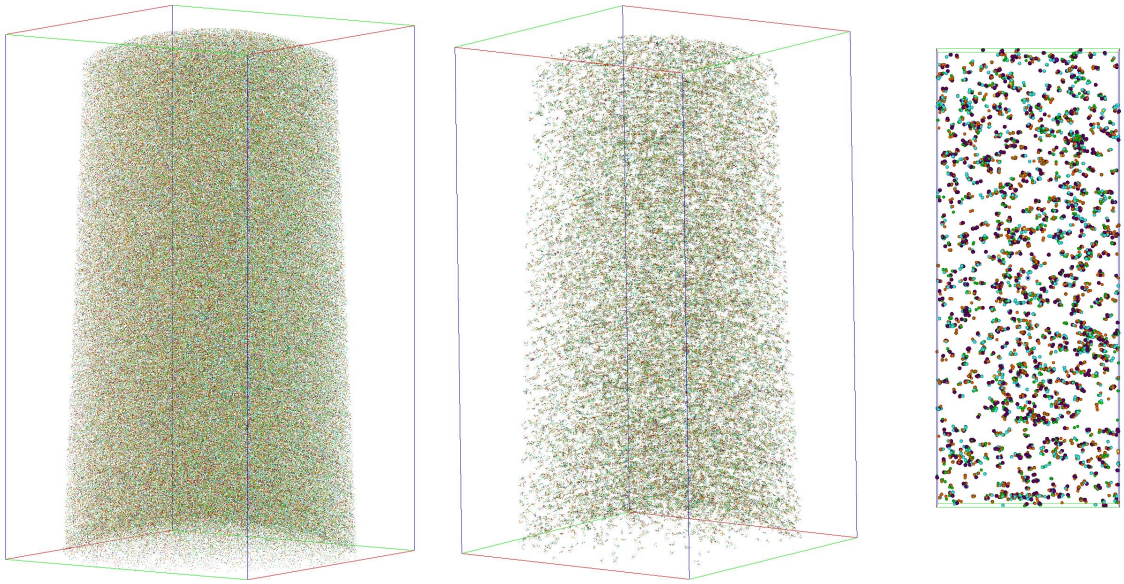

(a) (b) (c)

Figure 8.2: 3D APT reconstruction (dimensions 40 × 40 × 80 nm) of HPT deformed BMG-soft region (473.5 ± 12.3 Hv). (a) Raw data. (b) Clustered data. (c) 2.5 × 24 × 60 nm clustered region with atoms as spheres. (Purple = Zr atoms, Orange = Cu atoms, Cyan = Al atoms, Green = Ni atoms, Brown = Nb atoms).

The clustered data is shown in Figure 8.1b for the hard region and Figure 8.2b for the soft region. Here, Zr is presented in purple, Cu in orange, Al in cyan, Ni in green and Nb in brown colour for all reconstructions. It was observed that the clusters are homogeneously distributed over the entire reconstruction in both regions. A 2.5 × 24 × 60 nm^3 rectangular region of interest (ROI) was extracted from the centre of each reconstruction for better visualisation of the clustered regions (Figure 8.1c, Figure 8.2c). It is difficult to discern the changes in the clusters between the regions by eye. Thus, the most effective way would be the quantitative evaluation of these clusters in different hardness areas.

8.1.2 APT Clusters Results

As discussed earlier, the structural variations using solute-rich clusters (APT clusters) are targeted here for any association with hardness variations. To accomplish this objective, the clusters were structurally evaluated based on their size distributions, number densities, average volume fractions, and morphologies in both regions. At the same time, their chemistry was explored by comparing their average compositions in hard and soft regions. The individual details are provided in the following sub-sections.

8.1.2.1 Number Density of APT Clusters

The number densities of the clusters against their cluster sizes for different regions of TC-$Zr_{63.49}Cu_{13.59}Ni_{10.32}Al_{11.29}Nb_{1.28}$ (at. %) BMG are shown in Figure 8.3. For more straightforward volume calculations, a cylindrical ROI of about 2.0 M ions was extracted from every reconstruction. The number density of each cluster size range was obtained by dividing the total number of clusters in each size range by the volume of respective ROI.

Figure 8.3a indicates that the number densities and the cluster sizes range are different between both regions of this BMG. The size range for hard region-2 was the smallest with up to 81-100 atoms and the largest for hard region-3 with 141-160 atoms. The cluster size ranges for all three soft regions' samples were beyond the size range of hard regions. The variation in cluster size range provided clear discrimination between these two regions.

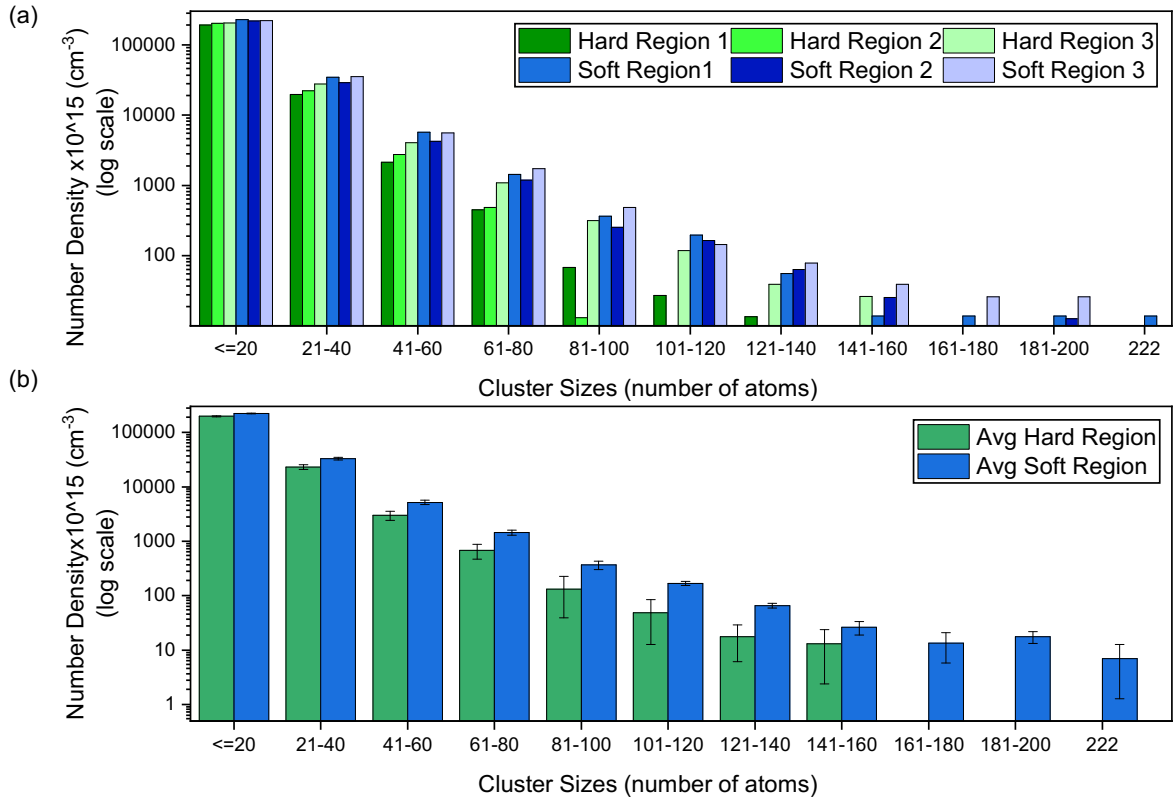

Figure 8.3: Experimental number density plots, a)- number density of clusters in all samples, b)- average number density of clusters in hard and soft regions, versus cluster sizes (atoms).

The number densities of various cluster sizes were found different in both regions. In most cases, the number densities of hard region samples were smaller than the soft regions. However, in some cases, the number densities were somewhat similar. For example, the number densities of the hard region-3 were analogous to or sometimes higher than soft region-2. The difference was prominent in the size range, proceeding to 181-200 atoms for soft region-2 and 141-160 atoms for hard region-3.

The average number densities of the hard and soft regions are shown in Figure 8.3b, along with the standard deviations among their samples. The average number densities of all the soft regions' cluster size ranges were significantly larger than the hard regions'. Moreover, the maximum cluster size range extended up to 222 atoms for the soft region, whereas it was confined to only 160 atoms in the case of the hard region.

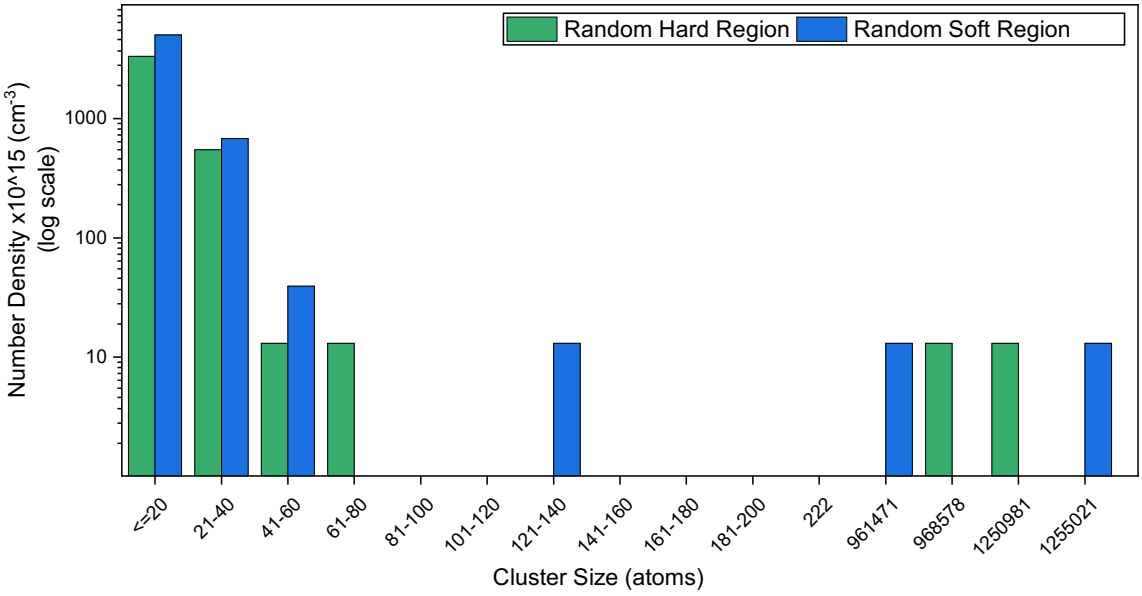

Figure 8.4: Random labelled number density plots for the hard and the soft regions versus cluster size (atoms).

The significance of these solute-based clusters was corroborated by comparing the APT datasets with their randomly labelled counterparts. The details of acquiring randomly labelled data are available in Section 4.4.5.4. The trend in the random datasets for all the regions (Figure 8.4 and Figure 9.5) was different from the actual datasets (Figure 8.3). Some massive-sized clusters (0.9–1.25 M atoms) were observed in the random data. The possibility of such large clusters was unlikely in the actual data; otherwise, it would visibly appear as a precipitate in the reconstruction. Besides these enormous clusters, smaller size clusters (<150 atoms) were also spotted. However, the number densities of these clusters were comparatively smaller than the actual data.

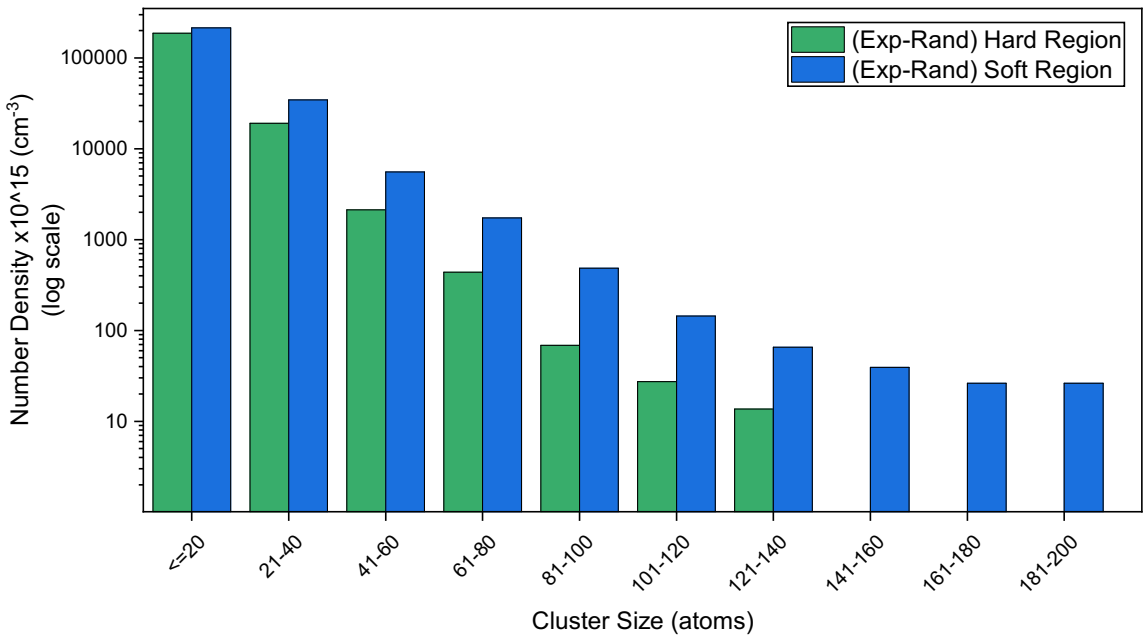

Figure 8.5: Experimental number density minus random number density plots for the hard and soft regions versus cluster size (atoms).

8.1.2.2 APT Cluster Size

The distribution of cluster sizes in different hard and soft regions was demonstrated with the help of box and whiskers plots. The boxes in Figure 8.6 show 25% to 75% cluster size data for each sample and the open circle inside the box indicates the average cluster size. The top and bottom whiskers highlight the distribution of the remaining 25 % of the data, and the solid points represent the outliers in each case.

Figure 8.6 highlights that the average cluster size of soft region samples is slightly larger than the samples of the hard region. The box size for the hard region-3 and soft region-1 were somewhat similar, but their outliers were different. Although the box size of the soft region-2 was smaller than hard region-3, its outliers' range was longer and thus contain larger-sized clusters than other hard regions.

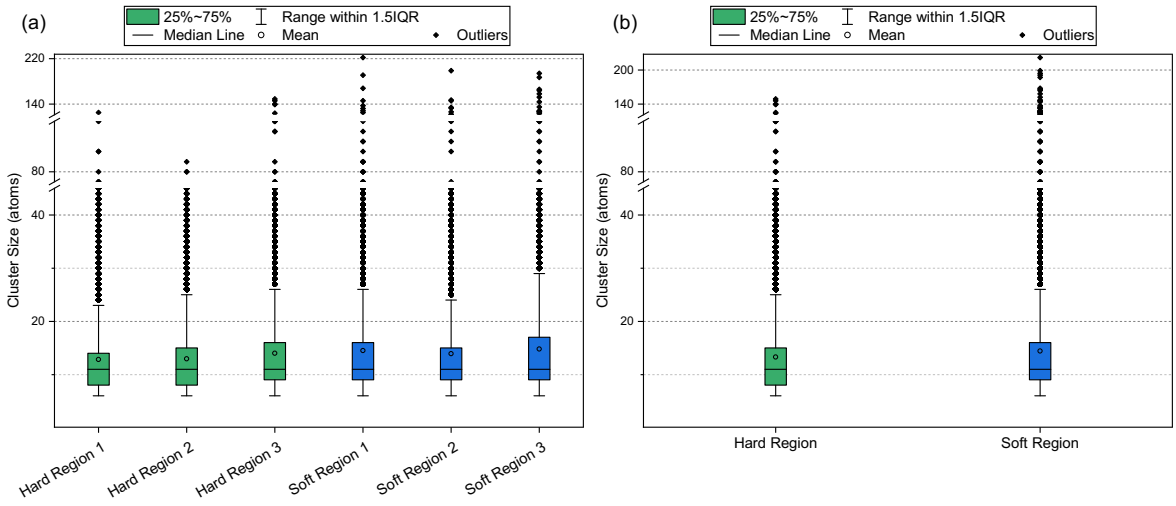

Figure 8.6: The box plot for cluster size (atoms) distribution for, a)- all samples, b)- combined plot for hard and soft regions.

8.1.3 Volume Fraction of APT Clusters

In this section, the volume fraction was analysed to compare the volumetric proportion of the clusters in different hardness regions. The volume of each cluster was computed from equation (4.3). The aggregated clusters' volume ratio to the ROI's volume was the volume fraction. The data of average clusters volume in the hard (0.341, 0.344, 0.372 nm^3) and the soft (0.387, 0.373, 0.396 nm^3) approximately indicated the ascending order of the cluster sizes from hard to soft. The details of the volume fractions of all the samples are shown in Table 8.1.

Table 8.1: Volume fraction of solute-rich clusters in all the hard and soft regions samples of TC-Zr-based BMG.

Region Solute-rich Clusters	Volume Fraction	Average Volume Fraction
Hard Region1	0.072	0.080±0.008
Hard Region2	0.078	
Hard Region3	0.088	
Soft Region 1	0.104	0.101±0.006
Soft Region 2	0.094	
Soft Region 3	0.104	

**The values are shown with standard deviations.*

There is a clear difference in the volume occupied by the clusters in the hard region compared to that in the soft region, as shown in Figure 8.7. It is understandable since the relatively larger number densities of the clusters in the soft regions enclosed more volume in the reconstruction.

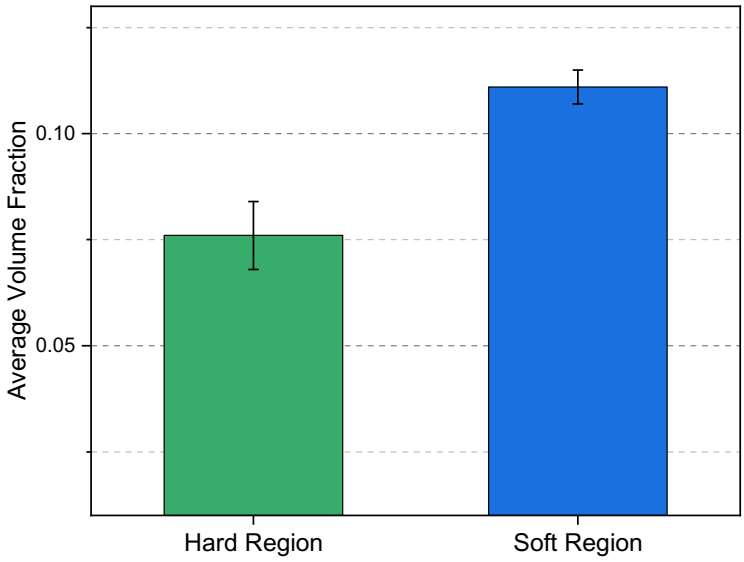

Figure 8.7: Volume fraction of (CuNiAlTi) clusters in hard and soft regions of TC- Zr-based BMG.

The size, number densities and volume fractions of these solute-rich clusters were increased as the region's local hardness decreases, referring to a softening trend which will be analysed further in the discussion section.

8.1.4 APT Clusters Morphology

It was observed from the results so far that the clusters' sizes and quantities are different in the hard and soft regions. However, it cannot be predicted whether their shapes are similar in both cases or not. The cluster shapes were observed through morphology maps, plotted using each cluster's aspect ratio and oblateness, based on the approach detailed in the 4.4.5.3. Each graph was divided into four quadrants: sphere, disc, rod and lath.

Figure 8.9 displays the distribution of the cluster morphologies for both regions, which were reasonably similar. The morphology plot of one of the hard region's samples (HR2) is shown in Figure 8.8 to specify different parts of this plot. The enormous-sized clusters were mostly spherical, whereas the majority of the small size clusters were disc-like. The quantities of lath- and rod-like clusters were relatively smaller. It should be noted here that these morphology maps were only used to approximate the cluster's shape for pseudo-comparison between the regions. Since the APT reconstructions were not spatially calibrated, these maps cannot exactly represent the cluster's shapes.

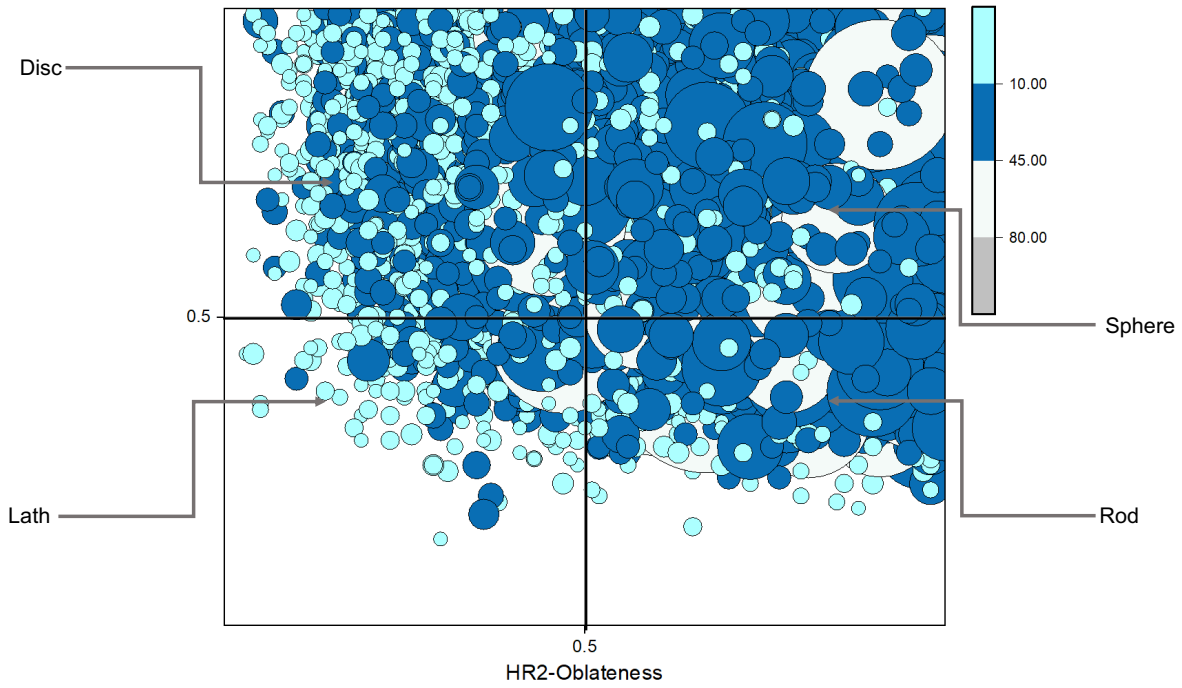

Figure 8.8: An example of the morphology plot of (Cu-Ni-Al-Ti) clusters in one of the hard regions (HR2).The four quadrants indicate the morphology types of the clusters; disc, sphere, lath or rod. The color of the bubbles indicates the size-range of the clusters whereas the number density of the clusters in a particular size-range is represented by the size of the bubbles.

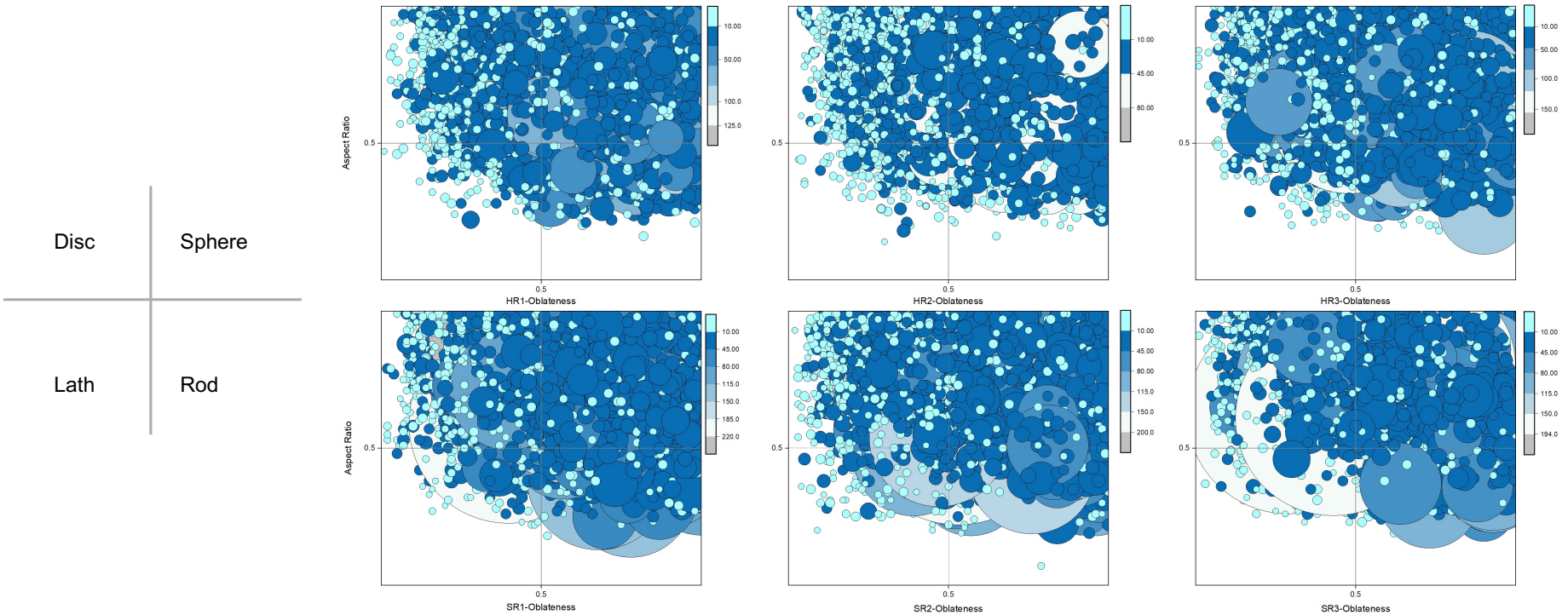

Figure 8.9: Morphology of (Cu-Ni-Al-Ti) clusters for all samples in hard regions (HR) and soft regions (SR).The four quadrants indicate the morphology types of the clusters; disc, sphere, lath or rod. The color of the bubbles indicates the size-range of the clusters whereas the number density of the clusters in a particular size-range is represented by the size of the bubbles.

8.1.5 Chemistry of APT Clusters

As the bulk compositions of the hard and soft regions were similar, this section focuses on the average compositions of clusters and matrices in both regions. Additionally, the number of atoms in the clusters and matrix was added to ensure that the bulk (cluster + matrix) results in a similar composition for both regions. The outcome is depicted in Table 8.2 and Figure 8.10. There was no significant difference in the average composition of clusters in both regions. A similar trend was observed in the average compositions of the matrices in hard and soft regions. Overall, it appeared that, just like their morphologies (Section 8.1.4), the average compositions of solute-rich clusters were also similar and did not fluctuate too much from hard to soft region. This settles the reason behind the similar bulk composition observed in the previous chapter and this section (Figure 8.10c) for different local hardness regions.

Table 8.2: Average compositions of (Cu-Ni-Al-Ti) clusters in hard and soft regions.

Regions \ Elements		Zr (at. %)	Cu (at. %)	Al (at. %)	Ni (at. %)	Nb (at. %)
Hard Region	Bulk Composition	54.36±0.32	17.10±0.10	9.92±0.08	13.55±0.27	5.08±0.06
	Cluster Composition	20.5±0.83	29.34±0.44	17.27±0.27	23.86±0.20	9.02±0.22
	Matrix Composition	58.90±0.21	15.43±0.05	9.01±0.07	12.06±0.22	4.60±0.05
Soft Region	Bulk Composition	54.68±0.48	16.82±0.23	10.04±0.18	13.26±0.25	5.20±0.17
	Cluster Composition	21.77±0.55	28.85±0.22	17.26±0.34	23.09±0.22	9.03±0.28
	Matrix Composition	61.79±0.75	14.22±0.31	8.48±0.19	11.14±0.32	4.37±0.16

**The composition values are shown with the standard deviation values.*

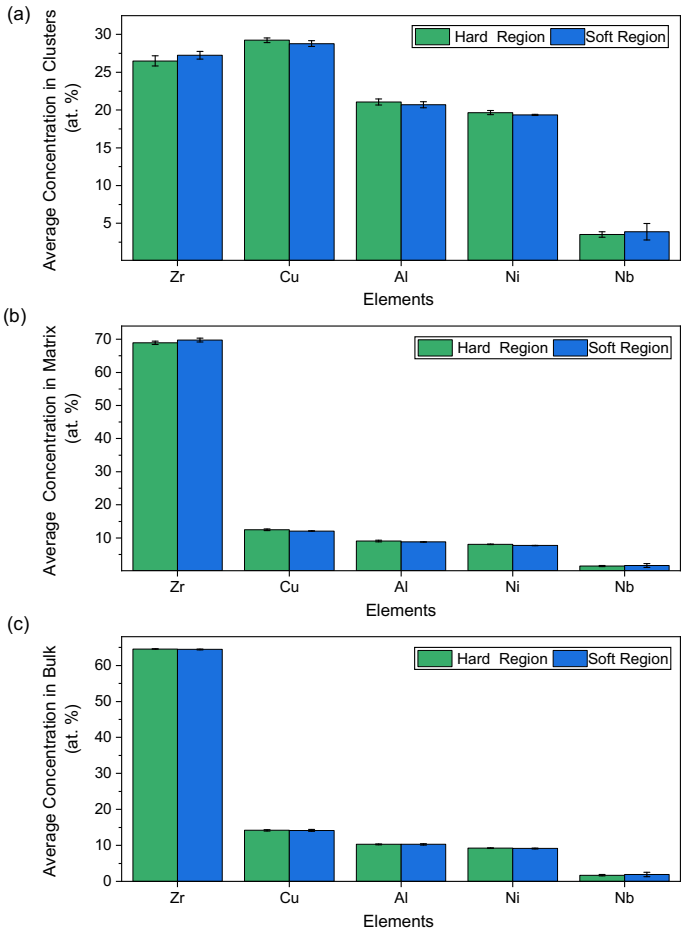

Figure 8.10: (a) Average bulk composition (at%) of clusters, (b) average composition (at%) of matrices and (c) average composition of the bulk (cluster + matrix) in hard and soft regions.

Although many solute-based clusters were observed inside the BMG, solutes were found inside the matrix. The percentage contribution of each element towards clusters' formation is shown in Figure 8.11 and Table 8.3. About 21% of each solute contributed to the cluster formation in the hard region and about 25-26% in the soft region. It is noteworthy that this increase seemed to link directly with the number densities of clusters in various regions. Likewise, there is more Zr left in the matrix of the hard region than the soft region.

Table 8.3: Total percentage contribution of each element towards clusters' and matrix formation.

Regions \ Elements		Zr (%)	Cu (%)	Al (%)	Ni (%)	Ti (%)
Hard Region	Clusters	4.17±0.49	20.97±2.15	20.83±2.22	21.61±2.36	20.99±2.07
	Matrix	95.83±0.49	79.03±2.15	79.17±2.22	78.39±2.36	79.01±2.07
Soft Region	Clusters	5.3±0.55	25.43±2.13	25.16±2.2	26.43±1.97	25.42±2.94
	Matrix	94.7±0.55	74.57±2.13	74.84±2.2	73.57±1.97	74.58±2.94

**The composition values are shown with the standard deviation values.*

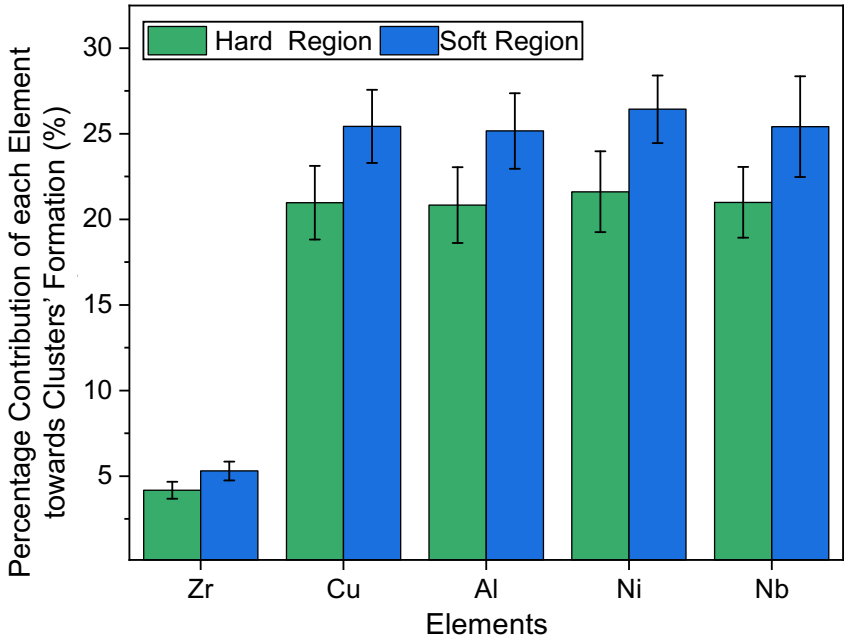

Figure 8.11: Percentage contribution (%) of each element in solute rich clusters.

The percentage of different elements, residual in the matrix were be obtained by:

$$\%\, i_{matrix} = 100 - \%\, i_{clusters} \tag{8.1}$$

$$\%\, i_{clusters} = \frac{Ni_{clusters}}{N_i} \times 100 \tag{8.2}$$

Where ;

$i = Zr, Cu, Ni, Al, Ti$
N_i= total number of atoms of element 'i' (clusters + matrix).
$Ni_{clusters}$= total number of atoms of element 'i' in the clusters.

8.2 Discussion

This section discusses the results of this chapter. APT clusters were explored through the APT cluster analysis in the locally variable hardness regions of TC-$Zr_{63.49}Cu_{13.59}Ni_{10.32}Al_{11.29}Nb_{1.28}$ (at. %) BMG. APT clusters in different hardness regions were compared with randomly distributed counter data. Randomised element identities did not fulfil the clustering criterion. The apparent difference between the experimental and random data (Figure 8.5) confirmed significant clusters in all the regions. The quantitative analyses of these solute-rich clusters based on their number density, size and volume fraction is summarised below.

- The number densities of the clusters in the soft regions were slightly larger than those in the hard regions for different cluster size ranges (Figure 8.3).

- The number density difference between the hard and soft regions was more pronounced for clusters with sizes larger than 20 atoms.

- The number density plots revealed that the cluster size range extended to ~222 atoms for soft regions. On the other hand, the cluster size range was limited to 149 atoms in hard regions.

- The cluster size distributions were relatively broader for soft regions than hard regions, as shown in Figure 8.6.

- The volume fraction of the clusters in the hard region (8 ± 0.8%) was lower than the soft region (10 ± 0.6%), as shown in Figure 8.7. It means that the minimum difference between the volume fraction of clusters in these regions was only 0.6%, whereas the maximum difference could rise to 3.4%.

8.2.1 Local Hardness Relation with APT Clusters

These results indicated a negative correlation between the solute-rich clusters in a region and its local hardness. The local hardness decreased as the proportion of these clusters increased. The reduced hardness of the region was conferred as an increase in the softening behaviour of that site, inducing ductility in the local region. It was contemplated that a ductile BMG can be obtained by increasing the number of these structural perturbations. The hardness difference between hard and soft regions of this BMG was less than 50 HV, yet this is quite appealing to pull out regional microstructure-property relation from it. Such distinction emphasises the effectiveness of the APT cluster analysis towards investigating structural heterogeneities in the Zr-based BMG.

8.2.2 APT Clusters and Deformation

It is imperative to consider the behaviour of solute-rich clusters during deformation to understand their role in material's plasticity. However, the plasticity of BMG materials is generally linked with the shear nucleation regions or STZs, which percolates during deformation to create shear bands. Earlier studies proposed the average size of the STZs to be around 0.48 nm^3 [119]. The average volume of solute-rich clusters in this chapter is ~0.35 ± 0.02 nm^3 for hard regions and ~0.38 ±0.02 nm^3 for soft regions (Section 8.1.3).

A direct comparison between the numerical values of the STZs and these clusters is difficult because both were acquired through unlike methods. However, some resemblance was observed between the average volumes of STZs and these clusters. Two possibilities were proposed in this scenario: 1) these clusters behave as nucleation initiators for STZs or, 2) interaction of neighbouring clusters under external field results in the transformation of these clusters into STZs. Nonetheless, it is just a speculation at this stage that requires further analysis for better understanding. The discussion on solute-rich clusters for their relationship with STZs will be continued in the next chapter.

8.2.3 Morphology and Chemical Composition of APT Clusters

No significant difference in the clusters' morphologies based on the local hardness values was observed, implying the extent of these clusters varies in different regions, despite their shapes. Spherical and disc-like structures were observed for the solute-rich clusters (Figure 8.9).

Similarly, the chemical compositions of the APT clusters compared to their surrounding matrix were presented. The average composition of these clusters was widely different from the average composition of the matrix in the region. This trend was similar for both hard and soft regions. The average atomic concentrations of all four solute elements (Ni, Cu, Al, Ti) were relatively higher in APT clusters than the matrix, contributing to ~78% of clusters' composition. Another critical feature was the mutual existence of Ni and Cu inside most of these clusters despite their positive enthalpy of mixing. It is an interesting observation because the solutes with positive enthalpy of mixing tend to repel each other and cause phase separation [227]. This BMG was observed as a monolithic BMG under TEM [245] and APT (Section 7.1), the combined presence of Ni and Cu was another evidence supporting the homogeneity of this material at bulk.

The atomic concentration of solvent (Zr) was higher in the matrix, but ~40 at. % of matrix composition was comprised of solute elements. The clusters' average compositions between the hard and the soft revealed no significant difference and a similar observation was noticed between their matrices, as shown in Figure 8.10. Hence, the average composition of APT matrices did not vary significantly between hard and soft regions.

8.3 Summary

This chapter demonstrated the first results to link the microstructural features with the local hardness variations in the BMGs, using APT. The APT clusters' number densities, sizes, and volume fractions were relatively larger in soft than hard regions. This chapter clearly linked the solute-based clusters and the regional hardness variations. The morphologies and chemistry of these clusters were found similar in both regions. Thus, it is not the chemistry but the extent and distribution of these clusters that caused local softening.

9 MICROSTRUCTURAL ANALYSIS OF VITRELOY-105

In this chapter, the microstructural variations are analysed in a deformed $Zr_{52.5}Cu_{17.9}Ni_{14.6}Al_{10}Ti_5$ (at. %) (Vitreloy-105) BMG through the solute-based clusters. The purpose of this chapter is to broaden our understanding of microstructural variations in BMGs upon deformation. The effect of both controlled deformation (before fracture) and uncontrolled deformation (until fracture) has been employed. The composition and the deformation treatment of the BMG in this chapter are different from the one discussed in the previous chapter (Chapter 8) for the sake of comparison. By the end of this chapter, the reader will be able to discern the relationship between the atomic-scale structure of BMGs in terms of the APT clusters in various regions and their local hardness.

9.1 Atom Probe Tomography (APT)

The microstructure of Vitreloy-105 was investigated using two samples, by APT. One of the samples was mechanically deformed below fracture by HPT. A three-point bending test fractured another HPT sample to analyse the fractured region (Section 4.1.1.2). Local hardness values were about 606 ± 6 HV for hard region samples and roughly 510 ± 12 HV for soft region samples (Section 4.1.4). As stated in the methodology chapter (Chapter 4), Vitreloy-105 showed a more significant difference between local hardness regions (~100 HV) than $Zr_{63.49}Cu_{13.59}Ni_{10.32}Al_{11.29}Nb_{1.28}$ BMG (~40 HV); therefore, it was expected to show more significant deviations in the clusters for hard and soft regions. In addition to this, the fractured region was analysed for the effect of uncontrolled deformation on the clusters. The experimental data were extensively studied for structural and chemical variations across hard, soft, and fractured regions throughout the chapter; the results were discussed and summarised in the end.

9.1.1 APT Cluster Analysis

The representative 3D reconstructions of the raw data and the solute-based clusters for all the regions are shown in Figure 9.1 to Figure 9.3. In all the reconstructions, Zr, Cu, Al, Ni and Ti are shown with purple, orange, cyan, green and blue colours, respectively. By eye, homogeneous distribution of all the elements was observed in the raw data of the reconstructions.

Despite the reconstruction appearing homogeneous, solute clusters were present in the dataset. The solute-based clusters were obtained through the DBSCAN algorithm. The 5NN heuristic approach detailed in Section 4.4.5.1 was used. The parameters were N_{min}=6 atoms with Cu, Ni, Al and Ti as solutes.

The extracted clusters are shown in the APT reconstruction (Figure 9.1b, Figure 9.2b and Figure 9.3b) , demonstrating the homogeneous distribution of the clusters throughout the reconstruction in all cases. The comparison between the raw and the clustered data indicated a significant presence of un-clustered solute atoms in the residual matrix.

A 2.5 × 24 × 60 nm^3 rectangular region from the centre of each reconstruction (Figure 9.1c, Figure 9.2c and Figure 9.3c) was extracted to visualise the distribution of these clusters in different regions. There was a large number of clusters in all cases. However, hard regions appeared to have comparatively fewer clusters than the other two regions. The clusters in soft and fractured regions were denser and bigger. Nonetheless, due to the large number of clusters, it was difficult to discriminate the clusters by eye, and a deeper investigation is required to discern their characteristics in different regions.

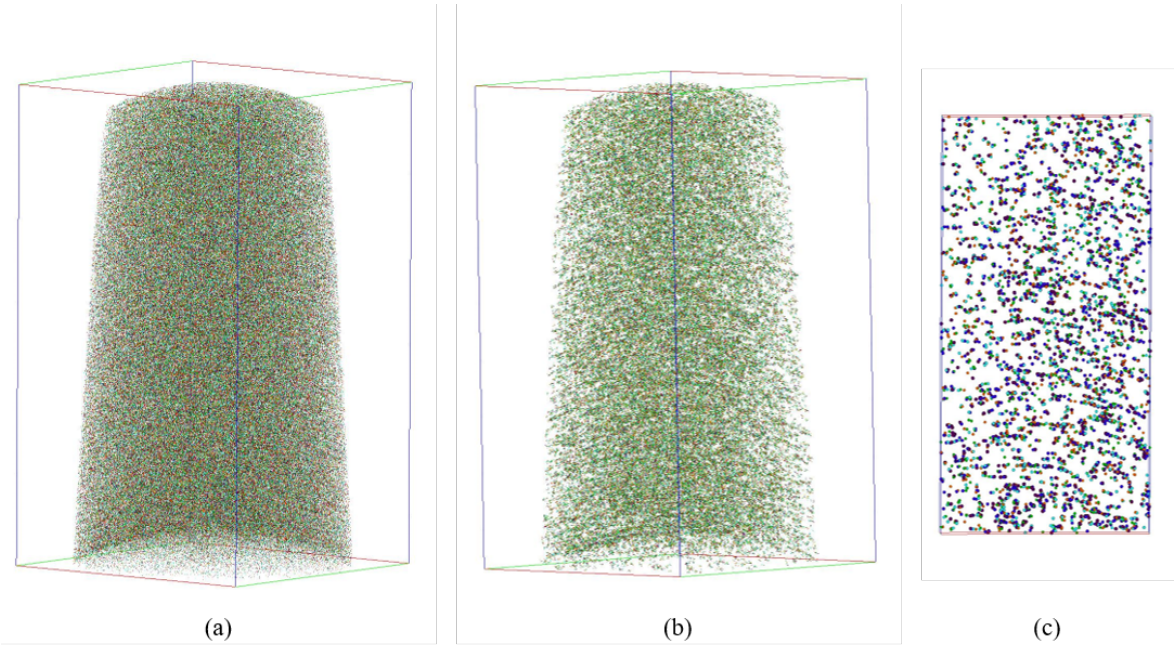

Figure 9.1: 3D APT reconstructions (dimensions 49 × 49 × 85 nm) of HPT deformed BMG-hard region (610 ± 6 HV). (a) Raw data. (b) Clustered data. (c) 2.5 × 24 × 60 nm clustered region with atoms as spheres. (Purple = Zr atoms, Orange = Cu atoms, Cyan = Al atoms, Green = Ni atoms, Blue = Ti atoms).

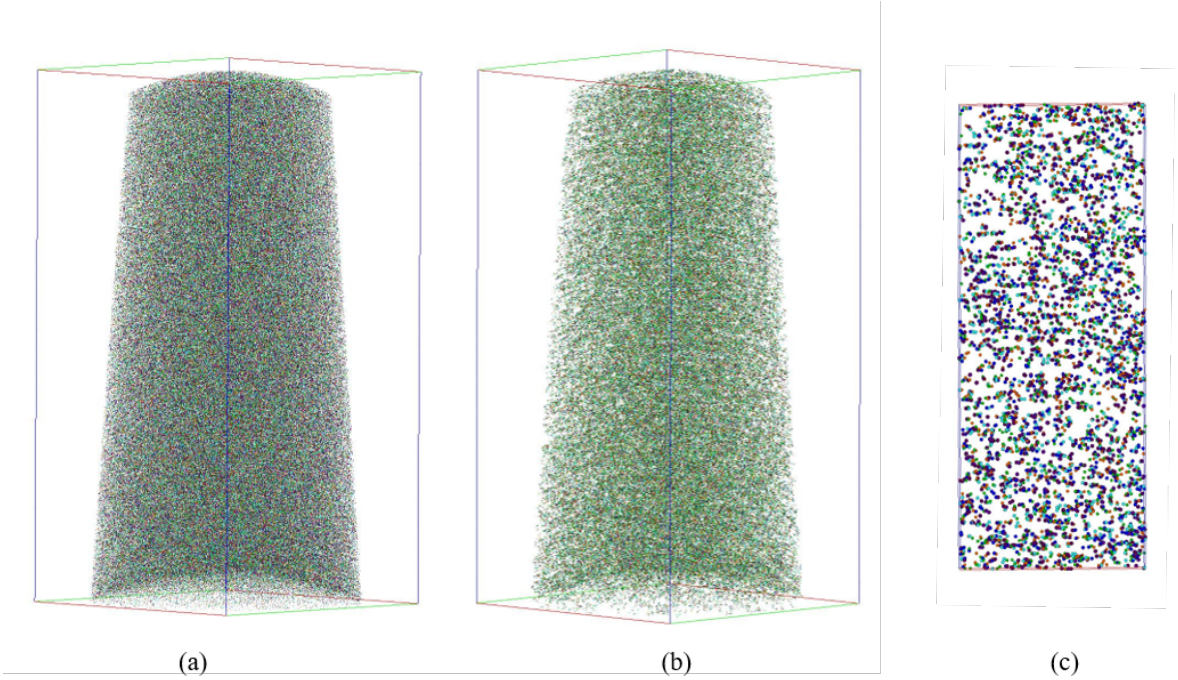

Figure 9.2: 3D APT reconstructions (dimensions 50 × 50 × 99 nm) of HPT deformed BMG-soft region (570 ± 12 HV). (a) Raw data. (b) Clustered data. (c) 2.5 × 24 × 60 nm clustered region with atoms as spheres. (Purple = Zr atoms, Orange = Cu atoms, Cyan = Al atoms, Green = Ni atoms, Blue = Ti atoms).

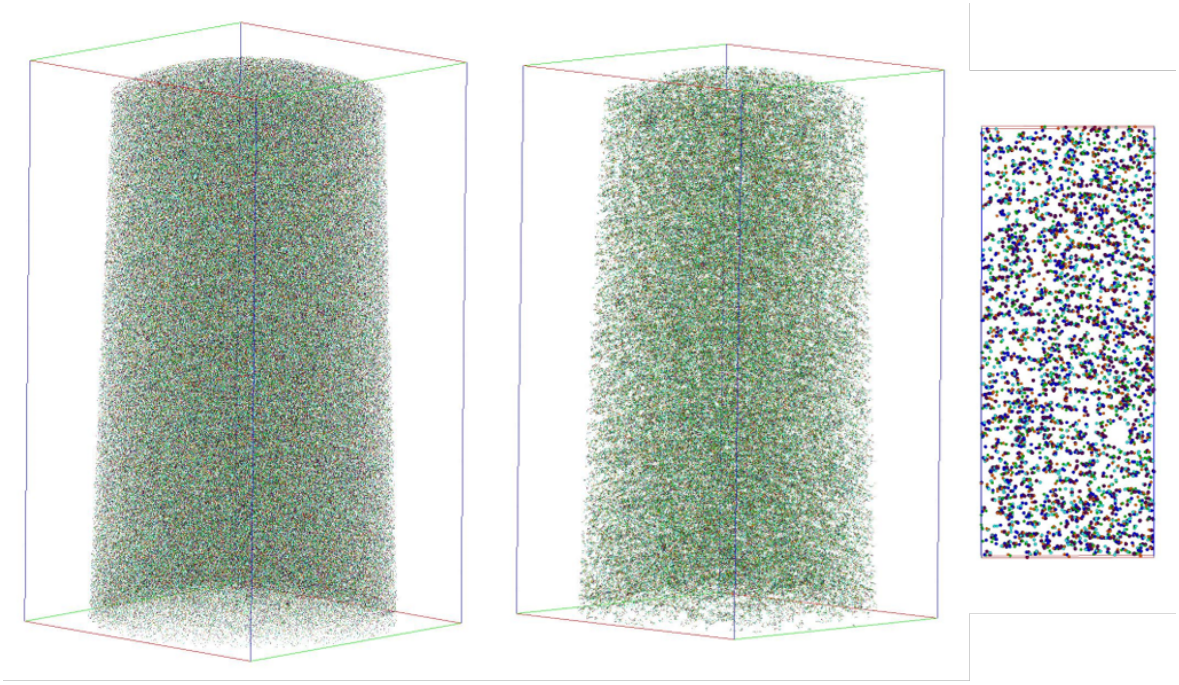

Figure 9.3: 3D APT reconstructions (dimensions 52 × 52 × 96 nm) of HPT deformed BMG-fractured region. (a) Raw data. (b) Clustered data. (c) 2.5 × 24 × 60 nm clustered region with atoms as spheres. (Purple = Zr atoms, Orange = Cu atoms, Cyan = Al atoms, Green = Ni atoms, Blue = Ti atoms).

9.1.2 APT Clusters Results

In this section, the solute-based clusters in hard, soft and fractured regions were quantitatively analysed in terms of their size, number density, volume fraction, morphology and chemistry.

9.1.2.1 Number Density of APT Clusters

The number densities of the clusters were calculated by dividing their cluster counts in each size range by the reconstruction volume. All the results presented in this section were calculated using IVAS 3.6.8 cluster analysis algorithm.

Figure 9.4 showed the number density of the clusters against cluster size (atoms) for hard, soft, and fractured regions of the HPT-Vitreloy-105 BMG. For this analysis, a cylindrical region of interest (ROI) of an equal number of atoms (~2M) for each sample was taken., The solvent (Zr) atoms were included in the cluster size calculation due to the amorphous nature of BMG. The cluster size was the sum of solute and solvent atoms in a cluster. Figure 9.4a shows the distribution of clusters across various size ranges for the three regions. Three datasets for each region were used to determine the diversity in size ranges among themselves and across different regions. Different maximum cluster size ranges were observed among samples of the same region. Figure 9.4b summarises the trend in average number densities with cluster sizes in all regions.

It is not unusual to observe variable cluster size ranges within a single region due to the amorphous nature of metallic glasses. This variation could arguably be linked to the specific nature of the field evaporation process (clustered evaporation) of the BMGs, which had likely caused some fluctuations across different datasets. Yet, was previously mentioned in section (1.1.1.1) that the origin of these high evaporation rate regions was presumably linked to the internal structure of the BMGs. So, any fluctuation in clusters by clustered evaporation could still be associated with the material's intrinsic property. Either way, it is important to take more than one sample to mark the range of cluster sizes inside a single region. Accordingly, the size difference among different regions was identified beyond the region's size fluctuation.

The possible presence of the clusters in a randomly labelled dataset is reported in Figure 9.5 for hard, soft, and fractured regions. The randomly labelled dataset was a random comparator of the actual experimental data, where the identities of the elements were randomised while keeping the concentration of each species constant (Section 4.4.5.4). A comparison between the observed and random datasets was initially made to emphasise the quantity of clusters beyond random distribution (Figure 9.5). While extracting the clusters, a larger than expected cluster was observed in all random labelled regions, comprising more than one million atoms. The number densities of the smaller size clusters were lower than in the experimental data. The clear difference between the experimental and random data validated the presence of solute-based clusters in the experimental data BMG (Figure 9.6).

Figure 9.6 reflects the number densities of the clusters in different regions above the randomly labelled dataset, i.e., “experimental minus random,” which actually shows the comparison between experimental datasets in Figure 9.4b and randomly labelled datasets in Figure 9.5. The number densities are grouped according to 20-atom cluster sizes. For small-sized solute-based clusters (<20 atoms), the number density is higher than random for all the regions, and their number densities are similar. For larger cluster sizes (>20 atoms), the difference in number density becomes more prominent.

Looking at the soft versus hard regions in Figure 9.6, for cluster sizes up to 160 atoms, the number densities of clusters in the soft regions are higher than in the hard region. Beyond cluster sizes of 160 atoms, although hard region-2 has few similar or higher number densities as soft regions, its size range (~200-220 atoms) differs from soft regions (~341-360 atoms). Although there are some noticeable discontinuities between cluster size 241 to 280 atoms for soft regions, it is evident that all the samples of soft regions have larger-sized clusters compared to hard regions.

When comparing the soft with the fractured region in Figure 9.6, a mixed trend for number densities is observed for cluster sizes above 21 atoms. The maximum cluster size range for the fractured regions (up to 727 atoms) broadens beyond the soft region's cluster sizes.

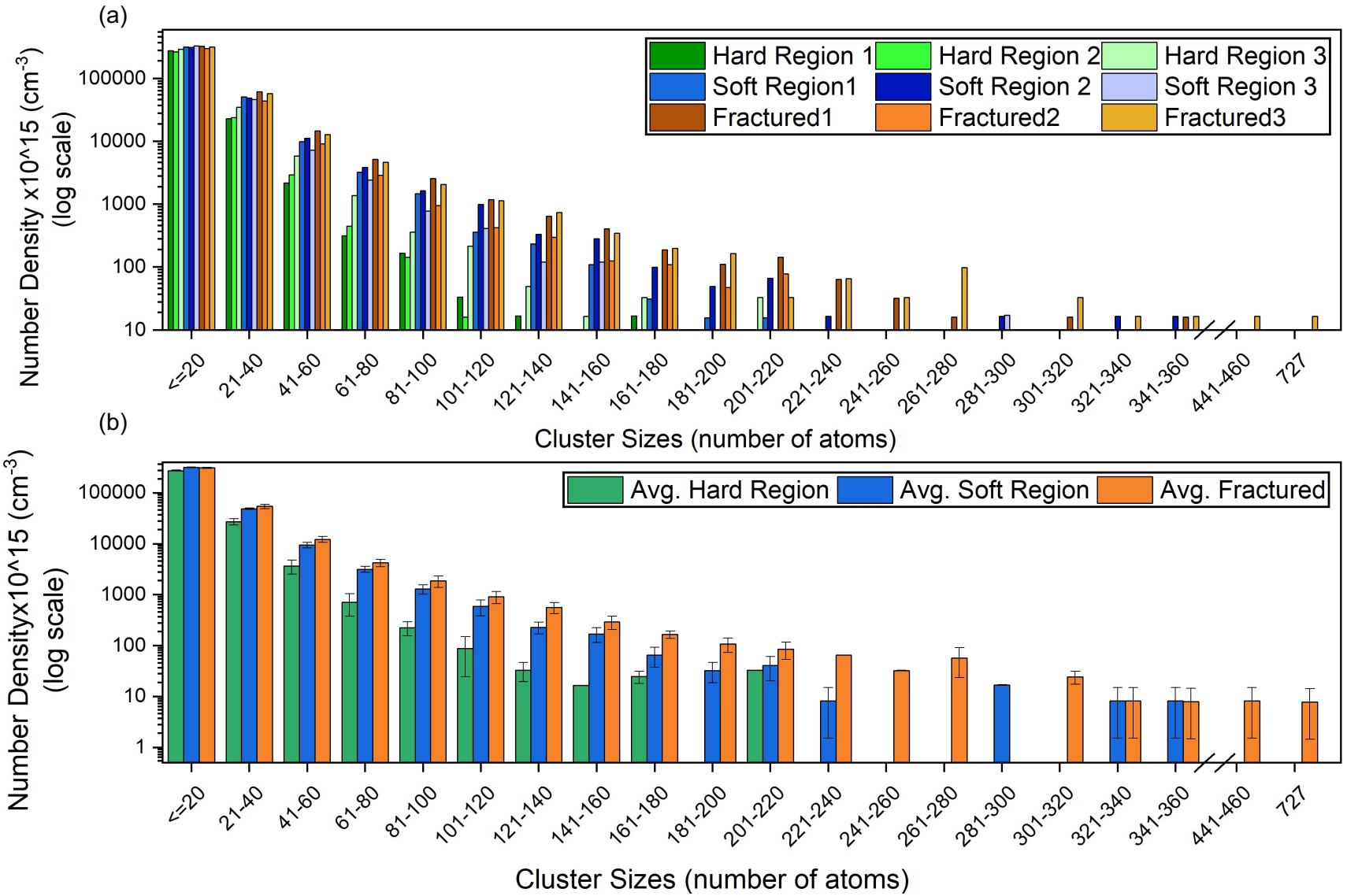

Figure 9.4: Experimental number density plots, (a) number densities of clusters in all samples, (b) average number densities of clusters in hard region, soft region and fractured region, versus cluster size (atoms) with their standard deviations.

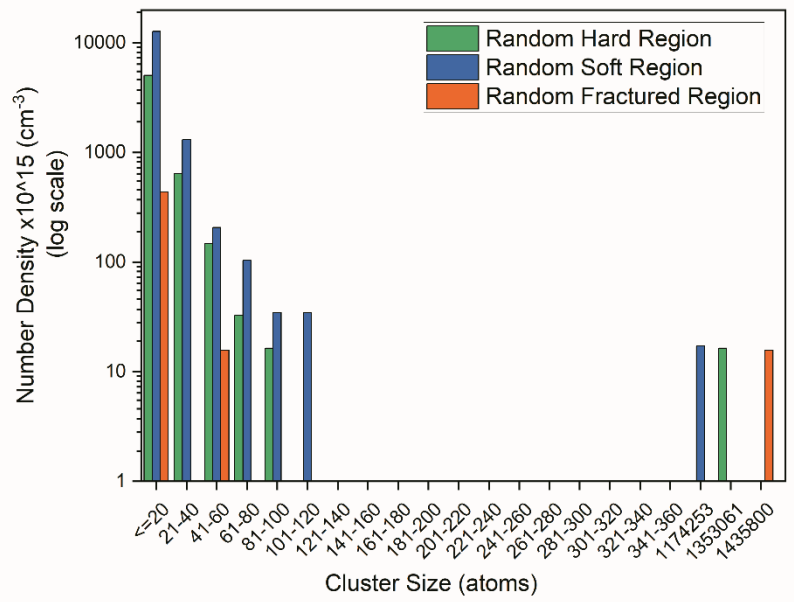

Figure 9.5: Random labelled number density plots for hard region, soft region and fractured region versus cluster size (atoms).

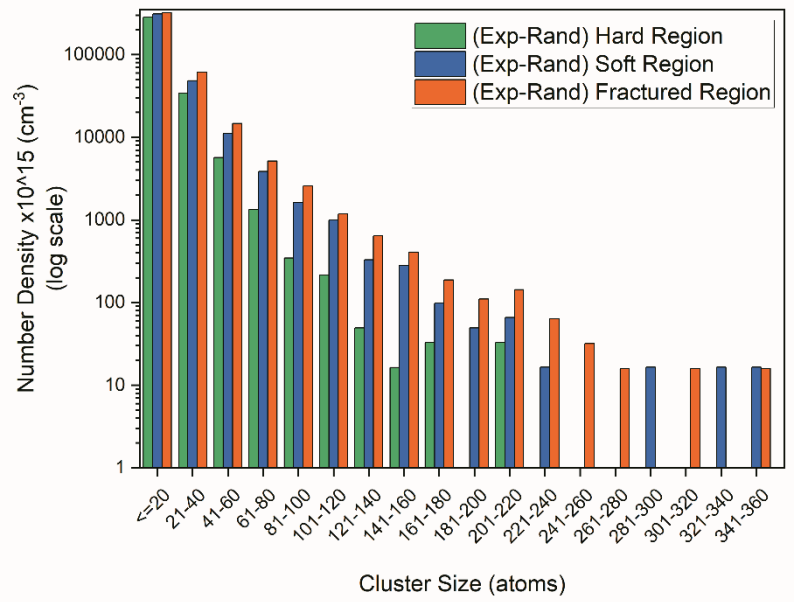

Figure 9.6: Experimental number density minus random number density plots for hard region, soft region and fractured region versus cluster size (atoms).

9.1.2.2 APT Cluster Size

The variation in cluster sizes for different regions are shown through the box plot in Figure 9.7. Apart from the deviations within samples of the same region, there was a clear difference in cluster size ranges of hard, soft, and fractured regions. The hardness of a fractured region is difficult to measure, yet it appeared as a softer region. The mean values of cluster size distribution showed an ascending order from hard, soft, to fractured regions.

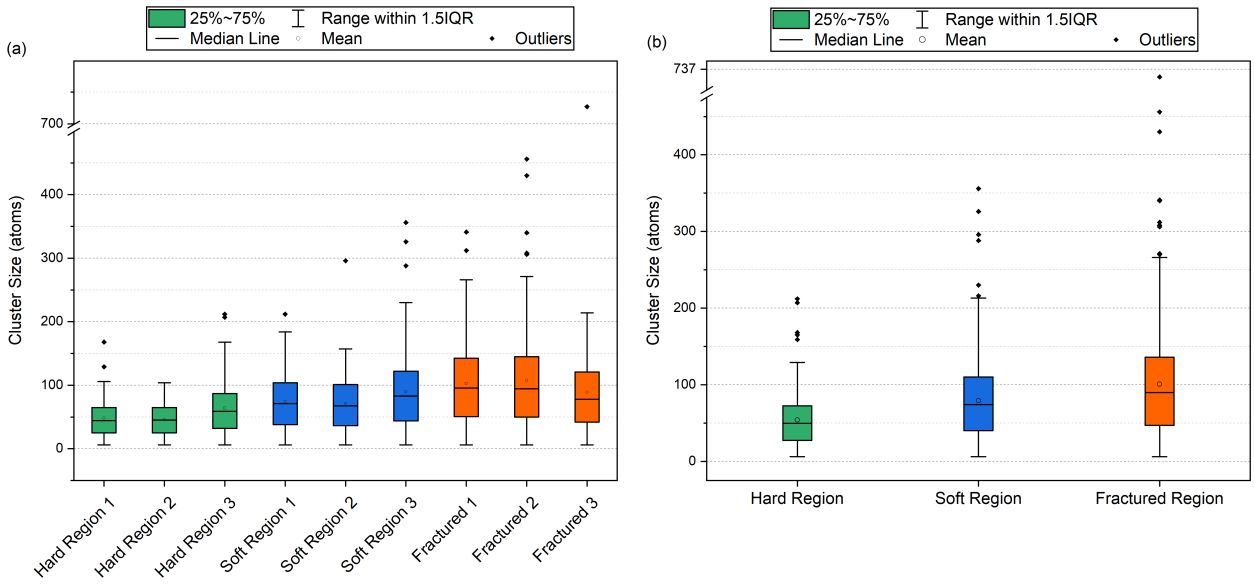

Figure 9.7: The box plot for cluster size (atoms) distribution for, (a) all samples, (b) combined plot for hard, soft and fractured regions.

9.1.3 Volume Fraction of APT Clusters

The volume fraction of the clusters in each region was computed by taking the aggregated volume of each cluster in a region to the total volume of its reconstruction. The volume of each cluster was calculated using equation (4.3). The data of average clusters volume in hard (0.295, 0.310, 0.34 nm^3), soft (0.358, 0.389, 0.399 nm^3), and fractured (0.38, 0.435, 0.44 nm^3) regions indicated ascending trend of the cluster sizes from hard to fractured regions. The results of the volume fractions are summarised in Figure 9.8 and Table 9.1, showing that the clusters occupy 9.7%, 14.5% and 15.3% of the volume of the total reconstruction in the hard, soft and fractured regions, respectively.

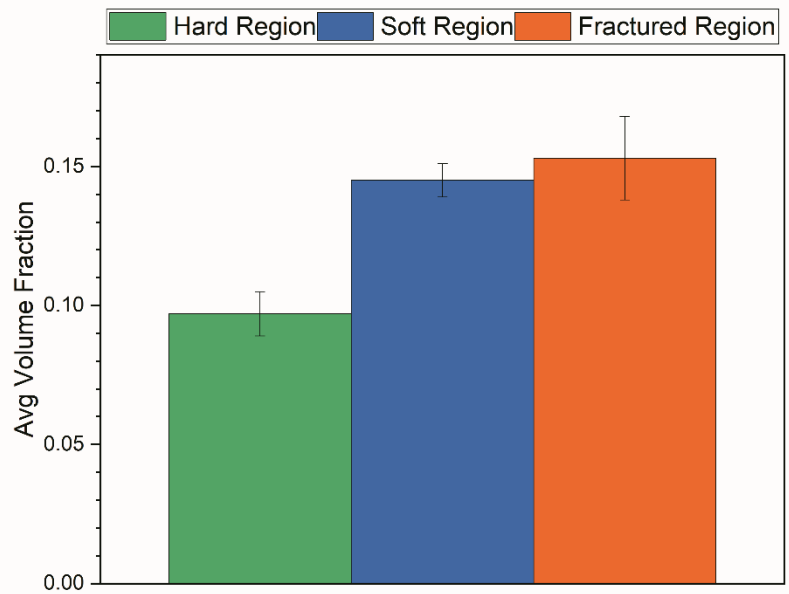

Figure 9.8: Volume fraction of solute-based clusters in hard, soft and fractured regions of HPT deformed Vitreloy-105 with their standard deviations.

Table 9.1: Volume fraction (CuNiAlTi) clusters in all the samples of hard, soft and fractured region of HPT deformed Vitreloy-105.

Region Solute-rich Clusters	Volume Fraction	Average Volume Fraction
Hard Region1	0.08821	0.097±0.008
Hard Region2	0.0899	
Hard Region3	0.0113	
Soft Region 1	0.1477	0.145±0.004
Soft Region 2	0.1383	
Soft Region 3	0.1505	
Fractured Region 1	0.1796	0.153±0.015
Fractured Region 2	0.1349	
Fractured Region 3	0.1714	

**The values are shown with standard deviations.*

The volume fraction of solute-based clusters in the fractured region was slightly higher yet similar to the soft region (considering the lower limit of its standard deviation) due to a smaller difference in their number densities and cluster size distributions. The APT clusters in the fractured region demonstrated a softening trend that will be analysed further in the discussion section.

9.1.4 Cluster Morphology

The cluster morphology maps were plotted using each cluster's aspect ratio and oblateness, based on the approach detailed in section 4.4.5.3. Each graph was divided into four quadrants: sphere, disc, rod and lath. Figure 9.9 displays the distribution of the cluster morphologies for all the regions. The purpose of these graphs was to observe any variations in the cluster morphologies among various regions and assess the shape of the major population of clusters in different regions. All three regions (hard, soft and fractured) depicted similar morphologies. The bigger sized clusters were spherical, as per Figure 9.9 for all the regions, whereas the majority of the small size clusters were disc-like. Since the APT reconstructions were not calibrated spatially due to absence of crystallographic features, these graphs cannot be used directly for the cluster size calculations. Nevertheless, in the comparison of hard, soft and fractured regions, most of the clusters had spherical or disc-like geometry.

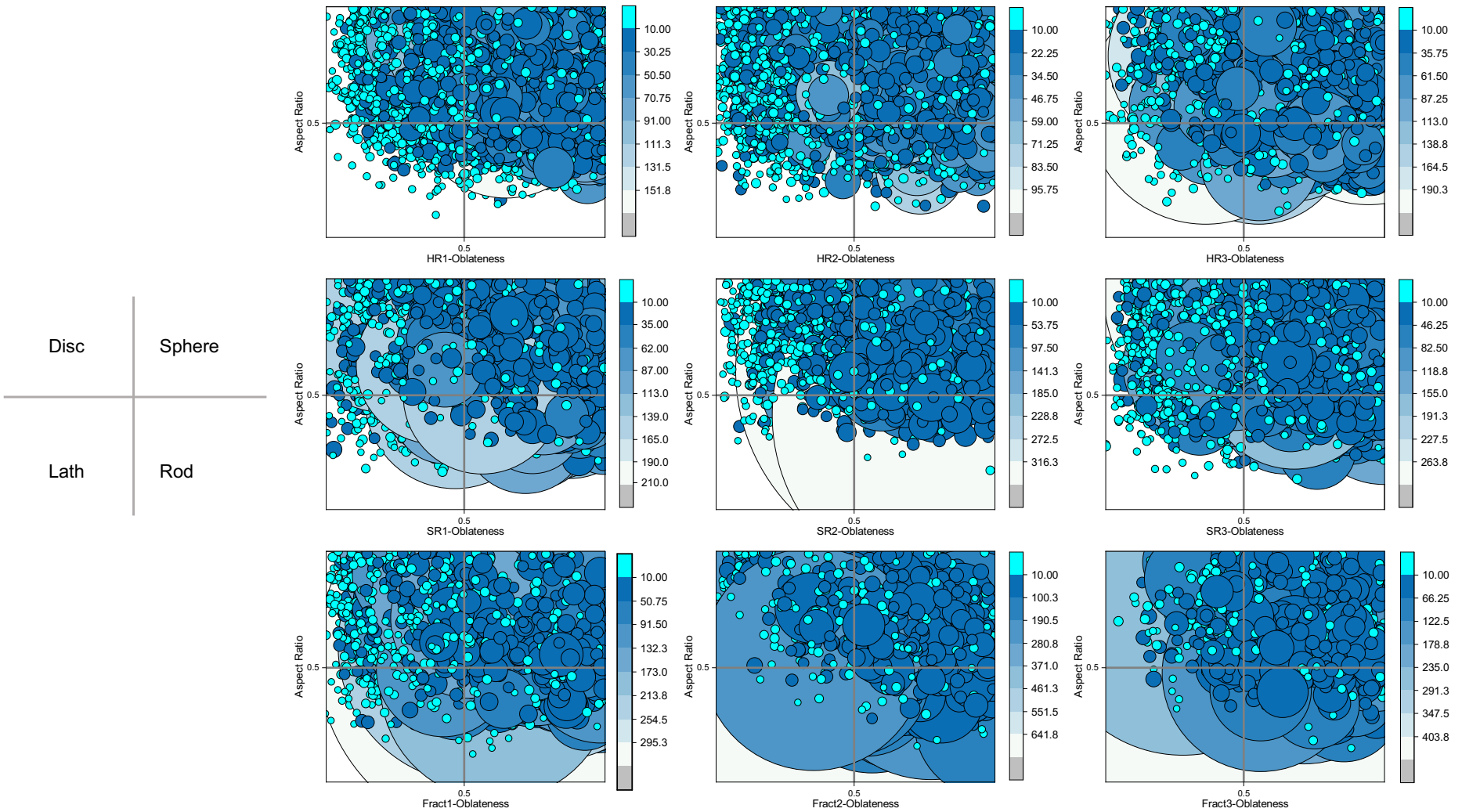

Figure 9.9: Morphology of solute-based clusters for all samples in hard regions (HR), soft regions (SR) and fractured regions (Fract). The four quadrants indicate the morphology types of the clusters; disc, sphere, lath or rod. The color of the bubbles indicates the size-range of the clusters whereas the number density of the clusters in a particular size-range is represented by the size of the bubbles.

9.1.5 Chemistry of APT Clusters

The average chemistry of solute-based clusters is demonstrated in this section. Before analysing their chemistry, it is important to look at the bulk composition of each sample for any fluctuations due to the evaporation and/or reconstruction process. Figure 9.10 summarises the average atomic concentration of each element in the bulk sample, clusters, and the matrix for all the regions. There was no significant difference in the bulk compositions of these regions; therefore, any fluctuation inside the cluster or matrix would be entirely due to the nature of the clusters. The average composition of APT clusters in every region was very similar and within the standard deviation values for each element. There were some differences in the compositions of Zr and Cu between the matrix of hard and fractured regions. A higher proportion of Zr was observed for the fractured region matrix, and Cu was slightly higher in the matrix of hard region.

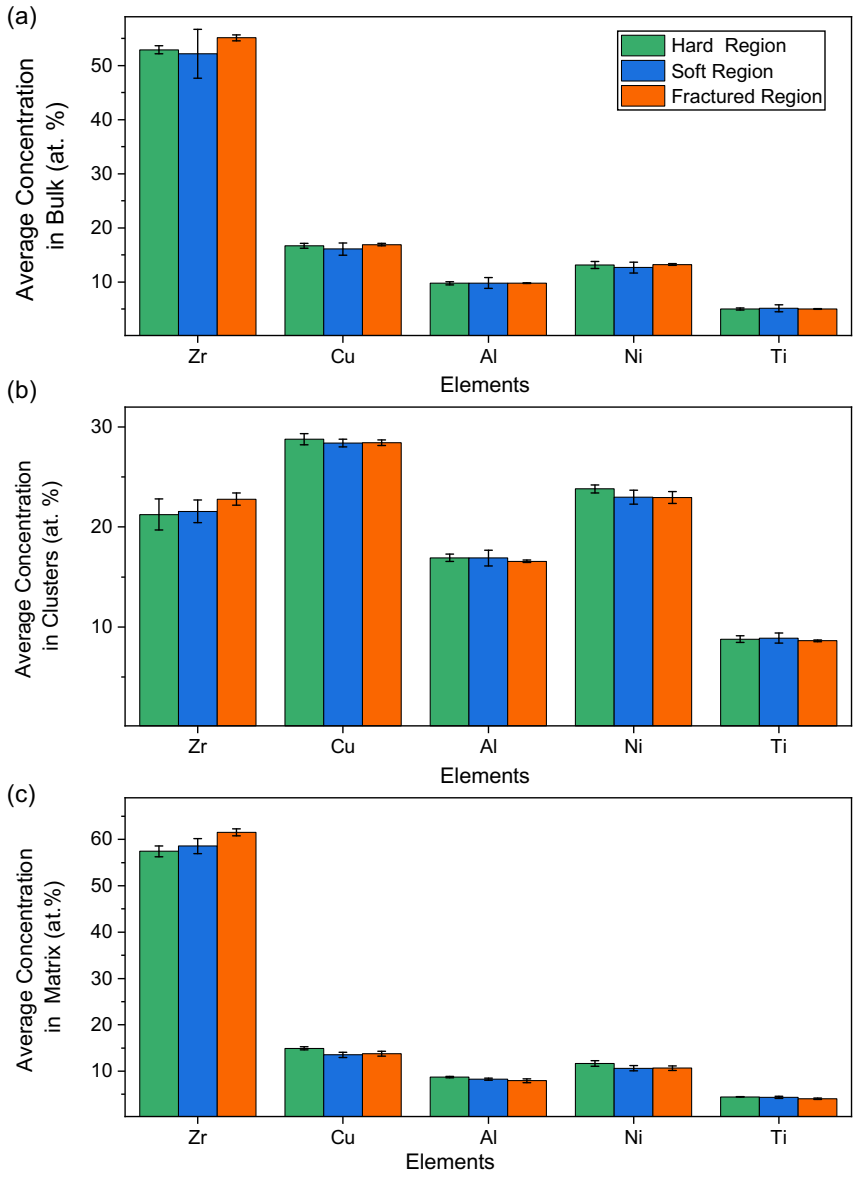

Figure 9.10: (a) Average bulk composition (at. %) of reconstruction, (b) average composition (at. %) of clusters, and (c) average composition (at. %) of matrix in hard, soft and fractured regions, with their standard deviations.

Although solute-based clusters exist inside the BMG, some proportion of solutes was observed inside the matrix. The percentage contribution of each element towards cluster formation is shown in Figure 9.11. About 21-22% of each solute contributed to the cluster formation in the hard region, which increased to about 30% in the soft region and about 33% in the fractured region. It is noteworthy that this increase seems to link directly with the number densities of clusters in various regions. Likewise, there was more Zr left in the matrix of the hard region compared to the other two regions as per Table 9.2.

The percentage of different elements residual in the matrix was obtained by:

$$\% \, i_{matrix} = 100 - \% \, i_{clusters} \tag{9.1}$$

$$\% \, i_{clusters} = \frac{Ni_{clusters}}{N_i} \times 100 \tag{9.2}$$

Where;

$i = Zr, Cu, Ni, Al, Ti$
N_i= total number of atoms of element 'i' (clusters + matrix).
$Ni_{clusters}$= total number of atoms of element 'i' in the clusters.

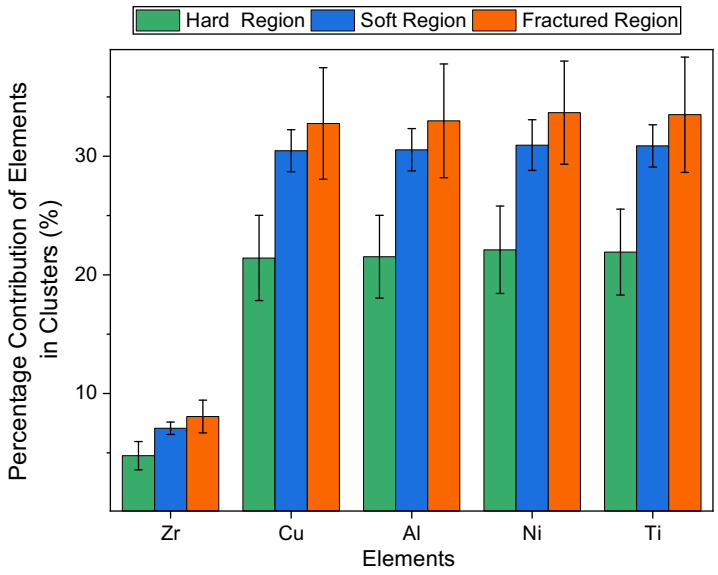

Figure 9.11: Percentage distribution (%) of each element in solute rich clusters with their standard deviations.

Table 9.2: Total % element distribution in the clusters of (Cu-Ni-Al-Ti) on average, and in the surrounding matrix for different regions of Vitreloy -105.

Region-Type \ Elements		Zr (%)	Cu (%)	Al (%)	Ni (%)	Ti (%)
Hard Region	Clusters	4.76±1.19	21.43±3.59	21.54±3.49	22.12±3.69	21.93±3.62
	Matrix	95.24±1.19	78.57±3.59	78.46±3.49	77.88±3.69	78.07±3.62
Soft Region	Clusters	7.08±0.53	30.48±1.77	30.55±1.78	30.95±2.13	30.88±1.78
	Matrix	92.92±0.53	69.52±1.77	69.45±1.78	69.05±2.13	69.12±1.78
Fractured Region	Clusters	8.07±1.37	32.77±4.7	32.99±4.8	33.69±4.34	33.51±4.86
	Matrix	91.93±1.37	67.23±4.7	67.01±4.8	66.31±4.34	66.49±4.86

**The composition values are shown with the standard deviation values.*

9.2 Discussion

This section discusses the evolution of the sub-atomic structural features relative to the different regions of $Zr_{52.5}Cu_{17.9}Ni_{14.6}Al_{10}Ti_5$ BMG, based on the above results.

9.2.1 APT Clusters and Local Hardness

The extent of solute-based clusters increased with the local hardness decrease. It was observed that if the identities of all the elements were randomised (random labelled), the integrity of the cluster analysis could not be assumed (Figure 9.5). After confirming the significance of the APT clusters, further analysis was performed. An inverse relation was observed between the solute-based clusters and local hardness regions. This was evidenced by four features of the cluster size distributions. Firstly, the number densities of the solute-based clusters were relatively smaller in the samples of the hard region as compared to the samples of the soft region (Figure 9.4). Secondly, the cluster size range was limited to 220 atoms in the hard region, whereas it extended to about 360 atoms in the soft region (Figure 9.7). Thirdly, the volume fraction of clusters in the hard (0.097 ± 0.008) was comparatively smaller than in the soft regions (0.145 ± 0.004), as per Figure 9.8. Lastly, it was not unusual that there was a clear difference in the volume occupied by clusters in the hard region compared to the soft region, which is obvious since the number densities of the clusters in the soft region were larger for all cluster sizes and therefore contained a bigger volume in the reconstruction.

The APT results of $Zr_{52.5}Cu_{17.9}Ni_{14.6}Al_{10}Ti_5$ BMG (Chapter 9) were aligned with $Zr_{63.49}Cu_{13.59}Ni_{10.32}Al_{11.29}Nb_{1.28}$ BMG's (Chapter 8), despite the dissimilarities between their compositions and deformation treatments, indicating a global tendency despite processing history. The solute-based clusters were proportional to the local softness of the Zr-based BMGs.

9.2.2 APT Clusters and Plasticity

Most of the BMG literature is based on the structural evolution relative to their macroscopic mechanical or thermodynamic properties rather than the localised microstructure-property relationships which is the subject of this thesis. This makes it difficult to compare the findings of the present study with the literature.

Since the local softness of a region is proportional to the extent of solute-rich clusters in that region, the enhanced regional plasticity can be studied through these clusters. The APT cluster results provided a remarkable outcome by making a direct link between regional softening and structural or chemical heterogeneities. The regional softening was only predicted by structural dynamics, in the previous studies.

The plastic flow in uncontrolled deformation was understood by observing the structural evolution in the fractured region. This was accomplished by considering the fractured region of Vireloy-105 in the cluster analysis. The main difference between the hard and soft regions and the fractured region was that the rough fractured surface could not be associated with local hardness because it had endured intense plastic deformation until fracture. The uncontrolled deformation caused severe microstructural changes, visible as multiple shear bands. The local hardness of this region can only be perceived through its correlation with the solute-rich clusters, based on our earlier understanding of hard and soft regions. If the cluster properties of size, number density, and volume fraction in the fractured region decreased compared to the hard and soft regions, the fractured region would have characteristics of a harder region and vice versa.

The behaviour of the fractured region was described based on the following results.

- The number density plots revealed more clusters in the soft and fractured regions for each cluster size range than in the hard region. The cluster size range was stretched for them like soft regions, indicating similar trend.

- The fractured region had the broadest range of cluster sizes inside its structure (~737 atoms), as per Figure 9.7. Its average cluster size was larger than both the hard and soft regions.

- The volume fraction of the clusters in the fractured region was slightly higher than in the soft region (~0.008). However, the experimental error for the soft and fractured regions overlapped, indicating similarity between soft and fractured regions in terms of their volume fraction (Figure 9.8).

Based on the above observations on the cluster distributions, it was concluded that the fractured region exhibited softening characteristics (section 2.6).

The shear band formation occurs from the percolation of the STZs. Earlier studies reported that the average size of the STZs was ~0.48 nm^3 (Section 2.6). The average volume of solute-based clusters in the present study for hard (0.32 ± 0.01 nm^3), soft (0.38 ±0.01 nm^3), and fractured (0.42 ± 0.02 nm^3) regions (section 9.1.3) suggested a qualitative correlation between STZs and the clusters of the present study. A ductile BMG exhibits reduced strength and hardness than brittle BMGs, demonstrating increased plasticity and softening characteristics. As mentioned earlier, the extent of the solute-based clusters was proportional to softening. The APT analysis in the hard, soft, and fractured regions could help improve understanding of the microstructural changes under deformation due to additional chemical and structural information.

9.2.3 Morphology and Chemistry of APT Clusters

It was observed that all three regions had similar morphologies, spanning mostly around spherical and disc-like structures, as per Figure 9.9. No significant difference among the cluster morphologies was observed in different regions. This implied that only the extent of these clusters varies with local hardness variations, not their shape.

The average compositions of the cluster, residual matrix, and the bulk were studied to discuss the similarities/differences among hard, soft, and fractured regions. The bulk APT compositions of all three regions were similar. Thus, any difference between the average composition of the clusters and the matrix would be based on the local atomic arrangement of that particular region. The composition analysis showed a significant difference between the average composition of the solute-based clusters and the residual matrix of each region (Figure 9.10). The clusters were found to be enriched with solute elements (Cu, Al, Ni, Ti), and about 75% of their composition is based on solutes. Zr (solvent), on the other hand, is enriched in the matrix region and is depleted in the clusters. However, a large portion of the matrix (> 35%) was still comprised of solute elements.

The atomic concentrations of all the elements in the clusters of different regions were within the standard deviations of each other. The cluster compositions of all the regions were quite similar. On the other hand, the composition of Zr was significantly higher in the fractured region than the hard region (> 2 at. %), yet the concentrations of other elements were similar. The higher Zr concentration can be attributed to the increased softening in the matrix of the fractured region [225]. This is quite likely due to severe uncontrolled deformation undergone by this region. Overall, the average compositions of clusters of all three regions and compositions of the matrix in hard and soft regions were similar.

The cluster analysis algorithm scans for regions with enriched solute elements (Cu, Ni, Al, Ti). Although these clusters had a diverse size range, a particular size of any cluster suggested that the immediate surroundings would be solute-lean, at least up to a certain distance, 'd_{max}' (Section 4.4.5.1). It implied that the clusters' immediate vicinity comprised all Zr atoms, free-volume, or both with the size equivalent to 'd_{max}'. The close surrounding of the solute-based clusters was presumably dilute of solutes.

9.2.4 Proposed Symmetry of APT Clusters

The behaviour and symmetry of these clusters was studied. It is difficult to determine the local ordering of these clusters through APT due to adverse effects on the spatial resolution by clustered evaporation. However, it was perceived through the literature. Zr-based BMGs with ~2-3.7 (at. %) of Ti reported to contributed in stabilising the icosahedral order (section 2.8). In the present study, about 20-33% of the Ti contributed to the solute-based clusters, whereas the remaining Ti resided within the matrix (Figure 9.11). This means that ~3.95-3.35 at. % of Ti was inside the matrix, from hard to fractured region, respectively. This concentration was similar to what was required for the icosahedral ordering in the Zr-based BMGs, as per literature. This speculates that the matrix may primarily have icosahedral ordering, suggesting crystal-like or non-icosahedral ordering for the clusters.

A published simulation study of Vitreloy-105 reported about 15.5% of fcc/hcp-like bonding [300], that resembled the volume fraction of the clusters in the present work (Figure 9.8). Approximately 7% crystal-like ordering and 18% mixed-ordering was observed in the computational simulation results of this thesis (Chapter 5), indicating crystal-like ordering in these clusters with some mixed ordering.

The possibility of icosahedral symmetry for the solute-based clusters was considered. In icosahedral symmetry, fewer inter cluster solute sites would be expected [87]. For instance, a 13 cluster icosahedron will have 20 cluster tetrahedral sites and no octahedral cluster site. The distribution would result in fewer solute-solute interactions than the one predicted in Miracle's ECP model or sometimes observed in multi-element BMGs. The octahedral sites are primary sites for β-solutes (Ni, Cu). A much higher solute-solute interaction was detected in the solute-based clusters (Figure 9.10b), reducing the resemblance between icosahedral ordering and the cluster symmetry of the present case. Thus, the matrix may likely have icosahedral ordering due to lesser solutes concentration, as demonstrated in Figure 9.10c but not the APT clusters.

Furthermore, the ordering in solute-rich clusters was assumed via information on the enthalpy of mixing of elements. The elements with positive enthalpy of mixing tend to avoid each other and may cause phase separation in metallic glasses (section 2.8). However, it was documented that the materials with positive mixing enthalpy are sometimes responsible for crystal-like ordering [301]. It is suggested that either a phase separation would occur or the elements with positive enthalpy of mixing will contribute to local ordering (micro-alloyed). No phase separation was observed in the present study regarding Ni and Cu (3.6 $kJmol^{-1}$), indicating the possibility of the local ordering in the clusters.

In a study, the regions enriched with Ni-Cu pair demonstrated different orders compared to the amorphous matrix, which mainly had icosahedral ordering [227]. Mutual presence of Ni and Cu was detected in about 90% of the solute-based clusters in the present study, enforcing the possibility of non-icosahedral or crystal-like ordering in the APT clusters (Figure 9.8). The face-centred cubic (fcc)-like clusters have higher symmetry and denser packing and are softer than icosahedral clusters [131]. The primary criterion of cluster identification in the APT cluster analysis suggested that the solute-based clusters must have denser packing. Additionally, the increasing order observed with the increase in softening of the region is reflective of their higher symmetry and softer nature, just like what was reportedly observed for fcc-like clusters. The collective information suggested that the solute-based clusters may have crystal-like ordering.

9.3 Summary

Cluster analysis was utilised to investigate the densely packed solute-based clusters in Vitreloy-105. The local hardness was successfully linked with structure using the cluster size, number density, and volume fraction. Additionally, the evolution of these clusters in the fractured region was analysed, which suggesting a softened region. Similar morphologies of the clusters were observed in the hard, soft, and fractured regions. It was discovered that the average composition of these clusters was also similar in different regions. These clusters were presumed to have crystal-like ordering and were found to facilitate softening.

10 CORRELATIVE INVESTIGATIONS (APT/TEM)

Correlative study is a common practice for obtaining an advanced perspective about microstructure-property relationship in materials by the combination of advanced microscopy, spectroscopy, or computational techniques. The strength of one manages the limitation of the other. In the same context, The APT results were cross-linked with the TEM results for the Zr-based BMGs. Accurate size and volume fraction measurements are primary strengths of TEM, whereas atomic-scale chemical information is the forte of APT. The strengths and limitations of both techniques are summarised in Table 10.1. TEM experiments and analyses were performed by a post-doc researcher, Dr. Keita Nomoto, from The University of Sydney and its sample preparation method is described in Chapter 4 of this thesis (Section 4.2.2). Whereas a complete correlative analysis between the APT and the TEM data was conducted by the author. The TEM results presented in this chapters have been published already [245].

Table 10.1: Summary table for the capabilities of TEM and APT.

#	Specifications	TEM	APT	Comments
1.	Size, Spacing	✓	X	TEM is good for acquiring accurate sizes (nm) and spacings, but atoms are floating in space with APT, so sizes in number of atoms are available
2.	Number Density (N_v)	X	✓	Volume density through TEM is possible based on calculations only. However, APT can directly provide number densities of clusters based on the volume of the dataset.
3.	Composition	X	✓	APT is particularly sensitive towards compositional analysis, especially involving elements with similar atomic numbers.
4.	Ordering/Symmetry	✓	X	Identification of MRO structure. But not very sensitive to the exact structure. Symmetries can be detected using an electron diffraction pattern.

In this chapter, the volume fraction results through APT and TEM were cross-linked. The SRO and MRO clusters were compared from both studies. At the end of the chapter, MRO clusters were presented in different hardness regions of Zr-based BMGs, using a TEM model. Their chemical surroundings were demonstrated by 3D APT reconstruction.

10.1 Volume Fraction via Correlative APT/TEM Study

The volume fractions of the clusters in variable hardness regions of TC-$Zr_{63.49}Cu_{13.59}Ni_{10.32}Al_{11.29}Nb_{1.28}$ (at. %) and HPT-$Zr_{52.5}Cu_{17.9}Ni_{14.6}Al_{10}Ti_5$ BMGs were plotted, as shown in Figure 10.1. The volume fraction of APT-solute-rich clusters increased from hard to soft regions in both the compositions of Zr-based BMGs. Similar trend was observed for TEM's clusters.

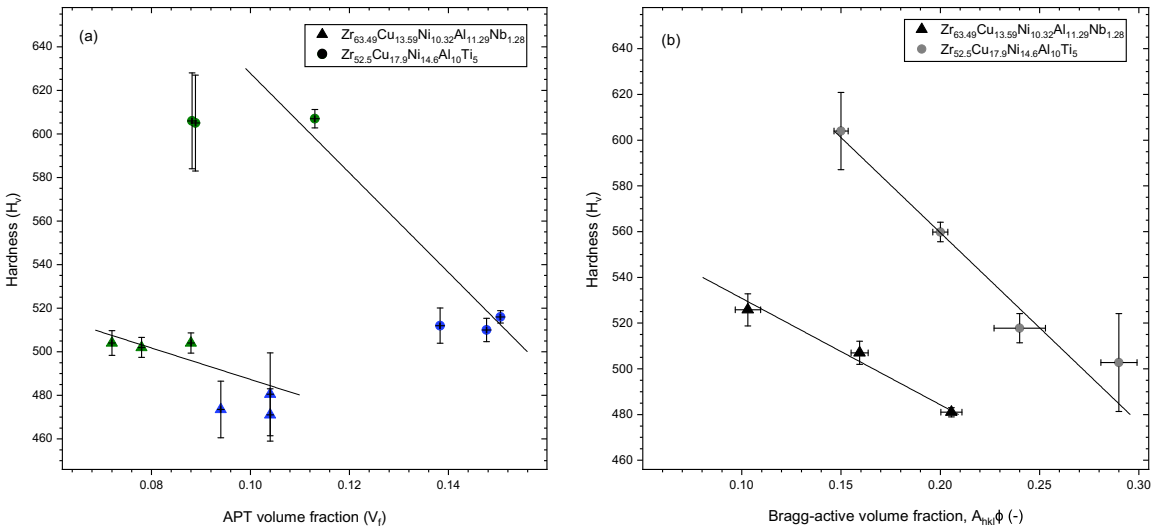

Figure 10.1: Volume fraction analysis of (a) APT solute-rich clusters and (b) MRO clusters via TEM, in different regions of TC-$Zr_{63.49}Cu_{13.59}Ni_{10.32}Al_{11.29}Nb_{1.28}$ and HPT-$Zr_{52.5}Cu_{17.9}Ni_{14.6}Al_{10}Ti_5$ BMGs against local hardness values. The hard and soft regions for the APT samples are indicated in green and blue colours respectively.

10.2 SRO clusters via Correlative APT/TEM Study

The TEM-SRO clusters were analysed through the pair distribution functions (PDFs). The nearest neighbour (NN) distances were calculated up to 4th NN by taking the average distances between the atoms inside the BMG. These measurements were considered without any discrimination between solute and solvent atoms. Not much difference was observed in the TEM-NNs for both compositions (Figure 10.1 and Figure 10.2).

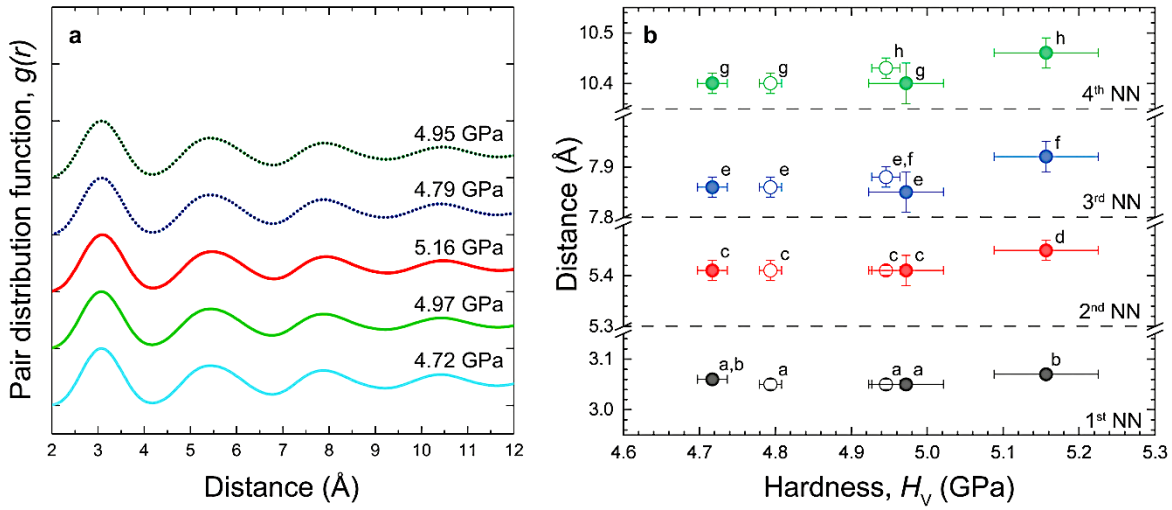

Figure 10.2: TEM-SRO analysis of $Zr_{63.49}Cu_{13.59}Ni_{10.32}Al_{11.29}Nb_{1.28}$ BMG. (a) PDFs of as-cast (solid lines) and TC (dotted lines) samples, (b) average values of the 1st- 4th nearest neighbor (NN) distances of as-cast (full symbol) and TC (open symbols) from 14 PDFs [245].

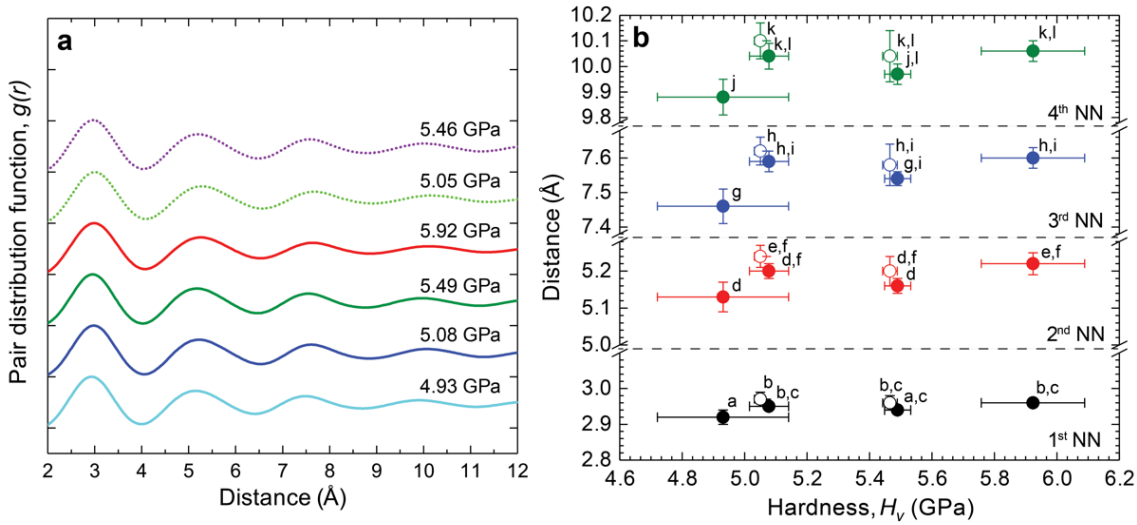

Figure 10.3: TEM-SRO analysis of $Zr_{52.5}Cu_{17.9}Ni_{14.6}Al_{10}Ti_5$ BMG. (a) PDFs of as-cast (solid lines) and TC (dotted lines) samples, (b) average values of the 1st- 4th NN distances of as-cast (full symbol) and TC (open symbols) from 14 PDFs. (supplementary material [245]).

In APT analysis, the number of atoms inside a cluster determined its size. However, comparison between TEM and APT clusters cannot be made unless APT clusters sizes are converted into a linear dimension i.e., nm. Therefore, the clusters' diameters were calculated from their volume measurements, assuming them as spheres by the following relation:

$$V = {}^{4}/_{3}\,\pi\left(\frac{d}{2}\right)^{3} \tag{10.1}$$

$$d = \left(\frac{6V}{\pi}\right)^{1/3} \tag{10.2}$$

The smallest cluster in APT comprised 6 atoms, and the respective cluster size was about 0.62 nm. An average distance from the atoms in the first coordination shell to its central atom is usually referred to as SRO, yet there are many different definitions to this term [302-304]. In the current work, the clusters with size less than 1nm (< 20 atoms) were considered SRO clusters. Therefore, clusters below 20 atoms were considered for the SRO analysis. It was earlier observed that the trend in number densities of the solute-rich clusters with less than 20 atoms was unclear (Section 8.1.2.1,Section 9.1.2.1). The difference between the hard and soft regions was prominent for cluster sizes above 20 atoms.

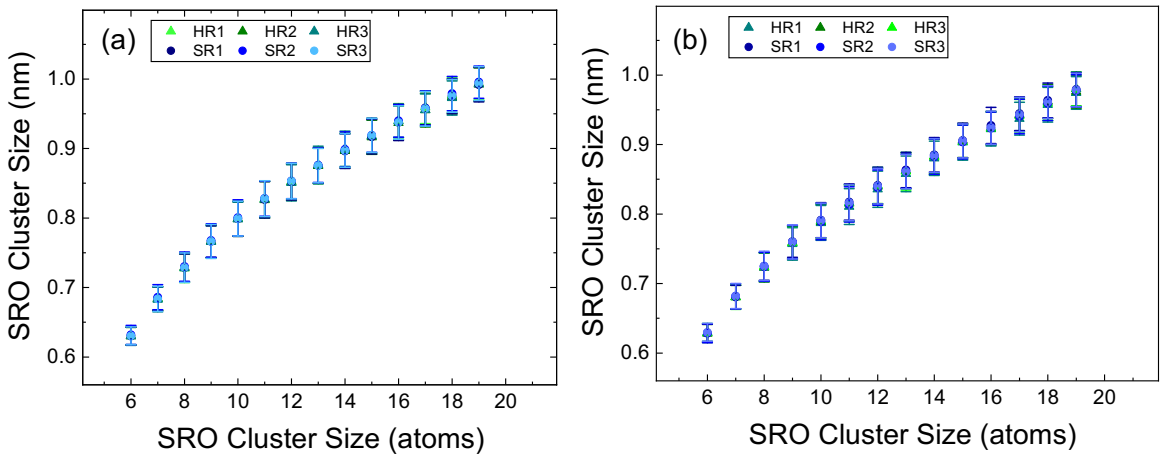

Figure 10.4: APT-SRO analysis of solute-rich clusters in difference local hardness regions of (a) TC-$Zr_{63.49}Cu_{13.59}Ni_{10.32}Al_{11.29}Nb_{1.28}$ and (b) HPT-$Zr_{52.5}Cu_{17.9}Ni_{14.6}Al_{10}Ti_5$ BMGs. The clusters below 1nm diameter clusters are considered in the SRO analysis.

SRO cluster sizes in both hard and soft region samples were overlapping each other, in both BMG compositions (Figure 10.4a, b).

10.3 MRO clusters via Correlative APT/TEM Study

The clusters with sizes > 1 nm were considered for the MRO analysis, in this study. The APT cluster sizes were taken as the average of cluster size range above 1nm. NBED method was used for acquiring TEM-MRO clusters. MRO clusters from APT and TEM were plotted against their respective hardness regions, as shown in Figure 10.5a and Figure 10.5b, respectively.

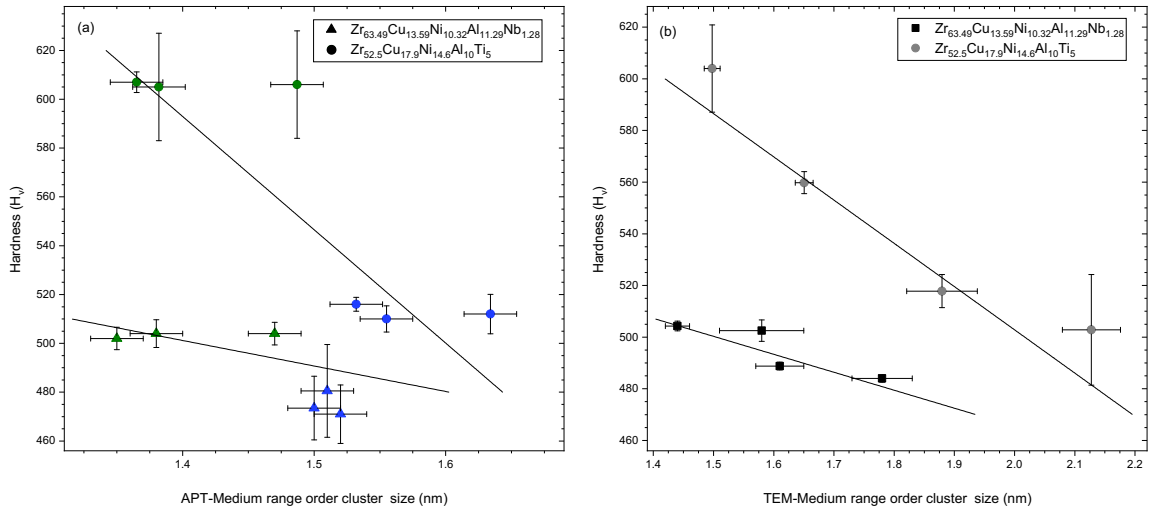

Figure 10.5: MRO analysis of (a) APT solute-rich clusters > 1nm diameter, and (b) MRO clusters via TEM, in different regions of TC-$Zr_{63.49}Cu_{13.59}Ni_{10.32}Al_{11.29}Nb_{1.28}$ and HPT-$Zr_{52.5}Cu_{17.9}Ni_{14.6}Al_{10}Ti_5$ BMGs against local hardness values. The hard and soft regions for the APT samples are represented in green and blue colours respectively.

A qualitative comparison was observed between MRO clusters from both techniques. The APT-MRO cluster size increased from hard to the soft regions regardless of the sample composition. A similar trend with hardness variations was observed for the TEM-MRO clusters.

10.4 Schematic Representation of Structural Heterogeneities in BMGs

TEM studies were utilised to perceive the behaviour of MRO clusters under shear deformation that were proposed as STZ nuclei [245]. The structural perturbations around these clusters were demonstrated by the colour gradient in Figure 10.6b which were applied based on the molecular dynamics simulation of binary metallic glass deformation [305]. From the model, it appeared that the shear stress from these clusters propagated to the surrounding less ordered matrix while rearranging the clusters under shear deformation. As shown in Figure 10.1b and Figure 10.5b, a more significant number of clusters with relatively larger sizes existed in soft regions than hard regions. Larger clusters would transform to larger STZs (Figure 10.6c) which will eventually act as shear band nucleus, as shown in Figure 10.6d. Their distribution in various regions was assessed based on their regional volume fractions.

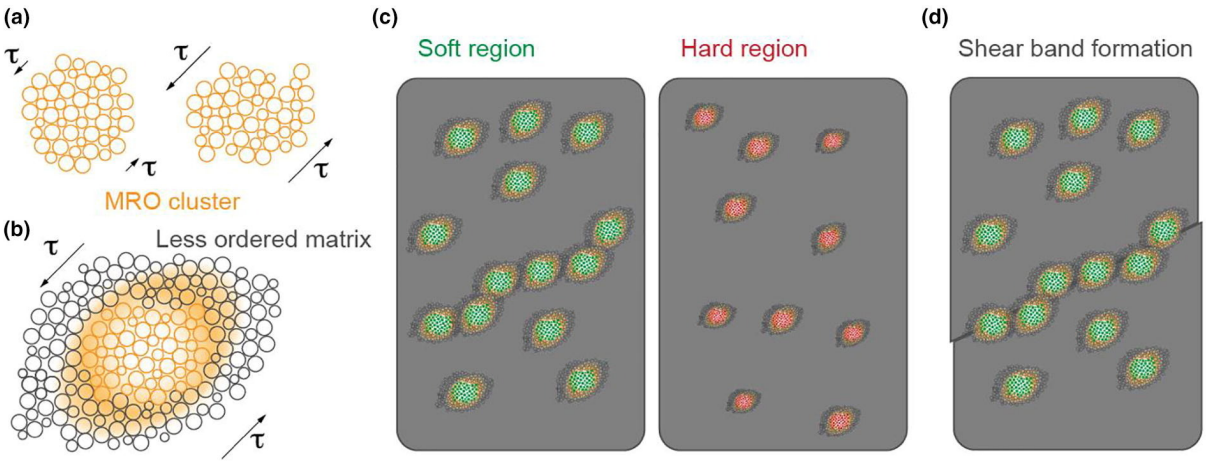

Figure 10.6: Schematic description of the role of MRO clusters in BMG deformation. (a) fcc-like MRO clusters acting as STZ nucleus, (b) structural perturbations transfer from the clusters to the less ordered matrix, (c) MRO clusters and their relatively easier percolation in the soft regions with larger and more number of clusters, (d) MRO clusters as shear bands nucleus by mutual linkage [245].

The chemical information of these clusters and their surrounding matrix were represented via 3D cube from the actual BMG data using APT, as shown in Figure 10.7. A small cubic region from the centre of the reconstruction was extracted to separately demonstrate the clustered (Figure 10.7a) and the matrix region (Figure 10.7c). It portrayed the distribution of different elements within clusters and the matrix of a Zr-based BMG. The 3D rotation of below ROI helped look for the free spaces around clusters.

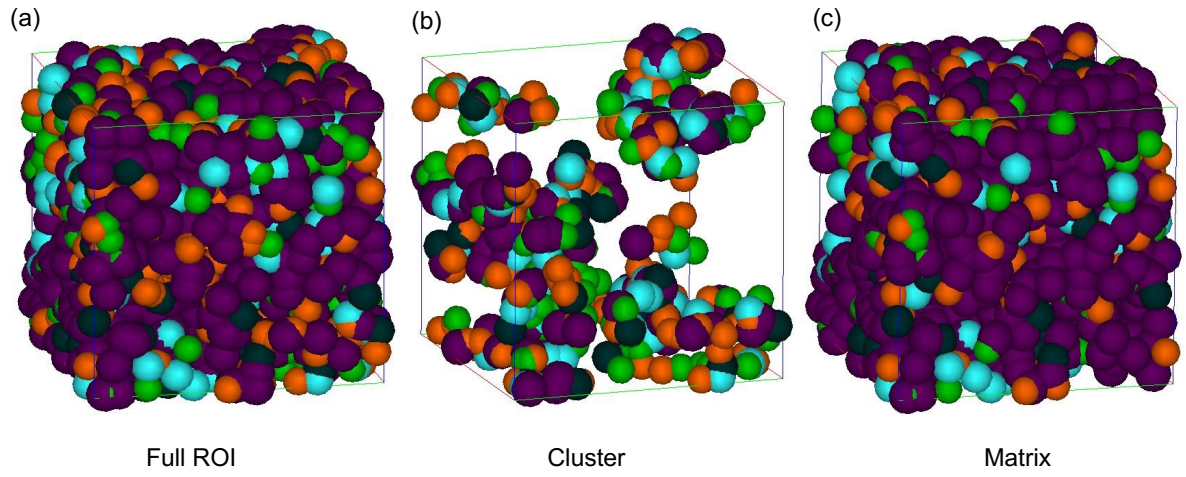

Figure 10.7: 3D APT reconstruction illustrating the distribution of elements in (a) the original region of interest (ROI) from the centre of the reconstruction, showing both clusters, matrix and free volume as white space, (b) the APT clusters and (c) the matrix. Zr (purple), Cu (orange), Ni (green), Al (cyan), Ti (dark green).

10.5 Discussion

Correlative APT/TEM is an increasingly popular approach for investigating fundamental characteristics of the materials from different techniques at once. It is highly unlikely to extract complete structural information from a single microscopy technique due to technical limitations, especially for complex structured materials such as BMGs. The correlation between the TEM and the APT studies was understood from the following points.

- The volume fraction of the APT clusters increased from hard to soft regions for both compositions of the Zr-based BMGs (Figure 8.7,Figure *9.8*). Correlative TEM/APT analysis confirmed a similar trend in both techniques (Figure 10.1). It should be noted that these values cannot be quantitatively compared because of the different assumptions applied while calculating the volume fractions in both techniques. Indirect calculations were applied for the volume fraction analysis of the MRO clusters in the TEM study [245], and the actual volume fraction of these clusters may likely be different. On the other hand, the chemical information of the clusters from the APT study was used for calculating their volume fraction. APT analysis relatively reported the actual volume fraction of these clusters inside the BMGs.

- No significant difference in the APT-SRO clusters (< 20 atoms) was found with local hardness variations (Figure 10.4). A similar observation was reported for SRO clusters, calculated from the TEM data (Figure 10.3). The results from both techniques confirm that local hardness variations were not linked to SRO clusters.

- On the other hand, APT-MRO cluster sizes (> 20 atoms) were increasing from the hard to the soft regions regardless of the sample composition (Figure 10.5a). Similarly, an inverse relationship was observed between the regional hardness and the TEM-MRO clusters (Figure 10.5b). This indicated similar trend for APT- and TEM-MRO clusters.

- It should be noted that it was a qualitative comparison between the TEM- and APT-clusters, in both SRO and MRO length scales. A quantitative comparison is not feasible due to different calculation methods applied for cluster size calculations in both techniques. However, similar trends in TEM/APT results suggested that TEM-clusters and APT-clusters are alternate names of same perturbations in the BMGs' structure.

- It was speculated that relatively higher number densities and larger cluster sizes will be observed in the soft regions, in the TEM model (Figure 10.6c). This speculation was experimentally confirmed by the number density results from APT analysis (Sections 8.2 and 9.2). Additionally, the 3D-APT reconstruction effectively demonstrated the distribution of elements within the APT-clusters and their surrounding matrix in a BMG, as shown in Figure 10.7. The presence of free volume was occasionally noticed at the junction of the APT-clusters (solute-rich clusters) and the surrounding matrix (Figure 10.7). However, it should be noted that the free volume cannot be easily determined through a 3D-APT reconstruction due its limited detector efficiency (57%) and further studies are required for free volume analysis.

- The structure of the TEM-MRO clusters was thoroughly analysed in the TEM study. The in-situ heating of the BMG and corresponding SAED patterns of the resulting metastable nanocrystals suggested face centred cubic (fcc) nanocrystals [245]. The emergence of these metastable nanocrystals from the MRO clusters recommended fcc crystal-like ordering for these clusters. NBED symmetry analysis suggested that fcc-like MRO clusters were spatially distributed in a less-ordered matrix [245].This conjecture complimented our initial speculation about the fcc crystal-like symmetry of APT clusters in the previous chapters (Section 8.2 and Section 9.2). However, further work is required to validate such an assumption.

A comparison between TEM and APT results was used for validating APT results. It was confirmed that the MRO clusters are responsible for softening characteristics inside the Zr-based BMGs. The addition of APT facilitated the characterisation of BMG by providing chemical information, number densities and volume fractions of these clusters. The researchers believed that the combination of the small-scale heterogeneities causes local softening, resulting shear bands [8, 105, 231, 245, 306]. In this way, the knowledge about actual volume fractions and chemistry of these MRO clusters has moved us one step closer to understanding the deformation mechanism and its mathematical formulation.

10.6 Summary

The combination of TEM and APT was successfully employed to relate the structural and compositional features of nanoscale domains (clusters) with the material's local hardness variations. It is the first time that the distribution of elements inside the clusters and their surroundings are presented experimentally. The MRO clusters explored in this study can be utilised in understanding the plasticity of BMGs due to their proportionality with the material's local softening.

11 CONCLUSIONS AND FUTURE WORKS

BMGs are promising engineering materials, and this research was initiated with the intent to examine their atomic structure using complementary analytical methods. The central theme running through the text was to emphasise the importance of APT in resolving the chemical and structural information of the atomic/nanoscale structural heterogeneities inside the Zr-based BMGs. The research's key findings are concluded in this chapter. Some suggestions about future work also follow. Referred to as solute-rich/solute-based or APT clusters, throughout this thesis, they were characterised using a sophisticated data mining approach on the APT data. These clusters were quantitatively assessed based on their size, number density, relative volume fraction and their chemistry.

11.1 Concluding Remarks

The key findings in the light of aims of this study are as follow.

Aim #1: To assess the nature of structural and chemical heterogeneities in Zr-based BMG through computational simulation.

Conclusion 1: AIMD was successfully applied for the investigation of structural and chemical heterogeneities in a Zr-based BMG.

The atomic structure of a Zr-based BMG was pre-assessed using an AIMD simulation. The simulation generated a wide variety of VPs, representing a diverse range of nanoscale motifs or cluster type structures in this type of BMG. About 37% of these were icosahedral-like, and 7% were crystal-like polyhedra, along with many other random types (Section 5.3), indicating structural heterogeneities.

The chemical analysis of the simulated BMG was considered using its solute-centred polyhedra e.g., Cu-, Ni-, Al-, Ti- centred polyhedra. A majority of these polyhedra were surrounded by Zr (solvent) in their first co-ordination shell (~76–90%). However, the remaining 10–24% were majorly surrounded by other solutes atoms instead of Zr (Section 5.4). This outcome suggested two distinct chemical arrangements (solvent-rich, solute-rich) inside the glassy structure. These results were useful as a precursor for the more detailed experimental analysis and were referred back and forth during the BMG analysis.

Aim#2: To develop a methodology for the quantitative and qualitative assessment of the BMG microstructure by APT.

Conclusion 2: APT can be successfully employed for chemical and structural analysis of BMGs, using optimised operating conditions.

The operational conditions of the APT were optimised to extract unprecedented information from the experimental data outcome for further analysis of Zr-based BMGs. Some critical features were addressed during the modification process. A customised peak-based mass spectrum peak ranging style with optimised operating parameters resulted in reduced error (<1.0 at. %) in the compositions (Section 6.4.4). The clustered evaporation phenomenon and its effect on the bulk composition of the BMG were assessed. It was confirmed that the clustered evaporation is an intrinsic feature of BMGs, and it has no adverse effect on the compositional outcome of the BMGs (Section 6.4.6).

A comparison between the composition of the local regions in TC- and HPT- BMGs determined that relatively low and high hardness regions had similar bulk composition in both types of BMGs (Sections 7.1.2, 7.2.2). No significant compositional changes were observed in the fractured region of HPT-BMG as well (Section 7.2.2). It was concluded that the regional hardness and deformation variations were not linked to the local regions' bulk composition. Moreover, the statistical analysis of the experimental data determined non-random solute distributions, confirming the feasibility for further microstructural analysis (Section 7.3).

Aim #3: To investigate the distinctive features inside the various high and low hardness regions by APT.

Conclusion 3: A quantitative approach determined the structural and chemical features of the nanoscale structural heterogeneities relative to the regions' local hardness variations.

The solute clustering was analysed for the local hard and soft regions of TC-$Zr_{63.49}Cu_{13.59}Ni_{10.32}Al_{11.29}Nb_{1.28}$, HPT-Vitreloy-105 and a fractured sample of HPT-Vitreloy-105. Atomic-scale heterogeneities were observed in the form of solute-rich clusters in TC- and HPT-BMGs. The chemical composition of these clusters and their surrounding matrix were distinctly different. The simulation study had previously indicated the presence of such discrete entities in the simulated BMG was confirmed experimentally by the APT results. This similarity complimented the decision of APT for BMG analysis. Most of the observed clusters contained all solute species and some proportion of the solvent (Zr). The matrix, on the other hand, comprised a higher fraction of Zr atoms and less than 40% contribution from all the solute atoms. A comparison between the chemistry of these clusters exhibited no noticeable difference in the clusters of hard, soft and/or fractured regions of BMGs (Sections 8.1.5 and 9.1.5), as shown in the Table 11.1. It is the first time, up to the author's knowledge, that the chemical information of these clusters and their surrounding matrix is experimentally reported.

Table 11.1: Average chemical composition of the solute-rich clusters obtained through the APT cluster analysis for different regions in TC- $Zr_{63.96}Cu_{13.36}Ni_{10.29}Al_{11.04}Nb_{1.25}$ and HPT- $Zr_{23}Cu_{28}Al_{17}Ni_{23}Ti_9$ BMGs.

BMG & Region-Type \ Elements		Vickers Hardness (HV)	Zr (at. %)	Cu (at. %)	Al (at. %)	Ni (at. %)	Nb (at. %)	Ti (at. %)
TC-Zr-based BMG	Hard Region	~503	26.50 ± 0.67	29.25 ± 0.31	21.06 ± 0.40	19.66 ± 0.26	3.53 ± 0.37	-
	Soft Region	~475	27.26 ± 0.51	28.80 ± 0.38	20.69 ± 0.40	19.35 ± 0.06	3.90 ± 1.09	-
HPT-Zr-based BMG	Hard Region	~606	21.25 ± 1.56	28.84 ± 0.56	17.26 ± 0.36	23.86 ± 0.41	-	8.79 ± 0.37
	Soft Region	~512	21.77 ± 1.95	28.85 ± 0.39	17.27 ± 0.77	23.29 ± 0.70	-	8.82 ± 0.48
	Fractured Region	-	23.20 ± 0.64	28.45 ± 0.32	16.66 ± 0.08	22.98 ± 0.54	-	8.71 ± 0.08

**The composition values are shown with the standard deviation values.*

Bigger-sized and a larger number of APT clusters were observed in the soft regions (clusters up to 220 atoms in TC- and 350 atoms in HPT-) compared to the respective hard regions (clusters up to 150 atoms in TC- and 210 atoms in HPT-) of BMGs. (Section 8.1.2, Section 9.1.2). The number densities of these clusters were slightly higher in soft regions (~200×10^{15} cm^{-3} and ~356×10^{15} cm^{-3} in TC- and HPT- BMGs) than the hard regions (~149×10^{15} cm^{-3} and ~212×10^{15} cm^{-3} in TC- and HPT- BMGs). Moreover, a lower magnitude of their volume fraction was observed in the hard regions (0.08 for TC- and 0.097 for HPT- BMGs) compared to their soft regions (0.10 for TC- and 0.145 for HPT- BMGs), (Section 8.1.3, Section 9.1.3). The number density, size and volume fraction of solute-rich clusters demonstrated an inverse relationship with their local hardness magnitudes, in Zr-based BMGs.

APT cluster analysis in a fractured region revealed that the cluster sizes and their number densities were grown larger than the clusters in the soft regions of the respective non-fractured BMG. This indicated that a fractured region tends to soften. The nature of these clusters was synonymous to the STZs, as described in literature (Section 2.6). Their link to STZs can be used for studying STZs' formation under external stimuli (Section 9.2.2).

Aim #4: To correlate the APT data with available TEM results to explore the microstructure-property relationships.

Conclusion#4: Correlative TEM/APT results complemented each other in terms of characterising the size, spacing, aspect ratio, volume fraction, composition and degree of crystallinity of clustered regions in the glass.

APT clusters were later characterised as SRO- and MRO clusters, based on their sizes. This classification clarified that the proportionality between the structural features and local softening holds for MRO clusters only. A correlative APT/ TEM study was conducted where similar trends between both studies were observed for the results of volume fractions (Section 10.1), and cluster sizes (Sections 10.2, 10.3) in Zr-based BMGs. In summary, the correlative study validated the APT results and the combined APT and TEM results helped better understand the BMGs' structure by overcoming the technical limitations of each of the techniques.

This thesis has successfully evaluated the nanoscale heterogeneities that are responsible for micron-scale hardness variations in Zr-based BMGs. APT was proven effective for quantitatively linking local softening with MRO-solute-rich clusters in thermally or mechanically processed Zr-based BMGs. This relationship existed regardless of the composition or the processing history of the BMGs, thus providing a critical structural link for the microstructure-property-processing relationship. The clusters explored in this study could be used for understanding the plasticity due to their effect on local softening. Although a complete understanding of dislocation theory for metallic glasses is outside the scope of this thesis, the results presented herein will be beneficial for understanding deformation mechanisms in these materials. Overall, this thesis has provided an operational framework for future investigations on the atomic-scale structural heterogeneities in BMGs.

11.2 Future Work

The relationship between microstructure-property-processing was tested on Zr-based BMGs only, in this thesis. This workflow should be carried forward for analysing structural heterogeneities in different BMGs, such as binary, ternary, higher-order Cu-based, Ti-based, Fe-based and other monolithic BMGs. This will help decide if it is a universal relationship or not. These detailed analyses along with the results presented in this thesis should be considered to develop an atomic model for describing the role of MRO clusters in the deformation of monolithic BMGs. The deformation mechanism in the atomic model could be used to link with one or more of the fundamental deformation theories of amorphous materials.

The quantitative approach presented herein has linked local softening to the nanoscale structural heterogeneities. Their distribution in the glassy matrix can be visually observed via the 3D-APT demonstration. Their link to STZs should be studied further since the STZs are of primary importance for understanding the deformation mechanism, shear band propagations and tailoring plasticity.

The strength of this research is the use of multiple material characterisation techniques altogether. The results from simulation, APT and TEM studies were found to correlate well with the findings and provide a better grip on the microstructural characterisation for BMGs. A hierarchical study is required for quantifying these nanoscale structural heterogeneities to their effect on the macroscopic structural properties in BMGs. This will facilitate effective material design and optimisation process, with reduced failure and optimised ductility.

In this thesis, the structural features with <15% population were found responsible for local property variations. Similar trend with < 25% VPs was also observed in the simulation data (Section 5.4). A unique approach was adopted where the solute-centred polyhedra comprising more solute atoms than the solvent atoms were separately considered and analysed instead of just their averaged atomic structure. Further analysis is required for validating the benefits of this approach in finding heterogeneities, in other simulated data.

3D additive manufacturing is an increasingly emerging field for fabricating BMGs. The advancements in this technology have helped attaining higher cooling rates and complex geometries that are difficult to achieve through casting processes. However, oxygen and/or nitrogen contaminations in a 3D-printed BMG can significantly reduce its mechanical properties compared to its as-cast counterpart [297]. One of the biggest advantages of using APT is its ability to do chemical analysis of samples. The methodological approach applied in this research can be used for obtaining atomic-scale chemical information of the 3D-printed BMGs. This will help optimise the operational parameters of the 3D processing, for improved structural properties of the 3D-builds.

One of the many ways of analysing glassy structure is to study the devitrified BMG through X-ray diffractions. It is hypothesised that these nanocrystals originate from the transitioning of structural heterogeneities (Section 2.7.2). A detailed investigation is required for analysing the thermal effects and chemical evolution of the nanoscale structure features, investigated herein, while transitioning into nanocrystals during the devitrification process. It will be useful for confirming the conjecture and for correlating X-ray diffraction results with APT studies.

REFERENCES

1. Löffler, J.F., *Metallic Glasses, Bulk*, in *Encyclopedia of Materials: Science and Technology*, K.H.J. Buschow, et al., Editors. 2003, Elsevier: Oxford. p. 1-12.
2. Li, B., et al., *Designed heterogeneities improve the fracture reliability of a Zr-based bulk metallic glass.* Materials Science and Engineering: A, 2015. **646**: p. 242-248.
3. Chen, Q., L. Liu, and S.-M. Zhang, *The potential of Zr-based bulk metallic glasses as biomaterials.* Frontiers of Materials Science in China, 2010. **4**(1): p. 34-44.
4. Jang, J.S., et al., *A Ni-free Zr-based bulk metallic glass with remarkable plasticity.* Journal of Alloys and Compounds, 2011. **509**: p. S109-S114.
5. Liu, Y.H., et al., *Super plastic bulk metallic glasses at room temperature.* science, 2007. **315**(5817): p. 1385-1388.
6. Kruzic, J.J., *Bulk metallic glasses as structural materials: a review.* Advanced Engineering Materials, 2016. **18**(8): p. 1308-1331.
7. Steenberge, N.v., *Study of structural changes of Zr-based bulk metallic glasses upon annealing and deformation treatments*. 2009: Universitat Autònoma de Barcelona.
8. Kim, J., et al., *Modulation of plastic flow in metallic glasses via nanoscale networks of chemical heterogeneities.* Acta Materialia, 2017. **140**: p. 116-129.
9. Hirata, A., et al., *Direct observation of local atomic order in a metallic glass.* Nature materials, 2011. **10**(1): p. 28-33.
10. Sarac, B., et al., *Origin of large plasticity and multiscale effects in iron-based metallic glasses.* Nature communications, 2018. **9**(1): p. 1-10.
11. Hufnagel, T.C., C.A. Schuh, and M.L. Falk, *Deformation of metallic glasses: Recent developments in theory, simulations, and experiments.* Acta Materialia, 2016. **109**: p. 375-393.
12. Cheng, Y. and E. Ma, *Atomic-level structure and structure–property relationship in metallic glasses.* Progress in materials science, 2011. **56**(4): p. 379-473.
13. Frank, J., *Three-dimensional electron microscopy of macromolecular assemblies: visualization of biological molecules in their native state*. 2006: Oxford university press.
14. Haley, D., et al., *Influence of field evaporation on Radial Distribution Functions in Atom Probe Tomography.* Philosophical Magazine, 2009. **89**(11): p. 925-943.
15. Ellis, B., *Perfectly Reasonable Deviations from the Beaten Track: The Letters of Richard P. Feynman.* Engineering and Science. **68**(1): p. 53-53.
16. Greer, A.L. and E. Ma, *Bulk metallic glasses: at the cutting edge of metals research.* MRS bulletin, 2007. **32**(8): p. 611-619.
17. Klement, W., R. Willens, and P. Duwez, *Non-crystalline structure in solidified gold–silicon alloys.* Nature, 1960. **187**(4740): p. 869-870.
18. Miller, M. and P. Liaw, *Bulk metallic glasses: an overview.* 2007.
19. Schroers, J., *The superplastic forming of bulk metallic glasses.* JOM, 2005. **57**: p. 35-39.
20. Inoue, A., T. Zhang, and T. Masumoto, *Zr–Al–Ni amorphous alloys with high glass transition temperature and significant supercooled liquid region.* Materials Transactions, JIM, 1990. **31**(3): p. 177-183.
21. Inoue, A., et al., *Preparation of 16 mm diameter rod of amorphous Zr65Al7. 5Ni10Cu17. 5 alloy.* Materials Transactions, JIM, 1993. **34**(12): p. 1234-1237.
22. Li, Y., et al., *Formation of Bulk Metallic Glasses and Their Composites.* MRS Bulletin, 2007. **32**(8): p. 624-628.
23. Concustell, A., et al., *Mechanical properties of a two-phase amorphous Ni–Nb–Y alloy studied by nanoindentation.* Scripta Materialia, 2007. **56**(2): p. 85-88.
24. Peker, A. and W.L. Johnson, *A highly processable metallic glass: Zr41. 2Ti13. 8Cu12. 5Ni10. 0Be22. 5.* Applied Physics Letters, 1993. **63**(17): p. 2342-2344.
25. Demetriou, M.D., et al., *Liquid-like platinum-rich glasses.* Scripta Materialia, 2011. **65**(9): p. 799-802.
26. He, Q., et al., *Locating bulk metallic glasses with high fracture toughness: Chemical effects and composition optimization.* Acta Materialia, 2011. **59**(1): p. 202-215.

27. Liu, Y., et al., *TiCuZrFeSnSiSc bulk metallic glasses with good mechanical properties for biomedical applications.* Journal of Alloys and Compounds, 2016. **679**: p. 341-349.
28. Xu, J. and E. Ma, *Damage-tolerant Zr-Cu-Al-based bulk metallic glasses with record-breaking fracture toughness.* Journal of Materials Research, 2014. **29**(14): p. 1489-1499.
29. Schroers, J., *Bulk metallic glasses.* Physics today, 2013. **66**(2): p. 32.
30. Inoue, A., *Stabilization of metallic supercooled liquid and bulk amorphous alloys.* Acta Materialia, 2000. **48**(1): p. 279-306.
31. Leamy, H., T. Wang, and H. Chen, *Plastic flow and fracture of metallic glass.* Metallurgical and Materials Transactions B, 1972. **3**(3): p. 699.
32. Masumoto, T. and R. Maddin, *The mechanical properties of palladium 20 a/o silicon alloy quenched from the liquid state.* Acta metallurgica, 1971. **19**(7): p. 725-741.
33. Cheng, Y., et al., *Cold versus hot shear banding in bulk metallic glass.* Physical Review B, 2009. **80**(13): p. 134115.
34. He, Q. and J. Xu, *Locating malleable bulk metallic glasses in Zr–Ti–Cu–Al alloys with calorimetric glass transition temperature as an indicator.* Journal of Materials Science & Technology, 2012. **28**(12): p. 1109-1122.
35. Sun, B., et al., *The critical criterion on runaway shear banding in metallic glasses.* Scientific reports, 2016. **6**(1): p. 1-10.
36. Dai, L.H., *8 - Shear Banding in Bulk Metallic Glasses*, in *Adiabatic Shear Localization (Second Edition)*, B. Dodd and Y. Bai, Editors. 2012, Elsevier: Oxford. p. 311-361.
37. NASA. *Space Technology Game Changing Development Bulk Metallic Glass Gears*. n.d [cited 2021 24th Oct]; Available from: <https://www.google.com/url?sa=t&rct=j&q=&esrc=s&source=web&cd=&cad=rja&uact=8&ved=2ahUKEwjMnvGQuuTzAhUadCsKHaCoDo8QFnoECAIQAQ&url=https%3A%2F%2Fwww.nasa.gov%2Fsites%2Fdefault%2Ffiles%2Fatoms%2Ffiles%2Ffs_bmgg_fs_160808.pdf&usg=AOvVaw0yFEIiSUIuCx0Xp7Xl5fiS>.
38. Nishiyama, N., K. Amiya, and A. Inoue, *Bulk metallic glasses for industrial products.* Materials Transactions, 2004. **45**(4): p. 1245-1250.
39. Takashima, K. and A. Ishida, *1.03 - Metals and Alloys*, in *Comprehensive Microsystems*, Y.B. Gianchandani, O. Tabata, and H. Zappe, Editors. 2008, Elsevier: Oxford. p. 53-73.
40. Sharma, P. and A. Inoue, *Chapter Twenty Seven - Metallic Glass*, in *Handbook of Silicon Based MEMS Materials and Technologies*, V. Lindroos, et al., Editors. 2010, William Andrew Publishing: Boston. p. 447-472.
41. Patel, S.K., et al., *Metallic Glasses: A Revolution in Material Science*, in *Metallic Glasses*. 2020, IntechOpen.
42. BHphotovideo. *SanDisk Cruzer Titanium U3 USB 2.0 Portable Data Storage Device - 4GB Capacity*. n.d [cited 2021 25th Oct]; Available from: <https://www.bhphotovideo.com/c/product/480936-REG/SanDisk_SDCZ7_4096_A11_Cruzer_Titanium_U3.html>.
43. Varshneya, A.K. and J.C. Mauro, *Chapter 1 - Introduction*, in *Fundamentals of Inorganic Glasses (Third Edition)*, A.K. Varshneya and J.C. Mauro, Editors. 2019, Elsevier. p. 1-18.
44. Zberg, B., P.J. Uggowitzer, and J.F. Löffler, *MgZnCa glasses without clinically observable hydrogen evolution for biodegradable implants.* Nature materials, 2009. **8**(11): p. 887-891.
45. Vilar, R., *1 - Laser surface modification of steel and cast iron for corrosion resistance*, in *Laser Surface Modification of Alloys for Corrosion and Erosion Resistance*, C.T. Kwok, Editor. 2012, Woodhead Publishing. p. 3-40.
46. Meagher, P., et al., *Bulk metallic glasses for implantable medical devices and surgical tools.* Advanced Materials, 2016. **28**(27): p. 5755-5762.
47. Liu, G.-y., et al., *Potential prospective application of Zr-based bulk metallic glasses in dental implant.* Materials transactions, 2015: p. M2015246.
48. Liquidmetal®. *Industrial*. 2021 [cited 2021 25th Oct]; Available from: <https://liquidmetal.com/industrial/>.
49. Liquidmetal®. *Consumer Products*. 2021 [cited 2021 25th Oct]; Available from: <https://liquidmetal.com/consumer/>.
50. Liquidmetal®. *Medical Devices*. 2021; Available from: <https://liquidmetal.com/medical/>.

51. Varshneya, A.K. and J.C. Mauro, *Chapter 8 - Elastic properties and hardness of glass*, in *Fundamentals of Inorganic Glasses (Third Edition)*, A.K. Varshneya and J.C. Mauro, Editors. 2019, Elsevier. p. 187-214.
52. Murali, P. and U. Ramamurty, *Embrittlement of a bulk metallic glass due to sub-Tg annealing.* Acta Materialia, 2005. **53**(5): p. 1467-1478.
53. Lewandowski*, J., W. Wang, and A. Greer, *Intrinsic plasticity or brittleness of metallic glasses.* Philosophical Magazine Letters, 2005. **85**(2): p. 77-87.
54. Gerling, R., F. Schimansky, and R. Wagner, *Two-stage embrittlement of amorphous Fe40Ni40P20 resulting from a loss of free volume and phase separation.* Acta Metallurgica, 1988. **36**(3): p. 575-583.
55. Van Steenberge, N., et al., *Effects of severe plastic deformation on the structure and thermo-mechanical properties of Zr55Cu30Al10Ni5 bulk metallic glass.* Journal of alloys and compounds, 2010. **500**(1): p. 61-67.
56. Li, B., S. Xie, and J.J. Kruzic, *Toughness enhancement and heterogeneous softening of a cryogenically cycled Zr–Cu–Ni–Al–Nb bulk metallic glass.* Acta Materialia, 2019. **176**: p. 278-288.
57. Kang, S.J., et al., *Intermediate structural state for maximizing the rejuvenation effect in metallic glass via thermo-cycling treatment.* Journal of Alloys and Compounds, 2019. **795**: p. 493-500.
58. Dieter, G.E. and D.J. Bacon, *Mechanical metallurgy*. Vol. 3. 1976: McGraw-hill New York.
59. Ren, Z.Q., et al., *Enhanced tensile strength and ductility of bulk metallic glasses Zr52. 5Cu17. 9Al10Ni14. 6Ti5 via high-pressure torsion.* Materials Science and Engineering: A, 2021. **803**: p. 140485.
60. Boucharat, N., et al. *Deformation-induced nanocrystallization in Al-rich metallic glasses*. in *Solid State Phenomena*. 2006. Trans Tech Publ.
61. Sort, J., et al., *Cold-consolidation of ball-milled Fe-based amorphous ribbons by high pressure torsion.* Scripta materialia, 2004. **50**(9): p. 1221-1225.
62. Kovács, Z., et al., *Deformation induced primary crystallization in a thermally non-primary crystallizing amorphous Al85Ce8Ni5Co2 alloy.* Scripta materialia, 2006. **54**(10): p. 1733-1737.
63. Wang, Y.B., et al., *Introducing a strain-hardening capability to improve the ductility of bulk metallic glasses via severe plastic deformation.* Acta Materialia, 2012. **60**(1): p. 253-260.
64. Meng, F., et al., *Reversible transition of deformation mode by structural rejuvenation and relaxation in bulk metallic glass.* Applied Physics Letters, 2012. **101**(12): p. 121914.
65. Meng, F., et al., *Reduction of shear localization through structural rejuvenation in Zr–Cu–Al bulk metallic glass.* Materials Science and Engineering: A, 2019. **765**: p. 138304.
66. Sarac, B., et al., *Structural modifications in sub-Tg annealed CuZr-based metallic glass.* Materials Science and Engineering: A, 2017. **707**: p. 245-252.
67. Hirata, A., et al., *Geometric frustration of icosahedron in metallic glasses.* Science, 2013. **341**(6144): p. 376-379.
68. Hirotsu, Y., et al., *Local atomic ordering and nanoscale phase separation in a Pd-Ni-P bulk metallic glass.* Physical Review B, 2006. **73**(1): p. 012205.
69. Ma, D., et al., *Elastic moduli inheritance and the weakest link in bulk metallic glasses.* Physical Review Letters, 2012. **108**(8): p. 085501.
70. Bernal, J. and J. Mason, *Packing of spheres: co-ordination of randomly packed spheres.* Nature, 1960. **188**(4754): p. 910-911.
71. Cohen, M.H. and D. Turnbull, *Metastability of amorphous structures.* Nature, 1964. **203**(4948): p. 964-964.
72. Bernal, J.D., *The Bakerian lecture, 1962. The structure of liquids.* Proceedings of the Royal Society of London. Series A, Mathematical and Physical Sciences, 1964. **280**(1382): p. 299-322.
73. Zallen, R., *The physics of amorphous solids*. 2008: John Wiley & Sons.
74. Cargill, G., *Dense random packing of hard spheres as a structural model for non-crystalline metallic solids Technical report(Structural model for noncrystalline metallic solids, particularly nickel phosphides, based on dense random packing of hard spheres).* 1969.

75. Polk, D., *The structure of glassy metallic alloys.* Acta metallurgica, 1972. **20**(4): p. 485-491.
76. Frank, F.t. and J. Kasper, *Complex alloy structures regarded as sphere packings. I. Definitions and basic principles.* Acta Crystallographica, 1958. **11**(3): p. 184-190.
77. Nelson, D.R. and F. Spaepen, *Polytetrahedral order in condensed matter.* Solid State Physics, 1989. **42**: p. 1-90.
78. Gaskell, P., *A new structural model for transition metal–metalloid glasses.* Nature, 1978. **276**(5687): p. 484-485.
79. Gaskell, P., *A new structural model for amorphous transition metal silicides, borides, phosphides and carbides.* Journal of non-crystalline solids, 1979. **32**(1-3): p. 207-224.
80. Lamparter, P., *Reverse monte carlo simulation of amorphous Ni80P20 and Ni81B19.* Physica Scripta, 1995. **1995**(T57): p. 72.
81. Evteev, A., A. Kosilov, and E. Levtchenko, *Atomic mechanisms of formation and structure relaxation of Fe83M17 (M: C, B, P) metallic glass.* Acta materialia, 2003. **51**(9): p. 2665-2674.
82. Sheng, H., et al., *Atomic packing and short-to-medium-range order in metallic glasses.* Nature, 2006. **439**(7075): p. 419-425.
83. Miracle, D.B., *A structural model for metallic glasses.* Nature materials, 2004. **3**(10): p. 697-702.
84. Jónsson, H. and H.C. Andersen, *Icosahedral ordering in the Lennard-Jones liquid and glass.* Physical review letters, 1988. **60**(22): p. 2295.
85. Xiao-Dong, W., Q. Min, and D. Chuang, *Bergman clusters related to bulk amorphous alloys and quasi-crystals.* Chinese physics letters, 2003. **20**(6): p. 891.
86. Qi, D. and S. Wang, *Icosahedral order and defects in metallic liquids and glasses.* Physical review B, 1991. **44**(2): p. 884.
87. Miracle, D., *The efficient cluster packing model–An atomic structural model for metallic glasses.* Acta materialia, 2006. **54**(16): p. 4317-4336.
88. Miracle, D.B., *The density and packing fraction of binary metallic glasses.* Acta materialia, 2013. **61**(9): p. 3157-3171.
89. Wang, A., J. Wang, and E. Ma, *Modified efficient cluster packing model for calculating alloy compositions with high glass forming ability.* Applied physics letters, 2007. **90**(12): p. 121912.
90. Yang, Y., et al., *Determining the three-dimensional atomic structure of an amorphous solid.* Nature, 2021. **592**(7852): p. 60-64.
91. Park, T., et al., *Tuning correlative atomic scale fluctuation and related properties in Ni–Nb–Zr metallic glasses.* Acta Materialia, 2019. **173**: p. 52-60.
92. Bragg, W.L. and J.F. Nye, *A dynamical model of a crystal structure.* Proceedings of the Royal Society of London. Series A. Mathematical and Physical Sciences, 1947. **190**(1023): p. 474-481.
93. Bagley, B. and D. Turnbull, *Structure Study of an Amorphous Electrodeposited Nickel‐Phosphorus Alloy.* Journal of Applied Physics, 1968. **39**(12): p. 5681-5685.
94. Wagner, C., *Structure of amorphous alloy films.* Journal of Vacuum Science and Technology, 1969. **6**(4): p. 650-657.
95. Cargill III, G., *Structural Investigation of Noncrystalline Nickel‐Phosphorus Alloys.* Journal of Applied Physics, 1970. **41**(1): p. 12-29.
96. Yue, X., et al., *The development of structure model in metallic glasses.* Materials Research 2017. **20**: p. 326-338.
97. Cohen, M.H. and D. Turnbull, *Molecular transport in liquids and glasses.* The Journal of Chemical Physics, 1959. **31**(5): p. 1164-1169.
98. Turnbull, D. and M.H. Cohen, *Free‐volume model of the amorphous phase: glass transition.* The Journal of chemical physics, 1961. **34**(1): p. 120-125.
99. Turnbull, D. and M.H. Cohen, *On the free‐volume model of the liquid‐glass transition.* The journal of chemical physics, 1970. **52**(6): p. 3038-3041.
100. Spaepen, F., *A microscopic mechanism for steady state inhomogeneous flow in metallic glasses.* Acta metallurgica, 1977. **25**(4): p. 407-415.

101. Johnson, W.L., J. Lu, and M.D. Demetriou, *Deformation and flow in bulk metallic glasses and deeply undercooled glass forming liquids—a self consistent dynamic free volume model.* Intermetallics, 2002. **10**(11-12): p. 1039-1046.
102. Falk, M.L. and J.S. Langer, *Dynamics of viscoplastic deformation in amorphous solids.* Physical Review E, 1998. **57**(6): p. 7192.
103. Demetriou, M.D. and W.L. Johnson, *Modeling the transient flow of undercooled glass-forming liquids.* Journal of applied physics, 2004. **95**(5): p. 2857-2865.
104. Egami, T., *Understanding the properties and structure of metallic glasses at the atomic level.* JOM, 2010. **62**(2): p. 70-75.
105. Argon, A., *Plastic deformation in metallic glasses.* Acta metallurgica, 1979. **27**(1): p. 47-58.
106. Langer, J., *Shear-transformation-zone theory of deformation in metallic glasses.* Scripta materialia, 2006. **54**(3): p. 375-379.
107. Fan, C., et al., *Structural model for bulk amorphous alloys.* Applied Physics Letters, 2006. **89**(11): p. 111905.
108. Miracle, D.B., et al., *Structure-forming principles for amorphous metals.* Materials Science and Engineering: A, 2004. **375-377**: p. 150-156.
109. Senkov, O., et al., *Atomic structure of Ca40+ XMg25Cu35− X metallic glasses.* Journal of Applied Physics, 2012. **111**(12): p. 123515.
110. Pan, D., et al., *Experimental characterization of shear transformation zones for plastic flow of bulk metallic glasses.* Proceedings of the National Academy of Sciences, 2008. **105**(39): p. 14769-14772.
111. Steif, P., F. Spaepen, and J. Hutchinson, *Strain localization in amorphous metals.* Acta Metallurgica, 1982. **30**(2): p. 447-455.
112. Argon, A., *Dislocations in Non-crystalline Media?*, in *Dislocation Modelling of Physical Systems*. 1981, Elsevier. p. 393-399.
113. Zink, M., et al., *Plastic deformation of metallic glasses: Size of shear transformation zones from molecular dynamics simulations.* Physical Review B, 2006. **73**(17): p. 172203.
114. Ziman, J., *A theory of the electrical properties of liquid metals. I: The monovalent metals.* Philosophical Magazine, 1961. **6**(68): p. 1013-1034.
115. Donati, C., et al., *Stringlike cooperative motion in a supercooled liquid.* Physical review letters, 1998. **80**(11): p. 2338.
116. Dong, F., et al., *Manipulating Internal Flow Units Toward Favorable Plasticity in Zr-based Bulk-metallic Glasses by Hydrogenation.* Journal of Materials Science & Technology, 2021.
117. Tong, Y., *Structural Aspects of Deformation in Bulk Metallic Glasses.* 2015.
118. Cohen, M.H. and G. Grest, *Liquid-glass transition, a free-volume approach.* Physical Review B, 1979. **20**(3): p. 1077.
119. Schuh, C.A., A.C. Lund, and T. Nieh, *New regime of homogeneous flow in the deformation map of metallic glasses: elevated temperature nanoindentation experiments and mechanistic modeling.* Acta Materialia, 2004. **52**(20): p. 5879-5891.
120. Ke, H.B., et al., *Structure Heterogeneity in Metallic Glass: Modeling and Experiment.* Journal of Materials Science & Technology, 2014. **30**(6): p. 560-565.
121. Liu, Y.H., et al., *Super plastic bulk metallic glasses at room temperature.* science, 2007. **315**(5817): p. 1385-1388.
122. McMillan, P., et al., *Nature Mater. 4, 680 (2005).* J. Mater. Chem, 2004. **14**: p. 1506.
123. Pelletier, J.-M., B. Van de Moortèle, and I. Lu, *Viscoelasticity and viscosity of Pd–Ni–Cu–P bulk metallic glasses.* Materials Science and Engineering: A, 2002. **336**(1-2): p. 190-195.
124. Lee, M., et al., *Improved plasticity of bulk metallic glasses upon cold rolling.* Scripta Materialia, 2010. **62**(9): p. 678-681.
125. Ketov, S., et al., *Rejuvenation of metallic glasses by non-affine thermal strain.* Nature, 2015. **524**(7564): p. 200-203.
126. Pan, J., et al., *Strain-hardening and suppression of shear-banding in rejuvenated bulk metallic glass.* Nature, 2020. **578**(7796): p. 559-562.
127. Egami, T. and D. Srolovitz, *Local structural fluctuations in amorphous and liquid metals: a simple theory of the glass transition.* Journal of Physics F: Metal Physics, 1982. **12**(10): p. 2141.

128. Park, J.M., D.H. Kim, and J. Eckert, *Internal state modulation-mediated plasticity enhancement in monolithic Ti-based bulk metallic glass.* Intermetallics, 2012. **29**: p. 70-74.
129. Wang, B., et al., *Nanometer-scale gradient atomic packing structure surrounding soft spots in metallic glasses.* npj Computational Materials, 2018. **4**(1): p. 1-11.
130. Li, W., Y. Gao, and H. Bei, *On the correlation between microscopic structural heterogeneity and embrittlement behavior in metallic glasses.* Scientific reports, 2015. **5**(1): p. 1-15.
131. Zhao, P., et al., *Influence of nanoscale structural heterogeneity on shear banding in metallic glasses.* Acta Materialia, 2017. **134**: p. 104-115.
132. Xing, L.-Q., et al., *Enhanced plastic strain in Zr-based bulk amorphous alloys.* Physical review B, 2001. **64**(18): p. 180201.
133. Feynman, R.P., *There's plenty of room at the bottom [data storage].* Journal of microelectromechanical systems, 1992. **1**(1): p. 60-66.
134. Gargarella, P., et al., *Structural evolution in Ti-Cu-Ni metallic glasses during heating.* APL materials, 2015. **3**(1): p. 016101.
135. Chuang, C.P., et al., *High‐Energy X‐Ray Diffraction Study of the Inhomogeneous Zr43Cu43Al7Ag7 Bulk‐Metallic Glasses.* Advanced Engineering Materials, 2013. **15**(4): p. 287-294.
136. Fu, X.L., Y. Li, and C.A. Schuh, *Temperature, strain rate and reinforcement volume fraction dependence of plastic deformation in metallic glass matrix composites.* Acta Materialia, 2007. **55**(9): p. 3059-3071.
137. Kajiwara, K., et al., *APFIM/TEM/SAXS studies of early stage crystallization of a Zr52. 5Cu17. 9Ni14. 6Al10Ti5 metallic glass.* Materials Science and Engineering: A, 2004. **375**: p. 738-743.
138. Zhang, X., et al., *Correlated unique variation of electrical resistivity to crystallization behavior of the Zr52. 5Cu17. 9Ni14. 6Al10Ti5 metallic glass.* Metals, 2019. **9**(12): p. 1298.
139. Zallen, R. and I. Wiley, *The physics of amorphous solids*. 1998, New York: Wiley.
140. Fujita, T., et al., *Atomic-scale heterogeneity of a multicomponent bulk metallic glass with excellent glass forming ability.* Physical review letters, 2009. **103**(7): p. 075502.
141. Sato, S., et al., *Effect of Al on local structures of Zr–Ni and Zr–Cu metallic glasses.* Materials transactions, 2005. **46**(12): p. 2893-2897.
142. Shariq, A., et al., *Exploring the next neighbourhood relationship in amorphous alloys utilizing atom probe tomography.* Ultramicroscopy, 2007. **107**(9): p. 773-780.
143. Kelly, T.F., et al., *Visions of atomic-scale tomography.* Microscopy Today, 2012. **20**(3): p. 12-16.
144. Ayache, J., et al., *Artifacts in transmission electron microscopy*, in *Sample preparation handbook for transmission electron microscopy*. 2010, Springer. p. 125-170.
145. Kisielowski, C., et al., *Detection of single atoms and buried defects in three dimensions by aberration-corrected electron microscope with 0.5-Å information limit.* Microscopy and Microanalysis, 2008. **14**(5): p. 469-477.
146. Voyles, P., et al., *Atomic-scale imaging of individual dopant atoms and clusters in highly n-type bulk Si.* Nature, 2002. **416**(6883): p. 826-829.
147. Erni, R., et al., *Atomic-resolution imaging with a sub-50-pm electron probe.* Physical review letters, 2009. **102**(9): p. 096101.
148. Voyles, P., D. Muller, and E. Kirkland, *Depth-dependent imaging of individual dopant atoms in silicon.* Microscopy and Microanalysis, 2004. **10**(2): p. 291-300.
149. Gibson, J., M. Treacy, and P. Voyles, *Atom pair persistence in disordered materials from fluctuation microscopy.* Ultramicroscopy, 2000. **83**(3-4): p. 169-178.
150. Hwang, J. and P. Voyles, *Variable resolution fluctuation electron microscopy on Cu-Zr metallic glass using a wide range of coherent STEM probe size.* Microscopy and Microanalysis, 2011. **17**(1): p. 67.
151. Zhu, F., et al., *Correlation between local structure order and spatial heterogeneity in a metallic glass.* Physical review letters, 2017. **119**(21): p. 215501.
152. Treacy, M., et al., *Fluctuation microscopy: a probe of medium range order.* Reports on Progress in Physics, 2005. **68**(12): p. 2899.

153. Oehring, M. and P. Haasen, *FIM-ATOM PROBE STUDIES OF THE DECOMPOSITION IN THE METALLIC GLASS Ni45 Pd35 P20.* Le Journal de Physique Colloques, 1986. **47**(C7): p. C7-275-C7-280.
154. Miller, M., et al., *Characterization of bulk metallic glasses with the atom probe.* Le Journal de Physique IV, 1996. **6**(C5): p. C5-217-C5-222.
155. Gault, B., et al., *Atom probe microscopy*. Vol. 160. 2012: Springer Science & Business Media.
156. Vurpillot, F., et al., *The spatial resolution of 3D atom probe in the investigation of single-phase materials.* Ultramicroscopy, 2000. **84**(3-4): p. 213-224.
157. Miller, M.K., et al., *Atom probe field ion microscopy.* 1996.
158. Larson, D.J., et al., *Local electrode atom probe tomography.* New York, US: Springer Science, 2013. **2**.
159. Miller, M., *Decomposition of bulk metallic glasses.* Materials Science and Engineering: A, 1998. **250**(1): p. 133-140.
160. Isheim, D., et al., *Nanometer-scale solute clustering in aluminum–nickel–ytterbium metallic glasses.* Materials Science and Engineering: A, 2003. **353**(1-2): p. 99-104.
161. Han, J.H., et al., *Phase separation in Zr56-xGdxCo28Al16 metallic glasses (0 <= x <= 20).* Acta materialia, 2014. **66**: p. 262-272.
162. Mattern, N., et al., *Structural and magnetic nanoclusters in Cu50Zr50− xGdx (x= 5 at.%) metallic glasses.* Acta materialia, 2012. **60**(5): p. 1946-1956.
163. Mattern, N., et al., *Phase separation in Cu46Zr47− xAl7Gdx metallic glasses.* Journal of Alloys and Compounds, 2011. **509**: p. S23-S26.
164. Shariq, A., T. Al-Kassab, and R. Kirchheim. *Study of Phase Separation in Zr53Co23. 5Al23. 5 Bulk Amorphous Alloy by Atom Probe Tomography*. in *2006 19th International Vacuum Nanoelectronics Conference*. 2006. IEEE.
165. Xiong, X., et al., *Atom probe analysis of the bulk amorphous Nd58Fe30Al10Dy2 ferromagnet.* Journal of Alloys and Compounds, 2012. **536**: p. 52-55.
166. Hono, K., et al., *Cu clustering and Si partitioning in the early crystallization stage of an Fe73.5Si13.5B9Nb3Cu1 amorphous alloy.* Acta materialia, 1999. **47**(3): p. 997-1006.
167. Shariq, A. and N. Mattern, *A study of phase separated Ni66Nb17Y17 metallic glass using atom probe tomography.* Ultramicroscopy, 2011. **111**(8): p. 1370-1374.
168. Laws, K.J., et al., *Analysis of dynamic segregation and crystallisation in Mg65Cu25Y10 bulk metallic glass using atom probe tomography.* Materials Science and Engineering A, 2012. **556**: p. 558-566.
169. Moody, M.P., et al., *Quantitative binomial distribution analyses of nanoscale like‐solute atom clustering and segregation in atom probe tomography data.* Microscopy research and technique, 2008. **71**(7): p. 542-550.
170. Moody, M.P., et al., *Contingency table techniques for three dimensional atom probe tomography.* Microscopy research and technique, 2007. **70**(3): p. 258-268.
171. Hyde, J., A. Cerezo, and T. Williams, *Statistical analysis of atom probe data: detecting the early stages of solute clustering and/or co-segregation.* Ultramicroscopy, 2009. **109**(5): p. 502-509.
172. Camus, E. and C. Abromeit, *Analysis of conventional and three-dimensional atom probe data for multiphase materials.* 1994. **75**(5): p. 2373.
173. Shariq, A., T. Al-Kassab, and R. Kirchheim, *Studying nearest neighbor correlations by atom probe tomography (APT) in metallic glasses as exemplified for Fe40Ni40B20 glassy ribbons.* Journal of alloys and compounds, 2012. **512**(1): p. 270-277.
174. Sarker, S., et al., *Icosahedra clustering and short range order in Ni-Nb-Zr amorphous membranes.* Scientific reports, 2018. **8**(1): p. 1-14.
175. Torres, K., et al., *The influence of voxel size on atom probe tomography data.* Ultramicroscopy, 2011. **111**(6): p. 464-468.
176. Srinivasan, S., et al., *Automated voxelization of 3D atom probe data through kernel density estimation.* Ultramicroscopy, 2015. **159**: p. 381-386.

177. Marceau, R., et al., *Quantitative atom probe analysis of nanostructure containing clusters and precipitates with multiple length scales.* Ultramicroscopy, 2011. **111**(6): p. 738-742.
178. Marceau, R.K., et al., *Solute clustering in Al–Cu–Mg alloys during the early stages of elevated temperature ageing.* Acta materialia, 2010. **58**(15): p. 4923-4939.
179. Marceau, R.K.W., *Design in Light Alloys by Understanding the Solute Clustering Processes During the Early Stages of Age Hardening in Al-Cu-Mg Alloys.* 2008.
180. Zhu, S., et al., *Design of solute clustering during thermomechanical processing of AA6016 Al–Mg–Si alloy.* Acta Materialia, 2021. **203**: p. 116455.
181. Dong, Y., et al., *Atom probe tomography interlaboratory study on clustering analysis in experimental data using the maximum separation distance approach.* Microscopy and Microanalysis, 2019. **25**(2): p. 356-366.
182. Vaumousse, D., A. Cerezo, and P. Warren, *A procedure for quantification of precipitate microstructures from three-dimensional atom probe data.* Ultramicroscopy, 2003. **95**: p. 215-221.
183. Marquis, E.A., et al. *On the use of density-based algorithms for the analysis of solute clustering in atom probe tomography data*. in *Proceedings of the 18th International Conference on Environmental Degradation of Materials in Nuclear Power Systems–Water Reactors*. 2019. Springer.
184. Ghamarian, I. and E. Marquis, *Hierarchical density-based cluster analysis framework for atom probe tomography data.* Ultramicroscopy, 2019. **200**: p. 28-38.
185. Poon, I.I.S.T., *Effect of microalloying Sn and (Sn+ Ag) in Al-1.1 Cu-1.7 Mg (at.%) on clustering, precipitation processes and microstructural evolution.* 2014.
186. Marquis, E.A. and J.M. Hyde, *Applications of atom-probe tomography to the characterisation of solute behaviours.* Materials Science and Engineering: R: Reports, 2010. **69**(4-5): p. 37-62.
187. Ceguerra, A.V., et al., *A three-dimensional Markov field approach for the analysis of atomic clustering in atom probe data.* Philosophical Magazine, 2010. **90**(12): p. 1657-1683.
188. Lefebvre, W., T. Philippe, and F. Vurpillot, *Application of Delaunay tessellation for the characterization of solute-rich clusters in atom probe tomography.* Ultramicroscopy, 2011. **111**(3): p. 200-206.
189. Miller, M. and E. Kenik, *Atom probe tomography: A technique for nanoscale characterization.* Microscopy and Microanalysis, 2004. **10**(3): p. 336-341.
190. Philippe, T., et al., *Clustering and nearest neighbour distances in atom-probe tomography.* Ultramicroscopy, 2009. **109**(10): p. 1304-1309.
191. Stephenson, L.T., et al., *New techniques for the analysis of fine-scaled clustering phenomena within atom probe tomography (APT) data.* Microscopy and Microanalysis, 2007. **13**(6): p. 448.
192. Sander, J., et al., *Density-based clustering in spatial databases: The algorithm gdbscan and its applications.* Data mining and knowledge discovery, 1998. **2**(2): p. 169-194.
193. Bilal, H., et al., *Atom Probe Analysis of a Zr-based Bulk Metallic Glass.* Microscopy and Microanalysis, 2021.
194. Tang, F., et al., *Optimization of pulsed laser atom probe (PLAP) for the analysis of nanocomposite Ti–Si–N films.* Ultramicroscopy, 2010. **110**(7): p. 836-843.
195. Kirchhofer, R., M.C. Teague, and B.P. Gorman, *Thermal effects on mass and spatial resolution during laser pulse atom probe tomography of cerium oxide.* Journal of nuclear materials, 2013. **436**(1-3): p. 23-28.
196. La Fontaine, A., et al., *Interpreting atom probe data from chromium oxide scales.* Ultramicroscopy, 2015. **159**: p. 354-359.
197. Pedrazzini, S., et al., *Nanoscale stoichiometric analysis of a high-temperature superconductor by atom probe tomography.* Microscopy and Microanalysis, 2017. **23**(2).
198. Peng, Z., et al., *Evaluation of analysis conditions for laser-pulsed atom probe tomography: example of cemented tungsten carbide.* Microscopy and Microanalysis, 2017. **23**(2): p. 431.
199. Zemp, J., et al., *Clustered field evaporation of metallic glasses in atom probe tomography.* IFES 2001, 2016. **162**: p. 35-41.

200. Zhang, Y., P.J. Warren, and A. Cerezo, *Effect of Cu addition on nanocrystallisation of Al-Ni-Sm amorphous alloy.* 47 th International Field Emission Symposium, 2002. **327**(1): p. 109-115.
201. Miller, M.K., et al., *APT characterization of some iron-based bulk metallic glasses.* Intermetallics, 2006. **14**(8-9): p. 1019-1026.
202. Yuan, C., et al., *Atomic-scale heterogeneity in large-plasticity Cu-doped metallic glasses.* Journal of Alloys and Compounds, 2019. **798**: p. 517-522.
203. Miller, M.K., R.G. Forbes, and SpringerLink, *Atom-Probe Tomography: The Local Electrode Atom Probe*. 2014, Boston, MA: Springer US.
204. Xie, K.Y., et al., *Overcoming challenges in the study of nitrided microalloyed steels using atom probe.* Ultramicroscopy, 2012. **112**(1): p. 32-38.
205. Miller, M.K., D. Reinhard, and D. Larson, *Detection and quantification of solute clusters in a nanostructured ferritic alloy.* Journal of Nuclear Materials, 2015. **462**: p. 428-432.
206. Gault, B., et al., *Estimation of the reconstruction parameters for atom probe tomography.* Microscopy and Microanalysis, 2008. **14**(4): p. 296-305.
207. Liu, C., et al., *Second phase effect on corrosion of nanostructured Mg-Zn-Ca dual-phase metallic glasses.* Journal of Magnesium and Alloys, 2021.
208. Wu, X., et al., *Continuous chemical redistribution following amorphous-to-crystalline structural ordering in a Zr-Cu-Al bulk metallic glass.* Journal of Materials Science & Technology, 2022. **101**: p. 285-293.
209. Mu, X., et al., *Unveiling the Local Atomic Arrangements in the Shear Band Regions of Metallic Glass.* Advanced Materials, 2021. **33**(12): p. 2007267.
210. Langer, J., *Dynamics of shear-transformation zones in amorphous plasticity: Formulation in terms of an effective disorder temperature.* Physical Review E, 2004. **70**(4): p. 041502.
211. Cheng, Y., E. Ma, and H. Sheng, *Atomic level structure in multicomponent bulk metallic glass.* Physical review letters, 2009. **102**(24): p. 245501.
212. Li, X., Z. Shi, and T. Zhang, *Effect of similar element substitution on Fe-B-Si-Mo bulk metallic glasses studied by experiment and ab initio molecular dynamics simulation.* Journal of Alloys and Compounds, 2019. **784**: p. 1139-1144.
213. Yu, K., et al., *Glass forming ability and bending plasticity evolutions in Zr-Co-Al bulk metallic glasses and their structural origin.* Journal of Non-Crystalline Solids, 2018. **488**: p. 52-62.
214. Sun, S. and P. Guan, *The critical model size for simulating the structure-dynamics correlation in bulk metallic glasses.* Science China Materials, 2021. **64**(6): p. 1545-1555.
215. Samavatian, M., et al., *Inherent relation between atomic-level stresses and nanoscale heterogeneity in Zr-based bulk metallic glass under a rejuvenation process.* Physica B: Condensed Matter, 2020. **595**: p. 412390.
216. Stoica, M., et al., *Changes in short-range order of Zr55Cu30Al10Ni5 and Zr55Cu20Al10Ni10Ti5 BMGs upon annealing.* Journal of alloys and compounds, 2010. **506**(1): p. 85-87.
217. Bei, H., S. Xie, and E.P. George, *Softening caused by profuse shear banding in a bulk metallic glass.* Physical review letters, 2006. **96**(10): p. 105503.
218. Kanungo, B.P., et al., *Characterization of free volume changes associated with shear band formation in Zr-and Cu-based bulk metallic glasses.* Intermetallics, 2004. **12**(10-11): p. 1073-1080.
219. Hajlaoui, K., et al., *Thermal expansion and indentation-induced free volume in Zr-based metallic glasses measured by real-time diffraction using synchrotron radiation.* Scripta materialia, 2004. **51**(9): p. 843-848.
220. Lewandowski, J. and A. Greer, *Temperature rise at shear bands in metallic glasses.* Nature materials, 2006. **5**(1): p. 15-18.
221. Van Steenberge, N., et al., *Microstructural inhomogeneities introduced in a Zr-based bulk metallic glass upon low-temperature annealing.* Materials Science and Engineering: A, 2008. **491**(1-2): p. 124-130.
222. Kim, K., et al., *Heterogeneity of a Cu 47.5 Zr 47.5 Al 5 bulk metallic glass.* Applied physics letters, 2006. **88**(5): p. 051911.

223. Chen, H., *Metallic glasses. Review.* Mater. Sci. Eng., 1976. **25**: p. 59.
224. Guo, F., S.J. Poon, and G.J. Shiflet, *Metallic glass ingots based on yttrium.* Applied Physics Letters, 2003. **83**(13): p. 2575-2577.
225. Wang, X., et al., *A plastic Zr–Cu–Ag–Al bulk metallic glass.* Acta Materialia, 2011. **59**(3): p. 1037-1047.
226. Oh, J., et al., *Phase separation in Cu43Zr43Al7Ag7 bulk metallic glass.* Scripta materialia, 2005. **53**(2): p. 165-169.
227. Idury, K.S., B. Murty, and J. Bhatt, *Thermodynamic modeling and composition design for the formation of Zr–Ti–Cu–Ni–Al high entropy bulk metallic glasses.* Intermetallics, 2015. **65**: p. 42-50.
228. Takeuchi, A. and A. Inoue, *Calculations of mixing enthalpy and mismatch entropy for ternary amorphous alloys.* Materials transactions, JIM, 2000. **41**(11): p. 1372-1378.
229. Luo, W., H. Sheng, and E. Ma, *Pair correlation functions and structural building schemes in amorphous alloys.* Applied physics letters, 2006. **89**(13): p. 131927.
230. Suryanarayana, C. and A. Inoue, *Bulk metallic glasses*. 2017: CRC press.
231. Du, X., et al., *Two-glassy-phase bulk metallic glass with remarkable plasticity.* Applied Physics Letters, 2007. **91**(13): p. 131901.
232. Hwang, J., et al., *Nanoscale structure and structural relaxation in Zr 50 Cu 45 Al 5 bulk metallic glass.* Physical review letters, 2012. **108**(19): p. 195505.
233. Hu, L., Y. Yue, and C. Zhang, *Abnormal sub-T g enthalpy relaxation in the CuZrAl metallic glasses far from equilibrium.* Applied Physics Letters, 2011. **98**(8): p. 081904.
234. Hirata, A., et al., *Local atomic structure analysis of Zr-Ni and Zr-Cu metallic glasses using electron diffraction.* Materials transactions, 2007. **48**(6): p. 1299-1303.
235. Takeuchi, T., et al., *Local atomic arrangements and electronic structure of Zr-Ni-Al bulk metallic glass:–Analysis by use of the relevant crystals–.* Materials Science and Engineering: A, 2007. **449**: p. 599-604.
236. Ma, D., et al., *Nearest-neighbor coordination and chemical ordering in multicomponent bulk metallic glasses.* Applied Physics Letters, 2007. **90**(21): p. 211908.
237. Miracle, D., W. Sanders, and O. Senkov, *The influence of efficient atomic packing on the constitution of metallic glasses.* Philosophical Magazine, 2003. **83**(20): p. 2409-2428.
238. Senkov, O., et al., *Local atomic structure of Ca-Mg-Zn metallic glasses.* Physical Review B, 2010. **82**(10): p. 104206.
239. Zhang, C., et al., *Fragile-to-strong transition in metallic glass-forming liquids.* The Journal of chemical physics, 2010. **133**(1): p. 014508.
240. Hirotsu, Y., T. Ohkubo, and M. Matsushita, *Study of amorphous alloy structures with medium range atomic ordering.* Microscopy research and technique, 1998. **40**(4): p. 284-312.
241. Xie, S., X. Zeng, and H. Qian, *Correlations between the relaxed excess free volume and the plasticity in Zr-based bulk metallic glasses.* Journal of alloys and compounds, 2009. **480**(2): p. L37-L40.
242. Best, J.P., et al., *Relating fracture toughness to micro-pillar compression response for a laser powder bed additive manufactured bulk metallic glass.* Materials Science and Engineering: A, 2020. **770**: p. 138535.
243. Johnson, K.L. and K.L. Johnson, *Contact mechanics*. 1987: Cambridge university press.
244. Kruzic, J.J., et al., *Indentation techniques for evaluating the fracture toughness of biomaterials and hard tissues.* Journal of the Mechanical Behavior of Biomedical Materials, 2009. **2**(4): p. 384-395.
245. Nomoto, K., et al., *Medium-range order dictates local hardness in bulk metallic glasses.* Materials Today, 2021.
246. Felfer, P., et al., *New approaches to nanoparticle sample fabrication for atom probe tomography.* Ultramicroscopy, 2015. **159**: p. 413-419.
247. Miller, M.K. and K.F. Russell, *Atom probe specimen preparation with a dual beam SEM/FIB miller.* Ultramicroscopy, 2007. **107**(9): p. 761-766.
248. Liu, H., et al., *EDP2XRD: a computer program for converting electron diffraction patterns into X-ray diffraction patterns.* Journal of Applied Crystallography, 2016. **49**(2): p. 636-641.

249. Morháč, M., et al., *Background elimination methods for multidimensional coincidence γ-ray spectra.* Nuclear Instruments and Methods in Physics Research Section A: Accelerators, Spectrometers, Detectors and Associated Equipment, 1997. **401**(1): p. 113-132.
250. Yao, L., et al., *Optimisation of specimen temperature and pulse fraction in atom probe microscopy experiments on a microalloyed steel.* Ultramicroscopy, 2011. **111**(6): p. 648-651.
251. Thuvander, M., et al., *Quantitative atom probe analysis of carbides.* Ultramicroscopy, 2011. **111**(6): p. 604-608.
252. Shariq, A., et al., *Investigations of field-evaporated end forms in voltage-and laser-pulsed atom probe tomography.* Ultramicroscopy, 2009. **109**(5): p. 472-479.
253. Gault, B., et al., *Advances in the calibration of atom probe tomographic reconstruction.* Journal of Applied Physics, 2009. **105**(3): p. 034913.
254. Miller, M. and A.-P. Tomography, *Analysis at the Atomic Level*. 2000, Kluwer Academic/Plenum Press, New York.
255. Hudson, D., G. Smith, and B. Gault, *Optimisation of mass ranging for atom probe microanalysis and application to the corrosion processes in Zr alloys.* Ultramicroscopy, 2011. **111**(6): p. 480-486.
256. Takahashi, J., K. Kawakami, and D. Raabe, *Comparison of the quantitative analysis performance between pulsed voltage atom probe and pulsed laser atom probe.* Ultramicroscopy, 2017. **175**: p. 105-110.
257. Dhara, S., et al., *Atom probe tomography data analysis procedure for precipitate and cluster identification in a Ti-Mo steel.* Data in brief, 2018. **18**: p. 968-982.
258. Moody, M.P., et al., *Qualification of the tomographic reconstruction in atom probe by advanced spatial distribution map techniques.* Ultramicroscopy, 2009. **109**(7): p. 815-824.
259. Loi, S.T., et al., *Electrostatic simulations of a local electrode atom probe: The dependence of tomographic reconstruction parameters on specimen and microscope geometry.* Ultramicroscopy, 2013. **132**: p. 107-113.
260. Chen, Y., et al., *Grain size stabilization of mechanically alloyed nanocrystalline Fe-Zr alloys by forming highly dispersed coherent Fe-Zr-O nanoclusters.* Acta Materialia, 2018. **158**: p. 340-353.
261. Karnesky, R.A., C.K. Sudbrack, and D.N. Seidman, *Best-fit ellipsoids of atom-probe tomographic data to study coalescence of γ′ (L12) precipitates in Ni–Al–Cr.* Scripta Materialia, 2007. **57**(4): p. 353-356.
262. Shariq, A., et al., *Exploring the next neighbourhood relationship in amorphous alloys utilizing atom probe tomography.* Ultramicroscopy, 2007. **107**(9): p. 773-780.
263. Perea, D.E., et al., *Determining the location and nearest neighbours of aluminium in zeolites with atom probe tomography.* Nature Communications, 2015. **6**(1): p. 7589.
264. Philippe, T., et al., *Point process statistics in atom probe tomography.* Ultramicroscopy, 2013. **132**: p. 114-120.
265. Miller, M., T. Shen, and R. Schwarz, *Atom probe studies of metallic glasses.* Journal of non-crystalline solids, 2003. **317**(1-2): p. 10-16.
266. Shu, H., et al., *Quantifying the spatial heterogeneity of points.* International Journal of Geographical Information Science, 2019. **33**(7): p. 1355-1376.
267. Blöchl, P.E., *Projector augmented-wave method.* Physical review B, 1994. **50**(24): p. 17953.
268. Kresse, G. and J. Hafner, *Ab initio molecular dynamics for liquid metals.* Physical review B, 1993. **47**(1): p. 558.
269. Kresse, G. and J. Furthmüller, *Efficiency of ab-initio total energy calculations for metals and semiconductors using a plane-wave basis set.* Computational materials science, 1996. **6**(1): p. 15-50.
270. Kresse, G. and J. Furthmüller, *Efficient iterative schemes for ab initio total-energy calculations using a plane-wave basis set.* Physical review B, 1996. **54**(16): p. 11169.
271. Kresse, G. and D. Joubert, *From ultrasoft pseudopotentials to the projector augmented-wave method.* Physical review b, 1999. **59**(3): p. 1758.
272. Voronoi, G., *New parametric applications concerning the theory of quadratic forms-Second announcement.* J. Reine Angew. Math, 1908. **134**: p. 198-287.

273. Senkov, O. and Y. Cheng, *Ab initio molecular dynamics simulation of the amorphous structure of Ca-Mg-Cu and Ca-Mg-Zn alloys.* Metallurgical and Materials Transactions A, 2013. **44**(5): p. 1980-1989.
274. Ding, J., Y. Cheng, and E. Ma, *Charge-transfer-enhanced prism-type local order in amorphous Mg65Cu25Y10: Short-to-medium-range structural evolution underlying liquid fragility and heat capacity.* Acta materialia, 2013. **61**(8): p. 3130-3140.
275. Trady, S., A. Hasnaoui, and M. Mazroui, *Atomic packing and medium-range order in Ni3Al metallic glass.* Journal of Non-Crystalline Solids, 2017. **468**: p. 27-33.
276. Ganesh, P. and M. Widom, *Signature of nearly icosahedral structures in liquid and supercooled liquid copper.* Physical Review B, 2006. **74**(13): p. 134205.
277. Jakse, N. and A. Pasturel, *Local order of liquid and supercooled zirconium by ab initio molecular dynamics.* Physical review letters, 2003. **91**(19): p. 195501.
278. Tahiri, M., A. Hasnaoui, and K. Sbiaai, *Atomic scale investigation of structural properties and glass forming ability of Ti 100− x Al x metallic glasses.* Metallurgical and Materials Transactions A, 2018. **49**(6): p. 2513-2522.
279. Pan, S.-P., et al., *Crystallization pathways of liquid-bcc transition for a model iron by fast quenching.* Scientific reports, 2015. **5**(1): p. 1-8.
280. Wang, C., K.J. Dong, and A. Yu. *Analysis of Voronoi clusters in the packing of uniform spheres*. in *AIP Conference Proceedings*. 2013. American Institute of Physics.
281. Ahn, K., et al., *Topological and chemical ordering induced by Ni and Nd in Al 87 Ni 7 Nd 6 metallic glass.* Physical Review B, 2004. **70**(22): p. 224103.
282. Tian, H., et al., *Ab initio molecular dynamics simulation of binary Cu64Zr36 bulk metallic glass: Validation of the cluster-plus-glue-atom model.* Journal of Applied Physics, 2011. **109**(12): p. 123520.
283. Sheng, H., et al., *Atomic packing in multicomponent aluminum-based metallic glasses.* Acta Materialia, 2008. **56**(20): p. 6264-6272.
284. Takeuchi, A. and A. Inoue, *Mixing enthalpy of liquid phase calculated by miedema's scheme and approximated with sub-regular solution model for assessing forming ability of amorphous and glassy alloys.* Intermetallics, 2010. **18**(9): p. 1779-1789.
285. Hu, L., et al., *Thermodynamic anomaly of the sub-T g relaxation in hyperquenched metallic glasses.* The Journal of chemical physics, 2013. **138**(17): p. 174508.
286. Pedersen, U.R., et al., *Geometry of slow structural fluctuations in a supercooled binary alloy.* Physical review letters, 2010. **104**(10): p. 105701.
287. Tanaka, H., et al., *Critical-like behaviour of glass-forming liquids.* Nature materials, 2010. **9**(4): p. 324-331.
288. Fdez-Gubieda, M., et al., *Evidence of strong short-range order in* $(Fe_{0.2}\ Co_{0.8})75Si_xB_{25-x}$ *amorphous alloys from EXAFS spectroscopy.* Physical Review B, 1996. **53**(2): p. 620.
289. Cerezo, A., et al., *Atom probe tomography today.* Materials Today, 2007. **10**(12): p. 36-42.
290. Hu, R., S. Jin, and G. Sha, *Application of atom probe tomography in understanding high entropy alloys: 3D local chemical compositions in atomic scale analysis.* Progress in Materials Science, 2022. **123**: p. 100854.
291. Kühbach, M., et al., *Community-Driven Methods for Open and Reproducible Software Tools for Analyzing Datasets from Atom Probe Microscopy.* Microscopy and Microanalysis, approved, 2021.
292. Kühbach, M., et al., *Community-Driven Methods for Open and Reproducible Software Tools for Analyzing Datasets from Atom Probe Microscopy.* Microscopy and Microanalysis, 2021: p. 1-16.
293. London, A.J., *Quantifying uncertainty from mass-peak overlaps in atom probe microscopy.* Microscopy and Microanalysis, 2019. **25**(2): p. 378-388.
294. Vurpillot, F., et al., *Thermal response of a field emitter subjected to ultra-fast laser illumination.* Journal of Physics D: Applied Physics, 2009. **42**(12): p. 125502.
295. Houard, J., et al., *Optical near-field absorption at a metal tip far from plasmonic resonance.* Physical Review B, 2010. **81**(12): p. 125411.
296. Kelly, T.F., et al., *Laser pulsing of field evaporation in atom probe tomography.* Current Opinion in Solid State and Materials Science, 2014. **18**(2): p. 81-89.

297. Best, J.P., et al., *Fracture and fatigue behaviour of a laser additive manufactured Zr-based bulk metallic glass.* Additive Manufacturing, 2020. **36**: p. 101416.
298. Best, J.P., et al., *Structural periodicity in laser additive manufactured Zr-based bulk metallic glass.* Applied Physics Letters, 2019. **115**(3): p. 031902.
299. Stepień, Z.M. and T.T. Tsong, *Formation of metal hydride ions in low-temperature field evaporation.* Surface science, 1998. **409**(1): p. 57-68.
300. Hui, X., et al., *Atomic structures of Zr-based metallic glasses.* Science in China Series G: Physics, Mechanics and Astronomy, 2008. **51**(4): p. 400-413.
301. Wang, Q., et al., *The atomic-scale mechanism for the enhanced glass-forming-ability of a Cu-Zr based bulk metallic glass with minor element additions.* Scientific reports, 2014. **4**(1): p. 1-5.
302. Celino, M., et al., *Role of defective icosahedra in undercooled copper.* Physical Review B, 2007. **75**(17): p. 174210.
303. Jakse, N., O. Le Bacq, and A. Pasturel, *Prediction of the local structure of liquid and supercooled tantalum.* Physical Review B, 2004. **70**(17): p. 174203.
304. Hirata, A., et al., *Geometric Frustration of Icosahedron in Metallic Glasses.* Science, 2013. **341**(6144): p. 376-379.
305. Şopu, D., et al., *Atomic-level processes of shear band nucleation in metallic glasses.* Physical review letters, 2017. **119**(19): p. 195503.
306. Liu, C. and R. Maaß, *Elastic fluctuations and structural heterogeneities in metallic glasses.* Advanced Functional Materials, 2018. **28**(30): p. 1800388.

APPENDIX A Supporting Information

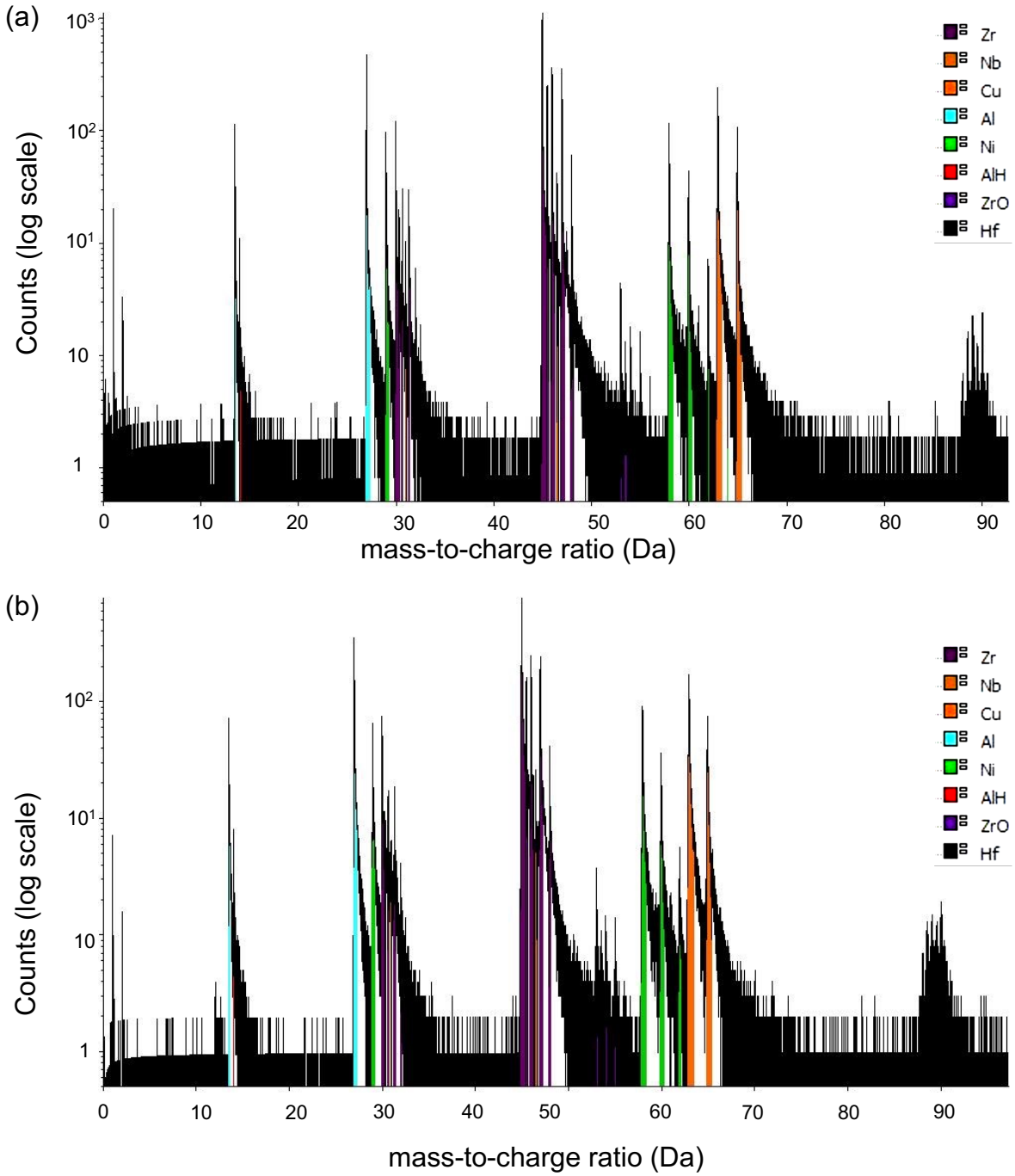

Figure A0.1: Typical mass spectrum of thermally cycled (TC-3(120 cycles)) $Zr_{63.78}Cu_{14.72}Ni_{10}Al_{10}Nb_{1.5}$ (at. %) BMG in the APT measurement (a) Hard Region with average hardness of ~ 503 HV, (b) Soft Region with average hardness of ~ 477 HV.

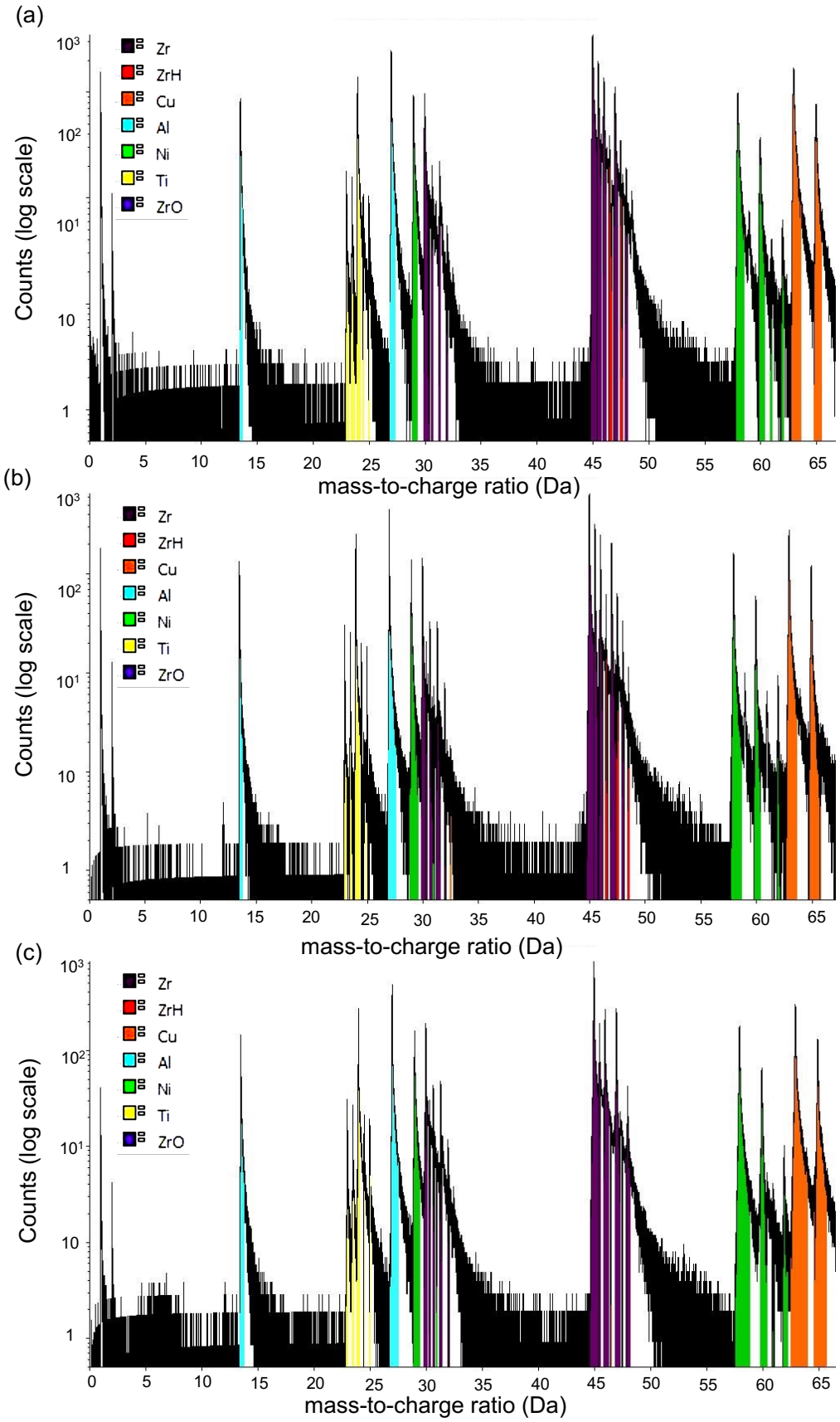

Figure A0.2: Typical mass spectrum of high-pressure torsion (HPT-P02) Vitreloy-105 BMG in the APT measurement (a) Hard region with average hardness of ~ 606 HV, (b) soft region with average hardness of ~ 510 HVand (c) (HPT-P04) Vitreloy-105 BMG fractured region.

Table A0.1: d_{max} values of different samples as per the 5th nearest neighbour (5NN) analysis for thermally cycled Zr-based BMGs (Chapter 3).

Region Type	Sample Name	CuAlTiNi-dmax
Hard Region	R18-59492-new	0.345
	R18-59563	0.355
	R18-59567	0.355
Soft Region	R18-59581	0.365
	R18-59584	0.365
	R18-59479	0.385

Table A0.2: d_{max} values of different samples as per the 5th nearest neighbour (5NN) analysis for high-pressure torsion Zr-based BMGs (Chapter 3).

Region Type	Sample Name	CuAlTiNi-dmax
Hard Region	R18-59882-new	0.315
	R18-59875-new	0.305
	R18-59797	0.315
Soft Region	R18-59799-2021	0.335
	R18-60190-new	0.335
	R18-60191-new	0.325
Fractured Region	R18-59900	0.345
	R18-60073	0.325
	R18-60075	0.335

Table A0.3: Cut-off values as the first peak width of partial PDFs of the respective bond pair to calculate coordination number and HA index (Chapter 5).

#	Reference Bond Pair	Cut-off Value
1	Zr-Zr	4.1
2	Ni-Ni	3.2
3	Al-Al	3.6
4	Cu-Cu	3.35
5	Ti-Ti	3.75
6	Zr-Ni	3.8
7	Zr-AL	3.95
8	Zr-Cu	3.75
9	Zr-Ti	3.95
10	Ni-Al	3.5
11	Ni-Cu	3.3
12	Ni-Ti	3.5
13	Al-Cu	3.5
14	Al-Ti	3.7
15	Cu-Ti	3.6

Table A0.4: Summary of different coordination polyhedra of Vitreloy-105 at 300 K (Chapter 5).

300 K	Total	Zr	Ni	Al	Cu	Ti
Voronoi Indices of >5 % Fraction Polyhedra		<0,2,8,5> <0,2,8,6> <0,1,10,4> <0,1,10,5>	<0,2,8,1> <0,3,6,1> <0,3,6,3> <0,2,8,0> <0,4,4,3> <0,0,12,0>	<0,3,6,4 > <0,0,12,0> <0,2,8,2> <0,1,10,2> <0,3,6,5>	<0,2,8,1> <0,2,8,2> <0,3,6,3>	<0,1,10,2> <0,0,12,0> <0,3,6,4> <0,2,8,4>
Full Icosahedra (%)	3.22	0.06	5.04	12.26	4.77	7.34
Icosahedral-like Polyhedra (%)	33.44	36.14	24.45	25.34	36.46	36.58
Mixed Polyhedra (%)	17.70	11.25	32.11	30.14	18.91	13.97
Crystal-like Polyhedra (%)	7.21	5.36	10.77	8.70	9.96	3.33
Other (%)	45.65	52.55	38.40	32.26	39.86	42.12

Table A0.5: Summary of different coordination polyhedra of Vitreloy-105 at 1000 K (Chapter 5).

1000 K		Zr	Ni	Al	Cu	Ti
Voronoi Indices of >5 % Fraction Polyhedra		<0,2,8,5> <0,1,10,4>	<0,2,8,1> <0,2,8,2> <0,3,6,3> <0,4,4,3> <0,3,6,1>	<0,3,6,4 > <0,0,12,0> <0,1,10,2> <0,2,8,2> <0,2,8,4>	<0,2,8,1> <0,2,8,2> <0,3,6,4> <0,3,6,3>	<0,1,10,2> <0,3,6,4>
Full Icosahedra (%)	2.16	0.14	2.86	10.10	2.76	3.27
Icosahedral-like Polyhedra (%)	29.88	30.62	24.83	29.39	30.98	33.90
Mixed Polyhedra (%)	14.25	10.03	20.99	20.76	17.86	12.89
Crystal-like Polyhedra (%)	6.24	4.47	11.80	7.16	7.42	2.51
Other (%)	53.7	59.21	51.32	39.75	48.4	49.94

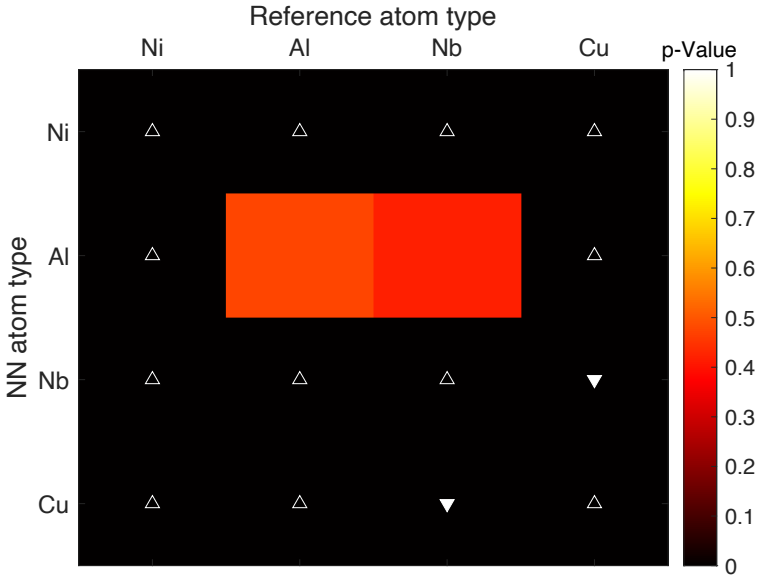

Figure A0.3: LH stat for the hard region (sample ID: R18-59492) of $Zr_{63.49}Cu_{13.59}Ni_{10.32}Al_{11.29}Nb_{1.28}$ (at. %) BMG. Upward triangles determine that the distance between solute-solute pair is decreasing, downward triangle means that the pair distance is increasing. For any other symbol, the values are uncertain. The darker value means that the outcome is non-random with a 95% confidence level.

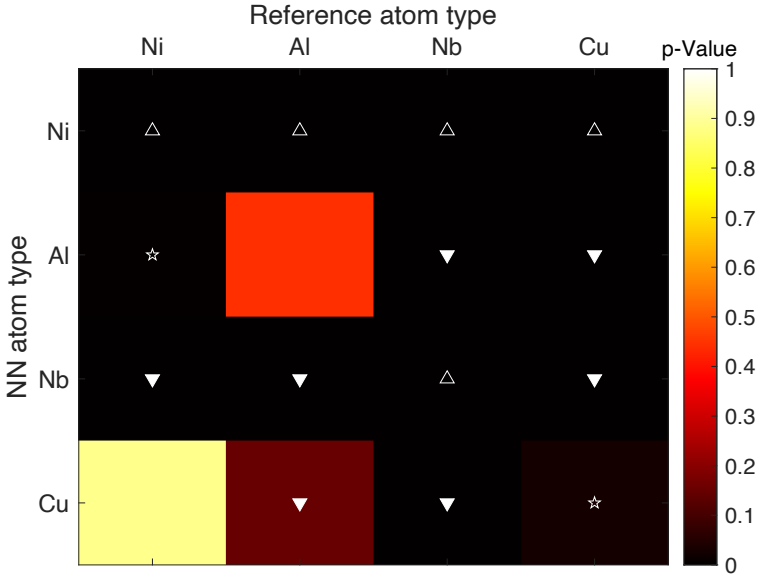

Figure A0.4: LH stat for the hard region (sample ID: R18-59563) of $Zr_{63.49}Cu_{13.59}Ni_{10.32}Al_{11.29}Nb_{1.28}$ (at. %) BMG. Upward triangles determine that the distance between solute-solute pair is decreasing, downward triangle means that the pair distance is increasing. For any other symbol, the values are uncertain. The darker value means that the outcome is non-random with a 95% confidence level.

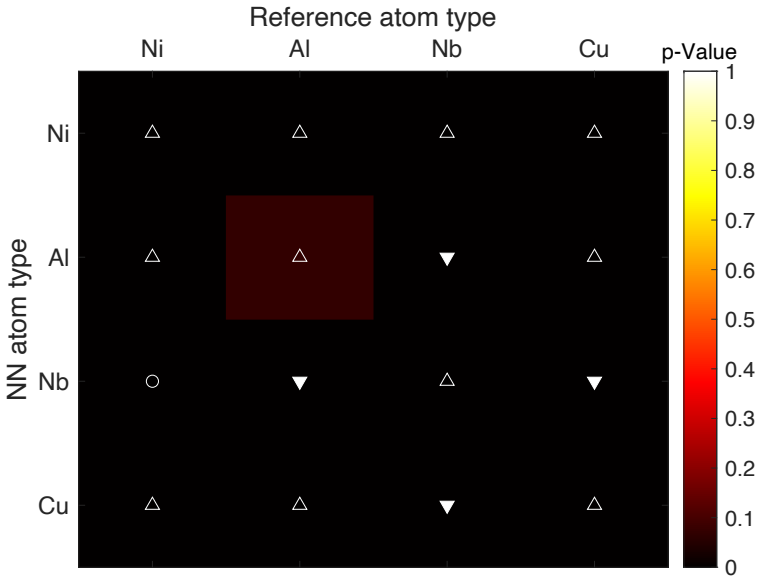

Figure A0.5: LH stat for the hard region (sample ID: R18-59567) of $Zr_{63.49}Cu_{13.59}Ni_{10.32}Al_{11.29}Nb_{1.28}$ (at. %) BMG. Upward triangles determine that the distance between solute-solute pair is decreasing, downward triangle means that the pair distance is increasing. For any other symbol, the values are uncertain. The darker value means that the outcome is non-random with a 95% confidence level.

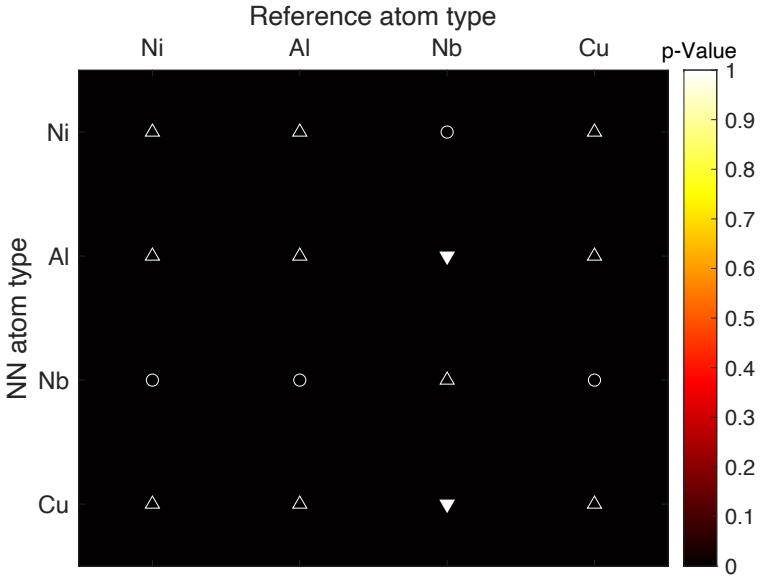

Figure A0.6: LH stat for the soft region (sample ID: R18-59479) of $Zr_{63.49}Cu_{13.59}Ni_{10.32}Al_{11.29}Nb_{1.28}$ (at. %) BMG. Upward triangles determine that the distance between solute-solute pair is decreasing, downward triangle means that the pair distance is increasing. For any other symbol, the values are uncertain. The darker value means that the outcome is non-random with a 95% confidence level.

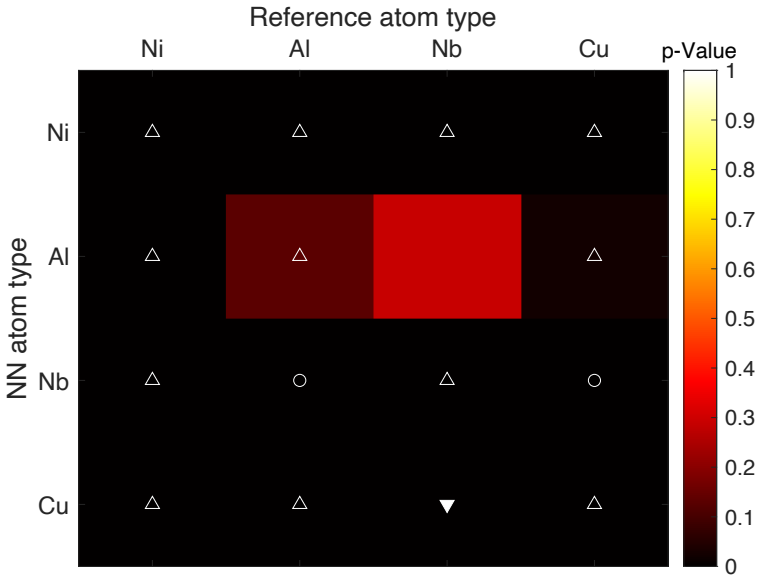

Figure A0.7: LH stat for the soft region (sample ID: R18-59581) of $Zr_{63.49}Cu_{13.59}Ni_{10.32}Al_{11.29}Nb_{1.28}$ (at. %) BMG. Upward triangles determine that the distance between solute-solute pair is decreasing, downward triangle means that the pair distance is increasing. For any other symbol, the values are uncertain. The darker value means that the outcome is non-random with a 95% confidence level.

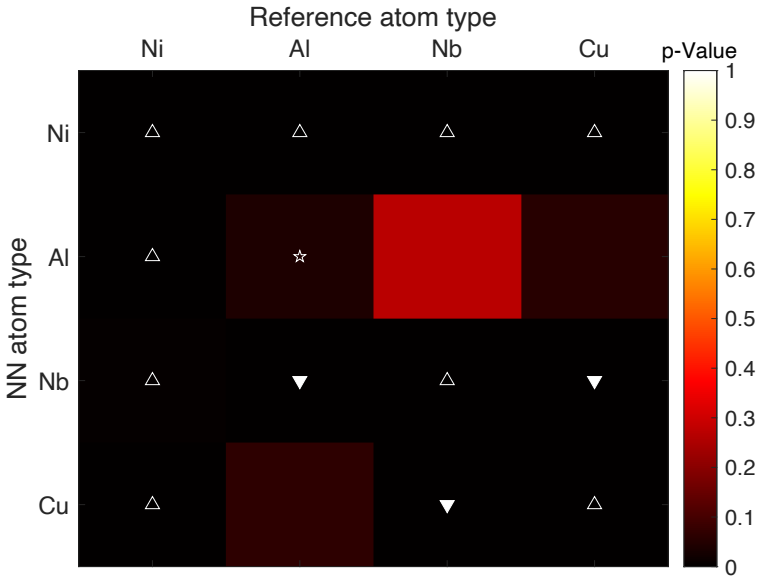

Figure A0.8: LH stat for the soft region (sample ID: R18-59584) of $Zr_{63.49}Cu_{13.59}Ni_{10.32}Al_{11.29}Nb_{1.28}$ (at. %) BMG. Upward triangles determine that the distance between solute-solute pair is decreasing, downward triangle means that the pair distance is increasing. For any other symbol, the values are uncertain. The darker value means that the outcome is non-random with a 95% confidence level.

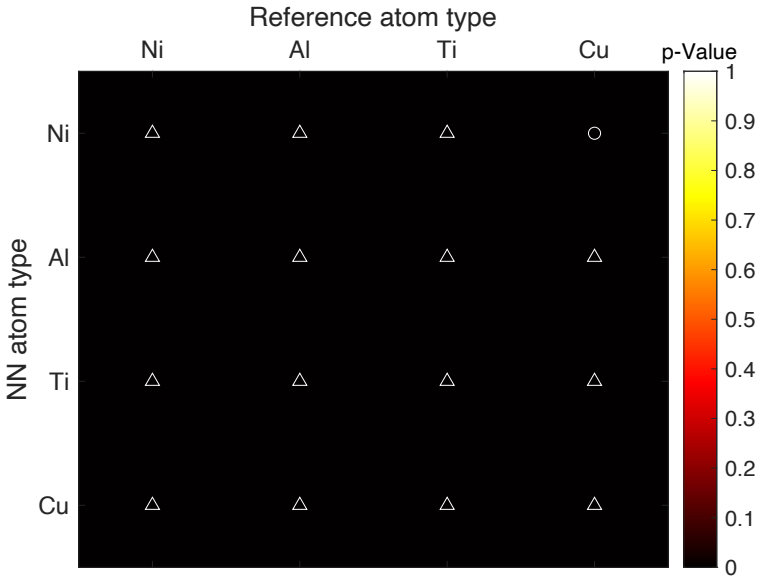

Figure A0.9: LH stat for the soft region (sample ID: R18-59799) of Vitreloy-105 BMG. Upward triangles determine that the distance between solute-solute pair is decreasing, downward triangle means that the pair distance is increasing. For any other symbol, the values are uncertain. The darker value means that the outcome is non-random with a 95% confidence level.

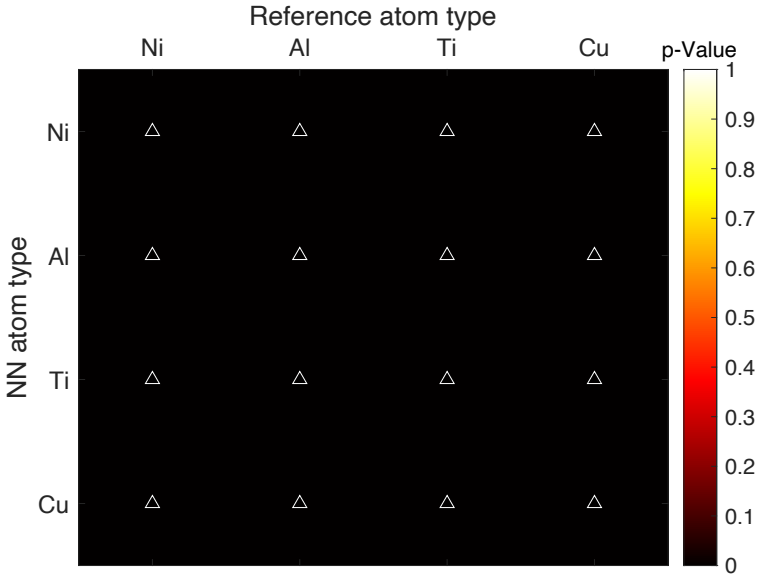

Figure A0.10: LH stat for the soft region (sample ID: R18-60190) of Vitreloy-105 BMG. Upward triangles determine that the distance between solute-solute pair is decreasing, downward triangle means that the pair distance is increasing. For any other symbol, the values are uncertain. The darker value means that the outcome is non-random with a 95% confidence level.

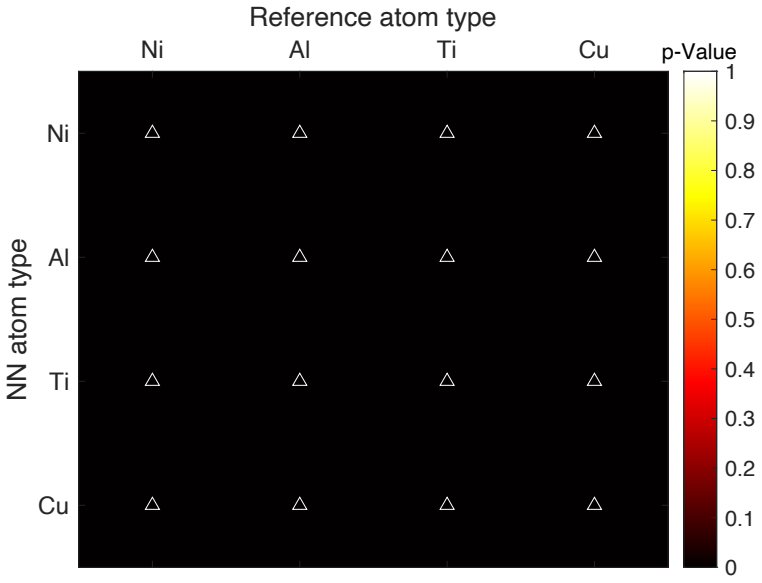

Figure A0.11: LH stat for the soft region (sample ID: R18-60191) of Vitreloy-105 BMG. Upward triangles determine that the distance between solute-solute pair is decreasing, downward triangle means that the pair distance is increasing. For any other symbol, the values are uncertain. The darker value means that the outcome is non-random with a 95% confidence level.

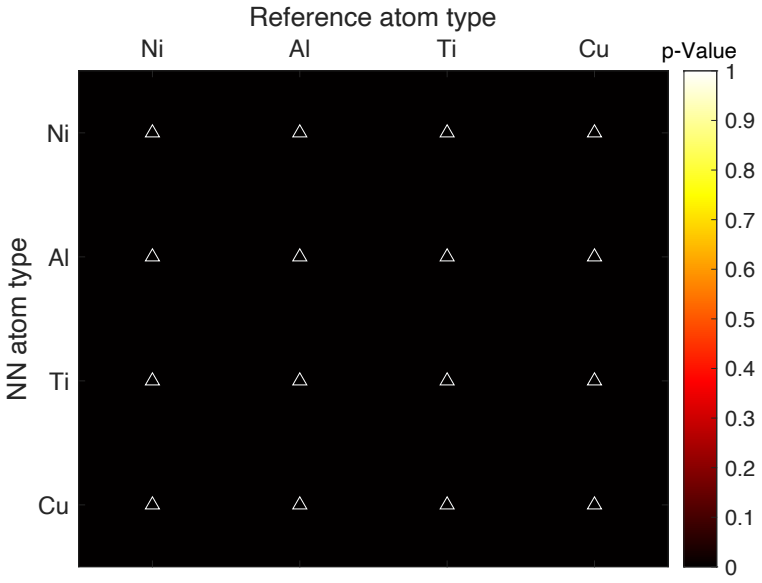

Figure A0.12: LH stat for the hard region (sample ID: R18-59875) of Vitreloy-105 BMG. Upward triangles determine that the distance between solute-solute pair is decreasing, downward triangle means that the pair distance is increasing. For any other symbol, the values are uncertain. The darker value means that the outcome is non-random with a 95% confidence level.

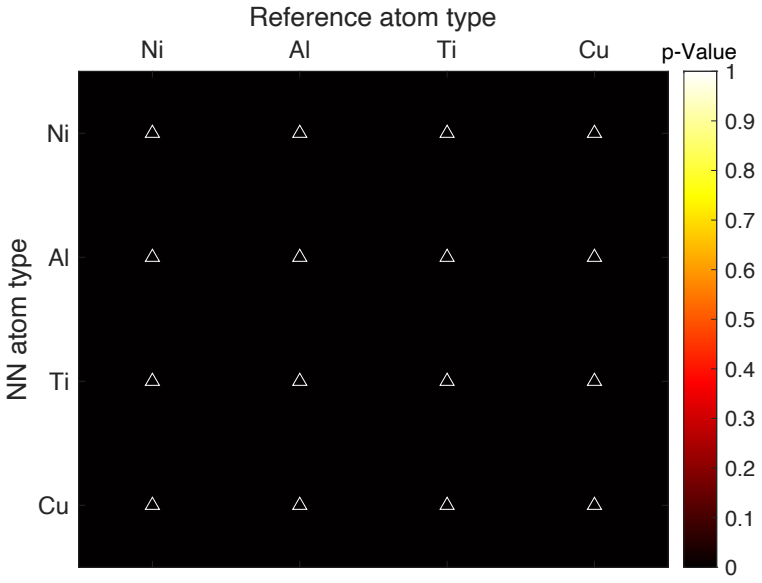

Figure A0.13: LH stat for the hard region (sample ID: R18-59882) of Vitreloy-105 BMG. Upward triangles determine that the distance between solute-solute pair is decreasing, downward triangle means that the pair distance is increasing. For any other symbol, the values are uncertain. The darker value means that the outcome is non-random with a 95% confidence level.

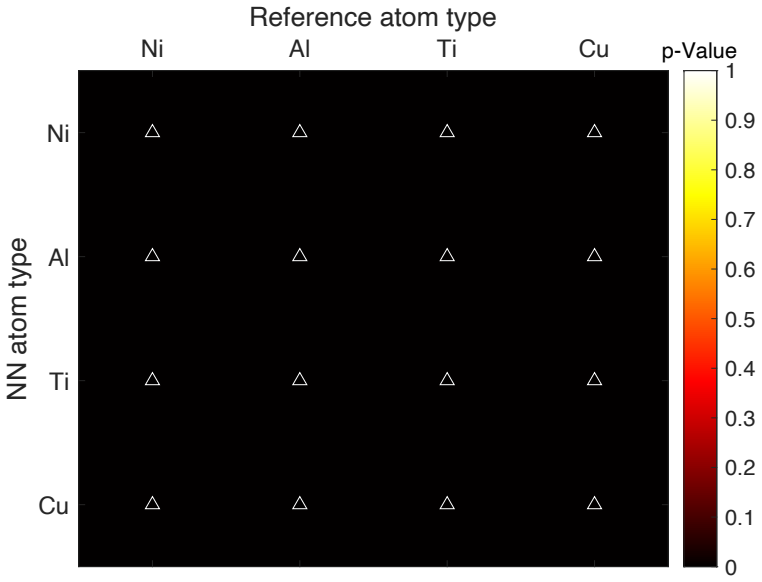

Figure A0.14: LH stat for the hard region (sample ID: R18-59887) of Vitreloy-105 BMG. Upward triangles determine that the distance between solute-solute pair is decreasing, downward triangle means that the pair distance is increasing. For any other symbol, the values are uncertain. The darker value means that the outcome is non-random with a 95% confidence level.

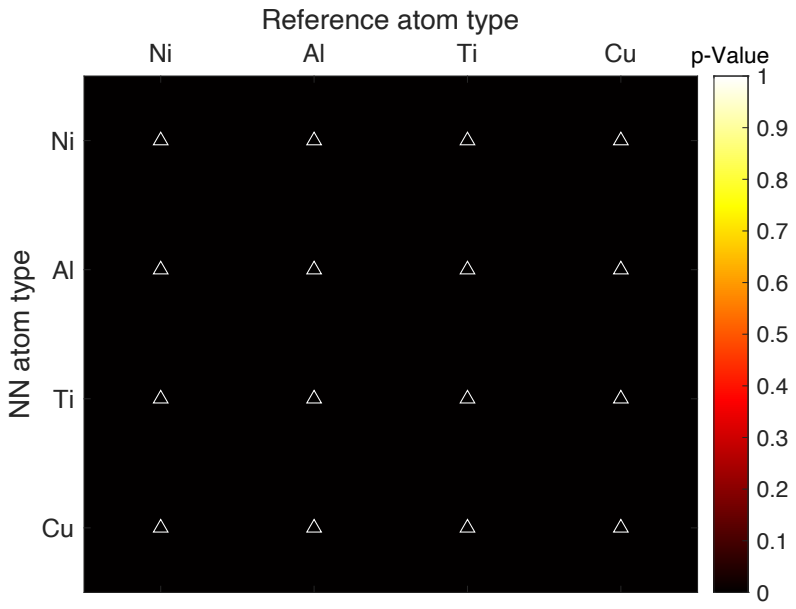

Figure A0.15: LH stat for the fractured region (sample ID: R18-59900) of Vitreloy-105 BMG. Upward triangles determine that the distance between solute-solute pair is decreasing, downward triangle means that the pair distance is increasing. For any other symbol, the values are uncertain. The darker value means that the outcome is non-random with a 95% confidence level.

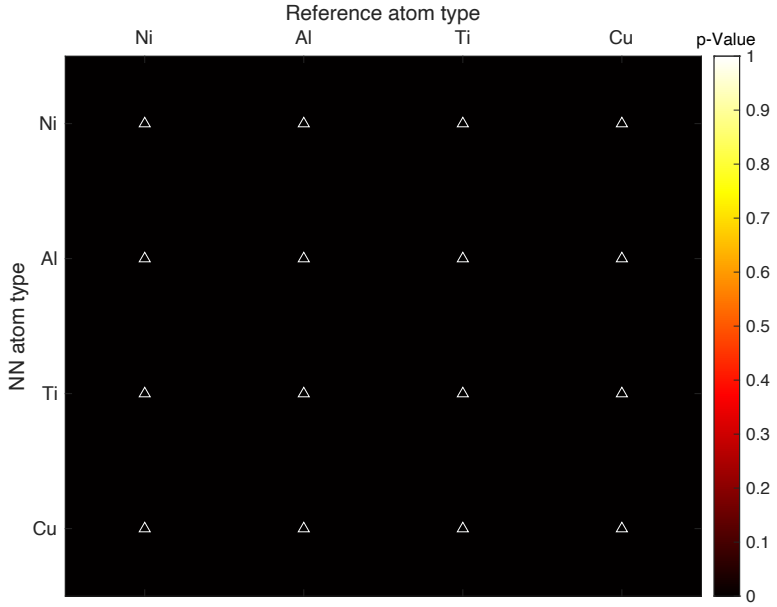

Figure A0.16: LH stat for the fractured region (sample ID: R18-60073) of Vitreloy-105 BMG. Upward triangles determine that the distance between solute-solute pair is decreasing, downward triangle means that the pair distance is increasing. For any other symbol, the values are uncertain. The darker value means that the outcome is non-random with a 95% confidence level.

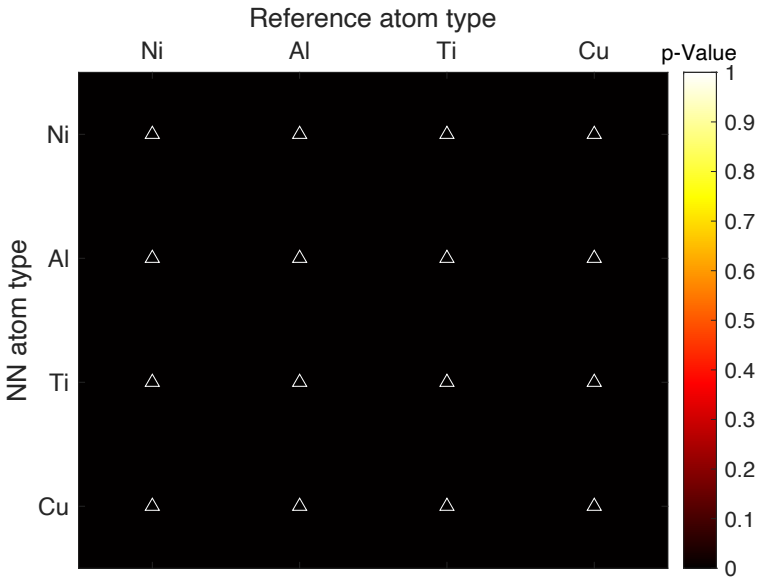

Figure A0.17: LH stat for the fractured region (sample ID: R18-60075) of Vitreloy-105 BMG. Upward triangles determine that the distance between solute-solute pair is decreasing, downward triangle means that the pair distance is increasing. For any other symbol, the values are uncertain. The darker value means that the outcome is non-random with a 95% confidence level.

APPENDIX B List of Publications

1. Nomoto, K., Li, B., Gammer, C., Ceguerra, A.V., Bilal, H., Hohenwarter, A., Eckert, J., Gludovatz, B., Ringer, S.P. and Kruzic, J.J.
   Deformation-induced medium-range order changes in bulk metallic glasses.
   Physical Review Materials. (IF: 3.989), 2022.
   DOI: 10.1103/PhysRevMaterials.6.043603

2. H. Bilal, K.Nomoto, A.V.Ceguerra, B.Gludovatz, J.Eckert, S.P.Ringer
   Atom prob analysis of a Zr-based bulk metallic glass.
   Microscopy & Microanalysis. (IF: 3.414), 2021.
   DOI: 10.1017/S1431927621012824

3. K.Nomoto, A.V.Ceguerra, C.Gammer, B.Li, H.Bilal, A.Hohenwater, B.Gludovatz, J.Eckert, S.P.Ringer, J.J.Kruzic.
   Medium-range order dictates local hardness in bulk metallic glasses.
   Materials Today (IF: 26.416), 2020.
   DOI: 10.1016/j.mattod.2020.10.032

4. H. Bilal, K.Nomoto, A.V.Ceguerra, B.Gludovatz, J.Eckert, S.P.Ringer
   Chemical analysis of structural heterogeneities defining plasticity in Zr-based BMGs. (In process of submission), Physical Review Letters. (IF: 15.2), 2021

5. O. J. Akinribide, B. A. Obadele, S. O. Akinwamide, H. Bilal, O. O. Ajibola, O. O. Ayeleru,... & P. A. Olubambi.
   Sintering of binderless TiN and TiCN-based cermet for toughness applications: Processing techniques and mechanical properties: A review.
   Ceramics International, *45*(17), 21077-21090, (IF: 3.64), 2019.
   DOI: 10.1016/j.ceramint.2019.07.191

6. H. Bilal, K.Nomoto, A.V.Ceguerra, B.Gludovatz, J.Eckert, S.P.Ringer, Analysing Zr-*Based Bulk Metallic Glasses (BMGs)with Clustered Evaporation in Atom Probe Tomography.*
   Ultramicroscopy *(In Progress),* (IF: 2.55).

APPENDIX C List of Presentations

1. "Bulk Metallic Glasses under Atom Probe Microscopy Analysis," poster presentation at the International Microscopy Congress 19 (IMC-19), 9 – 14 September 2018, Sydney, Australia.

2. "Scope of Atom Probe Tomography for the Analysis of Bulk Metallic Glasses," poster presentation at the 6th conference of Combined Australian Material Societies (CAMS), 27 – 29 November 2018, Wollongong, Australia.

3. "Effect of Operating Conditions on the Outcome of Bulk Metallic Glasses through Atom Probe Tomography," oral presentation at the Atom Probe Tomography User Meeting (APT&M 2019), 18 – 22 June 2019, Wisconsin, USA.

4. "Clustered Evaporation Analysis of Bulk Metallic Glasses by Atom Probe Tomography," oral presentation at the Australian Conference on Microscopy and Microanalysis 26 (ACMM-26), 16 – 20 February 2020, Canberra, Australia.

APPENDIX D Awards

- Paulette Isabel Jones Scholarship, 2021.
- Australian Microscopy and Microanalysis Society (AMMS) Travel Bursary award, 2020.
- Charles Kolling Travel award, 2018.
- Postgraduate Research Scheme (PRSS) Scholarship award recipient 2018 and 2019.